Jagiellonian University

Faculty of Physics, Astronomy and Applied Computer Science

OPTICAL PROPERTIES OF HOST GALAXIES IN GIANT RADIO SOURCES

PhD Thesis

by

Agnieszka Kuźmicz

The thesis was written under the supervision of

Prof. Stanisław Zoła

submitted to the Jagiellonian University
for the degree of Doctor of Philosophy in Astronomy

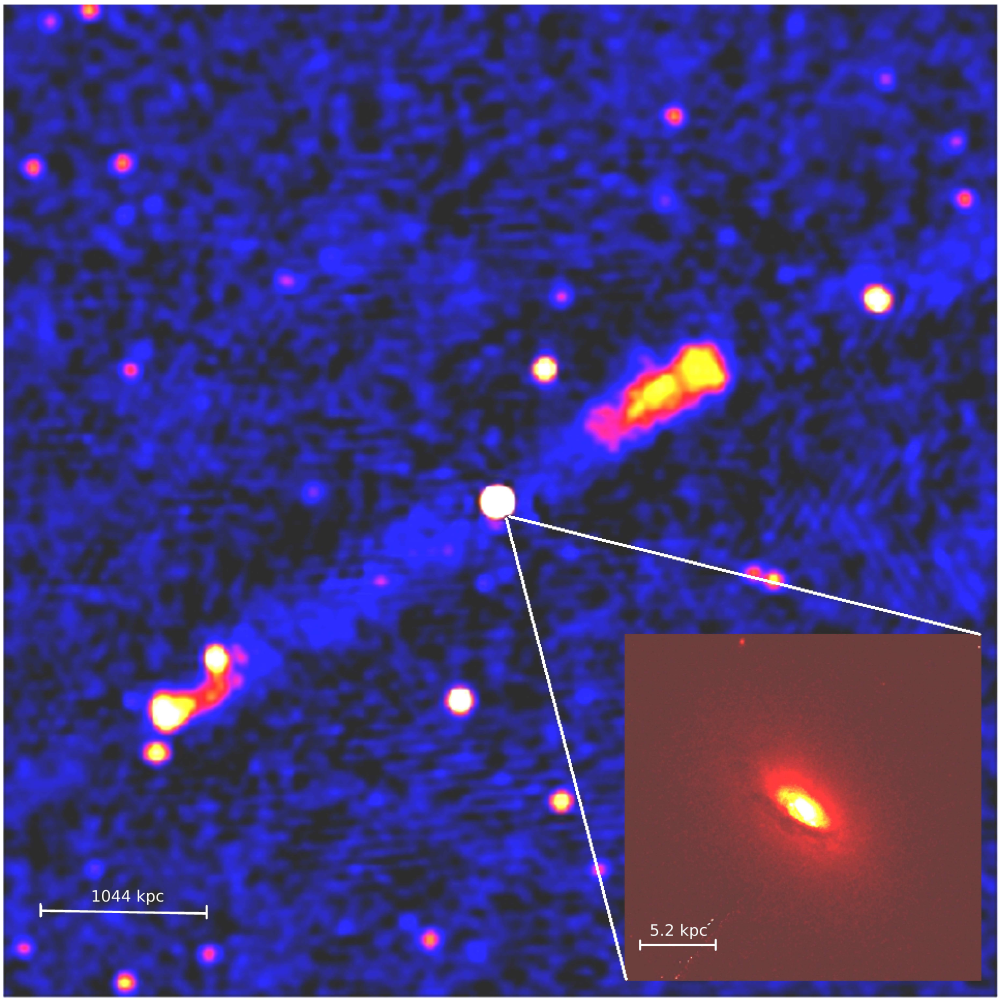

To my family

Abstract

Giant radio sources are the largest single objects in the Universe. The projected linear size of their radio structures, larger than 0.7 Mpc, makes them valuable objects to study many astrophysical problems. It is still unclear why only a small fraction of radio sources reaches such a large size. It is considered that it may be due to special external conditions, such as lower intergalactic medium density. Other investigators pointed out the internal properties of the "central engine" or an advanced age of the radio structure and/or recurrent radio activity as a possible cause.

In my Thesis I investigate the hypothesis that the giant radio sources can have very large radio structures due to specific properties of their central active nuclei. Because of lack of a representative sample of such objects, as many radio sources were not recognised to be giants, this hypothesis was not investigated in detail. By comparing the radio and optical surveys, a lot of gigantic-size radio sources have been recently discovered. I selected a sample of giant radio sources and compared the fundamental physical parameters of their active nuclei (such as black hole masses and accretion rates) with parameters of observed radio structures. As a result, I found out that when taking into account the optical and radio properties, giant radio sources have properties similar to those of smaller size and that giants do not have more powerful central engines than other radio sources. The results obtained in this work are consistent with evolutionary models of extragalactic radio sources, that predict that giants could be the more evolved (aged) sources compared with smaller ones. In addition, I discovered that the environment may play only a minor role in the formation of large-scale radio structures. In my thesis I showed out that giants have relatively large number of old star with solar-like metalicity. The stellar population composition of giant radio galaxies could be the only property that distinguishes them from other radio sources. This fact may suggest that different histories of the host galaxy formation may be the main reason why some of radio sources evolved to giant size.

Podziękowania

Dziękuję dr Markowi Jamrozy za opiekę naukową w trakcie studiów doktoranckich. Jestem Panu wdzięczna za poświęcony mi czas, za wszystkie rady, sugestie dotyczące prowadzonych badań, za inspiracje oraz za troskę o przebieg mojej "kariery" naukowej. To była przyjemność pracować z Panem. Dziękuję Panu za wszelkie okazane dobro ... po prostu – za dobre serce.

Dziękuję Prof. Stanisławowi Zole za opiekę naukową, wsparcie, oraz za to, że jako charyzmatyczny szef i promotor motywował mnie do bycia lepszym we wszystkich rzeczach, które robiłam.

Bardzo dziękuję mojemu mężowi Arturowi za cierpliwość do mnie oraz za to, że mnie wspierał podczas całych studiów doktoranckich, a zwłaszcza w ostatnim roku. Bez tej pomocy i poświęcenia skończenie rozprawy doktorskiej nie było by możliwe.
Dziękuję wszystkim tym, którzy dobrze mi życzyli i mnie wspierali w różnych momentach życia.

Chciała bym również podziekować Dorocie Kozieł-Wierzbowskiej za liczne rady i sugestie dotyczące mojej pracy.
Za dane do prowadzonych przeze mnie badań diękuję Dorocie, Rickowi White oraz Marianne Vestergaard.

Badania prowadzone w ramach doktoratu zostały częściowo sfinansowane ze środków Narodowego Centrum Nauki przyznanych na podstawie decyzji numer DEC-2011/01/N/ST9/00726 oraz grantu MNiSW 3812/B/H03/2009/36.

Contents

Chapter 1

Introduction

1.1 Active Galactic Nuclei

Active galactic nuclei (AGNs) are one of the most luminous objects in the Universe. They are observed at all wavebands - from radio to gamma ray. Their luminosity is not attributed to the light of stars but to powerful processes which take place in the central parts of the host galaxy. It is believed that radiation of AGN is caused by mass accretion on a supermassive black hole (SMBH) located in the center. In about 10% of all known galaxies the activity phenomenon is observed.

Usually an object is classified as an AGN, if at least one of the following properties is observed (Netzer 2006):

1. A compact nuclear region, brighter than the corresponding region in galaxies of similar Hubble type.
2. Nonstellar origin of continuum emission.
3. Nuclear emission lines indicate excitation by a nonstellar continuum.
4. Variable continuum and/or emission lines.

According to the commonly accepted picture of an AGN, a super massive black hole is located in the center of a galaxy. It is surrounded by an accretion disk where matter loses angular momentum and eventually is accreting onto the black hole (BH). The accretion processes cause a strong UV and X-ray radiation which ionize the clouds of gas moving with high velocities around the vicinity of the accretion disk. This region, where the broad emission lines have their origin, is named a broad line region (BLR). All of those components are surrounded by a gaseous and dusty torus. At a larger distance to the black hole, the clouds of gas move with lower velocities forming narrow line region (NLR), where narrow emission lines are produced. In radio loud objects we observe radio emission, visible as radio jets flowing from the vicinity of the BH in opposite directions and feeding radio lobes. A schematic view of an AGN structure is presented in Figure 1.1 and the typical values of its components and properties are listed in Table 1.1.

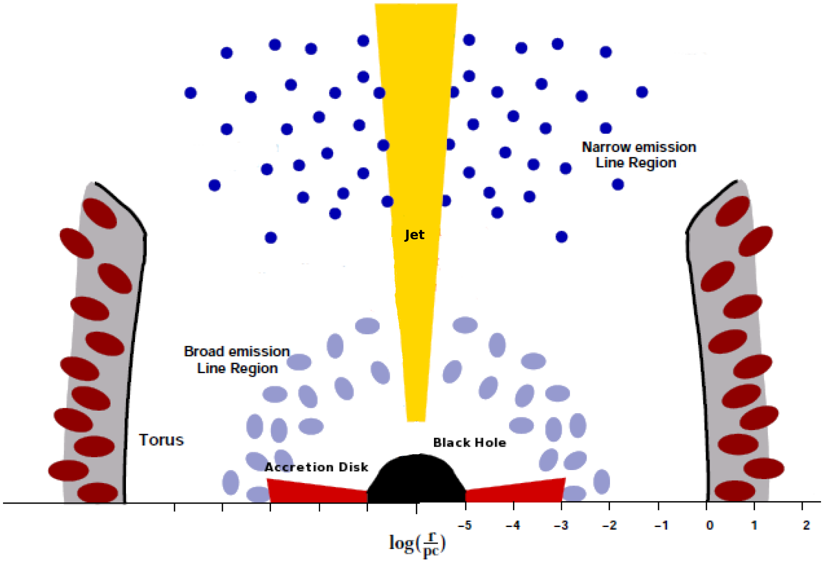

FIGURE 1.1: The schematic view of an AGN (Zier & Biermann 2002). The horizontal axis is logarithmically scaled to 1 pc.

TABLE 1.1: AGN components and their typical properties.

Parameter	Value
Black hole mass	10^5 - 10^9 $M_\odot$
Range of luminosities	10^{42}-10^{48}erg/s
Time scales of variability	minutes[1] to decades
Eddington ratio	0.01-1
Size of an accretion disk	$\sim 10^{-3}$ pc
Size of BLR	$\sim 10^{-2}$-1 pc
Velocity dispersion in BLR	>1000-2000 km/s
Temperature of BLR	$\sim 10^4$ K
Size of a torus	~10-100 pc
Dust temperature in a torus	few hundred K
Size of NLR	~100-10000 pc
Velocity dispersion in NLR	<1000-2000 km/s

[1] e.g. for the blazar PKS 2155-304 (Tremaine et al. 2002).

The above presented picture of AGN components is based on many observational and theoretical studies. However, our knowledge about its physics, dynamics and geometry is still incomplete. The spectroscopic data of innermost AGN regions give the evidence of the existence of a strong continuum emitting source, BLR, NLR and a dusty torus.

It is believed that accretion processes are responsible for observed X-ray, UV and optical continuum emission. They also can be responsible for occurence of winds and generation of radio jets. However, the nature of an accretion disk is still not well understood. The commonly used accretion models (Bondi 1952, Shakura & Syunyaev 1973, Abramowicz & Fragile 2013) usually simplify this extremely complicated process.

The observed broad and narrow emission lines are believed to originate in clouds of gas which move with high or low velocities, respectively. The strongest broad emission lines observed in spectra of AGNs are: Balmer lines, MgII, HeII, HeI, OI – low ionization lines; and NV, CIV, CIII – high ionization lines. They are not visible in all AGNs, whereas narrow lines are present in practically all AGNs. The most prominent narrow emission lines are: [OIII], [OII], [NII], [OI] and [SII]. Additionally, the broad Lyman and Balmer series as well as CIV have narrow components. It is believed that photoionisation is the main physical process responsible for generation of emission line, however, shocks created during radio jet propagation might also contribute to the excitation process (Davidson & Netzer 1979). The nature and origin of BLR is still an open question. It was proposed that BLR is related to outflows from the accretion disk (e.g Laor 2003, Tran 2003) and in some objects, the conditions for producing a BLR do not appear (e.g. in objects with low Eddington rates; Czerny, Różańska & Kuraszkiewicz 2004). The explanation of a probable origin of low ionization part of BLR was proposed by Czerny & Hryniewicz (2011) who worked out a model which describes the BLR appearance as a result of a strong dusty wind from the accretion disk.

In order to explain absorption of the optical and X-ray emission in some AGNs, the existence of gaseous and dusty torus was proposed. Earlier studies considered the properties of tori. It was proposed that the torus could consist of a large number of optically thick, dusty clouds (Krolik & Begelman 1988). Later Tristram et al. (2007) showed a strong evidence for a clumpy or filamentary dust structure of the torus. The origin of an AGN torus and the process of dust production is still not well known. There are some suggestions that AGNs do produce their own dust (Elvis, Marengo & Karovska 2002, Jiang et al. 2010). However, the most commonly considered sources of dust are supernovae (Bianchi & Schneider 2007) and asymptotic giant branch stars (Sedlmayr 1997).

1.2 AGN classification and unification scheme

AGNs are classified into various classes depending on properties observed at different wavebands. When taking into account the strengths of radio flux, AGNs can be divided into radio-loud and radio-quiet.

When we focus on the properties of optical/UV spectra one can distinguish the following AGN classes:

Broad Line or Type 1 AGNs - in their spectra the broad emission lines and bright continuum are observed. Radio Loud Quasars, Radio Quiet Quasars, Broad Line Radio Galaxies (BLRGs) and Seyfert Galaxies Type 1 belong to this class.

Narrow Line or Type 2 AGNs - with narrow emission lines and weak continuum: i.e. Narrow Line Radio Galaxies (NLRGs), Seyfert Galaxies Type 2.

Blazars or Type 0 AGNs - with weak emission lines and strong continuum emission originated in the radio jet - their emission is affected by relativistic effects.

The spectra of three AGN classes are presented in Figure 1.2 as examples.

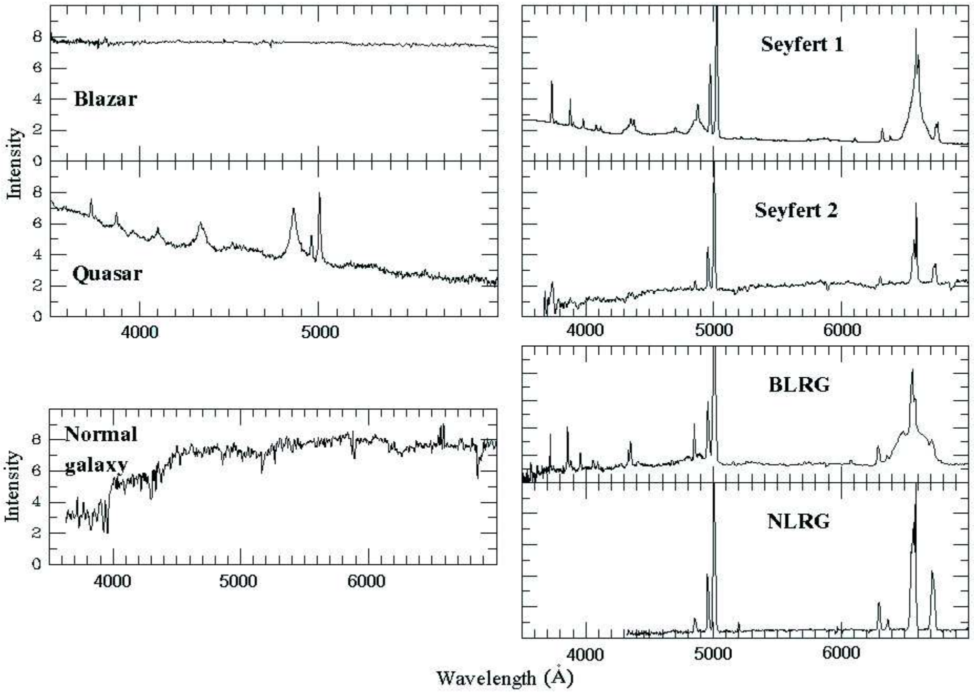

Figure 1.2: The typical optical spectra of different classes of AGN.

Because of large number of different types of AGNs and their properties, it was needed to find a unified model able to explain the variety of such objects. Such a scheme was proposed by Antonucci (1993) and further developed by Urry & Padovani (1995) for radio loud objects. This unification scheme proposes that the apparent differences between various types of AGNs are caused solely by their different orientation toward the observer (see Figure 1.3).

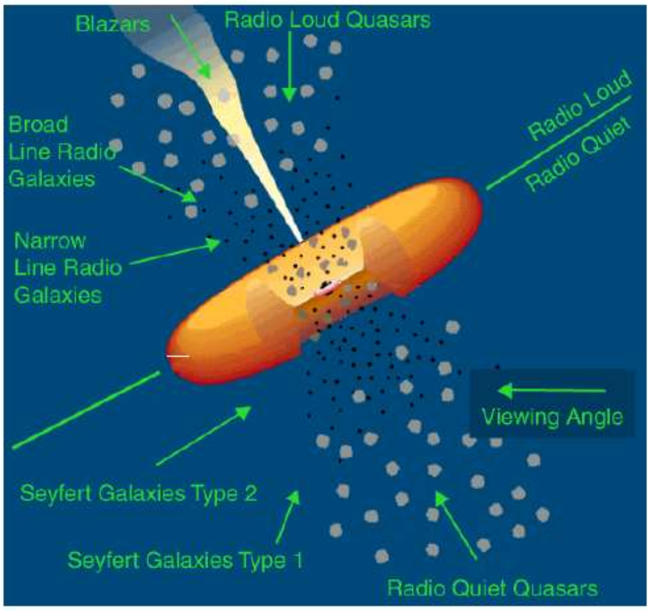

Figure 1.3: The classification of AGNs by Urry & Padovani 1995. The inclined line divides AGNs to radio-loud sources (presence of a jet; upper part) and radio-quiet sources (lower part).

1.2.1 Black hole masses

It is believed that the central BH plays an important role in an AGN duty cycle. The history of the SMBHs formation is still unclear and it is the subject of many studies (e.g. Marconi et al. 2004, King & Pringle 2006, Netzer et al. 2007, Volonteri & Begelman 2010). The most probable process of BH mass supplying is the accretion of matter from the host galaxy. There are two main parameters describing this process. The radiative accretion efficiency (η) which represents the efficiency of conversion of mass into radiation. It depends on the BH spin and the angular momentum of the accretion disk. The value of η is in the range of $\sim$0.04 to $\sim$0.4 (King & Pringle 2006). The second parameter is the Eddington ratio ($\dot{m}$) relating the AGN bolometric luminosity with the Eddington luminosity. For accretion disk around a rapidly rotating SMBH with mass $M_{BH}=10^8$ M$\odot$, the values of η=0.1 and luminosity typical of quasars, the mass accretion rate required to maintain the disk luminosity is about 1-10 M$\odot$/yr. Less luminous AGNs may have correspondingly smaller mass accretion rates.

There are few direct/indirect methods which make estimation of BH mass possible. They are depended on the AGN type and its cosmological distance. For Type 2 AGNs (where gas and dust block our view of the BLR), the emission of the water megamaser of the disk molecular gas in a galaxy is the most accurate way for BHs mass determination (Miyoshi et al. 1995). For Type 1 AGNs the most accurate way is the reverberation mapping virial method (to be discussed in Section 2.3.3). Also the dynamical methods, based on stellar or gas kinematics (e.g. Onken et al. 2007) are used, but they can be applied only to nearby and not very luminous AGNs.

The most useful, though indirect, method of BH mass determination is the single epoch virial method, discussed in Section 2.3.3. Other methods based on comparison of the dynamical SMBH mass estimations from observational properties of the host galaxy can also be very useful. The following correlations were found: BH mass - bulge luminosity ($M_{\rm BH}$-$L_{\rm bulge}$) relation (Kormendy & Richstone 1995); BH mass - bulge mass ($M_{\rm BH}$-$M_{\rm bulge}$) relation (Magorrian et al. 1998); BH mass - velocity dispersion ($M_{\rm BH}$-σ_*) relation (Ferrarese & Merritt 2000; Gebhardt et al. 2000; discussed in Section 3.2.2).

1.3 Radio sources

Radio sources (RSs) are one of the AGN classes. They exhibit a wide range of sizes and morphological structures at radio wavelengths. RSs can be extremely compact or very extended. In many cases their morphology is complex and not all of structures appear in every source. A powerful radio source consists of a central AGN and two jets pointed out in opposite directions, which are collimated outflows of charged particles (e.g. electrons, protons) moving with relativistic speeds in magnetic field. The jets blow up a large cocoon in the interstellar (ISM) or intergalactic (IGM) medium where they propagate and collide with ambient medium. The extended radio lobes are usually ended by the hot spots, explained as being due to a strong shock fronts, produced by the collision of supersonic jet with ambient medium.

RSs can be divided into some subclasses based on their morphology, properties of the optical identification or linear size. If we consider the radio morphology, two classes of RSs are distinguished: Fanaroff-Riley Type I (FRI) and Type II (FRII) (Fanaroff & Riley 1974). There is a relatively sharp transition in radio luminosity between FRIs and FRIIs corresponding to $P_{\rm 178MHz} \simeq 2 \times 10^{25}$W/Hz/sr. Most of sources with lower luminosity are of FRI type. FRI radio sources are edge-darkened - they are brightest towards the center and fade further from the core ending in huge radio lobes or plums, while FRII radio sources are edge-brightened - they are brightest at the edges where hot spots are located and rather faint near the bright radio core. The examples of FRI and FRII radio sources are presented in Figure 1.4. The dichotomy between FRI and FRII radio sources is still under debate. Many authors speculate about the physical explanation of this division. They proposed that the morphological difference between FRI and FRII sources can be explained by deceleration of jets caused by the environment (Gopal-Krishna & Wiita 2000) and/or due to differences in black hole spin and accretion processes (e.g. Baum, Zierbel, & O'Dea 1995; Meier 1999) or different jet composition (e.g. Celotti & Fabian

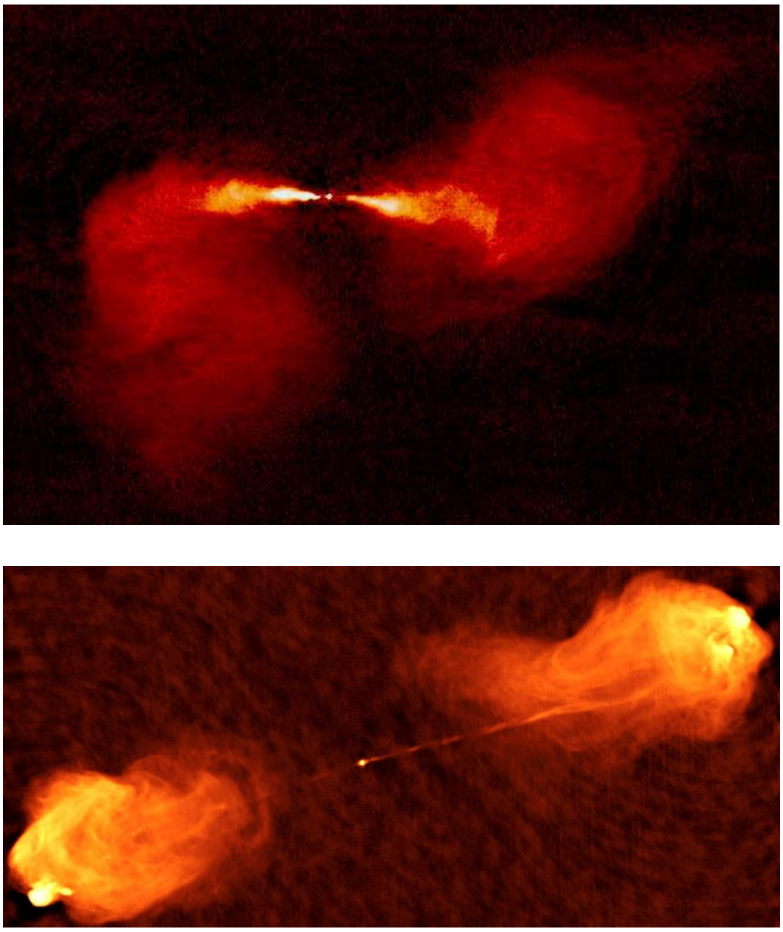

Figure 1.4: Top panel: FRI radio galaxy M84 (6cm VLA image); Bottom panel: FRII Radio Galaxy Cygnus A (6cm VLA image).

1993).

A morphological subtype of Fanaroff-Riley class, named double-double radio sources (DDRSs) is also distinguished. They consist of two pair of lobes: the older outer and younger inner ones, which represent different phases of radio activity (see Figure 1.5).

Looking at the optical properties of optically identified RSs, they can be divided to radio galaxies (RGs) and radio quasars (RQs). RGs are usually associated with optically extended objects and they show only narrow emission lines with full width at half maximum (FWHM) $\lesssim$1000 km/s. RQs are linked to bright compact objects where their nuclei outshine the host galaxy. Quasars (QSOs) show strong broad emission lines with FWHM>1000 km/s. At the radio wavelengths, RGs and RQs are very similar although radio quasars tend to have stronger radio cores (Saikia & Kulkarni 1994), one sided radio jets (Bridle & Perley 1984), more asymmetric morphology (Best et al. 1995), and highly polarized structures (Laing 1988).

Finally, if we take into account the linear size of radio structure of RSs, they can be

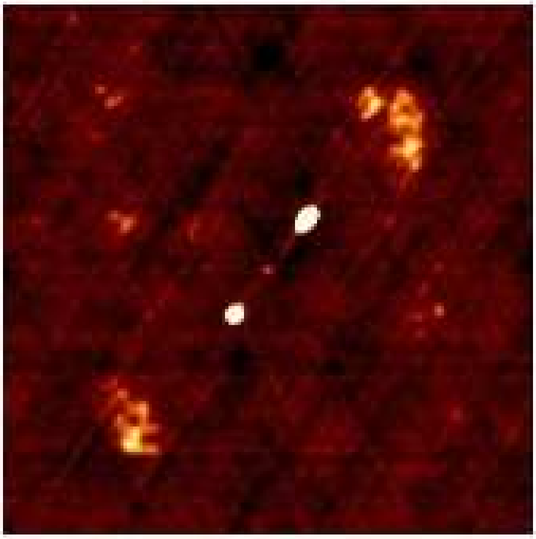

Figure 1.5: J1158+2621, a double-double radio galaxy (21cm VLA image).

divided to: gigahertz peaked spectrum radio sources with sizes <1 kpc and compact steep spectrum (CSS) radio sources of 1-20 kpc morphologies; RSs with medium linear sizes ∼100-700 kpc, and extremely large sources with complex structures extending to a few Mpc.

In spite of many studies of the mechanism of jet generation (e.g. Blandford & Znajeck 1977), we do not know exactly what is the physical process responsible for this phenomenon. Not only this mechanism, but also the evolution of radio structures is subject of debate. The typical time of a radio source activity phase is short, 10-100 Myr (Alexander & Leahy 1987, Liu, Pooley & Riley 1992). The observed range in RS sizes, from subgalactic (<1 kpc) to cluster scales (>1 Mpc), has been interpreted as an evidence for evolution of radio source size with age (e.g. Kaiser & Alexander 1997). It is believed that radio sources start their evolution as very compact GPS phase, pass through the CSS stage, classical medium size FR I or FR II radio sources and finally some may reach the phase of a giant radio source (GRS).

The relation between a BH mass and radio loudness has also been intensively studied, but the results are ambiguous so far. Many authors (e.g. Dunlop et al. 2003, Laor 2000, Marziani et al. 2003, McLure & Dunlop 2002, McLure & Jarvis 2004) have found that, on average, radio-louder AGNs possess larger BH masses. However, there are also many reports arguing against any dependence between these quantities (e.g., Cirasuolo et al. 2003, Ho 2002, Oshlack, Webster & Whiting 2002, Snellen et al. 2003, Woo & Urry 2002). Furthermore, the importance of the mechanical energy of jets and lobes released by BHs and the feedback on the surroundings has recently been realized (Cattaneo &

Best 2009, Merloni & Heinz 2008, Shankar et al. 2008). There are also evidences that the spin of the BH plays a significant role in AGNs radio activity (e.g. Ghisellini & Tavecchio 2008, Shankar et al. 2010, Sikora, Stawarz & Lasota 2007).

1.3.1 Optical properties of radio sources

The optical properties of various samples of RSs were studied by many authors. This topic is important for investigating the structure, the environment of a host galaxy and also the physical conditions of central regions of active nuclei. The radio loudness of AGNs still remains an debated issue. Radio observations of optically selected samples of active galaxies and quasars showed that only 10-40% of the objects are powerful radio sources (for reference see e.g. Cirasuolo et al. 2003, Jiang et al. 2007). Recently, thanks to large area radio surveys, the number of RSs with faint radio fluxes has grown enormously. Therefore, it is now possible to investigate the optical and radio properties of AGNs, based on statistically significant samples of objects (e.g. Cirasuolo et al. 2003, Hewett, Foltz & Chaffee 2001, Ivezic et al. 2002, Jiang et al. 2007, Shankar et al. 2010, White et al. 2000), and try to understand the connection between the optical emission (luminosity, BH mass and spin, accretion rate) and the radio (jet) activity.

It is well known that majority of radio sources are hosted by luminous, massive elliptical galaxies, often interacting with a close companion galaxy. However, there are few exceptions (e.g. Ledlow, Owen & Keel 1995) where a host galaxy is disk dominated. Considering the host galaxies of RSs, it was found that FRI and FRII radio sources differ in magnitude distributions, colors and the host galaxy structures (Zirbel & Baum 1995, Zirbel 1997). On average, FRII hosts are weaker and have bluer colors than those in FRI type. The environments of FRI and FRII radio galaxies are also different. Additionally, FRI sources are located in richer groups of galaxies, while these of FRII types avoid them up to z$\sim$0.5. On the other hand, FRII radio sources exist in rich cluster environments at high redshifts. The host galaxies of FRII type frequently have morphological features like tails, bridges or shells, that suggest that they arose due to collision or merger of galaxy pairs, while large fraction of FRIs show evidence of ongoing or past interactions with companion galaxies.

Based on the optical studies of Grandi & Osterbrock (1978), Steidel & Sargent (1991), Corbin (1992), Cohen & Osterbrock (1981) it was found that radio-loud and radio-quiet AGNs have very similar emission line properties and that differences between some of their spectral features are not significant. However, some differences were noticed between FRI and FRII sources. All broad line objects which are high excitation galaxies (with [OIII]/Hα>0.2 and equivalent width of [OIII]>3Å) show FRII morphology, while low excitation galaxies have both FRI and FRII morphologies (Buttiglione et al. 2010).

In general, it was found that emission lines luminosities are correlated with radio power (e.g. Rawlings et al. 1989, Rawlings & Saunders 1991, Baum & Heckman 1989a,b). This relation was also found for CSS sources (Morganti et al. 1997) and GPS sources (Labiano 2008). The obtained relation suggests that the radio and line luminosities of RSs are determined, to the first order, by the properties of their central engine (Willott et al. 1999). Other factors such as the environment may play a secondary role (Baum & Heckman 1989b). Another possibility is that the line and radio luminosities may be independently correlated with e.g. the amount of cold gas present in the kpc scales from the nucleus. The above-mentioned correlation is flatter for FRI than FRII radio sources. It was found that FRII sources produce emission lines which are about 5-30 times more prominent than those of FRI ones for the same total radio power (Zirbel & Baum 1995).

1.3.2 Giant radio sources

GRSs are defined as powerful extragalactic radio sources, hosted by galaxies or quasars, for which the projected linear size of their radio structure is larger than 0.72 Mpc (assuming $H_0 = 71$ km s^{-1}Mpc^{-1}, $\Omega_M = 0.27$, $\Omega_\lambda = 0.73$; Spergel et al. 2003)[2]. Looking through the new, "all-sky" radio surveys such as the Westerbork Northern Sky Survey (Rengelink et al. 1997), the NRAO VLA Sky Survey (NVSS; Condon et al. 1998), the Faint Images of the Radio Sky at Twenty centimeters (FIRST; Becker, White & Helfand 1995), the Sydney University Molonglo Sky Survey (Bock, Large & Sadler 1999) and the Seventh Cambridge Survey (McGilchrist et al. 1990) a large number of new giant sources was identified. Almost all of these GRSs are included in the samples of giants presented by Cotter, Rawlings & Saunders (1996), Lara et al. (2001), Machalski, Jamrozy & Zoła (2001), Machalski et al. (2006), Saripalli et al. (2005), Schoenmakers et al. (2001), as well as in the list of giants known before 2000 published by Ishwara–Chandra & Saikia (1999). To date, there are about 230 GRSs known and just a small fraction of them ($\sim$ 8%) are actually related to quasars, but the number of GRSs is still growing. The largest known GRS is the J1420$-$0545 source with the projected linear size equal to 4.69 Mpc (Machalski et al. 2008).

GRSs are very useful in studying a number of astrophysical problems, for example the evolution of RSs, the properties of the IGM at different redshifts or the nature of the central AGN. It is still unclear why such a small fraction of RSs reaches very large size

---

[2] Many authors, assuming $H_0 = 50$ km s^{-1}Mpc^{-1}, have used 1 Mpc as the defining size for GRSs. For the currently accepted cosmological parameters as given above, this size decreases to $\sim$0.72 Mpc.

– it may be due to special external conditions, such as lower IGM density, or due to the internal properties of the "central engine". Our knowledge about the nature of GRSs has improved somewhat following studies conducted in the last decade. However, these were focused almost exclusively on: the role of the properties of the IGM (Machalski & Jmrozy 2006, Subrahmanyan et al. 2008), the advanced age of the radio structure (e.g. Kuligowska et al. 2009, Machalski, Jamrozy & Saikia 2009), or recurrent radio activity (e.g. Machalski et al. 2011, Schoenmakers et al. 2000) as responsible for their gigantic size.

Usually giants are FRII radio sources but also some of them have FRI-like morphology (e.g. J0918+3151, J1032+5644) or intermediate FRIIs without hot spots at the lobes edges. The existence of FRI giant radio sources can be explained by the scenario in which jet propagates for some time in the powerful FRII mode and then transition to a lower power FRI mode takes place (due to decrease of accretion rate; Komberg & Pashchenko 2009).

Most of GRSs are observed at rather low redshifts (z<0.5). For several years, GRSs were not expected to be found at redshifts higher than z∼1, because of the strong density increase of IGM. Kapahi (1989) showed that the IGM density evolves as $\rho_{\rm IGM} \propto (1+z)^3$. Therefore, the large environmental densities hamper the radio structure linear-size evolution at high redshifts. However, Law-Green et al. (1995) discovered a GRS (4C39.24) hosted by a galaxy located at z=1.883. Moreover, a sample of relatively distant (0.3<z<0.9) and large radio galaxies were presented by Cotter, Rawlings & Saunders (1996). It seems that GRSs could be a tool to probe the cosmological evolution of IGM even up to high redshifts (z>0.5; Machalski, Kozieł-Wierzbowska & Jamrozy 2007), but as long as only a small number of GRSs is known, such studies can not be very meaningful. There are several reasons for detecting a small number of GRGs at high redshifts. The most important one is that distant RSs can not be identified in a simple way when using the modern interferometric radio survey maps available. Detecting steep-spectra and low surface-brightness radio-bridges connecting the radio core with hot spots for distant GRSs, is a quite challenging task but it would be possibly facilitated with the advent of novel low-frequency telescopes, such as the Low Frequency Array and the Square Kilometre Array. There are a number of efforts under way aimed to increase the number of high redshift GRSs. A new sample of largest radio sources (predominantly quasars) with 1<z<2 was presented by Kuligowska et al. 2009. The highest redshift GRS candidate, which is known up to date, is a giant radio quasar (GRQ) J1145-0033 located at z=2.055 (Kuźmicz, Kuligowska & Jamrozy 2011).

Chapter 2

Giant radio quasars

2.1 The sample

In my analysis I analyze 47 giant radio quasars (GRQs), out of which 23 are taken from the literature (for details see Table A.1). The remaining 24, which were not previously identified as GRQs, were selected from catalogues of radio quasars compiled by Gregg et al. (1996), Becker et al. (2001), White et al. (2000), and de Vries et al. (2006). The presented sample of giant-sized RQ is the largest to date and it also contains distant sources (at redshifts $z \sim 2$).

As a comparison sample, I selected 31 smaller, lobe-dominated radio quasars from the list of radio sources given by Nilsson (1998). In order to obtain a number of objects comparable to that of the GRQ sample, 18 quasars selected from the catalogues cited were added to the comparison sample. The linear sizes of these objects are close to the limiting size of 0.72 Mpc, that gives a smooth transition of the linear size between the smaller radio quasars and the GRQs. The sources from the comparison sample of lobe-dominated radio quasars meet the following criteria:

1. Their optical spectra are available in the Sloan Digital Sky Survey (SDSS; Adelman-McCarthy et al. 2008).
2. There is the MgII(2798Å) broad emission line visible in their spectra (as most of GRQ spectra studied here contain the MgII(2798Å) line). This condition limits the range of redshifts to $0.4 \lesssim \mathrm{z} \lesssim 2$; it was adopted in order to have similar properties of the optical spectra for all quasars and hence allows homogeneous measurements using the same methods for both samples.

3. The projected angular size of their radio structure is larger than 0.2 arcmin, allowing proper separation of the source components (lobes and core) in the FIRST maps (which have $5'' \times 5''$ angular resolution).

The final samples contain 47 GRQs and 49 smaller RQs, whose basic parameters are provided in Tables A.1 and A.2 respectively. The new GRQs, previously unrecognised, are marked in bold-face in Table A.1. Optical spectra from the SDSS as well as radio maps from the NVSS and FIRST surveys are available for almost all of these objects. In addition, the spectra of nine quasars published by White et al. (2000), Becker et al. (2001), de Vries et al. (2006) and Gopal-Krishna, Wiita & Saripalli (1989) were provided in electronic FITS format by R. White (these are marked by the letter W in Tables A.1 and A.2). The columns of Tables A.1 and A.2 contain: (1) J2000.0 IAU name; (2) and (3) J2000.0 right ascension and declination of the central position of the optical quasar; (4) redshift of the host object; (5) angular size in arcmin; (6) projected linear size in Mpc; (7) availability of the spectrum in the SDSS survey (S), or provided by White (W); availability of radio maps in NVSS or FIRST (N or F, respectively); (8) references to the identified object. Unfortunately, for two GRQs, J0631−5405 and J0810−6800, neither spectral nor radio data are available, therefore I excluded them from further analysis.

2.1.1 Sample biases

The results obtained in this work might, in some cases, be influenced by selection effects related to e.g. sensitivity of the radio surveys used for selecting extended sources. The sample of giant radio quasars was compiled in three stages and each of them may be somewhat affected by bias. Compact radio objects were selected first and next the optical counterparts were checked for spectra typical of quasars. The selection criteria for these two steps were described in detail in papers referenced in Section 2.1. In the third stage of the sample selection, the radio maps of several hundred candidates were inspected, looking for targets that have extended radio lobes in addition to pronounced radio cores. The NVSS and FIRST surveys have a completeness of 96 and 89% and a reliability of 99 and 94% at 5σ levels of 2.3 and 1.0 mJy, respectively (Cileigi et al. 1999). Therefore, due to the resolution effect, the FIRST survey could be incomplete for extended objects. I supplemented my search by checking the NVSS maps, which have a larger restoring beam size and hence a larger surface brightness sensitivity. However, because of the limited baselines, NVSS is insensitive to very extended coherent structures (larger than 15 arcmin). Fortunately, objects with such a large angular size are not believed to exist, at least at high redshifts. In addition, extended and aged radio sources could have weak double lobes not connected with a visible bridge of high-frequency radio emission. Therefore, it may be hard to recognize such a source as one homogeneous object, especially at high redshifts, where the inverse Compton losses against the cosmic microwave background (CMB) are large. Detecting a steep-spectrum and low-surface-brightness radio bridge, connecting the radio core with hot spots for distant objects, is therefore a challenging task and this may be a reason for overlooking of some (but not many) objects.

It is worth noting that in most of recent works on quasars, based on optical and radio data, candidates were first selected from optical catalogues of quasars and then their coordinates were correlated using catalogues of radio sources. The authors usually concentrated on point-like radio sources, not extended objects (there are some exceptions, e.g. de Vries et al. 2006). Jiang et al. (2007) considered extended radio structures, but analysed only those objects which had lobe separation smaller than 1 arcmin. The authors stressed that the extended radio quasars represented a very small fraction of the SDSS survey quasars. They also mentioned that quasars with the radio structure diameter greater than 1 arcmin are even more rare. Therefore, one has to realize that objects of the class studied here should be extremely rare.

The lobe-dominated radio quasars lie almost in the plane of the sky. Therefore, their measured radio luminosity is only weakly influenced by the relativistic beaming. In addition, it is possible to determine the proper physical size and volume occupied by the radio plasma for sources oriented in this manner. On the other hand, one should keep in mind, that giant radio quasars located at a small angle to the line of sight also exist. These were completely ignored as there was no possibility to determine their physical size.

Given all the drawbacks described above, it have been nonetheless shown, that GRQs do not comprise just a few objects as previously thought, but constitute a larger group. In addition to the sample of newly identified giants, I also added a set of previously known giant quasars to increase the number of objects considered here. In summary, the sample presented in this work could be somewhat limited by the described selection criteria and therefore not entirely homogeneous.

2.2 Radio data analysis

Using the Astronomical Image Processing System[1] (AIPS) package for radio data reduction and analysis, and maps from the NVSS and FIRST surveys, I measured the basic

---

[1] http://www.aips.nrao.edu/

parameters of the selected radio quasars, which subsequently were used to calculate their characteristics – defined in the following way:

1. The arm-length-ratio, Q, which is the ratio of distances (d_1 and d_2) between the core and the hot spots (peaks of radio emission), normalized in such a way that Q is always > 1 (for details see Figure 2.1).

2. The bending angle, B, which is the angle between the lines connecting the lobes with the core.

3. Lobes flux-density ratio, $F = S_1/S_2$, where S_1 is the flux density of the lobe further from the core and S_2 is the flux density of the lobe closer to the core.

4. The source total luminosity at 1.4 GHz, P_{tot}, which is calculated following the formula given by Brown, Webster & Boyle (2001):

   $$logP_{tot}(\mathrm{WHz^{-1}}) = \mathrm{logS_{tot}(mJy)} - (1+\alpha)\cdot\mathrm{log(1+z)} + \mathrm{2log(D_L(Mpc))} + 17.08 \quad (2.1)$$

   where α is the spectral index (the convention I used here is $S_\nu \sim \nu^\alpha$) and D_L was the luminosity distance. The total flux density (S_{tot}) of individual sources was measured from NVSS maps and the average spectral index was assumed for all sources as $\alpha = -0.6$, in accordance with Wardle et al. (1997). The core luminosity at 1.4 GHz (P_{core}) was calculated in a similar manner, but the S_{tot} in equation (2.1) was substituted by the core flux density (S_{core}). It was measured from the FIRST maps and the average spectral index value was adopted to be $\alpha = -0.3$, according to Zhang & Fan (2003).

5. The inclination angle, i, which is the angle between the jet axis and the line of sight (i.e. $i = 90°$ means that the object lies in the sky plane). The inclination angle was calculated in the following way (assuming that the Doppler boosting is the main factor underlying the asymmetries of a source):

   $$i = [arccos(\frac{1}{\beta_j}\cdot\frac{(s-1)}{(s+1)})] \quad (2.2)$$

   where $s = (Sj/Scj)^{1/2-\alpha}$, S_j is the peak flux-density of the lobe closer to the core. S_{cj} is the peak flux-density of the lobe further away from the core and β_j is the jet velocity in the units of c (Hocuk & Barthel 2010). For all objects I assumed $\beta_j = 0.6$, according to Wardle et al. (1997) and Arshakian & Longair (2004).

The resulting values of the above parameters for both samples of RQs are listed in Tables A.9 and A.10 presented in Appendix A. For two objects, i.e. J0439−2422 and

J1100+2314, I was not able to measure all of their parameters. There is no map of source J0439−2422 available in the FIRST catalogue and the radio structure of J1100+2314 is highly asymmetric making this determination unreliable. The detailed analyses of derived parameters are provided in Chapter 4.

The FIRST and NVSS radio maps of GRQs overlaid on Digital Sky Survey (DSS) optical images are presented in Appendix B.

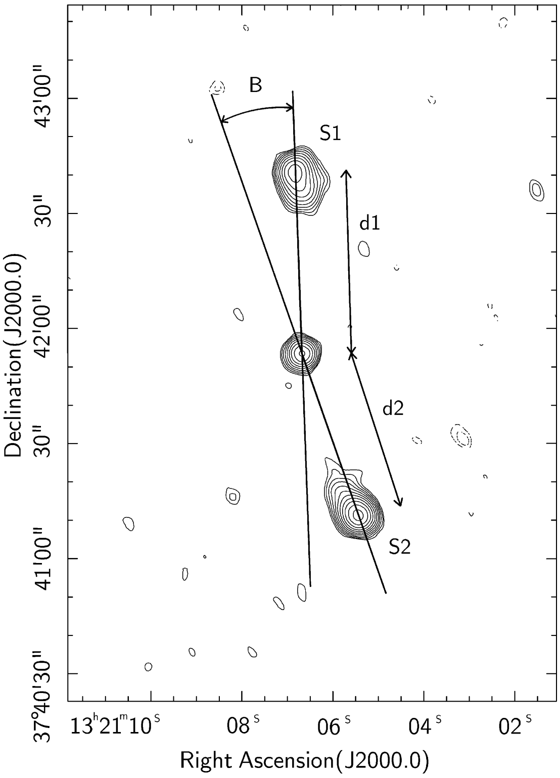

Figure 2.1: J1321+3741, an example of a GRQ. Radio contours are taken from the FIRST survey. Definitions of some parameters are provided here (i.e. B, S_1, S_2, d_1, d_2) and also described in the text.

2.3 Optical data analysis

2.3.1 Spectra reduction

The spectra of quasars were reduced also using the standard procedures of the Image Reduction and Analysis Facility[2] (IRAF) package. Each spectrum was corrected for galactic extinction taking into account values of the colour excess $E(B-V)$ and the B-band extinction (A_B) taken from the NASA/ IPAC Extragalactic Database. I calculated

---

[2] http://iraf.noao.edu/

the extinction parameter $R = E(B - V)/A_B$ for each quasar from my samples. The extinction-corrected spectrum was then transformed to its rest frame using the redshift value given in the SDSS or from the literature if the SDSS spectrum was not available.

2.3.2 Continuum subtraction and line parameters measurements

In order to obtain reliable measurements of emission lines, it is needed to subtract continuum emission, as optical and UV spectra of quasars are dominated by the power-law and Balmer continua. Using the IRAF package, I subtracted the power-law continuum from all spectra. The continuum was then fitted using a low order spline function in several windows, where no any emission lines are observed (i.e. 1320–1350Å, 1430–1460Å, 1790–1830Å, 3030–3090Å, 3540–3600Å and 5600–5800Å). Particularly in the UV band, the significant iron emission is observed, which is often blended with the MgII(2798Å) line. The procedure of subtracting the iron emission was similar to that described by Boroson & Green (1992). I used a Fe template in the UV band (1250–3090Å) as developed by Vestergaard & Wilkes (2001) and in the optical band (3535–7530Å) given by Veron-Cetty, Joly & Veron (2004). First, I broadened the iron template by convolving it with Gaussian functions of various widths and multiplying by a scalar factor. Next, I chose the best fit of this modified template to each particular spectrum and then subtracted it. After the subtraction of the Fe line emission, I added the previously determined power-law continuum fit and fitted it once again (in a similar manner as suggested by Vestergaard & Wilkes 2001). The “cleaned-up” spectra of giant radio quasars are presented in Appendix B.

The accurate fitting of the iron emission was not possible in some cases. It was due to either a low signal to noise ratio or too small fitting wavelength region. Iron emission was also not fitted when it was not required, i.e. when there was no emission lines in the fitting region or it was not possible to measure it.

For the purpose of my analysis I needed to measure the parameters of broad emission lines: CIV(1549Å), MgII(2798Å) and H_β(4861Å). In some cases, performing this measurement was difficult due to asymmetries of the line profiles (particularly highly ionized lines such as CIV), where it was hard to fit a Gaussian profile. In order to overcome this problem, I used the line measurement method described in Peterson et al. 2004. In Tables A.3 and A.4 I provided the respective widths of broad emission lines for GRQs and smaller radio quasars, respectively. I was not able to measure the MgII emission line parameters in the spectrum of GRQ J1408+3054, as it showed strong broad-absorption features which considerably affected the emission line profile.

2.3.3 Black hole mass determination

As it was mentioned in Section 1.2.1, the reverberation mapping virial method is considered to be the most accurate method of BH mass estimation in Type 1 AGNs (Peterson 1993). This method relies on the monitoring of emission line and continuum variations. The time delay between a certain pattern variations (which is the light travel time of photons from the central region emitting continuum to the line emitting region) is used to measure the size of BLR (more precisely - the size of a particular line emitting region). Assuming that the gas in the broad-line region is virialized in the gravitational field of a BH, its mass can be calculated as:

$$M_{\rm BH} = \frac{R_{\rm BLR} V_{\rm BLR}^2}{\rm G} \tag{2.3}$$

where G is the gravitational constant, $R_{\rm BLR}$ is the distance from the central BH to the broad-line region clouds, $V_{\rm BLR}$ is the broad-line region virial velocity, which can be estimated from the FWHM of a respective emission line as:

$$V_{\rm BLR} = f \cdot {\rm FWHM} \tag{2.4}$$

where f is a scaling factor, which depends on structure, kinematics, and orientation of the BLR (for randomly distributed broad line region clouds $f = \sqrt{3}/2$). The reverberation mapping virial method applied on the same source at different times, and considering different emission lines, is expected to provide consistent values of the BH mass e.g. Peterson & Wandel (2000). Based on this method, Kaspi et al. (2000, 2005) obtained an empirical relation between the BLR size of an AGN and its optical continuum luminosity (λL_λ) at 5100Å (and later also at 1450Å, 1350Å and in the 2–10 keV range):

$$R_{\rm BLR} \sim \lambda L_\lambda (5100\text{Å})^{0.70\pm0.03} \tag{2.5}$$

This relation makes it possible to use an approximation of the reverberation mapping method, called single epoch virial mass estimation. In this method, a BH mass is determined through a mass-scaling relation, where the FWHM of broad emission lines (e.g. CIV, MgII, H_β) and the monochromatic continuum luminosity (λL_λ) of a single-epoch spectrum is only needed. The BH mass is expressed as:

$$M_{\rm BH} = A \cdot 10^6 (\frac{\lambda L_\lambda}{10^{44} {\rm ergs}^{-1}})^B \cdot (\frac{\rm FWHM}{1000 {\rm kms}^{-1}})^2 M_\odot \tag{2.6}$$

where the calibration constants A and B depend on which emission line is considered. In order to determine BH mass of QSOs I applied the following equations:

$$M_{\rm BH}({\rm CIV1549Å}) = 4.57 \cdot 10^6 (\frac{\lambda {\rm L}_\lambda(1350{\rm Å})}{10^{44}{\rm ergs}^{-1}})^{0.53\pm0.06} \cdot (\frac{{\rm FWHM(CIV1549Å)}}{1000{\rm kms}^{-1}})^2 {\rm M}_\odot \quad (2.7)$$

$$M_{\rm BH}({\rm MgII2798Å}) = 7.24 \cdot 10^6 (\frac{\lambda {\rm L}_\lambda(3000{\rm Å})}{10^{44}{\rm ergs}^{-1}})^{0.5} \cdot (\frac{{\rm FWHM(MgII2798Å)}}{1000{\rm kms}^{-1}})^2 {\rm M}_\odot \quad (2.8)$$

$$M_{\rm BH}({\rm H}_\beta 4861{\rm Å}) = 8.13 \cdot 10^6 (\frac{\lambda {\rm L}_\lambda(5100{\rm Å})}{10^{44}{\rm ergs}^{-1}})^{0.50\pm0.06} \cdot (\frac{{\rm FWHM(H}_\beta{\rm 4861Å)}}{1000{\rm kms}^{-1}})^2 {\rm M}_\odot \quad (2.9)$$

Equations (2.7) and (2.9) were taken from Vestergaard & Peterson (2006), while equation (2.8) from Vestergaard & Osmer (2009).
The monochromatic continuum luminosities λL_λ can be computed as follows:

$$\lambda L_\lambda = 4\pi D^2_{\rm Hubble} \lambda f_\lambda \quad (2.10)$$

where $D_{\rm Hubble}$ is the comoving radial distance and f_λ is the flux in the rest frame at wavelengths λ equal to 1350Å, 3000Å or 5100Å. The resulting rest frame fluxes, monochromatic continuum luminosities and BH masses for giant radio quasars and smaller quasars are given in Tables A.3, A.7 and Tables A.4, A.8 respectively.

2.4 Radio properties

I checked some general relations between radio parameters for both samples of sources. On the optical versus radio-luminosity plane my objects trace the regime of radio loudness (ratio of radio-to-optical luminosity) between 50 and 1000 and overlap with the FIRST-2dF sample of quasars of Cirasuolo et al. (2003).

In Figure 2.2 I present the dependence between 1.4 GHz total luminosity and the redshift of quasars. It is important to note that due to selection criteria, i.e. the presence of the MgII(2798Å) emission line in the spectra, the comparison sample of smaller RQs (sources marked as open circles in Figure 2.2 and subsequent figures) contains only objects in the redshift range of $0.4 \lesssim z \lesssim 2$ (for details see Section 2.1). Such a cut-off in the redshift range of quasars from the comparison sample should not, however, affect the main results, since the majority of GRQs have redshifts in a similar range. Therefore, the non-existence of smaller RQs in the upper-left part of Figure 2.2 is artificial, whereas the absence of GRQs in the lower-right corner of this figure is the result of sensitivity limit of the radio surveys which were used for sources recognition and measurements of their radio properties. It is known that in flux-limited samples one should expect correlations between the radio luminosity and the redshift, since for larger distances we are able to detect only those sources which are luminous enough, and faint sources at higher redshifts are below the detection limit. For quasar samples in my work a dependence between redshift and total

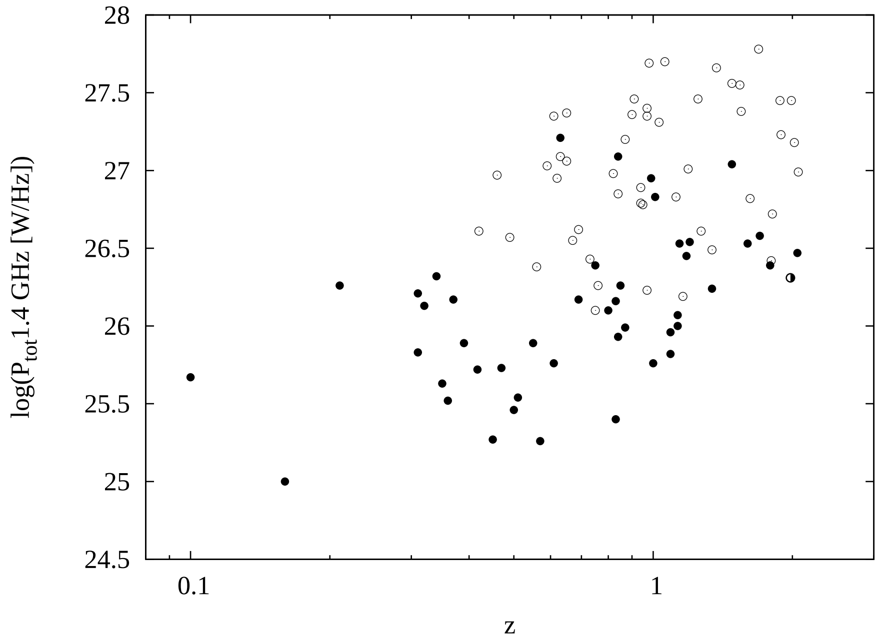

FIGURE 2.2: 1.4 GHz total radio luminosity as a function of redshift. The GRQs are marked with solid circles and quasars from the comparison sample are marked by open circles. J1623+3419, which is marked by a half-solid circle, has a projected linear size of 0.5 Mpc but, after correction for the inclination angle, its linear size is larger than 0.72 Mpc. Such a notation is used in all Figures throughout this chapter.

radio luminosity can be seen, but the correlation is not as strong as for the sample of GRSs from Ishwara–Chandra & Saikia (1999) who studied a smaller sample of giants. The Spearman rank correlation coefficient for the GRQs is 0.50, whereas for the GRSs from the paper cited above its value is 0.90. This shows that the selection effects for the quasar sample are not as strong as for other radio galaxies and GRS samples of Ishwara–Chandra & Saikia (1999), though they may still have affected some of my results. In Figure 2.3 I present the relation between luminosity (P) and the linear size (D). The P–D diagram is a helpful tool in investigation of evolution of radio sources and was frequently used to test evolutionary models (e.g. Blundell, Rawlings & Willott 1999, Kaiser, Dennett-Thorpe & Alexander 1997). In order to draw this diagram I used the real linear size of the sources, which was derived by taking into account the inclination angle, i, as $D^{*} = D/sin(i)$, where D is the projected linear size (given in Tables A.1 and A.2 derived as the sum of d_1 and d_2 - for details see Figure 2.1). The diagrams show that GRQs have, on average, lower core and total radio luminosities. The trend which can be observed in P–D diagrams is consistent with the predictions of evolutionary models and can suggest that, under favourable conditions, the luminous, smaller and probably younger RQs may evolve in time into aged and lower-luminosity GRQs. The non-existence of objects in the bottom-left part of Figure 2.3 may be due to selection

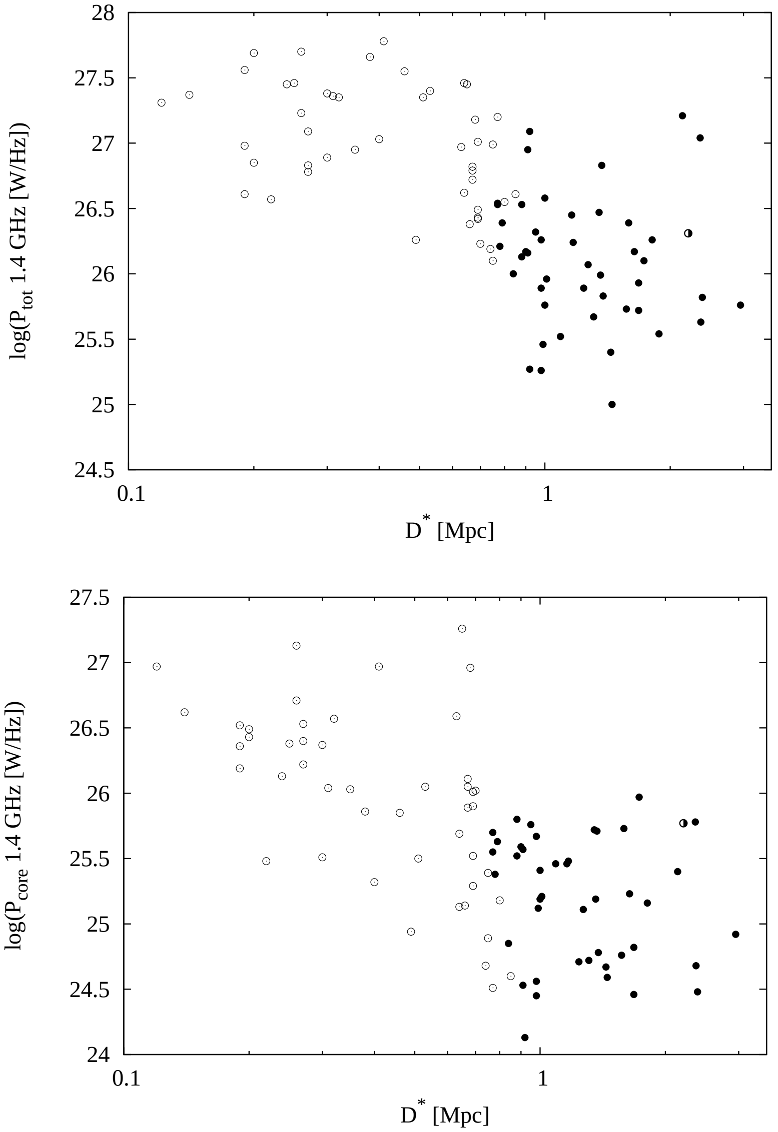

FIGURE 2.3: Luminosity–linear size diagrams. The top panel shows the 1.4 GHz total radio luminosity and the bottom one shows the core luminosity. The observed trend is consistent with evolutionary model predictions.

effects. Because of the surface-brightness limit, some extended objects with very low total radio luminosities might have been ovelooked.

I present the relation between the total and core radio luminosities in Figure 2.4. There is a strong correlation between these two quantities for radio quasars. I derived the correlation coefficient of 0.76 and the slope of the linear fit equals to 0.84 ± 0.08, steeper than the slope of 0.59 ± 0.05 obtained by Ishwara–Chandra & Saikia (1999) for GRSs. The strong correlation between the core and the total luminosities in the population of giant-size radio galaxies was also mentioned by Machalski & Jmrozy (2006). This correlation can be attributed to the Doppler beaming of a pc-scale jet and can reflect

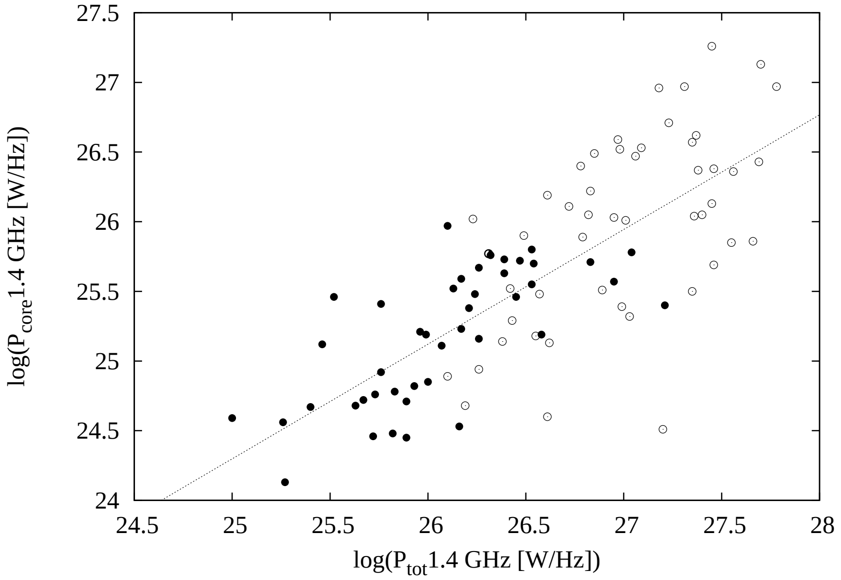

FIGURE 2.4: Core radio luminosity against the total radio luminosity for RQs. A strong correlation is visible. A linear fit to the data points is given by the line $logP_{core} = (0.84 \pm 0.08)logP_{tot} + (3.20 \pm 2.00)$.

different inclination angles of nuclear jets, and thus the inclination of the entire radio source axis to the observer's line of sight. Relatively more luminous cores (in comparison with the total luminosity) should be observed for highly projected sources (i.e. quasars). Therefore, in GRQs one could expect to observe relatively stronger cores than in giant-size radio galaxies. On the other hand, evolutionary effects (well visible in Figure 2.3) can explain the clear difference of radio luminosities between giant radio quasars and smaller quasars. The observed correlation between the total and core radio luminosities can be also a result of evolution of smaller radio quasars toward larger ones. If we assume that *P–D* diagrams are a consequence of a radio source evolution, it is clearly seen that during the radio structure growth, the total and core luminosity of radio sources decreases.

2.5 Black hole masses for GRQs and comparison sample

In order to obtain the central BH mass of quasars in my samples, I used measurements of CIV, MgII and H_β emission lines and the mass-scaling relations (equations 2.7, 2.8 and 2.9). The mass values obtained are in the range of $1.4 \cdot 10^8 M_\odot < M_{BH} < 12.3 \cdot 10^8 M_\odot$ when using the MgII emission line and $0.05 \cdot 10^8 M_\odot < M_{BH} < 33.7 \cdot 10^8 M_\odot$ when using the H_β emission line. For some GRQs and quasars from the comparison sample, it was possible to compare the results obtained on the basis of different emission-line measurements. In Figure 2.5 I present the relation between the mass values calculated from MgII versus H_β lines and those from CIV versus MgII lines, respectively. I found that the mass estimations based on the MgII line, on average, tend to be smaller than those obtained using the H_β emission line (the linear fit to the data points is given by the relation: $M_{BH}H_\beta = 2.74(\pm 0.98) \cdot M_{BH}\text{MgII} + 7.23(\pm 9.19)$, and the mass estimations based on the CIV line are larger than those obtained using the MgII line ($M_{BH}\text{CIV} = 0.69(\pm 0.12) \cdot M_{BH}\text{MgII} + 0.87(\pm 0.50)$. The above results are consistent with comparisons of BH masses estimated earlier by other authors (e.g. Dietrich et al. 2009, Vestergaard & Osmer 2009, Vestergaard & Peterson 2006).

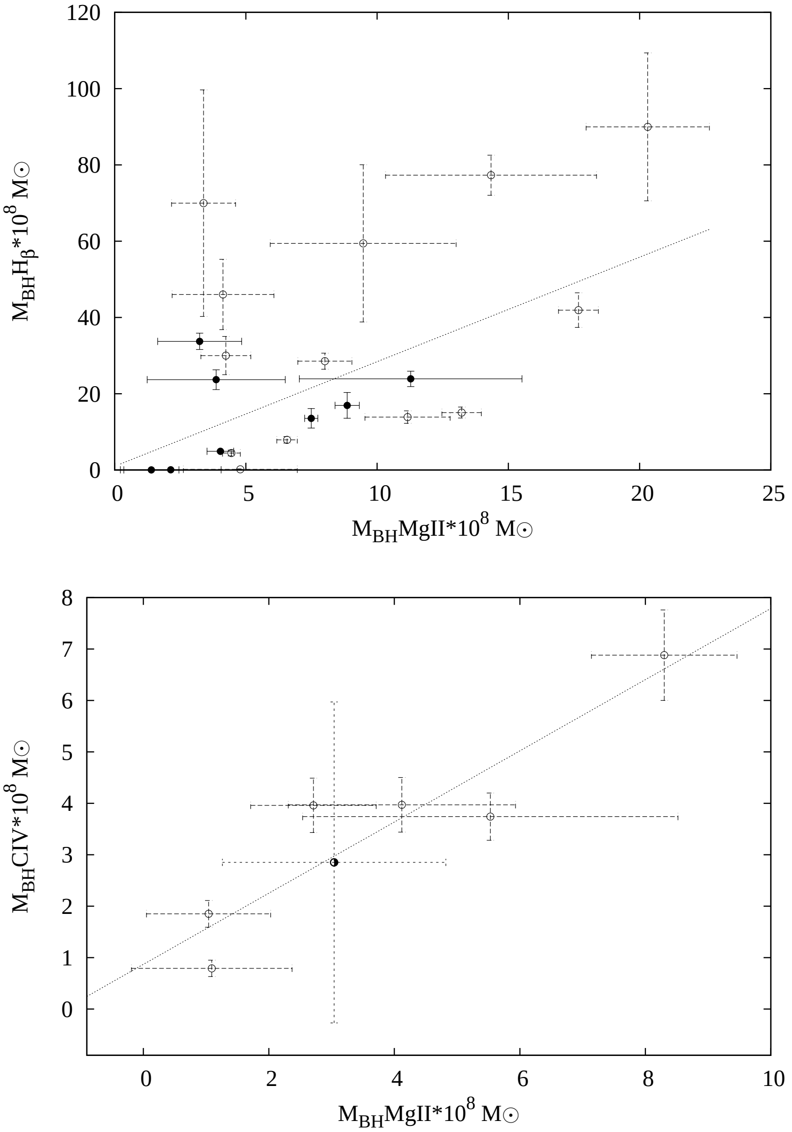

FIGURE 2.5: Comparison of BH mass values estimated using measurement of different emission lines. Top: MgII versus H_β BH masses. Bottom: MgII versus CIV BH mass. The linear fits to data points are described in the text.

2.6 Black hole mass vs. radio properties

In the paper by Komberg & Pashchenko (2009), it is claimed that in the jet-formation models some dependence of the jet power and BH mass should be expected. The assumption that giants are formed due to a longer activity phase of the central AGN and/or more frequent duty cycles can imply, that their BH masses should be larger because of longer accretion episodes. In Figure 2.6 I present the relations between the total and core radio luminosities and the BH mass. It can be seen, however, that there

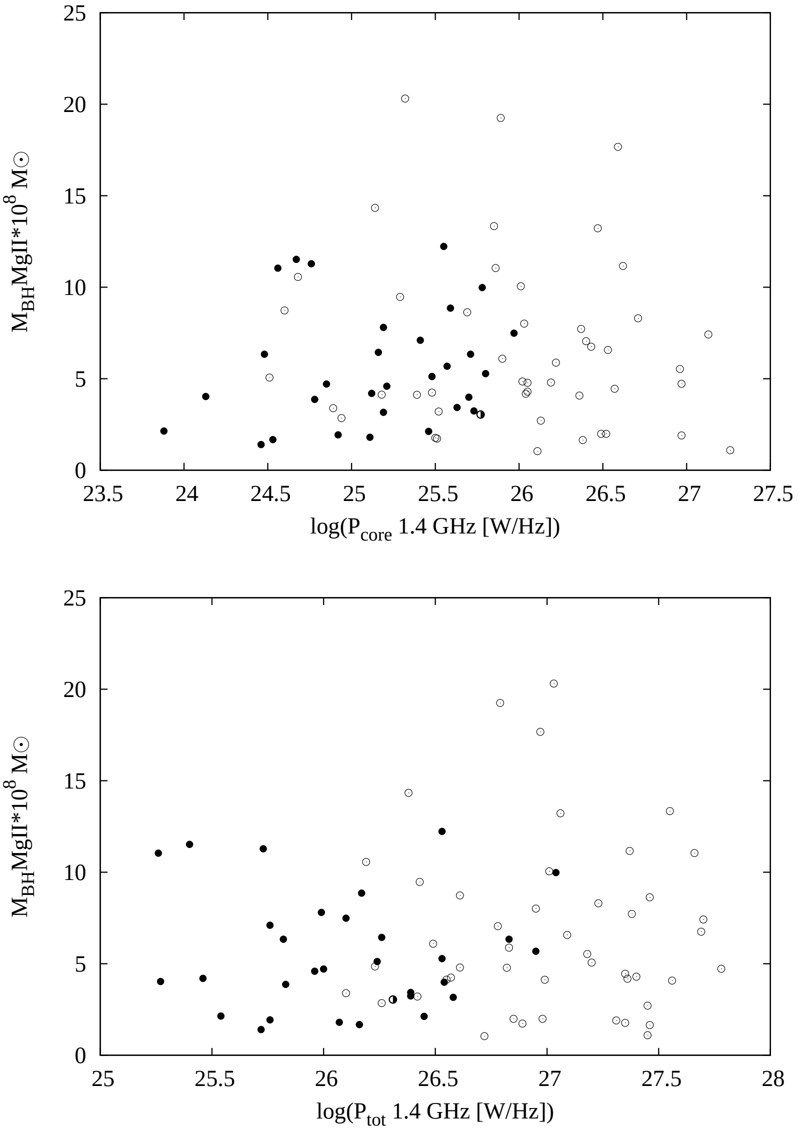

FIGURE 2.6: Relations between BH mass and radio luminosity at 1.4 GHz. Top panel: BH mass vs. core luminosity. Bottom panel: BH mass vs. total luminosity.

is no correlation between the BH mass and neither the core luminosity nor the total luminosity for both GRQs and smaller RQs.

I also looked if any relation exists between BH mass and the real linear size of radio quasar structures. For the H_β mass estimations (Figure 2.7) it can be clearly observed that the dependence between linear size of radio structures and their BH mass is quite significant. Surprisingly enough, the relation based on the H_β mass estimations for GRQs does not at all resemble that for quasars from the comparison sample. The slope of the linear fit for the sample of smaller quasars is steeper than that for the GRQ sample. This result suggests that GRQs can be considered to represent another group of objects that differ physically from smaller quasars. I fitted linear functions independently to the data of GRQs and to the comparison sample. The best fits obtained are as follows: $M_{BH}H_\beta = 9.05(\pm 8.84) \cdot D^* + 1.17(\pm 13.81)$ and $M_{BH}H_\beta = 86.01(\pm 29.29 \cdot D^* + 0.29(\pm 14.82)$ for GRQs and the comparison sample, with correlation coefficients of 0.31 and 0.68, respectively. For the MgII BH mass estimations (Figure 2.8), no obvious dependence has been found but I plotted the fitted lines from Figure 2.7, taking into account the scaling factor between H_β and MgII BH mass estimations (equal to 2.74). It is obvious that giants and smaller radio quasars fulfil these relations quite well. Moreover, for the CIV mass estimation a weak correlation is also observed (Figure 2.9) but there are no difference between giants and smaller radio quasars. The best fit is represented by a line $M_{BH}CIV = 10.78(\pm 5.33) \cdot D^* - 1.42(\pm 3.95)$ with a correlation coefficient of 0.67. Despite of deriving a high value of correlation coefficient, reliability of this correlation is questionable since it mostly depends on two points at high redshift but with largest

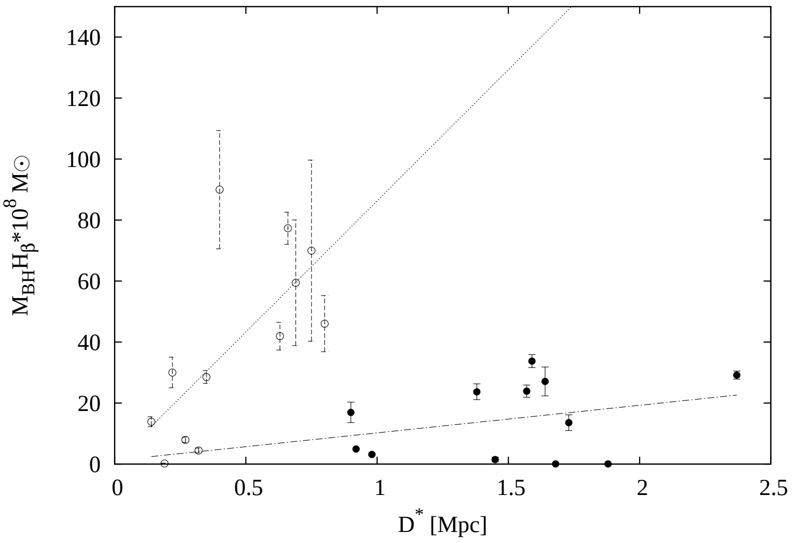

FIGURE 2.7: Dependence between the BH mass derived from the H_β emission line and the real linear size of the radio structure.

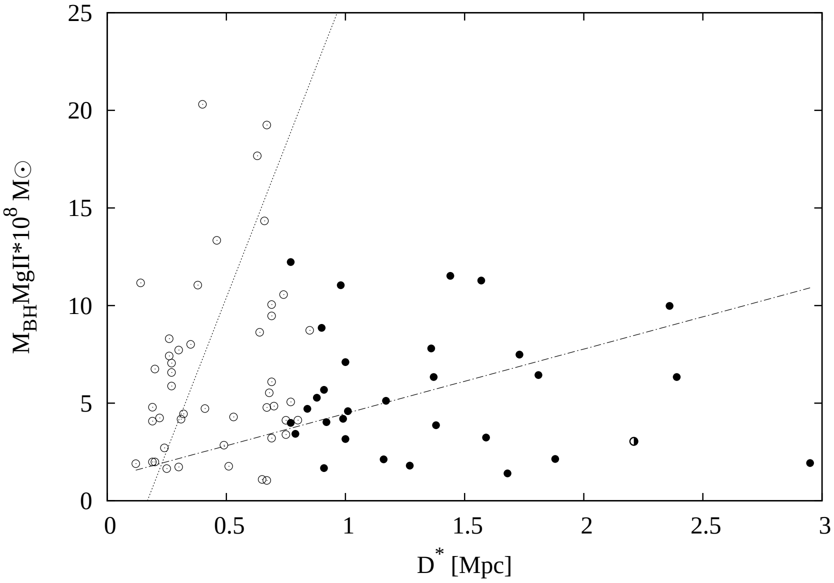

FIGURE 2.8: Dependence between the BH masses derived from the MgII emission line, and the real linear sizes of the radio structures. The straight lines are reproduced from Figure 2.7 (see the text for details).

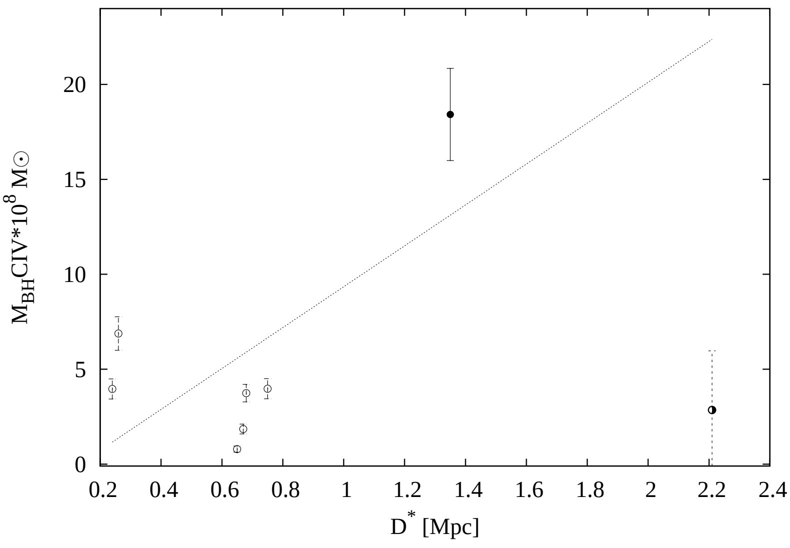

FIGURE 2.9: Dependence between the BH mass derived from the CIV emission line and the real linear size of the radio structure.

uncertainties. The result obtained (particularly for the H_β mass estimations) indicates that there may be some difference between GRQs and smaller radio quasars. It is hard to find a physical process to account for such behaviour though. Some authors (e.g. Decarli et al. 2008, Kaspi et al. 2007) suggested that the formation of different emission lines occurred in different regions of the broad-line region. Therefore, GRQs and smaller radio quasars may differ with respect to the external structures of the broad-line region, while their central parts could be similar. The question now is how to reconcile this fact. According to the previously analysed relations for GRQs and smaller quasars, I did not see any clear distinction between these two types of RQs. There is a possibility that there can be a difference in age between GRQs and smaller quasars and the composition of the broad-line region could be different for young and old quasars. However, the number of sources analysed here is too small to allow for any definite conclusions. For example, the correlation seen in Figure 2.7 becomes weaker if we shift the defining minimum GRQ size from 0.72 Mpc to some smaller value. Generally, apart from the above speculations on the composition of the broad-line region, I can conclude that the apparent relationship between the linear size of the radio structure and the BH mass supports the evolutionary origin of GRQs: as time increases, the BH mass becomes larger and the size of the radio structure grows.

2.7 Accretion rate

Using obtained BH masses and the optical monochromatic continuum luminosities (λL_λ) I calculated the accretion rates for my sample of quasars. The accretion rate is computed as $\dot{\rm m}(\lambda)=L_{\rm bol}/L_{\rm Edd}$, where $L_{\rm bol}$ is the bolometric luminosity, assumed as

$$L_{\rm bol} = C_\lambda \lambda L_\lambda \tag{2.11}$$

where C_λ is equal: 9.0 for λ=5100Å (according to Kaspi et al. 2000), 5.9 for λ=3000Å (according to Metcalf & Magliocchetti 2006) and 4.6 for λ=1350Å (according to Vestergaard 2004). Following Dietrich et al. (2009), the Eddington luminosity $L_{\rm Edd}$ is given by

$$L_{\rm Edd} = 1.45 \cdot 10^{38} {\rm M_{BH}/M_\odot ergs^{-1}} \tag{2.12}$$

The resulting values of $L_{\rm bol}$, $L_{\rm Edd}$ and $\dot{\rm m}(\lambda)$ for giant radio quasars and smaller quasars are listed in Tables A.5 and A.6, respectively. In Figure 2.10 I present the BH masses as a function of accretion-rate values, which are calculated based on the CIV, MgII and H_β emission lines as well as the respective continuum luminosities, taking into account the scaling factors between H_β, CIV and MgII mass estimations. As can be seen, the accretion rate is apparently higher for less massive BHs. A similar result was obtained by Dietrich et al. (2009) for a sample of quasars and by Mathur (2000) for narrow-line Seyfert galaxies. The result is consistent with the scenario that quasars increase their BH mass solely due to the accretion process. When there is no matter left, the accretion rate decreases, while a large amount of mass could have been accumulated in the central BH during previous accretion episodes. In the scenario described by Mathur (2000),

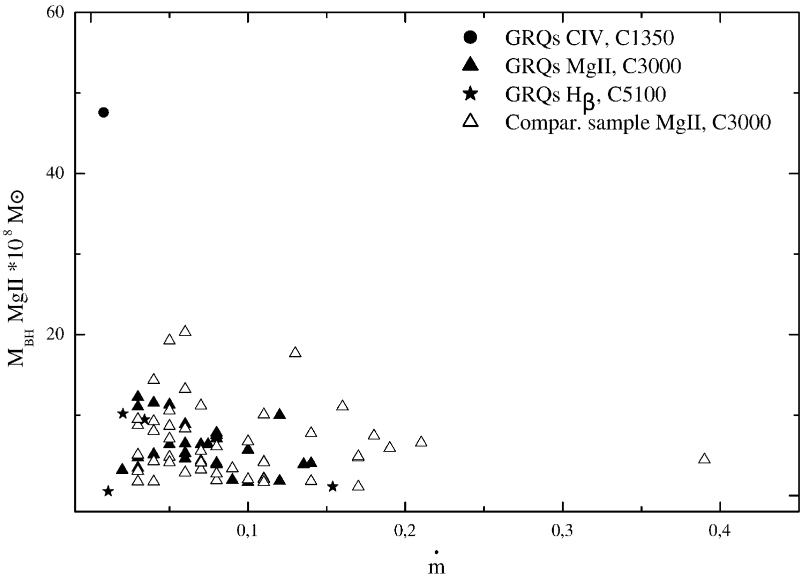

FIGURE 2.10: The dependence between BH mass and accretion rate $\dot{m}(\lambda)$. The solid and open symbols denote GRQs and smaller-size RQ, respectively. Different symbols (circles, triangles and stars) represent estimations of the accretion rate based on measurements of different emission lines (MgII, CIV and H_{β}) and luminosities (at λ=1350Å, λ=3000Å or λ=5100Å).

the accretion rate was high in the early stages of AGNs evolution and drops later on, therefore, one may expect that at higher redshifts objects with larger accretion rates should be observed. However, Figure 2.11 shows, that for my samples of quasars, no dependence between the accretion rate and the redshift is seen.

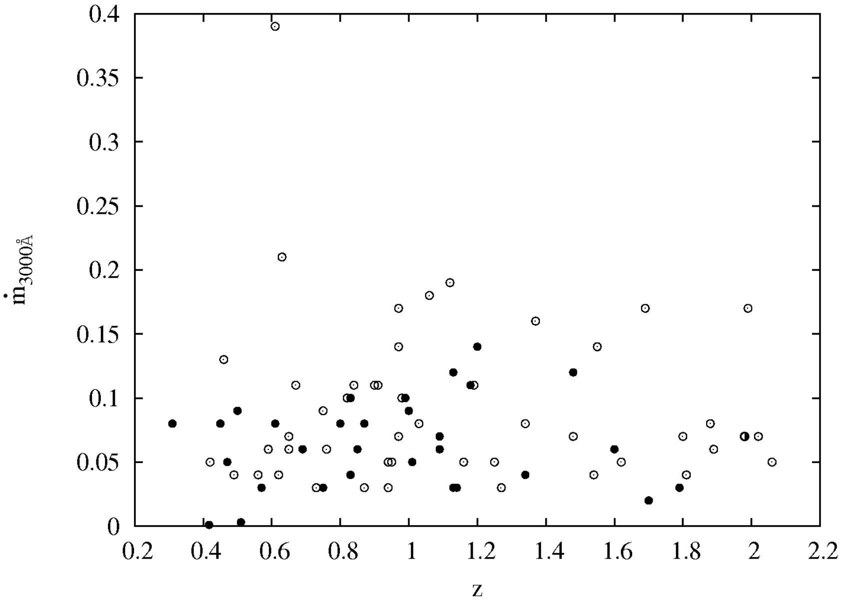

FIGURE 2.11: BH accretion rate versus redshift. No any correlation is seen.

The accretion rates for GRQs and for the comparison sample are consistent with typical values of 0.01÷1 for AGNs. The obtained lower value for GRQs implies that these sources are more evolved systems, for which the e-folding time to increase their BH mass (for a definition see e.g. Shankar et al. 2004) is longer than in the case of smaller-size quasars. The obtained mean values of accretion rates ($\dot{m}$(3000Å)) are 0.07 ± 0.03 and 0.09 ± 0.07, respectively for GRQs and smaller-size RQ. The dependence between accretion rate and real linear size of radio structure is presented in Figure 2.12.

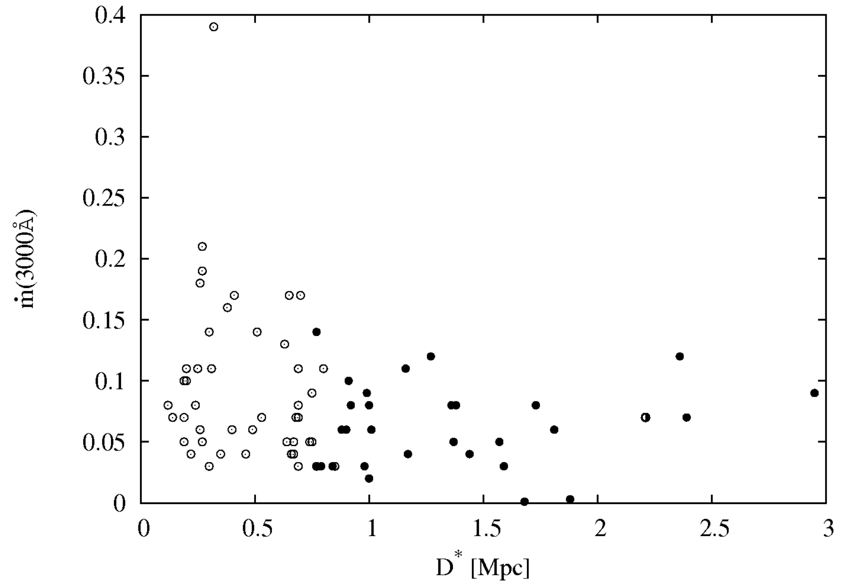

Figure 2.12: Accretion rate versus real linear size of radio structure.

Figure 2.13 presents the dependence between the accretion rate $\dot{m}$(3000Å) and the total as well as the core radio luminosities. There is a distinct trend of larger accretion rates to be observed in quasars with larger radio luminosities. The linear fits for $\dot{m}$(3000Å) are described by: $\dot{m}$(3000Å)=0.17($\pm$0.05)$log(P_{tot})$−5.80($\pm$1.32), $\dot{m}$(3000Å)= 0.20($\pm$0.04)$log(P_{core})$−6.35($\pm$1.03), with correlation coefficients equal to 0.37 and 0.50, respectively.

2.8 J1145−0033 – a candidate for the most distant GRQ

The J1145−0033 GRQ is an remarkable object which should be considered separately. It is located at the redshift of z=2.05221±0.00062 (according to the data from the 9th SDSS release) that is very rare in case of “giants”. The radio structure of J1145−0033 was mapped in the 1.4-GHz VLA FIRST and NVSS surveys. In the FIRST map it is visible as a compact core that coincides well with the QSO and possible hot spots without

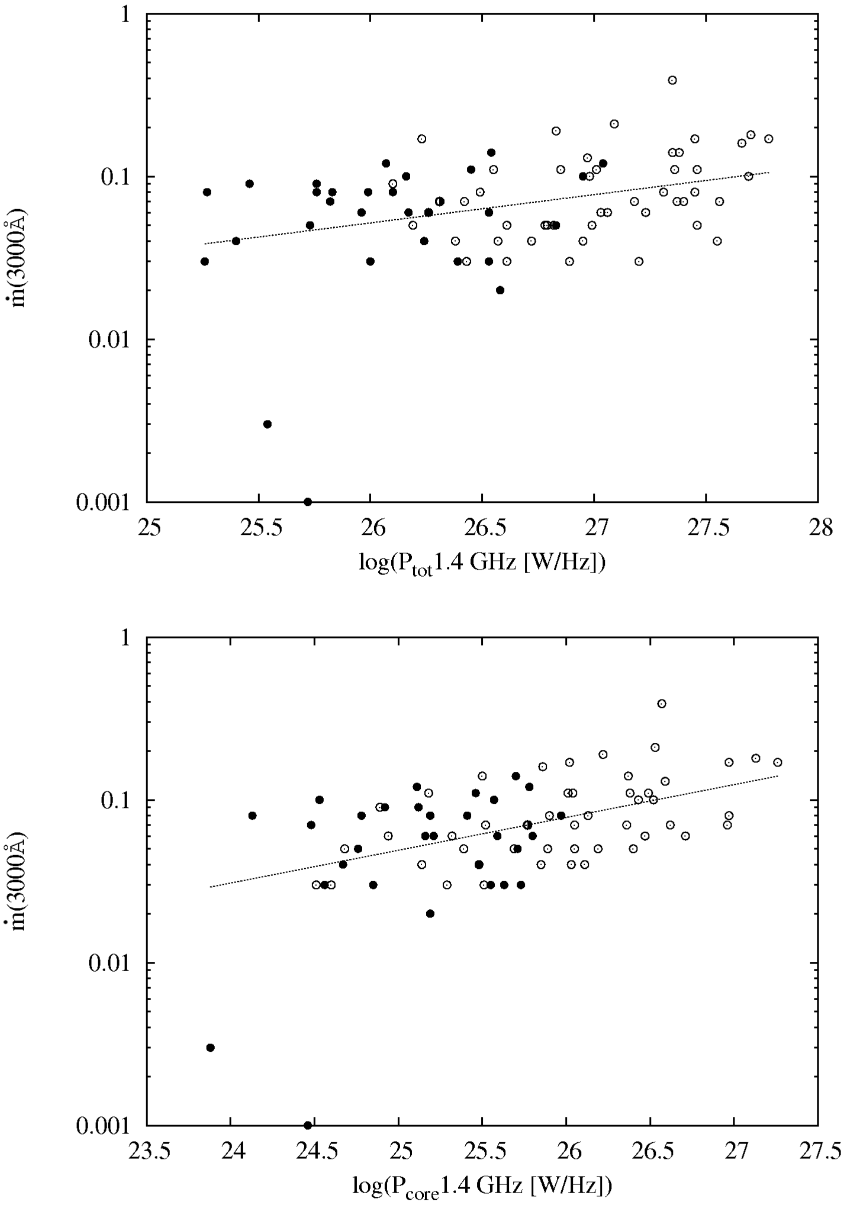

FIGURE 2.13: Accretion rate as a function of total radio luminosity (top panel) and core radio luminosity (bottom panel).

any visible optical counterparts up to the brightness limit of the SDSS. J1145−0033 appears as a 14.5 mJy triple source in the NVSS map. Figure 2.14 presents the contour maps from the NVSS and FIRST surveys overlaid on the optical DSS image. The NVSS contours display a weak structure around the core, oriented at an angle of about 70° to the symmetry axis of the main radio structure. This could be a remnant of some backflow. The bridge between the radio core and hot spots is constrained at ∼3×rms level of the NVSS map.

As it was mentioned in Section 1.3.2, the strong cosmological size evolution of powerful

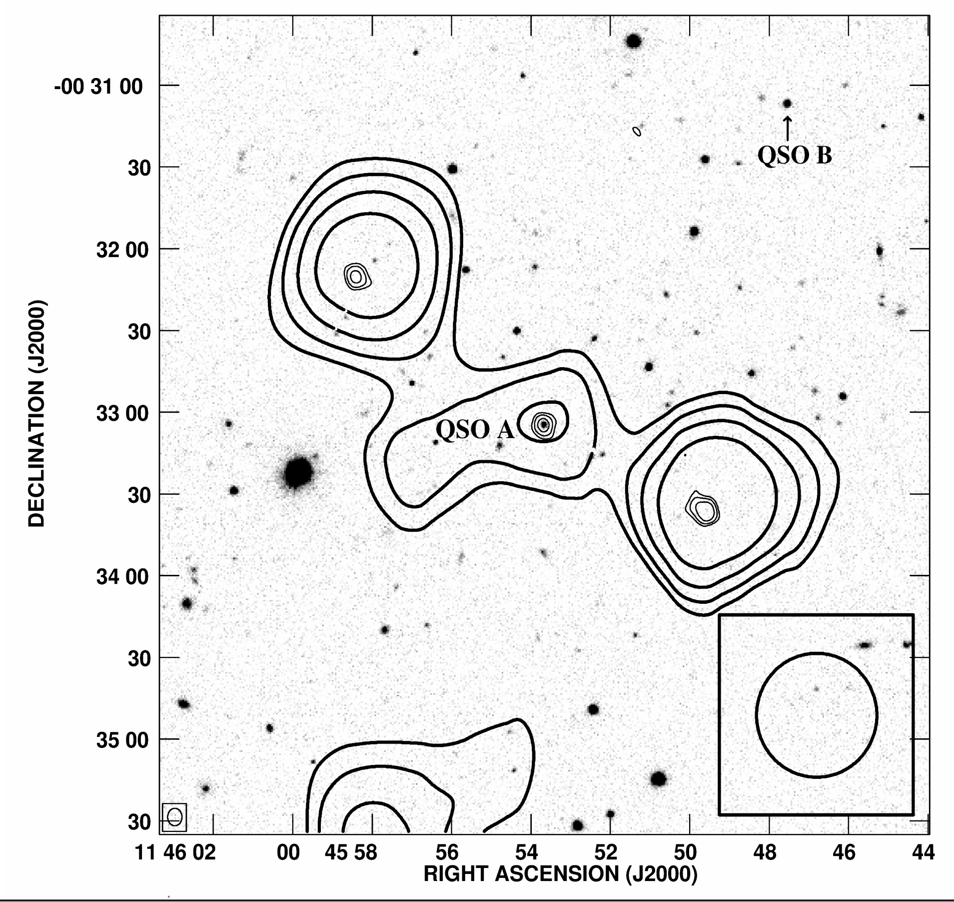

FIGURE 2.14: The 1.4-GHz VLA maps of the GRQ J1145-0033 taken from the NVSS survey (bold contours) and from the FIRST survey (thin contours) overlaid on the optical image from the DSS. The contour levels are: 1, 1,41, 2, 2,83×1 mJy/beam and 1, 2, 4×0.6 mJy/beam for the NVSS and FIRST surveys, respectively. The ellipses in the right and left bottom corners represent the resolution of the FIRST and NVSS surveys, respectively. Labels QSO 'A' and QSO 'B' mark the position of the J1145−0033 QSO and the companion J1145−0031 QSO, respectively.

radio sources and the decrease in surface brightness with redshift ($\propto (1+z)^{-4}$) make the detection of extended sources difficult. Moreover, the suppression of bridge emission by inverse Compton losses against the CMB increases strongly with redshift. Therefore, the "tailless hot-spots" of large sources at high redshifts could be easily mistaken for unrelated sources. The magnetic field equivalent to the microwave background at the redshift of that of J1145−0033 is ∼2.8nT, ∼5 times larger than the minimum magnetic field of this source (Kuźmicz, Kuligowska & Jamrozy 2011). Certainly energy losses in this GRQ will be dominated by the inverse Compton scattering. Emission from inverse Compton scattered CMB photons, in the form of diffuse, extended X-rays between the radio core and hot-spots, has been detected in a number of GRSs at large redshifts ($z \gtrsim 1$; Erlund, Fabian & Blundell 2008; Laskar et al. 2010). The three components of J1145−0033 can indeed appear as isolated sources. However, the major axis of the

Table 2.1: The observational and derived parameters of GRQ J1145−0033 and the companion QSO J1145−0031.

Parameter	Value
QSO A	
IAU name	J1145−0033
‘B’ α (J2000.0) [h m s]	11 45 53.67
δ (J2000.0) [^{o} $'$ $''$]	−00 33 04.6
z	2.052
d [arcmin]	2.642
D [Mpc]	1.340
$\mathrm{S_{total}}$1.4GHz (NVSS) [mJy]	14.52
$\mathrm{S_{core}}$1.4GHz (FIRST) [mJy]	3.86
$log\mathrm{P_{total}}$1.4GHz [W/Hz]	26.47
$log\mathrm{P_{core}}$1.4GHz [W/Hz]	25.72
$\mathrm{M_{BH}}$(CIV)[$10^{8}\mathrm{M}_{\odot}$]	18.42±2.43
i [^{o}]	82
FWHM(CIV) [Å]	61.12
$log\lambda\mathrm{L}_{\lambda}$ (1350Å)	44.867
$\dot{\mathrm{m}}_{1350}$	0.013
BI [km/s]	0
AI [km/s]	1576
QSO B	
IAU name	J1145−0031
α (J2000.0) [h m s]	11 45 47.55
δ (J2000.0) [^{o} $'$ $''$]	−00 31 06.7
z	2.045
$\mathrm{M_{BH}}$(CIV)[$10^{8}\mathrm{M}_{\odot}$]	16.60±1.60
FWHM(CIV) [Å]	51.4
$log\lambda\mathrm{L}_{\lambda}$ (1350Å)	45.06
$\dot{\mathrm{m}}_{1350}$	0.022

western hot-spot is aligned with the compact core. If the lobe-components were actually foreground unrelated sources, we would expect them to have visible optical counterparts. I cross-checked the radio positions of the hot-spots with the SDSS image, but no such objects up to the SDSS limiting magnitude could be identified. The alignment of the two side sources with the core, symmetry of their radio flux, as well as the small value (∼1) of arm-length ratio of both lobes, provide an evidence that the three components are elements of one structure. However, still some doubts are raised by large asymmetry of polarized emission between the two lobes (Kuźmicz, Kuligowska & Jamrozy 2011). In order to confirm the three radio structures indeed belong to a single source, deep multifrequency radio observations, particularly at low frequencies are required.

The basic data for J1145−0033 (thereafter named as QSO ‘A’) are collected in Table 2.1 (also presented in tables included in Appendix A).

The QSO 'A' has a 'companion' QSO, first recognized by Kirkman & Tytler (2008) who studied the absorption in a large sample of QSO pairs (separated in the plane of sky by <3 Mpc). The companion QSO, J1145−0031 (thereafter named as QSO 'B'), is located at RA: 11 45 47.55, Dec: −00 31 6.72 (J2000.0). It has a redshift of 2.04466±0.00058 (according to the data from 9th SDSS release). My estimation of a BH mass for the 'B' QSO is $10^{9.22\pm0.04}M_{\odot}$. That result is the same as that obtained by Wilhite et al. (2007) ($10^{9.26\pm0.02}M_{\odot}$). Only 29 QSOs out of 615 from the Wilhite et al. (2007) sample have BH masses larger than that of the QSO 'B', and the highest BH mass they obtained is $10^{9.55}M_{\odot}$. Contrary to the giant radio quasar, the 'B' QSO is an radio-quiet object. The separation between J1145−0033 and J1145−0031 is $149''$, that gives the actual distance between them as 1.23 Mpc. While the separation of the binary QSO is too large for direct gravitational interactions to trigger accretion, it still could be located in an overdense environment, where interactions with other galaxies can support its activity (e.g., Djorgovski 1991, Hopkins et al. 2008). The idea of using QSOs to indicate dense regions in the early universe is not new (e.g. Djorgovski 1999, Djorgovski et al. 1999). While it is unclear to date, whether high-redshift QSOs reside in protoclusters, a compelling evidence for overdensities have been found around a handful of z>4 radio galaxies (e.g., Hennawi et al. 2010). Absorption measurements in the vicinity of QSO pairs can be used for determination of IGM density in the corresponding regions (Kirkman & Tytler 2008, Hennawi et al. 2006). The absorption seems to be much higher than that calculated solely from the QSO luminosity (Guimaraes et al. 2007). This result implies that the QSOs are situated in regions where the IGM is overdense by a factor of ∼5 (Guimaraes et al. 2007). There are also other hints (e.g. correlation between a small-scale excess of galaxy and QSO clustering) suggesting that the QSOs are likely to be found in dense environments (Bowen et al. 2006, Hennawi et al. 2006). If this is the case also in the vicinity of the QSO pair, it may be hard to explain how the radio structure of J1145−0033 evolved to a Mpc scale in such an overdense environment. I searched the SDSS database looking for more companions at similar redshift as that of QSOs 'A' and 'B' within the circle of 19.7 arcmin in diameter (which corresponds to 10 Mpc) around the QSOs pair, but no such objects have been found.

Interestingly enough, the optical spectrum of J1145−0033 shows high ionization broad absorption lines (BAL), which makes it a member of a rare category of quasars. (Trump et al. 2006). The BAL classification is usually based on a value of the balnicity index (BI; Weymann 1991) that defines the strength of its absorption features. In the case of QSO 'A', the classification was performed using an absorption index (AI; Trump et al. 2006), which is more sensitive for narrower absorption lines. For J1145−0033 QSO the BI=0, but AI=1576 km/s (Trump et al. 2006).

The BAL phenomenon is observed in about 10−20% (depending on the selection criteria) of the entire QSO population (Weymann 2002, Tolea, Krolik & Tsvetanov 2002, Hewett & Foltz 2003, Reichard et al. 2003, Trump et al. 2006). BAL are believed to be caused by high-velocity gas outflows during the accretion processes. Two scenarios have been proposed to explain this phenomenon. In the first one, BAL regions exist in both BAL and non-BAL quasars, and the BAL quasars are just normal QSOs but seen along a particular line-of-sight (Weymann 1991). The second scenario states that BAL are present only during relatively short (possibly episodic) evolutionary phases of QSO activity, which occur most likely at an early stage of their evolution (e.g. Becker et al. 2000). Among of BAL quasars only a small fraction are radio-loud objects and most of them have core-dominated radio morphologies. They belong to the CSS and GPS objects, which are considered to be young radio sources of linear sizes less than 20 kpc. The BAL quasars with extended radio structures are extremely rare. Only eight BAL quasars with extended FRII radio structure are known to date (Greeg et al. 2006). In almost all cases their projected linear size is within the range of 117−585 kpc, and one of them (J1408+3054, Greeg et al. 2006) is considered to be a GRQ with the linear size of 1.65 Mpc.

The inclination angle of J1145−0033 radio structure is about 82^o, which means that the lobes lie almost exactly in the celestial plane. This may suggest that BAL could be just due to orientation of the source. Such an orientation implies that the gas outflows could be explained by a radiatively accelerated wind from the accretion disk or gas evaporating from a dusty torus (Punsly 2006). While this explanation seems quite plausible, the rarity of FR II BAL quasars and their observed anticorrelation between the BI and the radio loudness (Greeg et al. 2006) may not justify such an origin of outflows. Brotherton, De Breuck & Schaefer (2006) found that the polar outflows are present also in FR II radio quasars (e.g. PKS 0040−005), therefore the two facts seem to support the alternative origin of BAL, as being shown up only at some episodic evolutionary phases of QSOs (e.g. Greeg et al. 2006). This scenario is also consistent with the result obtained for QSO pairs by Kirkman & Tytler (2008), who found that QSOs display episodic activity with time scales of 0.3–10 Myr.

The obtained values for the BH masses of QSO 'A' and 'B' are relatively high and their accretion rates are small in comparison with BHs from the comparison sample of smaller-size QSOs. The parameters of both 'A' and 'B' quasars, are however very similar, which may suggest that they are different QSOs with regard to either some internal properties of their host galaxies or external properties of their common IGM. Their evolution could be very similar, except for the presence of radio emission from one of them. The small accretion rates of 0.013 and 0.022, respectively for QSOs 'A' and 'B', are close to the lower limit of radio-loud QSOs (which is ∼0.01; Gu et al. 2001). The large BH masses and small accretion rates of these QSOs could be explained, according to Netzer et al. (2007), by occurring of at least one earlier episode of faster BH growth with a high (~ 1) accretion rate. There are several radio galaxies that show structures of multi-episodes of AGN activity (Saikia & Jamrozy 2009; see an example in Figure 1.5) but, at present, there is only one known QSO that displays radio structures originating from two different cycles of nuclear activity: 4C02.27 (Jamrozy, Saikia & Konar 2009).

2.9 Results

I have presented a comparison of radio and optical properties for a sample of giant radio quasars and smaller radio quasars. It is worth mentioning that the measurements were obtained in a similar and homogeneous way for all sources from both the GRQ and comparison samples. Therefore, only the absolute values might be in some way, if at all, affected by some global calibration errors. The final results are summarized below:

1. Based on the P–D diagram, I found that there is a continuous distribution of GRQs and smaller radio quasars. Therefore, I can conclude that the GRQs could have evolved, over time, out of smaller radio quasars, which seems to be consistent with the RS evolutionary model predictions.

2. The values of BH masses estimated for both samples are similar to those of powerful AGNs. The BH masses estimated using the MgII emission line are in the range $1.6 \cdot 10^8 M_\odot < M_{BH} < 12.2 \cdot 10^8 M_\odot$ and $1.0 \cdot 10^8 M_\odot < M_{BH} < 20.3 \cdot 10^8 M_\odot$ for GRQs and smaller radio quasars, respectively. I did not find that more massive BHs are located in GRQs.

3. I did not find any significant correlation between the BH mass and the radio luminosity. However, using the H_β and CIV line BH mass estimations, a weak correlation between the linear size of the radio structure and the BH mass has been noticed. This might suggest that the linear size of giants could be related to their central engines. Surprisingly enough, the same relation but based on the H_β analysis results, is different for GRQs and for smaller radio quasars, which could suggest an inherent difference between these type of objects. However, this result should be taken with some caution as it was obtained only for a small number of quasars. The relation between the linear size of the radio structure and the BH mass supports the evolutionary origin of GRQs as well.

4. The accretion rate for more massive BHs is smaller than that for less massive ones. It is consistent with the scenario that quasars increase their BH mass during the accretion process. The obtained mean value of accretion rate is equal to 0.07 for GRQs and 0.09 for smaller radio quasars. The lower value for GRQs suggests that GRQs are more evolved (aged) sources and the accretion process has slowed down or is almost over. The difference of $\dot{m}(\lambda)$ and BH mass between small-size radio quasars and large-size ones is, however, not statistically significant, which could indicate similarities in their evolution. I found also a weak correlation between the accretion rates and the core radio luminosity, that confirms some connection between the accretion processes and the radio emission (e.g. Lacy et al. 2001, Wang, Ho & Staubert 2003).

5. The results obtained from the measurements based on the H_β and CIV emission lines seem to be more homogeneous than those based using the MgII line. The BH masses derived from the H_β and CIV mass-scaling relations have also smaller uncertainties than those determined from the MgII line. The large uncertainties in the case of MgII measurements are due to the fact that this line is strongly affected by the Fe emission. Moreover, the large uncertainty of the mass-scaling relation slope for the MgII line is also due to the absence of reverberation data from systematic monitoring.

Chapter 3

Giant radio galaxies

3.1 The sample

In this part of my analysis I used 45 known giant radio galaxies (GRGs) for which the optical spectra were available in the 9th SDSS release and in the Isaak Newton Telescope (INT) archive databases[1]. The basic parameters and references are listed in Table C.1 where the columns contain: (1) J2000.0 IAU name; (2) and (3) J2000.0 right ascension and declination of the central position of the optical galaxy; (4) redshift of the host galaxy; (5) angular size in arcmin; (6) projected linear size in Mpc; (7) availability of the spectrum from the SDSS survey (S), or INT archive database (I); availability of radio maps from NVSS or FIRST (N or F, respectively); (8) references to the identified object. Some of the GRGs studied here have also visible double-double radio morphology. This double-double giant radio galaxies (DDGRGs) are marked in Table C.1 by an asterisk. As a comparison sample, I chose FRII type radio galaxies taken from Kozieł-Wierzbowska & Stasińska (2011) for which the optical and radio data were catalogued. This sample contains 401 FRII radio galaxies (including giant and double-double radio galaxies; DDRGs). As the authors mentioned, it is not a complete sample in any sense (it can not be used to study e.g. luminosity functions), but covers a wide range of radio powers and sizes of radio structures (for details of selection criteria see Kozieł-Wierzbowska & Stasińska 2011). Excluding GRGs and DDRGs, the final comparison sample contains 385 RGs. The excluded GRGs and DDRGs are marked in Tables C.1, C.4 by double and triple asterisk, respectively.

---

[1] http://casu.ast.cam.ac.uk/casuadc/ingarch/query

3.1.1 Sample biases

As mentioned in Section 2.1.1, similarly to giant radio quasars, the results for GRGs may be affected by selection effects related to sensitivity of the radio surveys that were used for selecting extended sources. Additionally, the inverse Compton losses against CMB can make invisible a steep spectrum and low surface brightness radio bridge connecting the radio core with hot spots in case of distant objects. Apart from the aspects described in Section 2.1.1, the sample of GRGs was reduced to those objects for which the optical spectra in the FITS format were available. Due to this criterion, I considered only GRGs with SDSS r magnitudes of their host galaxies fainter than 14.5 and brighter than 20.3. The lower magnitude limit still gives a sufficient S/N ratio of their optical spectra. The same criterion was applied to the comparison sample considered in this chapter.

3.2 Radio and optical data analysis

3.2.1 Radio data

I measured the basic parameters of radio structure for the GRGs sample in a similar way as it was described in Section 2.2. The measured parameters were: arm-length ratio Q, bending angle B, flux-density ratio F, total luminosity P_{tot}, core luminosity P_{core}, and an inclination angle i. For P_{tot} calculations I adopted the average spectral index $\alpha = -0.75$ and for P_{core} $\alpha = -0.5$ ($S_{\nu} \sim \nu^{\alpha}$). All obtained values for GRGs are listed in Table C.3, while the FIRST and NVSS radio maps, overlaid on the DSS optical images, are presented in Appendix D. For the FRII smaller-size radio galaxies sample only the P_{tot} was available and therefore no comparison of other parameters (e.g. P_{core} and radio structure parameters) with these obtained for GRGs was possible.

3.2.2 Spectra reduction and black hole mass determination

The INT spectra of giant radio galaxies were preliminary reduced and flux as well as wavelength calibrated using standard procedures of the IRAF package. The next reduction steps were done for all GRGs (from INT and SDSS) in a similar way as for the sample of giant radio quasars (see Section 2.3.1). The continuum fitting was done using the Starlight Spectral Synthesis Code[2] (Cid Fernandes et al. 2005) which fits the stellar continuum based on the superposition of stellar spectra. I used 150 stellar spectra templates (extracted from the evolutionary synthesis models of Bruzual & Charlot 2003)

---

[2] http://www.astro.ufsc.br/starlightst

with various ages (1 Myr$\leq$t$_*\leq$18 Gyr) and metallicities (0.005$\leq$Z/Z$_\odot\leq$2.5). The upper age limit is inconsistent with the currently accepted age of the Universe (13.7 Gyr) but taking into account uncertainties in stellar evolution, cosmological parameters, observations and in the fits themselves, this inconsistency is merely formal (Asari et al. 2007). The narrow spectral windows, where emission lines are expected, have been excluded in the fitting procedure. Apart from the continuum fitting, star formation, chemical enrichment histories and velocity dispersion parameters were also modelled. The continuum fits and spectra of GRGs are presented in Appendix D.

To determine BH masses I used the M$_{\rm BH}$-σ_* method which is a very useful way of BH mass estimation in active galaxies. It is based on a tight correlation between a BH mass and the velocity dispersion of stars in the galactic bulge (Ferrarese & Merritt 2000, Gebhardt et al. 2000). It is described by the relation:

$$log(\frac{\rm M_{BH}}{\rm M_\odot}) = \alpha + \beta log(\frac{\sigma_*}{\rm 200kms^{-1}}) \tag{3.1}$$

where the recent estimations of the α and β constants are:
$\alpha = 8.12 \pm 0.08$, $\beta = 4.24 \pm 0.41$ based on a sample of 49 sources (Gültekin et al. 2009) and $\alpha = 8.13 \pm 0.05$, $\beta = 5.13 \pm 0.34$ based on a sample of 64 sources (Graham 2011). The values of the above constants were estimated by many authors who obtained very similar results of the α constant but a bit different ones for the β parameter spanning over a range from 3.75 to 5.3. This discrepancy is believed to be a consequence of systematic differences in the adopted values of σ_* (e.g. Tremaine et al. 2002). In my analysis I used the values of the constants given by Graham (2011) because the sample used in their determination was larger and gave a smaller intrinsic scatter of the M$_{BH}$-σ_* relation. Hereafter, the BH mass derived using the equation 3.1 will be denoted as M$_{\sigma*}$. Resulting BH masses are presented in Table C.2. For four GRGs it was not possible to obtain a good stellar continuum fit, therefore, their BH masses were not estimated. I plot the spectra of those galaxies without continuum fit in Appendix D.

3.3 Radio properties

In order to check the flux limitation of the radio galaxies samples, I plotted in Figure 3.1 the dependence between the 1.4GHz total radio luminosity and the redshift. A similar trend to that noticed for the sample of radio quasars is also seen: the radio luminosity increases with redshift. This trend is likely due to selection effects (discussed in Section 2.4). The Sperman rank correlation coefficient for the linear fit is equal to 0.59 and it is smaller than that for GRG samples used in earlier studies (Ishwara–Chandra

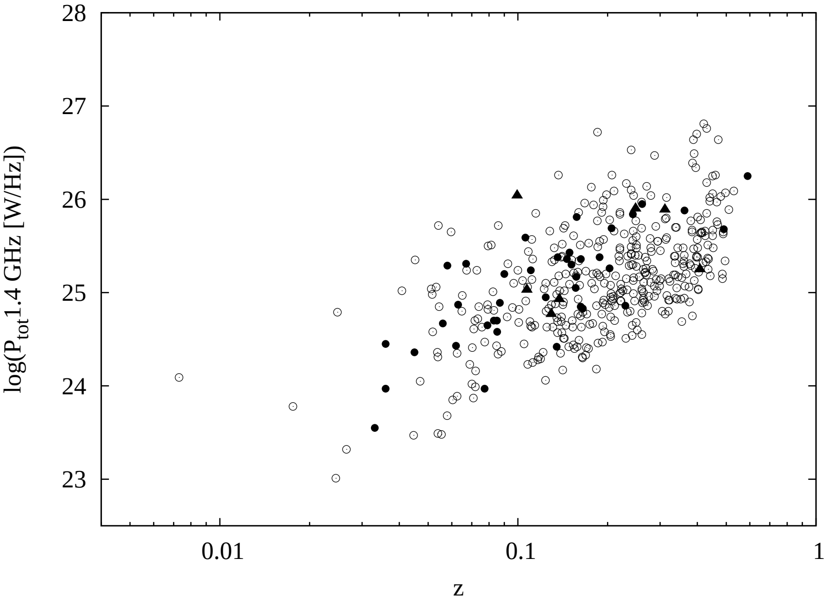

FIGURE 3.1: 1.4 GHz total radio luminosity as a function of redshift. The GRGs are marked with solid circles and smaller FRII radio galaxies with open circles. Such a notation is used in all diagrams in this chapter. Some of GRGs were also classified as DDRSs. These are marked by solid triangles.

& Saikia 1999). Therefore, the new sample of GRGs considered in this chapter is not so strongly flux limited as the earlier studied samples were.

The *P-D* diagram is plotted in Figure 3.2. The observed behaviour is consistent with evolutionary tracks for radio sources. The first phase of RSs evolution also can be seen in this diagram. There are few extremely compact radio galaxies with low total radio luminosities in the FRII radio galaxies sample. According to predictions of dynamics and luminosity evolution models of radio sources, three phases of evolution are expected to be present. While lobes expand (within the host galaxy), the radio luminosity rises with radio source size increase to the moment when synchrotron losses become dominant. After this point, the radio luminosity steadily decreases with increasing source size and finally passes throughout the phase of sharp decrease of luminosity when the inverse Compton losses, resulting from the CMB energy density, dominate the synchrotron losses (Kaiser & Best 2007, An & Baan 2012).

3.4 Black hole masses vs. radio properties

In order to check the role of AGNs in generation of the Mpc scale radio structures, I compared their BH masses with their other internal properties. If we assume that giants are formed due to longer or/and restarting AGN activity phases, larger BH masses

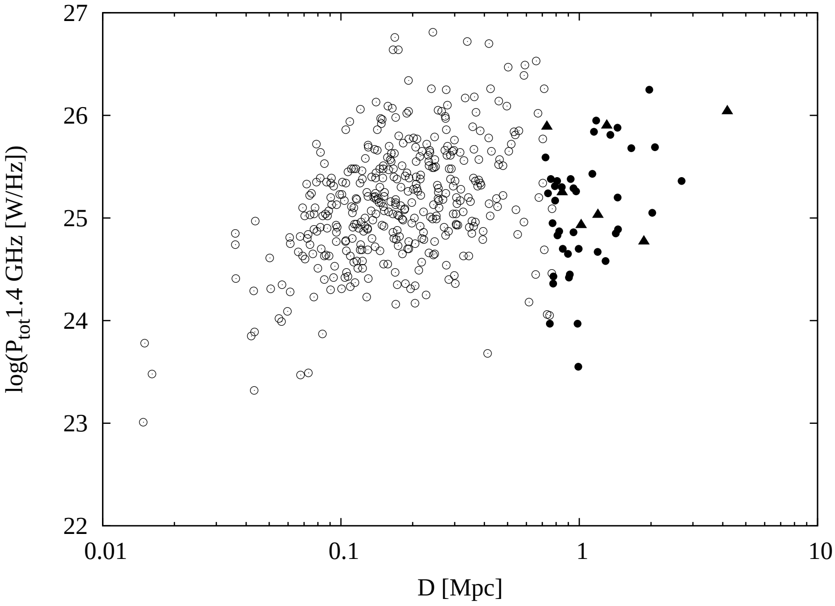

FIGURE 3.2: Luminosity-linear size diagram for GRGs and smaller FRII RGs.

should be expected as a result of longer accretion time of matter onto a BH. In Figure 3.3, where the dependence between $log\mathrm{M}_{\sigma*}$ and projected linear size is plotted, the behaviour similar to that observed for GRQs (Figure 2.7) is not visible.

Relations between a BH mass and the linear size of radio structures are similar for giant

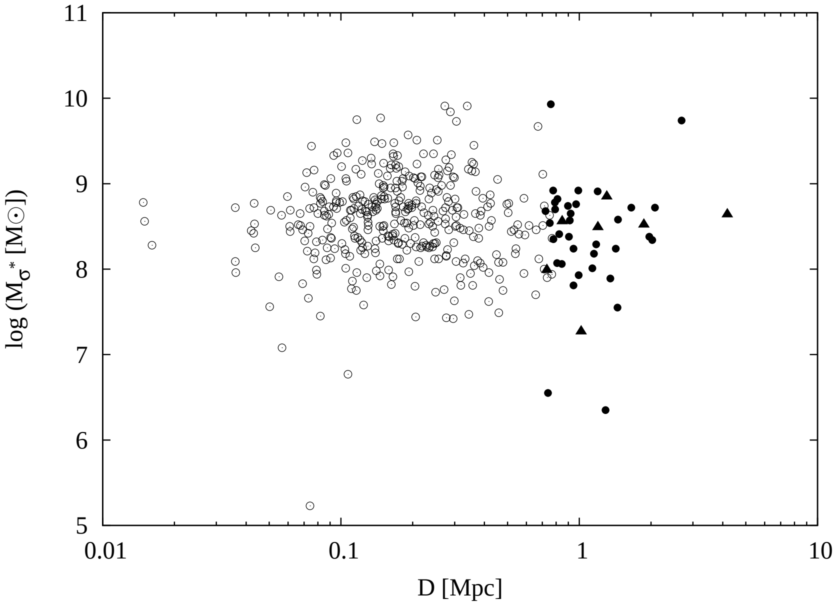

FIGURE 3.3: Relation between $log\mathrm{M}_{\sigma*}$ and logarithm of projected linear size for GRGs and smaller FRII radio galaxies.

and smaller FRII type radio galaxies, but different than that for giant radio quasars (Figure 2.7). Assuming that the different $M_{BH}-D$ relation for GRQs is real and indeed may be explained by a different composition of BLR in young and old radio sources, such an explanation could not be applied to giant radio galaxies. This is because their BH masses were determined using the $M_{\sigma*}$ method, which is based only on the velocity dispersion of stars in the galactic bulge and not related to BLR in any sense.

$M_{\sigma*}$ as a function of total radio luminosity is shown in Figure 3.4. It can be seen that no any correlation between the two parameters is present. The distribution of $log M_{\sigma*}$ and $log P_{tot}$ spans a wide range of values for both samples. The mean values of $log(M_{\sigma*}[M\odot])$ and $log(P_{tot}[W/Hz])$ for the sample of GRGs are: 8.4±0.7 and 25.1±0.6, and for the smaller FRII radio galaxies sample 8.6±0.6 and 25.2±0.6, respectively. Also, the BH masses of DDGRGs are considered separately, it can be seen that there is no difference visible between double-double and other radio galaxies. Concluding, my results indicate that giant radio galaxies do not have larger BH masses than smaller in size radio galaxies.

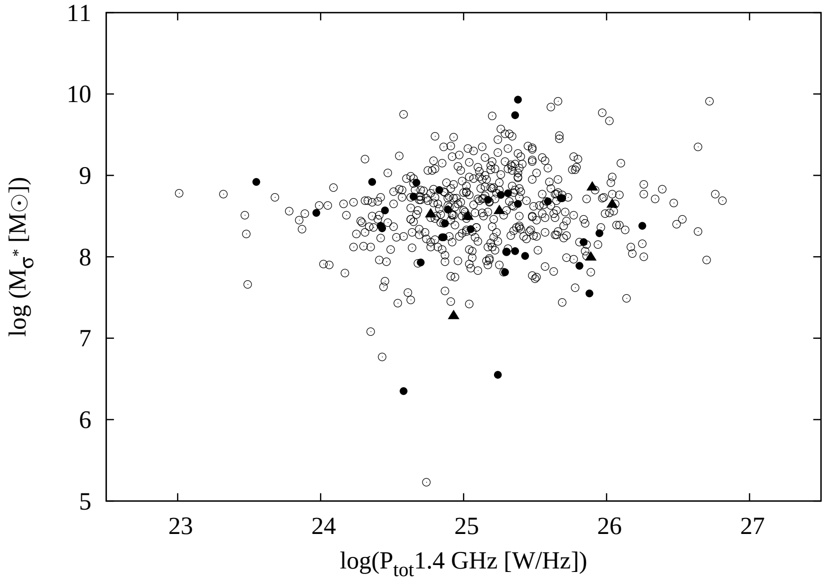

FIGURE 3.4: Relation between logarithms of $M_{\sigma*}$ and total radio luminosity.

3.5 The evolution from Compact Steep Spectrum to Giant Radio Galaxies

To test the hypothesis that radio sources begin as very compact objects and then evolve to larger and more complex radio structures (as postulated by evolutionary models of RSs e.g. Kaiser & Alexander 1997) and to verify processes of BH mass growth during

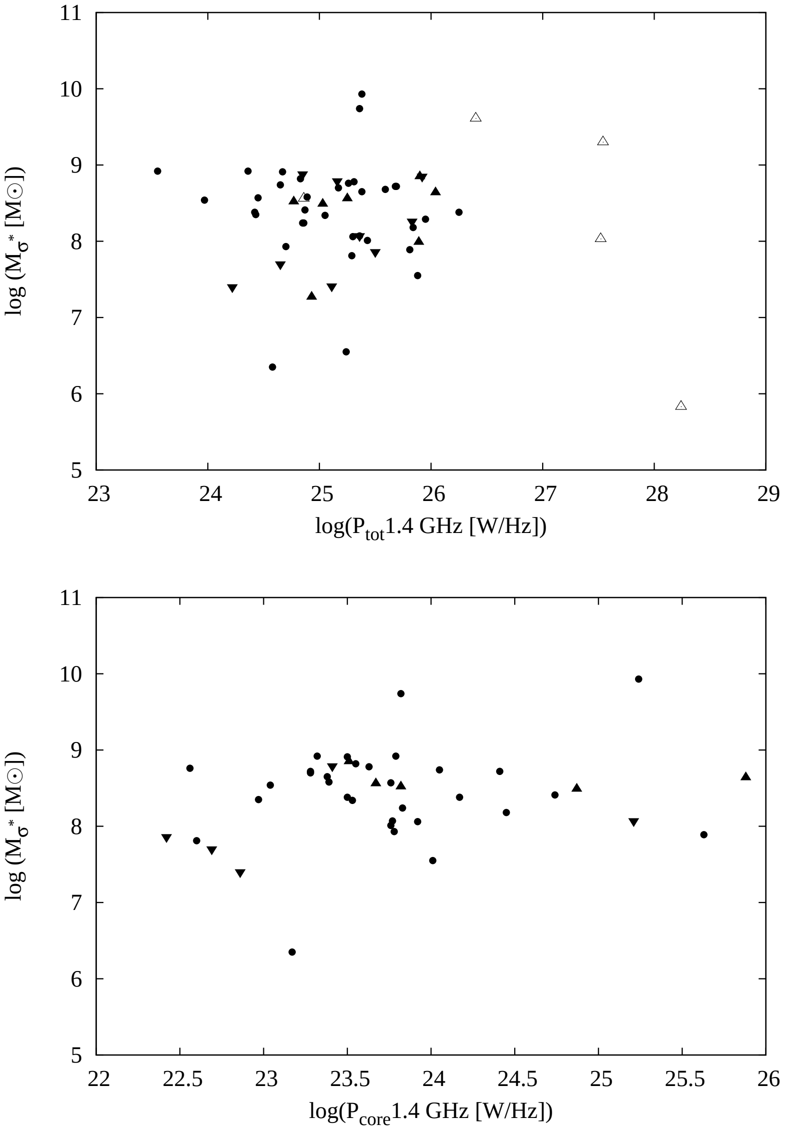

FIGURE 3.5: The dependence between $log\mathrm{M}_{\sigma*}$ and total radio luminosity (top panel), and core radio luminosity (bottom panel) for samples of GRGs (solid circles), DDGRGs (solid triangles), smaller size DDRGs (solid upturned triangles) and CSS radio galaxies (open triangles). The same notation is used in next two Figures.

this process, I collected additional samples of RGs. They contain CSS radio galaxies (5 sources) taken from the sample described by Czerny et al. (2009) and DDRGs (8 radio galaxies with small size and 7 giant radio galaxies) taken from the sample of Nandi & Saikia (2012) and other publications listed in Table C.4. The main selection criterion was the availability of their SDSS optical spectrum. The basic parameters of those classes of RSs are listed in Table C.4. Using the same methods as described in Section 3.2, I determined their BH masses, total and core radio luminosities and plotted them in Figure 3.5. I did not place small FRII radio galaxies (from Kozieł-Wierzbowska &

Stasińska 2011) in the graph for the sake of clarity (for comparison see Figure 3.4). It is seen that no any evolutionary behaviour in the $M_{\sigma*}$-P_{tot} plane can be seen. Young CSS radio galaxies have BH with masses similar to these of old GRGs confirming my finding described earlier. This might suggest that there is no relation between BH masses and the linear size of RSs. However, the number of sources is small and future studies based on larger samples of different types of RGs are needed to test this hypothesis more reliably.

There are estimations of ages t_{RS} for few objects from my sample in the literature. For four CSS radio galaxies it was determined based on the continuous injection model (Myers & Spangler 1985, Carilli et al. 1991). This model assumes that a RS is continuously being supplied by a constant flow of relativistic particles. The ages of double-double, giant and smaller size FRII radio galaxies were determined using the Jaffe-Perola model (Jaffe & Perola 1973) which assumes single injection of particles with subsequent scattering in a pich angle. This method gives more precise results than the continuous injection model for extended radio lobes (Jamrozy et al. 2008). For J1247+6723 CSS radio galaxy instead of the synchrotron age, its kinematic age was determined based on the measurement of the hot spot separation speed. The parameters derived for these sources are given in Table C.4.

In Figure 3.6 I plotted the *log* of linear size against $log t_{\mathrm{RS}}$. The trend that older radio sources have larger linear sizes can be noticed. It is consistent with studies of Murgia (2003), Parma et al. (1999) and Jamrozy et al. (2008). The number of radio galaxies in Figure 3.6 is very small due to the selection criteria which were used to complete the samples. The lack of optical spectroscopic data significantly cuts down the number of objects with available estimations of a radio source age.

The dependence between $log t_{\mathrm{RS}}$ and logarithm of $M_{\sigma*}$ is plotted in Figure 3.7. It can be seen that there is no clear relation between those parameters. This fact may suggest that BH masses do not grow significantly during a RS lifetime (this is also confirmed in Figure 3.5) or that such a relation can be different at subsequent evolutionary phases of RS. However, to verify this hypothesis, a larger sample of RSs with both homogeneous measurements of RS ages and spectroscopic data is required.

3.6 Stellar populations

The star formation history of a host galaxy is another aspect considered in my work. During modelling of a galaxy continuum using the Starlight Synthesis Code (see Section 3.2.2), we can get an information what stellar population mixture in a particular

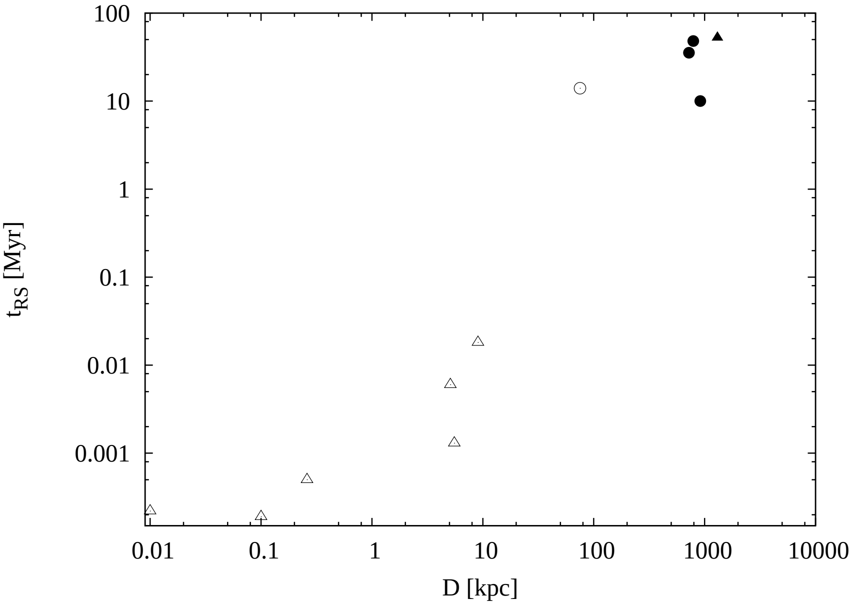

FIGURE 3.6: The dependence between logt$_{\rm RS}$ and logarithm of projected linear size.

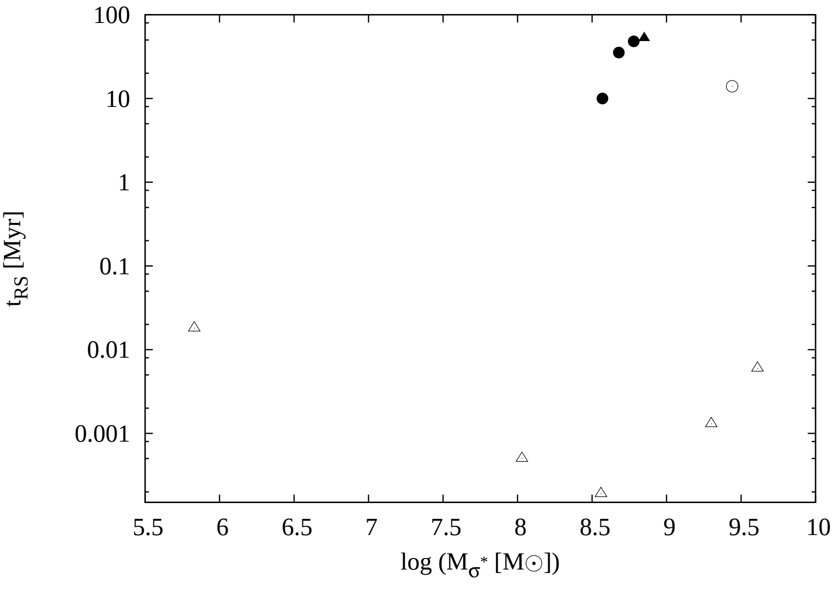

FIGURE 3.7: The dependence between logt$_{\rm RS}$ and logarithm of $\mathrm{M}_{\sigma *}$.

galaxy is. It can be expressed by the light-fraction population vector x_j which gives the percentage fraction of a galaxy light (luminosity) which comes from stars of a given age and metallicity (Cid Fernandes et al. 2004). I plotted the histograms which present the age distribution of stellar populations expressed by x_j in Figure 3.8. The histograms were generated for compact steep spectrum, giant and double-double radio galaxies for different metallicities from Z=0.005 to Z=2.5. The plotted x_j vector is a mean value of light-fraction population vectors obtained for each object from the studied samples. The summarized light-fraction population vector Σx_j (the sum of x_j over all range of metallicity) is plotted in Figure 3.9. Double-double giant radio galaxies were included both in GRGs and DDRGs samples. It can be seen that the star formation histories for the studied objects are somewhat similar but there are also some differences.

Majority of stars have ages in two ranges: from 1 to 10 Myr and from 1 to 11 Gyr in CSS radio galaxies. Most of them have low metallicities but also high metallicity stars are observed in those two age ranges. In GRGs the significant number of stars have advance ages with the medium and high metallicities and only a small fraction of young stars with low Z. In DDRGs a significant number of stars have ages in the whole range with low and high metallicities. The two maxima of stellar ages are also seen in 1-10 Myr and 1-11 Gyr ranges. The older stellar populations might be related to the cosmological epoch when the galaxy mergers were very frequent.

Next, I compared the star formation histories with the radio activity phase. The approximated scales of a RS radio activity phase are marked in Figure 3.9. It can be seen that the metal poor young stellar populations were born at the time when radio emission occured. According to hydrodynamical simulations of jet propagation in an early phase of radio activity (before cocoon expansion), cold clouds are compressed and star formation increases, but later, when the cocoon has propagated, the temperature of clouds and the ISM increases and star formation quenches in a time of $\sim$2-3×1 Myr (Tortora 2009). This is due to higher temperature of clouds and ambient medium that increases the critical mass for gravitational collapse and increases the stripping outer regions of clouds due to instabilities. Such a scenario could explain larger number of young stars in the case of DDRGs and, to some extent, in GRGs, but not in CSS radio galaxies. It is also possible that some earlier phases of radio activity were present during the host galaxy life, but detection of such old radio structures is very difficult or even impossible due to very low radio luminosities of presumably old radio lobes. However, based on arguments listed above, drawing a conclusion that radio activity can trigger significantly the star formation in a galaxy may be somewhat exaggerated and requires further investigation.

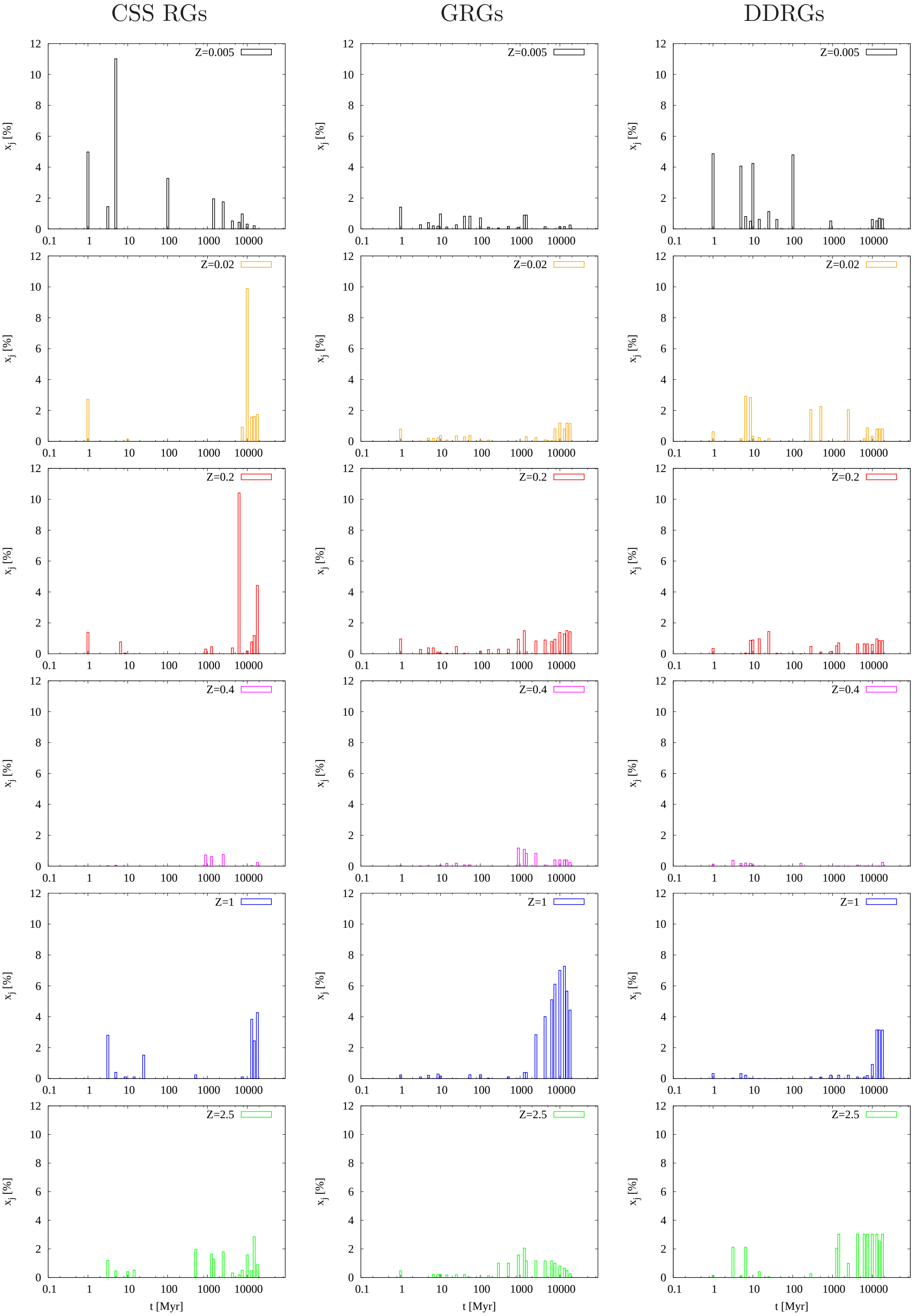

FIGURE 3.8: Age distribution of the light fraction x_j population vector for different metallicities and different types of RSs: left panel: CSS radio galaxies, middle panel: GRGs, right panel: DDRGs.

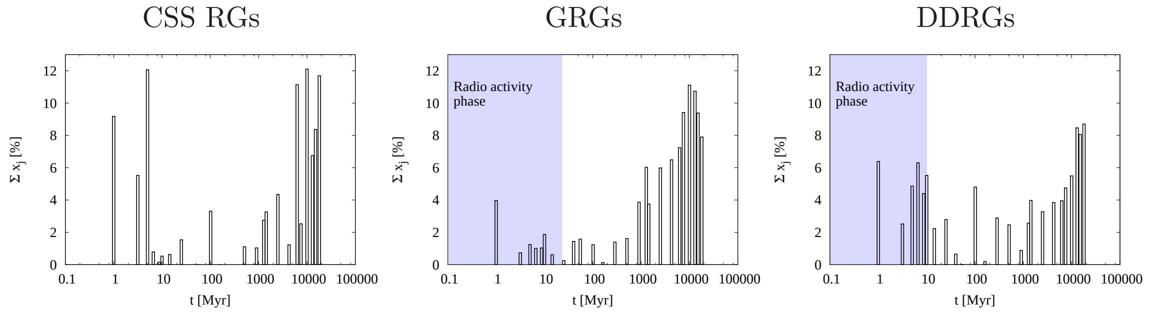

FIGURE 3.9: The age distribution shown as summarized light-fraction population vector Σx_j.

3.7 Results

In this section I presented the comparison between radio and optical properties of giant and smaller size FRII type radio galaxies. I can conclude the obtained results as follows:

1. The distribution of GRGs and smaller size FRII radio galaxies on the *P*-*D* plane is consistent with predictions of RS evolutionary models. According to them, GRGs have evolved out of smaller RGs.

2. I did not find any correlation between BH masses and the total radio luminosities as well as the linear size of radio structures. The distribution of $M_{\sigma *}$ and P_{tot} are the same for both considered samples of RGs. The relation between BH masses and the linear size of radio structures, similar to that observed for RQs, is not seen for RGs. If we assume that the origin of such a relation may be due to different composition of BLR in giant and smaller-size RSs, we should not expect to see it in radio galaxies. The $M_{\sigma *}$ estimations for the latter are based on velocity dispersion measurements and they should not be related to BLR properties in any aspect.

3. The correlation between the synchrotron age and the projected linear size of RGs (with sizes from few kiloparsecs up to megaparsec scales) exists, in accordance with earlier studies.
   I did not find any significant correlation between t_{RS} and $M_{\sigma *}$. This may suggest that BH mass does not grow during RSs lifetime or that such a relation can be different at various evolutionary phases of radio sources. However, a small number of objects for which both the age estimations and spectroscopic data are available, does not allow for a firm conclusion.

4. The DDRGs do not constitute a distinct group of AGNs. All measured parameters are comparable with those obtained for other radio sources. This suggests that their hosts are very similar to those of other RGs with the exception of the recurrent radio activity phenomenon.

5. The analysis of stellar populations in CSS, giant and double-double radio galaxies shows that star formation histories of GRGs were different than these for CSS radio galaxies and DDRGs. The host galaxies of GRGs mainly consist of old stars with high metallicities.

Chapter 4

Comparison of radio quasars and radio galaxies

In the next step, a comparison of properties of giant radio quasars and giant radio galaxies based on obtained results was done. Despite of the fact that methods used for determination of parameters presented in this thesis (i.e. BH mass values) were different for both classes of giants, such a comparison could be meaningful as these methods are considered to be the most accurate for each class of objects.

4.1 Radio properties

Some authors (e.g. Kaspi et al. 2005) have suggested that giants should have more prominent cores, as stronger nuclear activity is necessary to produce larger linear sizes of their radio structure. Ishwara–Chandra & Saikia (1999) attempted to verify this hypothesis for giant size radio galaxies by plotting a diagram of the core prominence, f_c, which is the ratio of the core luminosity to the total luminosity of a radio source, but they did not find giants to have more prominent cores. I plotted a similar diagram for samples of giant radio galaxies, giant radio quasars and radio quasars from the comparison sample (see Figure 4.1) and I arrived to a similar conclusion. Such a result is in agreement with the existence of the core luminosity-total luminosity correlation visible in Figure 4.1 where smaller RSs have more luminous cores but also larger total luminosities than GRSs.

I also investigated the asymmetries of radio structures in both giant radio quasars and galaxies samples. It is well known that a non-uniform environment (i.e. non-uniform density on both sides of the core) can be one of the factors underlying radio structure

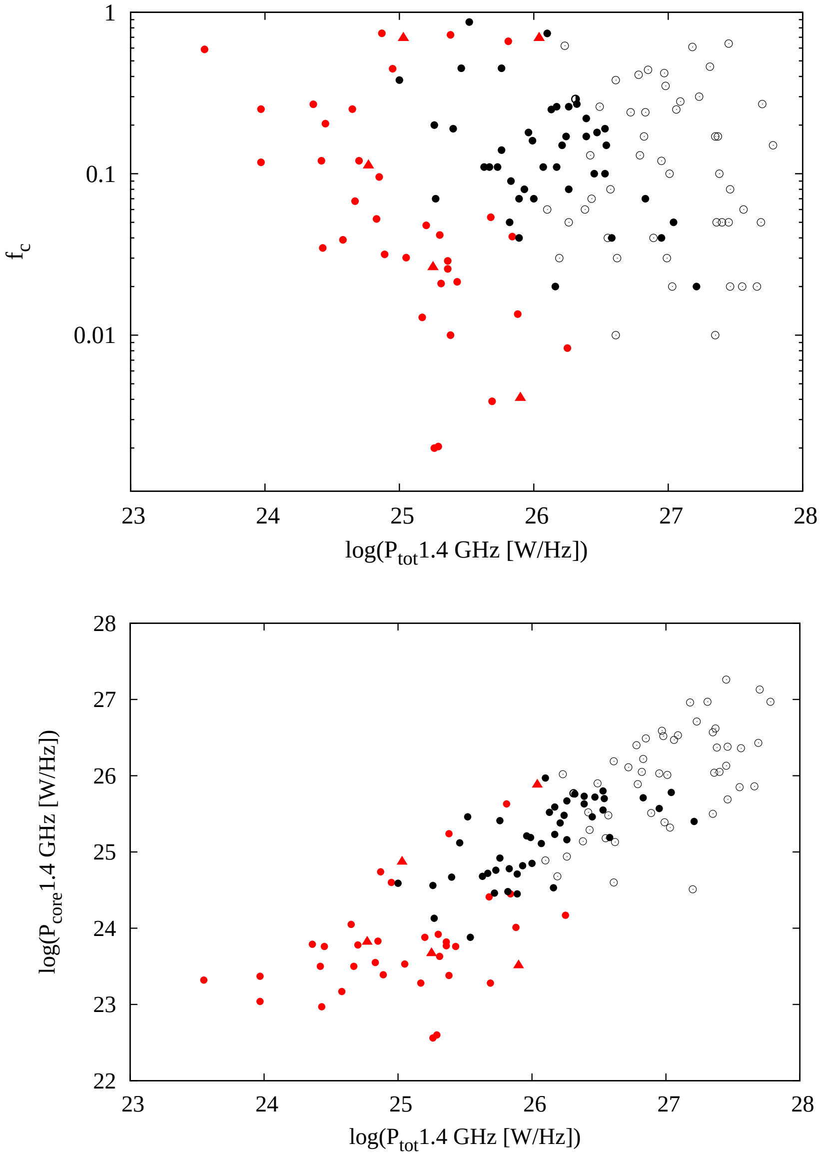

FIGURE 4.1: Top panel: core prominence against total radio luminosity. Bottom panel: core radio luminosity versus the total radio luminosity for RQs. A strong correlation is visible. Black colour: solid and open circles correspond to GRQs and smaller size RQs respectively, the half solid circle denotes QSO J1623+3419 (as in Figure 2.2); red colour: solid circles represent GRGs while solid triangles - DDGRGs. Such a notation is used in all Figures throughout this chapter.

asymmetries, which can be described by the arm-length ratio Q (e.g. Scheuer 1995). The distribution of this parameter for giant and smaller size RQs from the comparison sample is presented in Figure 4.2 (top panel). I found that GRQs seem to be more symmetric than smaller RQs (there were no GRQs with $Q>2.4$ in my sample). However, the mean values of the Q parameter for GRQs and for the comparison sample are 1.41 ± 0.36 and 1.65 ± 0.61, respectively. Taking into account large uncertainties of the obtained values of the Q parameter, no statistically significant conclusion about differences in radio structures morphology between giant radio quasars and galaxies can be drawn based on the investigated samples. This indicates that GRQs and smaller sources evolve in a similar IGM. I also compared GRQs arm length ratios with those obtained for GRGs (bottom panel in Figure 4.2). The distribution of the Q parameter is very similar for both samples. The mean value for all GRSs is equal to 1.41 ± 0.36, exactly the same as the one computed for GRQs. My results agree well with those of Ishwara–Chandra & Saikia (1999), who found that the mean value of the Q parameter for GRSs is 1.39;

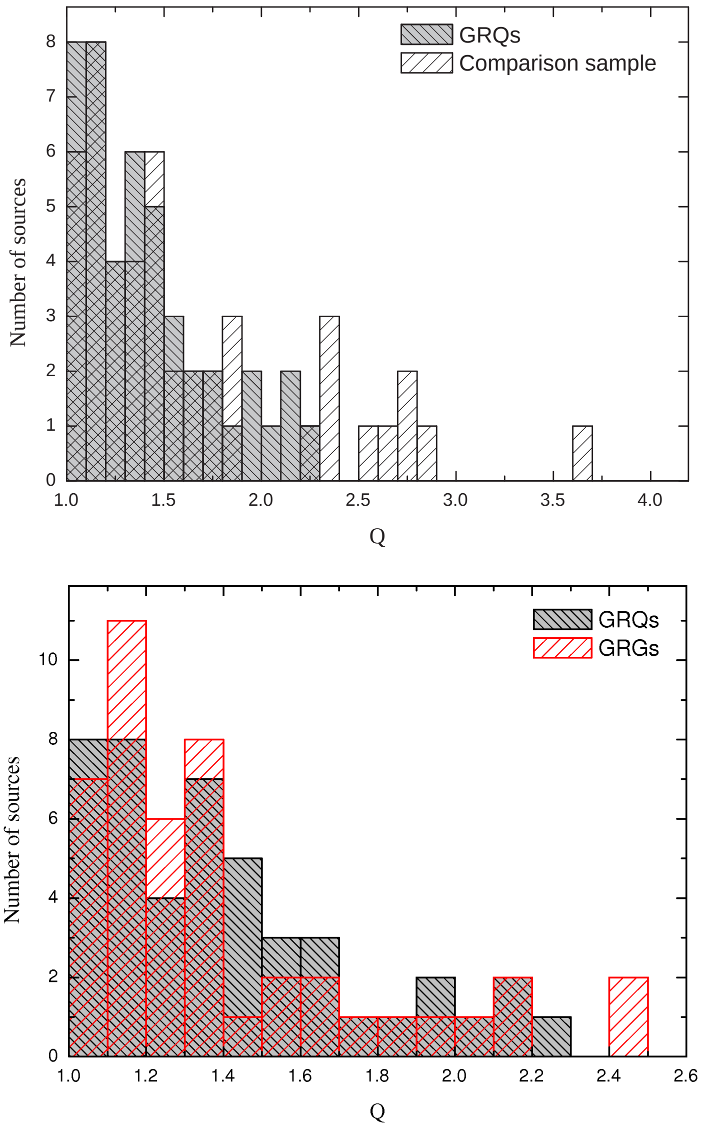

FIGURE 4.2: Distributions of the arm-length-ratio parameter Q. The top panel shows all GRQs and the comparison sample of RQs, while the bottom one includes GRQs (black boxes) and GRGs (red boxes). The observed distribution of the Q parameter suggests that the IGM in which the GRQs evolve has no different properties than that around the smaller size sources.

for a comparison sample based on smaller 3CR sources they obtained a smaller Q value of 1.19.

Determination of values of the bending angle B and the lobe flux-density ratio F gives a similar result for both samples of quasars, with mean values of B=7°.4 ± 5°.89, F=1.45±1.16 and B=8°.5 ± 7°.31, F=2.28±5.53 for GRQs and the comparison sample, respectively. The mean values of the bending angle and the lobe flux-density ratio for all giant radio sources (galaxies and quasars) are: B=6°.9 ± 6°.03 and F=1.13±0.89. The distributions of B and F for GRSs are presented in Figure 4.3. The obtained results show, that there are no any significant differences in the environmental properties of the IGM within which giant and smaller size RSs evolve. No significant differences among

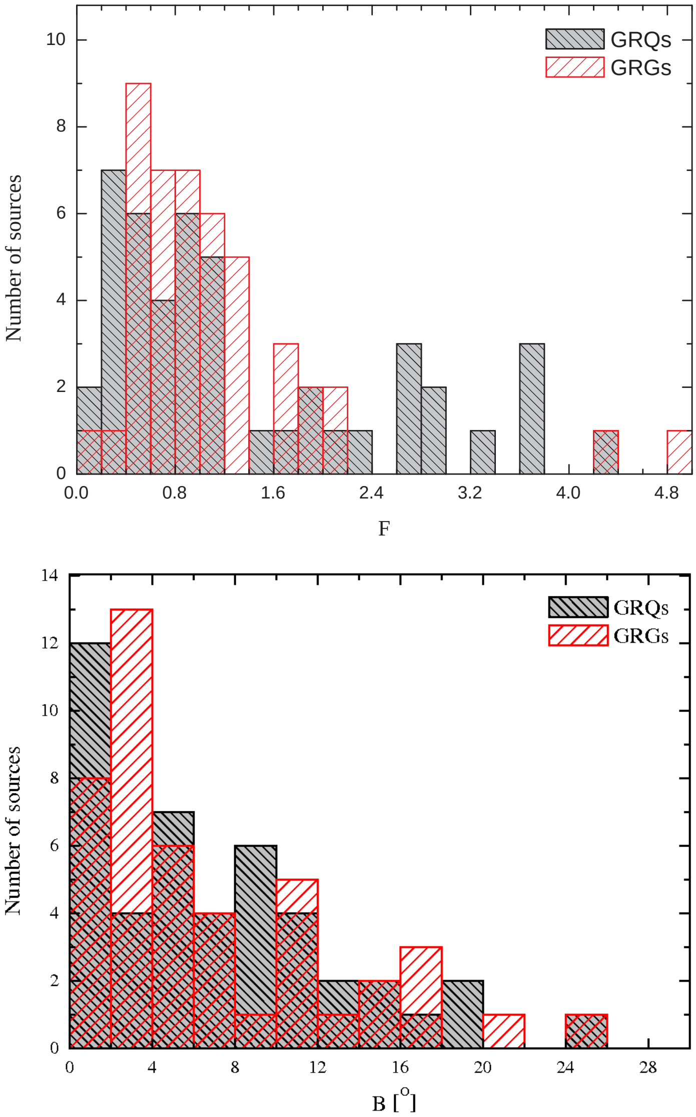

FIGURE 4.3: Distribution of flux-density ratios (top panel) and bending angles (bottom panel) for giant radio quasars and galaxies. No significant difference can be seen.

Q, B, F parameters between the samples of giant radio quasars and galaxies can also be noticed.

Furthermore, I checked the distribution of the inclination angle (see Figure 4.4) of objects analysed in this work. I found, that for the sample of RQs, most objects have inclinations between $60^{\rm o}$ and $90^{\rm o}$. This result is inconsistent with the models of the AGN unification scheme, in which, following Urry & Padovani (1995), the inclination angles for QSOs have values between $0^{\rm o}-45^{\rm o}$. In those objects with an inclination angle larger than $45^{\rm o}$, the broad-line region should be partially or totally obscured by a dusty

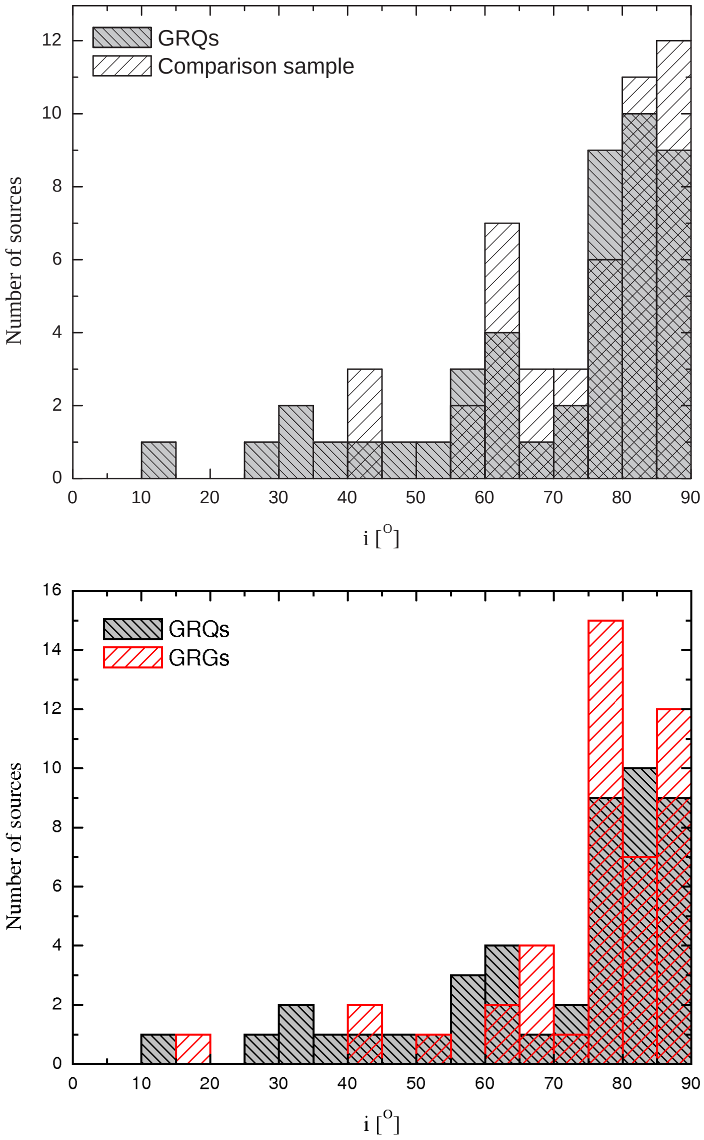

FIGURE 4.4: Distribution of the inclination angles, i, for samples of RQs (top panel) and for giant radio quasars and galaxies (bottom panel). For the definition of the inclination angle see Section 2.2. For i=90° the jets and lobes lie in the plane of the sky.

torus and the broad emission lines should not be as prominent as we observe in the spectra from the QSO sample. A plausible explanation of the observed distribution of inclinations is that there could be no dusty torus in some AGNs (Elitzur 2008) or that we are dealing with a clumpy or receding torus (i.e. Nenkova et al. 2008), thus broad emission lines can be observed even in QSOs with high inclinations. The most asymmetric radio structure is observed in the quasar J1623+3419 which has the inclination angle of i=13^o. Such a small value suggests that, more properly, it should be classified as a blazar. Further observations are needed to confirm whether its observed radio structure is actually related to a unique radio source. Contrary to that for giant radio quasars, the distribution of inclinations of giant radio galaxies is consistent with the AGN unification scheme.

4.2 Black hole masses vs. radio properties

The dependence between BH mass and the projected linear size is presented in Figure 4.5. I obtained similar mean values of log(M$_{BH}[M\odot]$) for GRSs and the comparison samples equal to 8.51 ± 0.54 and 8.59 ± 0.49, respectively. It can also be seen that BH masses of RGs span over a wider range of values. This could be a result of uncertainties introduced by the BM mass determination method as the mass scaling relations are less accurate than the the M-σ^* method.

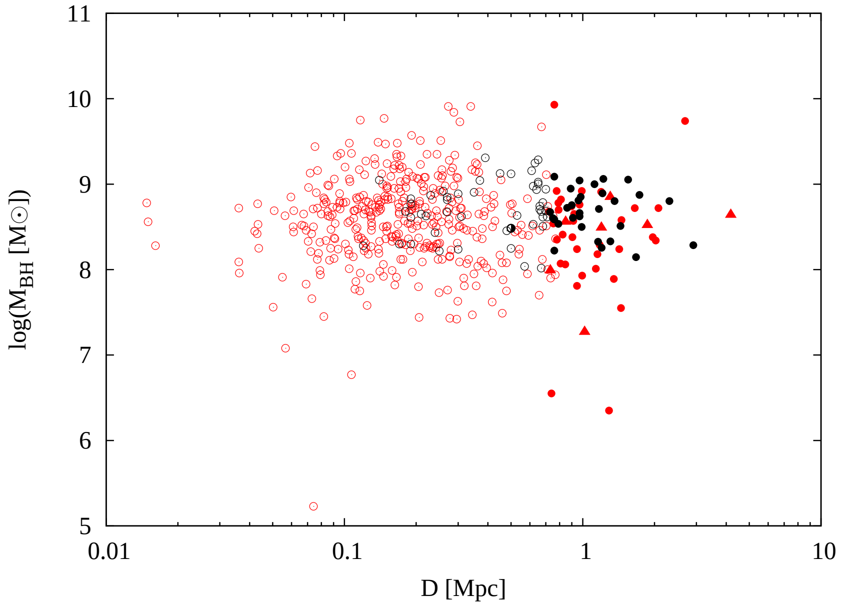

Figure 4.5: Dependence between BH masses and projected linear sizes in the logarithmic scale. Red open circles represent smaller FRII radio galaxies. Meaning of other symbols is the same as in Figure 4.1.

Figure 4.6 presents the dependence between BH masses and total as well as core radio luminosities. The core radio luminosities were not available for sample of smaller size FRII radio galaxies and therefore they are not shown in this graph. There are no any dependence visible between radio luminosities and BH masses.

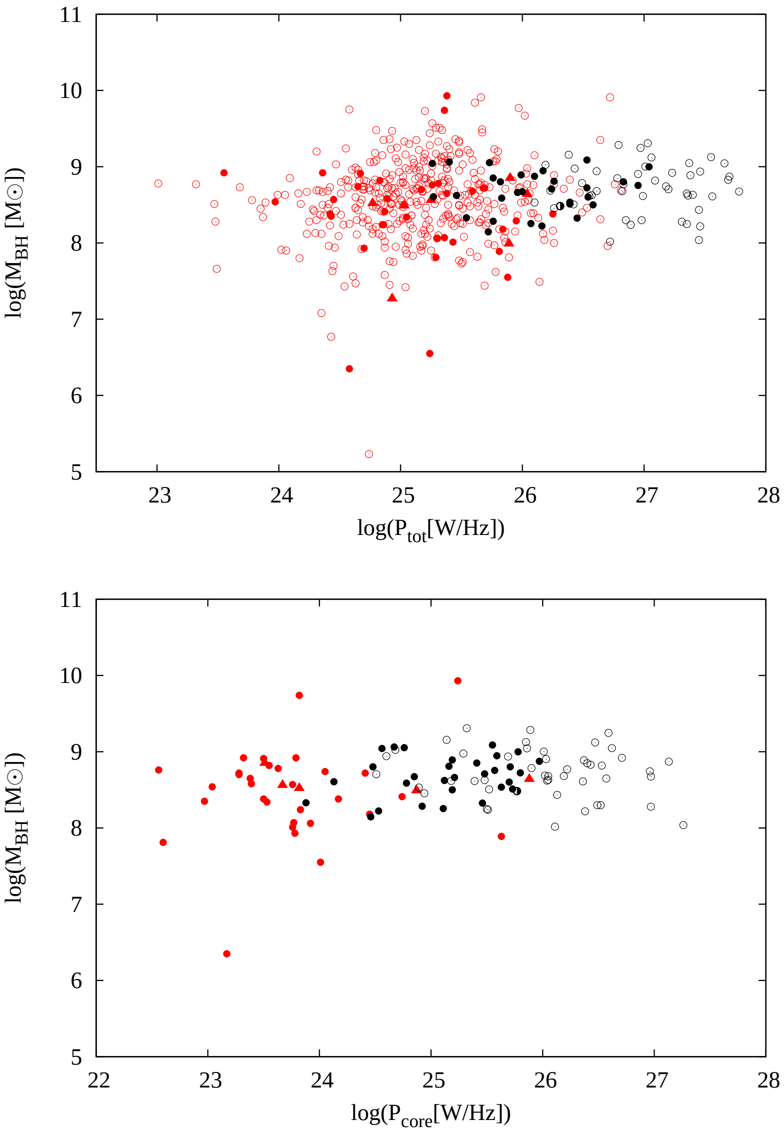

Figure 4.6: The dependence between BH masses and total radio luminosities (top panel), and core radio luminosities (bottom panel) in logarithm scales for QSOs and RGs.

Finally, looking at the dependence between BH mass and redshift for samples of RSs studied in this chapter (Figure 4.7), one can see that there is a tendency of a BH mass moderate growth with cosmic time from z=2 to z=0.5 and then its decline towards z=0. The problem of BH mass growth was investigated by a number of authors (e.g. Trakhtenbrot & Netzer 2012). They studied large samples of optically selected objects. As a result, usually they obtained that BH masses increase with redshift to an upper limit of about $\sim 10^{10}M_{\odot}$ (at z$\sim$2) and then remain at the same level. Such a trend could be strongly biased by selection effects arising from flux-limited samples. From my analysis performed for samples of giant and smaller size radio sources, I have obtained a similar result for RGs but an opposite one for RQs, for which BH masses tend to decrease with redshift. Such a behaviour obtained for RQs may be a result of the single epoch virial method used for their BH mass determination. Due to its large uncertainties, the observed behaviour could be just spurious.

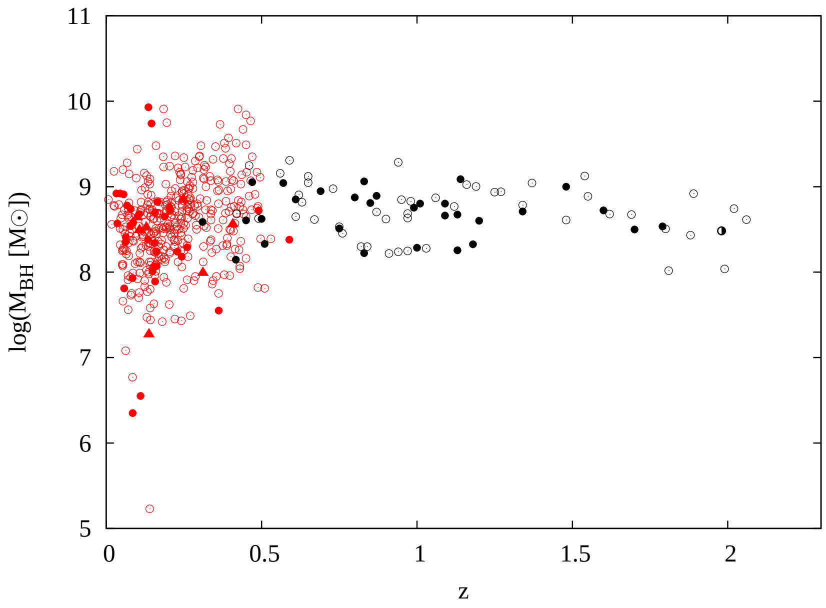

FIGURE 4.7: The relation between *log* M_{BH} and redshift for QSOs and RGs.

4.3 Results

1. There is no evidence that giant radio sources have more prominent radio cores, which could suggest that giants are similar to smaller objects if we take into account their energetics at radio wavelengths.

2. The arm-length ratio and bending-angle values for giant radio galaxies, giant radio quasars and smaller size RQs are all similar. This indicates that there is no significant difference of the environmental properties of the IGM within which giant and smaller RSs evolve.

3. Statistically, the inclination angles obtained for the samples of quasars studied here are inconsistent with the traditional AGN unification scheme. Inclinations larger than 45° could, however, be explained based on recent results from studies of dusty tori properties. The inclinations obtained for sample of giant radio galaxies have the same distribution as that for giant radio quasars. Therefore, the distribution of i for GRGs is in a good agreement with the unification scheme.

4. The BH masses of giant radio quasars and galaxies derived using different methods are comparable. Some bias between mass estimations is obvious but it does not qualitatively change the obtained results.

5. The similarities of parameters obtained for giant radio quasars and galaxies allow to consider them as the same class of objects when investigating properties of their extended radio structure.
6. It should be mentioned that in such studies, lack of spectroscopic data is a severe limitation. This fact restricts the sample of GRSs only to the brightest ones in the optical band. Also the investigations are limited to relatively nearby galaxies due to detection limits of radio and optical surveys.

Chapter 5

Conclusions

In this thesis I have investigated possible reasons why some radio galaxies have gigantic size of their radio structures. Especially I checked if central engines of GRGs are more powerful than that in smaller size radio sources. This was done by investigating the properties of host galaxies in these sources, including the black hole masses. Other possible models of GRSs origin were also considered, such as environment properties in which jets propagate as well as radio sources ages. To achieve the goals, samples of giant quasars and giant galaxies were collected. The new sample of giant radio quasars is the largest one known to date. Except for 23 already known, it contains also 24 newly recognised giants. The direct and indirect relations between host galaxies and their radio properties were investigated. By comparing BH masses and accretion rates with total and core radio luminosities, sizes of radio structures and (in some cases) their ages, it was possible to characterize qualitatively the significance of the central engine in generation of gigantic radio structures.

In summary, taking into account the optical and radio properties, I can conclude that except for the size of radio structures, giant radio sources are similar to smaller size radio sources in any other aspect. In particular, their BH masses are comparable to those of smaller radio sources and in case of giant radio quasars, also accretion rates are not significantly different than that of smaller ones. I did not find any significant correlation between the BH masses and radio luminosities of objects considered. It rather seems that the BH mass is not related to radio activity and its recurrency. According to several studies on BH mass evolution with cosmic time, the masses have grown much earlier than the observed radio activity phase occured. Therefore, even if a BH mass has had some influence on an object radio emission - the relation between these parameters can be hard to detect at present.

The distribution of arm-length ratios and bending-angle values for both radio quasars and giant radio galaxies samples are very similar. That indicates that there is no significant differences in environmental properties of the IGM within which giant and smaller radio sources evolve. Of course, more precise studies of IGM (when estimations of IGM density and pressure could be provided) may give more accurate results.

Summing up, the results of my analysis indicate that the giants are evolved (aged) radio sources and that their host galaxy properties are very similar to smaller size radio sources. The properties of environment may play only a minor role in the formation of large-scale radio structures. The only property different for giants and other radio sources is the composition of their stellar population. GRSs have relatively large number of old stars with solar-like metallicity. This gives some hints that the host galaxy stellar formation history, and not properties of the central engine, may be a key factor to distinguish giants from other radio sources.

The results obtained in this work can be used as a base in new studies of radio sources in the future. Firstly, the sample of giant radio quasars can be used for other astrophysical investigations e.g. studies of the evolution of individual radio sources. Also the interesting fact is the recurrent radio activity. There is a relatively large number of double-double giant radio sources. This fact indicates that the recurrence phenomenon may be present in majority of GRSs, but high resolution and low frequency radio observations are needed to confirm this hypothesis. According to the results obtained in this work, it is necessary to provide a detailed analysis of a galaxy formation history. Also through multifrequency analysis of giant radio sources, the global view of a host galaxy and radio source physics can be provided. Such studies can be crucial to give the final answer why some of RSs have very large sizes.

Bibliography

Abramowicz M.A., Fragile P.C., 2013, LRR, 16, 1

Adelman-McCarthy J.K., et al., 2008, ApJS, 175, 297

Alexander P., Leahy J.P., 1987, MNRAS, 225, 1

An T., Baan W.A., 2012, ApJ, 760, 77

Antonucci R.R.J., 1993, ARA&A, 31, 473

Arshakian T.G., Longair M.S., 2004, MNRAS, 351, 727

Asari N.V., Cid Fernandes R., Stasińska G., Torres-Papaqui J.P., Mateus A., Sodre L. Jr., Schoenell W., Gomes J.M., MNRAS, 2007, 381, 263

Baum S.A., Heckman T., 1989a, ApJ, 336, 681

Baum S.A., Heckman T., 1989b, ApJ, 336, 702

Baum S.A., Zirbel E.L., O'Dea C.P., 1995, ApJ, 451, 88

Becker R.H., White R.L., Helfand D.J., 1995, ApJ, 450, 559

Becker et al., 2000, ApJ, 538, 72

Becker R.H., White R.L., Gregg M.D., Laurent-Muehleisen S.A., et al., 2001, ApJS, 135, 227

Best P.N., Bailer D.M., Longair M.S., Riley J.M., 1995, MNRAS, 275, 1171

Best P.N., Kauffmann G., Heckman T.M., Ivezic Z., 2005, MNRAS, 362, 9

Bhatnagar S., Krishna G., Wisotzki L., 1998, MNRAS, 299, 25

Bianchi S., Schneider R., 2007, MNRAS, 378, 973

Blandford R.D., Znajeck R., 1977, MNRAS, 179, 433

Blundell K.M., Rawlings S., Willott C.J., 1999, AJ, 117, 677

Bock D.C.-J., Large M.I., Sadler E.M., 1999, AJ, 117, 1578

Bondi H., 1952, MNRAS, 112, 195

Boroson T.A., Green R.F., 1992, ApJS, 80, 109

Bowen D.V., et al., 2006, ApJ, 645, 105

Bridle A.H., Perley R.A., 1984, ARAA, 22, 319

Brotherton M.S., De Breuck C., Schaefer J.J., 2006, MNRAS, 372, 58

Brown M.J.I., Webster R.L., Boyle B.J., 2001, AJ, 121, 2381

Bruzual G., Charlot S., 2003, MNRAS, 344, 1000

Buttiglione S., et al., 2010, A&A, 509, 6

Carilli C.L., Perley R.A., Dreher J.W., Leahy J.P., 1991, ApJ, 383, 554

Cattaneo A., Best P.N., 2009, MNRAS, 395, 518

Celotti A., Fabian A.C., 1993, MNRAS, 264, 228

Cid Fernandes R., Gu Q., Melnick J., Terlevich E., Terlevich R., Kunth D., Rodrigues L.R., Joguet B., 2004, MNRAS, 355, 273

Cid Fernandes R., Mateus A., Sodré L., Stasińska G., Gomes J.M., 2005, MNRAS, 358, 363

Ciliegi P., et al., 1999, MNRAS, 302, 222

Cirasuolo M., Magliocchetti M., Celotti A., Danese L., 2003, MNRAS, 341, 993

Cohen R.D., Osterbrock D.E., 1981, ApJ, 243, 81

Condon J.J., Cotton W.D., Greisen E.W., Yin Q.F., Perley R.A., Taylor G.B., Broderick J.J., 1998, AJ, 115, 1693

Corbin M.R., 1992, ApJ, 391, 577

Cotter G., Rawlings S., Saunders R., 1996, MNRAS, 281, 1081

Czerny B., Różańska A., Kuraszkiewicz J., 2004, A&A, 428, 39

Czerny B., Siemiginowska A., Nikiel-Wroczyński B., Stawarz Ł., 2009, ApJ, 698, 840

Czerny B., Hryniewicz K., 2011, A&A, 525, 8

Davidson K., Netzer H., 1979, RevMP, 51, 715

Decarli, R., Labita, M., Treves, A., Falomo, R., 2008, MNRAS, 387, 1237

Dietrich M., Mathur S., Grupe D., Komossa S., 2009, ApJ, 696, 1998

Djorgovski S.G., 1991, ASPCS, 21, 349

Djorgovski S.G., 1999, ASPCS, 193, 397

Djorgovski S., Thompson D.J., Vigotti M., Grueff G., 1990, PASP, 102, 113

Djorgovski S G., Odewahn S.C., Gal R.R., Brunner R.J., de Carvalho R.R., 1999, ASPCS, 191, 179

Dunlop J.S., McLure R.J., Kukula M.J., Baum S.A. O'Dea C.P. Huges D.H., 2003, MNRAS, 340, 1095

Elitzur M., 2008, NewAR, 52, 274

Elvis M., Marengo M., Karovska M., 2002, ApJ, 567, 107

Erlund M.C., Fabian A.C., Blundell K M., 2008, MNRAS, 386, 1774

Fanaroff B.L., Riley J.M., 1974, MNRAS, 167, 31

Ferrarese L., Merritt D., 2000, ApJ, 539, 9

Gebhardt K., et al., 2000, ApJ, 539, 13

Ghisellini G., Tavecchio F., 2008, MNRAS, 387, 1669

Gopal-Krishna, Wiita P.J., Saripalli L., 1989, MNRAS, 239, 173

Gopal-Krishna, Wiita P.J., 2000, A&A, 363, 507

Graham A.W., et al., 2011, MNRAS, 412, 2211

Grandi S.A., Osterbrock D.E., 1978, ApJ, 220, 783

Gregg M.D., Becker R.H., White R.L., Helfand D.J., McMahon R.G., Hook I.M., 1996, AJ, 112, 407

Gregg M.D.,Becker R.H., Vries W., 2006, ApJ, 641, 210

Guimaraes R., et al., 2007, MNRAS, 377, 657

Gültekin K., et al., 2009, ApJ, 698, 198

Hennawi J F., et al., 2010, ApJ, 719, 1672

Hennawi J.F., et al., 2006, AJ, 131, 1

Hewett P.C., Foltz C.B., Chaffee F.H., 2001, AJ, 122, 518

Hewett P.C., Foltz C.B., 2003, AJ, 125, 1784

Hine R.G., 1979, MNRAS, 189, 527

Hintzen P., Ulvestad J., Owen F., 1983, AJ, 88, 709

Ho L.C., 2002, ApJ, 564, 120

Hocuk S., Barthel P.D., 2010, A&A, 523, 9

Hopkins P.F., Hernquist L., Cox T J., Kere, D., 2008, ApJS, 175, 356

Ishwara-Chandra C.H., Saikia D.J.,1999, MNRAS, 309, 100

Ivezic, M.J., et al., 2002, AJ, 124, 2364

Jaffe W.J., Perola G.C., 1973, A&A, 26, 423

Jamrozy M., Konar C., Machalski J., Saikia D.J., 2008, MNRAS, 385, 1286

Jamrozy M., Konar C., Saikia D.J., Machalski J., 2009, ASPCS, 407, 137

Jamrozy M., Saikia D.J., Konar C., 2009, MNRAS, 399, 141

Jägers W.J., Miley G.K., van Breugel W.J.M., Schilizzi R.T., Conway R.G., 1982, A&A, 105, 278

Jägers W.J., 1987, A&AS, 71, 75

Jiang L., et al., 2007, ApJ, 656, 680

Jiang L., et al., 2010, Nat., 464, 380

Joshi S.A., Nandi S., Saikia D.J., Ishwara-Chandra C.H., Konar C., 2011, MNRAS. 414. 1397

Kaiser C.R., Alexander P., 1997, MNRAS, 286, 215

Kaiser C.R., Best P.N., 2007, MNRAS, 381, 1548

Kaiser C.R., Dennett-Thorpe J., Alexander P., 1997, MNRAS, 292, 723

Kapahi, V.K., 1989, AJ, 97, 1

Kaspi S., Smith P.S., Netzer H., Maoz D., Jannuzi B.T., Giveon U., 2000, ApJ, 533, 631

Kaspi S., Maoz D., Netzer H., Peterson B.M., Vestergaard M., Jannuzi B.T., 2005, ApJ, 629, 61

Kaspi S., Brandt W.N., Maoz D., Netzer H., Schneider D.P., Shemmer O., 2007, ApJ, 659, 997

King A.R., Pringle J.E., 2006, MNRAS, 373, 90

Kirkman D., Tytler D., 2008, MNRAS, 391, 1457

Komberg B.V., Pashchenko I.N., 2009, ARep, 53, 1086

Konar C., Saikia D.J., Jamrozy M., Machalski J., 2006, MNRAS, 372, 693

Kormendy J., Richstone D., 1995, ARA&A, 33, 581

Kozieł-Wierzbowska D., Stasińska G., 2011, MNRAS, 415, 1013

Krolik J.H., Begelman M.C., 1988, ApJ, 329, 702

Kuligowska E., 2007, Master Thesies "Search for giant size radio galaxies at large redshift", Jagiellonian University

Kuligowska E., Jamrozy M., Kozieł-Wierzbowska D., Machalski J., 2009, AcA, 59, 431

Kuźmicz, A., Kuligowska, E., Jamrozy, M., 2011, AcA, 61, 71

Labiano A., 2008, A&A, 488, 59

Lacy M., Laurent-Muehleisen S.A., Ridgway S.E., Becker R.H., White R.L., 2001, ApJ, 551, 17

Laing R.A., 1988, Nat., 331, 149

Laing R.A., Riley J.M., Longair M.S., 1983, MNRAS, 204, 151

Laor A., 2000, ApJ, 543, 111

Laor A., 2003, ApJ, 590, 86

Lara L., Marquez I., Cotton W.D., Feretti L., Giovannini G., Marcaide J.M., Venturi T., 2001, A&A, 378, 826

Laskar T., Fabian A.C., Blundell K.M., Erlund M.C., 2010, MNRAS, 401, 1500

Law-Green J.D.B., Eales S.A., Leahy J.P., Rawlings S., Lacy M., 1995, MNRAS, 277, 995

Ledlow M.J., Owen F.N., & Keel W.C., 1998, ApJ, 495, 227

Lin Y., Shen Y., Strauss M.A., Richards G.T., Lunnan R., 2010, ApJ, 723, 1119

Liu R., Pooley G., Riley J.M., 1992, MNRAS, 257, 545

Liu F.K., Zhang Y.H., 2002, A&A, 381, 757

Machalski J., Jamrozy M., Zoła S., 2001, A&A, 371, 445

Machalski J., Jamrozy M., 2006, A&A, 454, 95

Machalski J., Jamrozy M., Zoła S., Kozieł D., 2006, A&A, 454, 85

Machalski J., Kozieł-Wierzbowska D., Jamrozy M., 2007, AcA, 57, 227

Machalski J., Chyży K.T., Stawarz Ł., Kozieł D., 2007, A&A, 462, 43

Machalski J., Koziel-Wierzbowska D., Jamrozy M., Saikia D.J., 2008, ApJ, 679, 149

Machalski J., Jamrozy M., Saikia D.J., 2009, MNRAS, 395, 812

Machalski J., Jamrozy, M., Stawarz Ł., Kozieł-Wierzbowska, D., 2011, ApJ, 740, 58

Mack K.H., Klein U., O'Dea C.P., Willis A.G., 1997, A&AS, 123, 423

Magorrian J., et al., 1998, AJ, 115, 2285

Marconi A., Risaliti G., Gilli R., Hunt L.K., Maiolino R., Salvati M., 2004, MNRAS, 351, 169

Marziani P., Zamanov R.K., Sulentic J.W., Calvani C., 2003, MNRAS, 345, 1133

Mathur S., 2000, MNRAS, 314, 17

McGilchrist M.M., Baldwin J.E., Riley J.M., Titterington D.J., Waldram E.M., Warner P.J., 1990, MNRAS, 246, 110

Morganti R., Tadhunter C.N., Dickson R., Shaw M., 1997, A&A, 326, 130

McLure R.J., Dunlop J.S., 2002, MNRAS, 331, 795

McLure R.J., Jarvis M.J., 2004, MNRAS, 353, 45

Meier D.L., 1999, ApJ, 522, 753

Merloni A., Heinz S., 2008, MNRAS, 388, 1011

Metcalf R. B., Magliocchetti M., 2006, MNRAS, 365, 101

Miyoshi M., et al., 1995, Nat., 373, 127

Murgia M., 2003, PASA, 20, 19

Myers S.T., Spangler S.R., 1985, ApJ, 291, 52

Nandi S., Saikia D.J., 2012, BASI, 40, 121

Nenkova M., Sirocky M.M., Nikutta R., Ivezic, Z., Elitzur, M., 2008, ApJ, 685, 160

Netzer H., 2006, LNP, 693, 1

Netzer H., Lira P., Trakhtenbrot B., Shemmer O., Cury I., 2007, ApJ, 671, 1256

Nilsson K., 1998, A&AS, 132, 31

Onken C. A., et al., 2007, ApJ, 670, 105

Oshlack A., Webster R., Whiting M., 2002, ApJ, 576, 81

Parma P., de Ruiter H.R., Mack K.H., van Breugel W., Dey A., Fanti R., Klein U., 1996, A&A, 311, 49

Parma P., Murgia M., Morganti R., Capetti A., de Ruiter H. R., Fanti R., 1999, A&A, 344, 7

Peterson B.M., 1993, PASP, 105, 207

Peterson B.M., et al., 2004, AJ, 613, 682

Peterson B.M., Wandel A., 2000, ApJ, 540, 13

Punsly B., 2006, ApJ, 647, 886

Rawlings S., Saunders R., Eales S.A., Mackay C.D., 1989, MNRAS, 240, 701

Rawlings S., Saunders R. 1991, Nature, 349, 138

Reichard T.A., et al., 2003, AJ, 125, 1711

Rengelink R.B., Tang Y., de Bruyn A.G., Miley G.K., Bremer M.N., Röttgering H.J.A., Bremer M.A.R., 1997, A&AS, 124, 259

Riley J.M., Warner P.J.,1990, MNRAS, 246, 1

Sadler E.M., et al., 2007, MNRAS, 381, 211

Saikia D.J., Konar C., Kulkarni V.K., 2006, MNRAS, 366, 1391

Saikia D.J., Kulkarni V.K., 1994, MNRAS, 270, 897

Saikia D.J., Jamrozy M., 2009, BASI, 37, 63

Saripalli L., Hunstead R.W., Subrahmanyan R., Boyce E., 2005, AJ, 130, 896

Scheuer, P.A.G., 1995, MNRAS, 277, 331

Schoenmakers A.P., et al., 1998, A&A, 336, 455

Schoenmakers A.P., 1999, PhD-thesis “A population of Giant Radio Galaxies”, Utreht University

Schoenmakers A. P., de Bruyn A. G., Röttgering H. J. A., van der Laan H., Mack K.-H., Kaiser C. R., 2000, Proc. Perspectives on Radio Astronomy: Science with Large Antenna Arrays, 165

Schoenmakers A.P., Mack K.-H., de Bruyn A.G., R ottgering H.J.A., Klein U., van der Laan H., 2000, A&AS, 146, 293

Schoenmakers A.P., de Bruyn A.G., Röttgering H.J.A., van der Laan H., 2001, A&A, 374, 861

Sedlmayr E., 1997, Ap&SS, 251, 103

Shakura N.I., Syunyaev R.A., 1973, A&A, 24, 337

Shankar F., Salucci P., Granato G.L., De Zotti G., Danese L., 2004, MNRAS, 354, 1020

Shankar F., Cavaliere A., Cirasuolo M., Maraschi L., 2008, ApJ, 676, 131

Shankar F., Sivakoff G.R., Vestergaard M., Dai X., 2010, MNRAS, 401, 1869

Shen Y., Greene J.E., Strauss M.A., Richards G.T., Schneider D.P., 2008, ApJ, 680, 169

Silk J., Rees M., 1998, A&A, 331, 1

Sikora M., Stawarz Ł., Lasota J.-P., 2007, ApJ, 658, 815

Snellen I.A.G., Lehnert M.D., Bremer M.N., Schilizzi R.T., 2003, MNRAS, 342, 889

Spergel D.N., et al., 2003, ApJS, 148, 175

Steidel C.S., Sargent W.L.W., 1991, ApJ, 382, 433

Subrahmanyan R., Saripalli L., Safouris V., Hunstead R. W., 2008, ApJ, 677, 63

Tolea A., Krolik J.H., Tsvetanov Z., 2002, ApJ, 578, 31

Tortora C., Antonuccio-Delogu V., Kaviraj S., Silk J., Romeo A.D., Becciani U., 2009, MNRAS, 396, 61

Trakhtenbrot B., Netzer H., 2012, MNRAS, 427, 3081

Tran H. D., 2003, ApJ, 583, 632

Tremaine S. et al., 2002, ApJ, 574, 740

Tristram K.R.W., et al. 2007, A&A, 474, 837

Trump J.R., et al., 2006, ApJS, 165, 1

Veron-Cetty M.-P., Joly M., Veron P., 2004, A&A, 417, 515

Vestergaard M., 2004, ApJ, 601, 676

Vestergaard M., Osmer P., 2009, ApJ, 699, 800

Vestergaard M., Pterson B.M., 2006, ApJ, 641, 689

Vestergaard M., Wilkes B.J., 2001, ApJS, 134, 1

Volonteri M., Begelman M.C., 2010, MNRAS, 409, 1022

de Vries W.H., Becker R.H., White R.L., 2006, AJ, 131, 666

Urry C.M., Padovani P., 1995, PASP, 107, 803

Wang J.M., Ho L.C., Staubert R., 2003, A&A, 409, 887

Wardle J.F.C., Aaron S.E., 1997, MNRAS, 286, 425

Weymann R.J., Morris S L., Foltz C.B., Hewitt P.C., 1991, ApJ, 373, 23

Weymann R.J., 2002, ASPC, 255, 329

White R.L., Becker R.H., 1992, ApJS, 79, 331

White R.L., et al., 2000, ApJS, 126, 133

Wilhite B.C., Brunner R.J., Schneider D.P., Vanden Berk D.E., 2007, ApJ, 669, 791

Willis A.G., Strom R.G., Wilson A.S., 1974, Nat., 250, 625

Willott C.J., Rawlings S., Blundell K.M., Lacy M., 1999, MNRAS, 309,1017

Woo J-H., Urry M., 2002, ApJ, 581, 5

Zier C., Biermann P.L., 2002, A&A, 396, 91

Zirbel E.L., Baum S.A., 1995, ApJ, 448, 521

Zirbel E.L., 1997, ApJ, 476, 489

Zhang J.S., Fan J.H., 2003, ChJAA, 3, 415

Abbreviations

AI	**A**bsorption **I**ndex
AGN	**A**ctive **G**alactic **N**uclei
AIPS	**A**stronomical **I**mage **P**rocessing **S**ystem
BAL	**B**road **A**bsorption **L**ine
BH	**B**lack **H**ole
BI	**B**alnicity **I**ndex
BLR	**B**road **L**ine **R**egion
BLRG	**B**road **L**ine **R**adio **G**alaxy
CMB	**C**osmic **M**icrowave **B**ackground
CSS	**C**ompact **S**teep **S**pectrum Object
DDGRG	**D**ouble-**D**ouble **G**iant **R**adio **G**alaxy
DDRG	**D**ouble-**D**ouble **R**adio **G**alaxy
DDRS	**D**ouble-**D**ouble **R**adio **S**ource
DSS	**D**igital **S**ky **S**urvey
FIRST	**F**aint **I**mages of the **R**adio **S**ky at **T**wenty centimetres
FRI	**F**anarof **R**iley type **I**
FRII	**F**anarof **R**iley type **II**
FWHM	**F**ull **W**idth at **H**alf **M**aximum
GRG	**G**iant **R**adio **G**alaxy
GRQ	**G**iant **R**adio **Q**asar
GRS	**G**iant **R**adio **S**ource
IGM	**I**nter **G**alactic **M**edium
ISM	**I**nter **S**ellar **M**edium
INT	**I**saak **N**ewton **T**elescope
IRAF	**I**mage **R**eduction **A**nalysis **F**acility

NLR	**N**arrow **L**ine **R**egion
NLRG	**N**arrow **L**ine **R**adio **G**alaxy
NVSS	**N**RAO **V**LA **S**ky **S**urvey
QSO	**Q**uasi**S**tellar **O**bject
RG	**R**adio **G**alaxy
RQ	**R**adio **Q**asar
RS	**R**adio **S**ource
SDSS	**S**loan **D**idital **S**ky **S**urvey
SMBH	**S**uper **M**asive **B**lack **H**ole

Appendix A

Parameters of GRQs

This appendix presents the samples of GRQs and smaller-size RQs (Tables A.1, A.2 respectively). The description of the columns is as follows:

Column 1: J2000.0 IAU name.

Column 2 and *Column 3:* J2000.0 right ascension and declination of the central position of the optical quasar.

Column 4: Redshift of the host object.

Column 5: Angular size in arcmin.

Column 6: Projected linear size in Mpc.

Column 7: Availability of the spectrum from the SDSS survey (S), or provided by White (W); availability of radio maps from NVSS or FIRST (N or F, respectively).

Column 8: References to the identified object.

In next tables I listed the measured and calculated parameters of sources from both samples (Tables A.9, A.3, A.5, A.7 for GRQs and Tables A.10, A.4, A.6, A.8 for comparison sample of RQs). The objects for which there was any of the calculated parameters were removed from Tables.

In Tables A.3 and A.4 - parameters of the optical spectra (Section 2.3.3):

Column 1: J2000.0 IAU name.

Column 2: FWHM of broad emission line.

Column 3, 4, 5: Flux in the rest frame at wavelength λ equal to 1350Å, 3000Å and 5100Å respectively.

Column 6, 7, 8: Monochromatic continuum luminosity wavelength 1350Å, 3000Å and 5100Å respectively.

In Tables A.5 and A.6 - optical luminosities and accretion rates (Section 2.7):

Column 1: J2000.0 IAU name.

Column 2, 3, 4: Logarithm of bolometric luminosity at wavelength 1350Å, 3000Å and 5100Å respectively.

Column 5, 6, 7: Logarithm of Eddington luminosity estimated using CIV, MgII, H_β emission lines.

Column 8, 9, 10: Accretion rate.

In Tables A.7 and A.8 - computed BH masses (Section 2.3.3)

Column 1: J2000.0 IAU name.

Column 2, 3, 4: BH masses estimated using CIV, MgII, H_β emission lines.

In Tables A.9 and A.10 I placed radio data described in Section 2.2:

Column 1: J2000.0 IAU name.

Column 2: Logarithm of total radio power.

Column 3: Logarithm of core radio power.

Column 4: Bending angle.

Column 5: Arm-length ratio.

Column 6: Flux-density ratio.

Column 7: Inclination.

Table A.1: List of giant-size (> 0.72 Mpc) radio quasars.

IAU name (1)	α(J2000.0) (h m s) (2)	δ(J2000.0) (^{o} ’ ”) (3)	z (4)	d arcmin (5)	D Mpc (6)	Avail. Data (7)	Ref. (8)
J0204−0944	02 04 48.29	−09 44 09.5	1.004	6.035	2.914	S,N,F	1
J0210+0118	02 10 08.26	+01 18 42.3	0.870	2.618	1.214	W,N,F	1
J0313−0631	03 13 32.88	−06 31 58.0	0.389	3.090	0.973	S,N	2
J0439−2422	04 39 09.20	−24 22 08.0	0.840	1.960	0.899	N	3
J0631−5405	06 32 01.00	−54 04 58.7	0.204	5.200	1.040	-	4
J0750+6541	07 50 34.43	+65 41 25.4	0.749	3.271	1.439	S,N	5
J0754+3033	07 54 48.86	+30 33 55.0	0.796	3.842	1.730	S,N,F	6
J0754+4316	07 54 07.96	+43 16 10.6	0.347	8.061	2.360	S,N,F	7
J0801+4736	08 01 31.97	+47 36 16.0	0.157	5.438	0.876	S,N,F	7
J0809+2912	08 09 06.22	+29 12 35.6	1.481	2.184	1.118	S,N,F	6, 8
J0810−6800	08 10 55.10	−68 00 07.7	0.231	6.500	1.420	-	9
J0812+3031	08 12 40.08	+30 31 09.4	1.312	2.427	1.203	S,N,F	8
J0816+3347	08 16 35.49	+33 47 48.79	0.510	3.543	1.306	S,N,F	10
J0819+0549	08 19 41.12	+05 49 42.7	1.701	1.923	0.987	S,N,F	8
J0842+2147	08 42 39.96	+21 47 10.4	1.182	2.314	1.156	S,N,F	8
J0902+5707	09 02 07.20	+57 07 37.9	1.595	1.678	0.862	S,N,F	9, 8
J0918+2325	09 18 58.15	+23 25 55.4	0.688	2.079	0.885	S,N,F	11
J0925+4004	09 25 54.72	+40 04 14.2	0.471	4.379	1.546	S,N,F	11
J0937+2937	09 37 04.04	+29 37 04.8	0.451	2.640	0.909	S,N,F	6, 11
J0944+2331	09 44 18.80	+23 31 18.5	0.987	1.870	0.899	S,N,F	11
J0959+1216	09 59 34.49	+12 16 31.6	1.089	1.964	0.966	S,N,F	12
J1012+4229	10 12 44.29	+42 29 57.0	0.364	3.088	0.933	S,N,F	9
J1020+0447	10 20 26.87	+04 47 52.0	1.131	1.478	0.733	S,N,F	12
J1020+3958	10 20 41.15	+39 58 11.2	0.830	2.663	1.217	W,N,F	9
J1027−2312	10 27 54.91	−23 12 02.0	0.309	2.860	0.774	N	3
J1030+5310	10 30 50.91	+53 10 28.6	1.197	1.698	0.749	S,N,F	8
J1054+4152	10 54 03.27	+41 52 57.6	1.090	4.702	2.314	S,N,F	11

Table A.1 continued

IAU name (1)	α(J2000.0) (h m s) (2)	δ(J2000.0) (^{o} ’ ”) (3)	z (4)	d arcmin (5)	D Mpc (6)	Avail. Data (7)	Ref. (8)
J1056+4100	10 56 36.26	+41 00 41.3	1.785	1.543	0.791	S,N,F	12
J1130−1320	11 30 19.90	−13 20 50.0	0.634	4.812	1.977	N	13
J1145−0033	11 45 53.67	−00 33 04.6	2.052	2.642	1.340	S,N,F	14
J1148−0403	11 48 55.89	−04 04 09.6	0.341	3.265	0.945	N,F	15
J1151+3355	11 51 39.68	+33 55 41.8	0.851	2.083	0.959	S,N,F	11
J1229+3555	12 29 25.56	+35 55 32.5	0.828	1.672	0.761	S,N,F	16
J1304+2454	13 04 51.42	+24 54 45.9	0.605	2.431	0.977	W,N,F	11
J1321+3741	13 21 06.42	+37 41 54.0	1.135	1.531	0.759	S,N,F	11
J1340+4232	13 40 34.70	+42 32 32.2	1.343	2.309	1.173	S,N,F	11
J1353+2631	13 53 35.92	+26 31 47.5	0.310	2.803	0.761	W,N,F	11, 17
J1408+3054	14 08 06.21	+30 54 48.5	0.837	3.618	1.658	S,N,F	11
J1410+2955	14 10 36.80	+29 55 50.9	0.570	2.483	0.970	W,N,F	6
J1427+2632	14 27 35.61	+26 32 14.5	0.363	3.822	1.158	S,N,F	17
J1432+1548	14 32 15.54	+15 48 22.4	1.005	2.824	1.364	S,N,F	15
J1445+3051	14 45 27.06	+30 51 29.0	0.417	5.090	1.674	S,N,F	10
J1504+6856	15 04 12.77	+68 56 12.8	0.318	3.140	0.867	N	5
J1723+3417	17 23 20.80	+34 17 58.0	0.206	3.787	0.760	W,N,F	18
J2042+7508	20 42 37.30	+75 08 02.5	0.104	10.052	1.138	N	19
J2234−0224	22 34 58.76	−02 24 18.9	0.550	3.236	1.241	N,F	1
J2344−0032	23 44 40.04	−00 32 31.7	0.503	2.658	0.973	W,N,F	1

References: (1) Becker et al. (2001); (2) Machalski, Kozieł-Wierzbowska & Jamrozy (2007); (3) Ishwara–Chandra & Saikia (1999); (4) Saripalli et al. (2005); (5) Lara et al. (2001); (6) Gregg et al. (1996); (7) Schoenmakers (1999); (8) Kuligowska et al. (2009); (9) de Vries et al. (2006); (10) Machalski, Jamrozy & Zoła (2001); (11) White et al. (2000); (12) Kuligowska (2007); (13) Bhatnagar, Krishna & Wisotzki (1998); (14) Kuźmicz, Kuligowska & Jamrozy (2011); (15) Hintzen, Ulvestad & Owen (1983); (16)

Shen et al. (2008); (17) Nilsson (1998); (18) Jägers et al. (1982); (19) Riley & Warner (1990).

Table A.2: List of smaller-size (< 0.72 Mpc) radio quasars.

IAU name (1)	α(J2000.0) (h m s) (2)	δ(J2000.0) (° ' ") (3)	z (4)	d arcmin (5)	D Mpc (6)	Avail. Data (7)	Ref. (8)
J0022−0145	00 22 44.29	−01 45 51.1	0.691	1.432	0.610	N,F	1
J0034+0118	00 34 19.18	+01 18 35.8	0.841	1.364	0.664	W,N,F	1
J0051−0902	00 51 15.12	−09 02 08.5	1.265	1.379	0.696	S,N,F	1
J0130−0135	01 30 43.00	−01 35 08.2	1.160	1.306	0.650	W,N,F	1
J0245+0108	02 45 34.07	+01 08 14.2	1.537	0.883	0.453	S,N,F	3
J0745+3142	07 45 41.66	+31 42 56.5	0.461	1.795	0.626	S,N,F	3
J0811+2845	08 11 36.90	+28 45 03.6	1.890	0.507	0.259	S,N,F	3
J0814+3237	08 14 09.23	+32 37 31.7	0.844	0.239	0.187	S,N,F	3
J0817+2237	08 17 35.07	+22 37 18.0	0.982	0.395	0.190	S,N,F	3
J0828+3935	08 28 06.85	+39 35 40.3	0.761	1.077	0.477	S,N,F	3
J0839+1921	08 39 06.95	+19 21 48.9	1.691	0.523	0.269	S,N,F	3
J0904+2819	09 04 29.63	+28 19 32.8	1.121	0.379	0.188	S,N,F	3
J0906+0832	09 06 49.81	+08 32 58.8	1.617	1.307	0.671	S,N,F	4
J0924+3547	09 24 25.03	+35 47 12.8	1.342	1.345	0.683	S,N,F	5
J0925+1444	09 25 07.26	+14 44 25.9	0.896	0.665	0.311	S,N,F	3
J0935+0204	09 35 18.51	+02 04 19.0	0.649	1.200	0.498	S,N,F	3
J0941+3853	09 41 04.17	+38 53 49.1	0.616	0.853	0.346	S,N,F	3
J0952+2352	09 52 06.36	+23 52 43.2	0.970	1.466	0.702	S,N,F	2
J1000+0005	10 00 17.65	+00 05 23.9	0.905	0.521	0.245	S,N,F	3
J1004+2225	10 04 45.75	+22 25 19.4	0.982	1.097	0.526	S,N,F	3
J1005+5019	10 05 07.10	+50 19 31.5	2.023	1.300	0.660	S,N,F	2
J1006+3236	10 06 07.58	+32 36 27.9	1.026	0.246	0.119	S,N,F	3
J1009+0529	10 09 43.56	+05 29 53.9	0.942	1.377	0.654	S,N,F	2
J1010+4132	10 10 27.50	+41 32 39.0	0.612	0.525	0.212	S,N,F	3
J1023+6357	10 23 14.61	+63 57 09.3	1.194	1.294	0.648	S,N,F	6
J1100+1046	11 00 47.81	+10 46 13.6	0.422	0.549	0.182	S,N,F	3
J1100+2314	11 00 01.14	+23 14 13.1	0.559	1.577	0.610	S,N,F	5

Table A.2 continued

IAU name (1)	α(J2000.0) (h m s) (2)	δ(J2000.0) (^{o} ’ ”) (3)	z (4)	d arcmin (5)	D Mpc (6)	Avail. Data (7)	Ref. (8)
J1107+0547	11 07 09.51	+05 47 44.7	1.799	1.324	0.678	S,N,F	2
J1107+1628	11 07 15.04	+16 28 02.2	0.632	0.652	0.267	S,N,F	3
J1110+0321	11 10 23.84	+03 21 36.4	0.966	1.055	0.504	S,N,F	3
J1118+3828	11 18 58.53	+38 28 53.5	0.747	1.407	0.619	S,N,F	5
J1119+3858	11 19 03.20	+38 58 53.6	0.734	1.419	0.620	S,N,F	5
J1158+6254	11 58 39.76	+62 54 27.1	0.592	0.968	0.385	S,N,F	3
J1217+1019	12 17 01.28	+10 19 52.0	1.883	0.466	0.238	S,N,F	3
J1223+3707	12 23 11.23	+37 07 01.8	0.491	0.597	0.216	S,N,F	3
J1236+1034	12 36 04.52	+10 34 49.2	0.667	1.694	0.711	S,N,F	3
J1256+1008	12 56 07.66	+10 08 53.5	0.824	0.382	0.174	S,N,F	3
J1319+5148	13 19 46.25	+51 48 05.5	1.061	0.466	0.228	S,N,F	3
J1334+5501	13 34 11.71	+55 01 24.8	1.245	1.274	0.641	S,N,F	3
J1358+5752	13 58 17.60	+57 52 04.5	1.373	0.733	0.373	S,N,F	3
J1425+2404	14 25 50.65	+24 04 02.8	0.653	0.339	0.141	S,N,F	3
J1433+3209	14 33 34.26	+32 09 09.5	0.935	0.630	0.299	S,N,F	3
J1513+1011	15 13 29.30	+10 11 05.4	1.546	0.586	0.301	S,N,F	3
J1550+3652	15 50 02.01	+36 52 16.8	2.061	1.334	0.676	S,N,F	4
J1557+0253	15 57 52.83	+02 53 28.9	1.988	1.121	0.571	S,N,F	2
J1557+3304	15 57 29.94	+33 04 47.0	0.953	0.562	0.268	S,N,F	3
J1622+3531	16 22 29.90	+35 31 25.1	1.475	0.365	0.187	S,N,F	3
J1623+3419	16 23 36.45	+34 19 46.3	1.981	0.984	0.501	S,N,F	2
J2335−0927	23 35 34.68	−09 27 39.2	1.814	1.305	0.668	S,N,F	1

References: (1) Becker et al. (2001); (2) de Vries et al. (2006); (3) Nilsson (1998); (4) Kuligowska et al. (2009); (5) White et al. (2000); (6) Kuligowska (2007).

Table A.3: Parameters of optical spectra for GQRs.

IAU name		FWHM	f_λ 1350Å	f_λ 3000Å	f_λ 5100Å	$log\lambda L_\lambda$ 1350Å	$log\lambda L_\lambda$ 3000Å	$log\lambda L_\lambda$ 5100Å
		Å	10^{-17} erg cm^{-2} s^{-1} $Å^{-1}$			erg s^{-1}		
J0204−0944	MgII	34.19	–	10.13	–	–	44.61	–
J0210+0118	MgII	49.61	–	46.57	–	–	45.17	–
J0750+6541	MgII	38.55	–	27.98	14.36	–	44.76	44.50
	H_β	199.30						
J0754+3033	MgII	48.59	–	53.77	10.65	–	45.17	44.70
	H_β	139.90						
J0754+4316	H_β	226.37	–	–	30.2	–	–	44.53
J0801+4736	H_β	125.23	–	–	3.69	–	–	42.97
J0809+2912	MgII	46.91	–	44.45	–	–	45.48	–
J0812+3031	MgII	30.91	–	11.14	–	–	44.72	–
J0816+3347	MgII	60.67?	–	3.80	2.99	–	43.67	43.62
	H_β	13.58						
J0819+0549	CIV	75.57	–	1.50	–	–	44.09	–
	MgII	58.94						
J0842+2147	MgII	33.16	–	10.96	–	–	44.74	–
J0902+5707	CIV	31.09	–	10.40	–	–	44.89	–
	MgII	47.90						
J0918+2325	MgII	55.91	–	54.28	8.92	–	45.08	44.52
	H_β	173.43						
J0925+4004	MgII	62.30	–	109.20	20.40	–	45.10	44.60
	H_β	196.95						
J0937+2937	MgII	41.23	–	78.80	14.70	–	44.92	44.42
	H_β	98.86						
J0944+2331	MgII	43.36	–	34.92	–	–	45.13	–
J0959+1216	MgII	46.95	–	14.32	–	–	44.81	–
J1020+0447	MgII	57.04	–	6.56	–	–	44.49	–

Table A.3 continued

IAU name		FWHM	f_λ 1350Å	f_λ 3000Å	f_λ 5100Å	$log\lambda L_\lambda$ 1350Å	$log\lambda L_\lambda$ 3000Å	$log\lambda L_\lambda$ 5100Å
		Å	10^{-17} erg cm^{-2} s^{-1} $Å^{-1}$			erg s^{-1}		
J1020+3958	MgII	66.70	–	33.48	–	–	45.00	–
J1030+5310	MgII	36.46	–	26.04	–	–	45.13	–
J1054+4152	MgII	49.00	–	23.03	–	–	45.01	–
J1056+4100	CIV	34.41	–	2.841	–	–	44.39	–
	MgII	51.61						
J1145−0033	CIV	61.12	16.07	5.38	–	44.87	44.74	–
J1151+3355	MgII	51.11	–	29.15	–	–	44.95	–
J1229+3555	MgII	31.93	–	13.52	–	–	44.60	–
J1304+2454	MgII	47.98	–	79.83	–	–	45.15	–
	H_β	189.27						
J1321+3741	MgII	73.96	–	15.56	–	–	44.87	–
J1340+4232	MgII	52.94	–	8.22	–	–	44.69	–
J1353+2631	MgII	41.75	–	136.10	35.48	–	44.86	44.51
	H_β	206.40						
J1410+2955	MgII	69.94	–	47.28	–	–	44.88	–
J1427+2632	H_β	195.90	–	–	42.12	–	–	44.72
J1432+1548	MgII	52.83	–	18.82	–	–	44.88	–
J1445+3051	MgII	68.39	–	1.39	4.58	–	43.10	43.64
	H_β	12.52						
J1723+3417	H_β	64.88	–	168.40	139.60	–	44.62	44.77
J2344−0032	MgII	41.18	–	70.72	–	–	44.96	–

Table A.4: Parameters of optical spectra for smaller-size RQ.

			f_λ			$log\lambda L_\lambda$		
IAU name	FWHM		1350Å	3000Å	5100Å	1350Å	3000Å	5100Å
		Å	10^{-17} erg cm^{-2} s^{-1} $Å^{-1}$			erg s^{-1}		
J0034+0118	MgII	56.34	–	11.80	–	–	44.58	–
J0051−0902	MgII	64.84	–	11.51	–	–	44.81	–
J0130−0135	MgII	61.47	–	23.58	–	–	45.06	–
J0245+0108	CIV	35.54	–	12.67	–	–	44.96	–
	MgII	61.03						
J0745+3142	CIV	186.40	–	499.50	107.50	–	45.74	45.30
	MgII	53.84						
	H_β	173.80						
J0811+2845	CIV	27.10	59.34	12.92	–	45.40	45.08	–
	MgII	54.05						
J0814+3237	MgII	32.17	–	17.93	–	–	44.74	–
J0817+2237	MgII	45.24	–	41.95	–	–	45.21	–
J0828+3935	MgII	41.57	–	15.63	–	–	44.61	–
J0839+1921	CIV	21.60	–	23.96	–	–	45.29	–
	MgII	36.12						
J0904+2819	MgII	36.98	–	58.68	–	–	45.44	–
J0906+0832	CIV	38.41	–	8.01	–	–	44.79	–
	MgII	48.46						
J0924+3547	MgII	46.75	–	19.14	–	–	45.06	–
J0925+1444	MgII	39.36	–	32.33	–	–	45.03	–
J0935+0204	MgII	61.33	–	92.04	17.1	–	45.26	44.76
	H_β	142.40						
J0941+3853	MgII	59.18	–	42.59	9.19	–	44.89	44.45
	H_β	234.00						
J0952+2352	MgII	36.19	–	53.89	–	–	45.31	–
J1000+0005	MgII	30.90	–	12.99	–	–	44.65	–
J1004+2225	MgII	44.52	–	18.23	–	–	44.84	–

Table A.4 continued

IAU name		FWHM	f_λ			$log\lambda L_\lambda$		
			1350Å	3000Å	5100Å	1350Å	3000Å	5100Å
		Å	10^{-17} erg cm^{-2} s^{-1} $\AA^{-1}$			erg s^{-1}		
J1005+5019	CIV	18.18	78.57	9.60	–	–	44.98	–
	MgII	46.60						
J1006+3236	MgII	34.69	–	8.954	–	–	44.57	–
J1009+0529	MgII	68.01	–	71.05	–	–	45.41	–
J1010+4132	MgII	28.88	–	233.60	35.86	–	45.62	45.04
	H_β	65.89						
J1023+6357	MgII	48.48	–	53.00	–	–	45.43	–
J1100+1046	MgII	49.35	–	60.94	11.07	–	44.76	44.25
	H_β	21.30						
J1100+2314	MgII	66.57	–	100.50	31.02	–	45.19	44.91
	H_β	296.03						
J1107+0547	CIV	33.64	–	6.66	–	–	44.76	–
	MgII	40.26						
J1107+1628	MgII	36.98	–	180.00	33.76	–	45.53	45.04
	H_β	88.07						
J1110+0321	MgII	29.41	–	16.59	–	–	44.79	–
J1118+3828	MgII	39.03	–	29.22	3.46	–	44.87	44.17
	H_β	431.77						
J1119+3858	MgII	64.70	–	31.08	6.27	–	44.88	44.41
	H_β	345.40						
J1158+6254	MgII	66.27	–	185.80	44.74	–	45.50	45.11
	H_β	284.30						
J1217+1019	CIV	20.56	59.73	5.42	–	45.39	44.70	–
	MgII	38.45						
J1223+3707	MgII	50.07	–	34.43	9.27	–	44.63	44.29
	H_β	264.00						
J1236+1034	MgII	38.83	–	53.47	11.31	–	45.05	44.60

Table A.4 continued

IAU name	FWHM		f_λ 1350Å	f_λ 3000Å	f_λ 5100Å	$log\lambda L_\lambda$ 1350Å	$log\lambda L_\lambda$ 3000Å	$log\lambda L_\lambda$ 5100Å
		Å	10^{-17} erg cm^{-2} s^{-1} $\AA^{-1}$			erg s^{-1}		
	H_β	272.90						
J1256+1008	MgII	33.46	–	15.93	–	–	44.67	–
	H_β	33.74						
J1319+5148	MgII	39.67	–	76.29	–	–	45.52	–
J1334+5501	MgII	55.70	–	21.12	–	–	45.06	–
J1358+5752	MgII	45.54	–	67.78	–	–	45.62	–
J1425+2404	MgII	56.62	–	89.40	19.66	–	45.25	44.83
	H_β	131.60						
J1433+3209	MgII	45.42	–	2.924	–	–	44.02	–
J1513+1011	CIV	23.23	–	36.67	–	–	45.42	–
	MgII	42.70						
J1550+3652	CIV	21.99	41.78	4.80	–	45.28	44.69	–
	MgII	47.58						
J1557+0253	CIV	10.42	34.97	4.69	–	45.19	44.66	–
	MgII	24.83						
J1557+3304	MgII	52.94	–	25.46	–	–	44.97	–
J1622+3531	MgII	43.02	–	10.56	–	–	44.86	–
J1623+3419	CIV	25.17	14.37	2.59	–	44.80	44.40	–
	MgII	48.20						
J2335−0927	CIV	14.18	60.11	1.14	–	45.38	44.00	–
	MgII	35.59						

Table A.5: Optical luminosity and accretion rate for GRQs.

IAU	$logL_{bol}$			$logL_{Edd}$			$\dot{m}$		
name	1350Å	3000Å	5100Å	CIV	MgII	Hβ	1350	3000	5100
		erg s^{-1}			erg s^{-1}				
J0204−0944	–	45.38	–	–	46.45	–	–	0.09	–
J0210+0118	–	45.94	–	–	47.05	–	–	0.08	–
J0750+6541		45.53	45.45		47.12	47.78		0.03	0.01
J0754+3033	–	45.94	45.66	–	47.04	47.29	–	0.08	0.02
J0754+4316	–	–	45.48	–	–	47.63	–	–	0.01
J0801+4736	–	–	43.92	–	–	46.33	–	–	0.004
J0809+2912	–	46.25	–	–	47.16	–	–	0.12	–
J0812+3031	–	45.49	–	–	46.42	–	–	0.12	–
J0816+3347		44.44	44.57		47.03	44.61		0.003	0.92
J0819+0549	45.29	44.86	–	47.49	46.66	–	–	0.02	–
J0842+2147	–	45.51	–	–	46.49	–	–	0.11	–
J0902+5707	45.97	45.67	–	47.08	46.88	–	–	0.06	–
J0918+2325	–	45.85	45.48	–	47.11	47.39	–	0.06	0.01
J0925+4004	–	45.87	45.55	–	47.21	47.54	–	0.05	0.01
J0937+2937	–	45.69	45.38	–	46.77	46.85	–	0.08	0.03
J0944+2331	–	45.90	–	–	46.92	–	–	0.10	–
J0959+1216	–	45.58	–	–	46.82	–	–	0.06	–
J1020+0447	–	45.26	–	–	46.83	–	–	0.03	–
J1020+3958	–	45.77	–	–	47.22	–	–	0.04	–
J1030+5310	–	45.90	–	–	46.76	–	–	0.14	–
J1054+4152	–	45.78	–	–	46.96	–	–	0.07	–
J1056+4100	45.34	45.16	–	46.83	46.70	–	–	0.03	–
J1145−0033	45.53	45.51	–	47.43	–	–	0.01	–	–
J1151+3355	–	45.73	–	–	46.97	–	–	0.06	–
J1229+3555	–	45.37	–	–	46.39	–	–	0.10	–
J1304+2454	–	45.92	–	–	47.01	47.57	–	0.08	–
J1321+3741	–	45.64	–	–	47.25	–	–	0.03	–
J1340+4232	–	45.47	–	–	46.87	–	–	0.04	–
J1353+2631	–	45.63	45.46	–	46.75	47.54	–	0.08	0.01
J1410+2955	–	45.65	–	–	47.20	–	–	0.03	–
J1427+2632	–	–	45.67	–	–	47.59	–	–	0.01
J1432+1548	–	45.65	–	–	46.96	–	–	0.05	–
J1445+3051	–	43.87	44.59	–	46.18	44.39	–	0.01	1.60
J1723+3417	–	45.39	45.73	–	–	46.66	–	–	0.12
J2344−0032	–	45.723	–	–	46.78	–	–	0.09	–

Table A.6: Optical luminosity and accretion rate for small-size radio quasars.

IAU	$logL_{bol}$			$logL_{Edd}$			$\dot{m}$		
name	1350Å	3000Å	5100Å	CIV	MgII	Hβ	1350	3000	5100
		erg s^{-1}			erg s^{-1}				
J0034+0118	–	45.35	–	–	46.87	–	–	0.03	–
J0051−0902	–	45.58	–	–	47.10	–	–	0.03	–
J0130−0135	–	45.83	–	–	47.19	–	–	0.05	–
J0245+0108	46.05	45.73	–	47.23	47.13	–	0.07	0.04	–
J0745+3142	–	46.51	46.26	–	47.41	47.78	–	0.13	0.03
J0811+2845	46.06	45.85	–	47.00	47.08	–	0.11	0.06	–
J0814+3237	–	45.51	–	–	46.46	45.89	–	0.11	–
J0817+2237	–	45.98	–	–	46.99	–	–	0.10	–
J0828+3935	–	45.38	–	–	46.62	–	–	0.06	–
J0839+1921	46.33	46.06	–	46.95	46.84	–	0.24	0.17	–
J0904+2819	–	46.21	–	–	46.93	–	–	0.19	–
J0906+0832	45.82	45.56	–	47.18	46.84	–	0.04	0.05	–
J0924+3547	–	45.83	–	–	46.95	–	–	0.08	–
J0925+1444	–	45.81	–	–	46.78	–	–	0.11	–
J0935+0204	–	46.03	45.72	–	47.28	47.34	–	0.06	0.02
J0941+3853	–	45.66	45.41	–	47.07	47.62	–	0.04	0.01
J0952+2352	–	46.080	–	–	46.85	–	–	0.17	–
J1000+0005	–	45.42	–	–	46.38	–	–	0.11	–
J1004+2225	–	45.61	–	–	46.79	–	–	0.07	–
J1005+5019	46.21	45.75	–	46.74	46.90	–	0.30	0.07	–
J1006+3236	–	45.34	–	–	46.44	–	–	0.08	–
J1009+0529	–	46.18	–	–	47.45	–	–	0.05	–
J1010+4132	–	46.40	46.00	–	46.81	46.81	–	0.39	0.15
J1023+6357	–	46.20	–	–	47.16	–	–	0.11	–
J1100+1046	–	45.53	45.20	–	46.84	45.43	–	0.05	0.59
J1100+2314	–	45.96	45.87	–	47.32	48.05	–	0.04	0.01

Table A.6 continued

IAU	$logL_{bol}$			$logL_{Edd}$			ṁ		
name	1350Å	3000Å	5100Å	CIV	MgII	Hβ	1350	3000	5100
		erg s^{-1}			erg s^{-1}				
J1107+0547	45.87	45.54	–	47.09	46.67	–	0.06	0.07	–
J1107+1628	–	46.31	45.99	–	46.98	47.06	–	0.21	0.09
J1110+0321	–	45.57	–	–	46.41	–	–	0.14	–
J1118+3828	–	45.64	45.12	–	46.69	48.01	–	0.09	0.001
J1119+3858	–	45.65	45.37	–	47.14	47.94	–	0.03	0.003
J1158+6254	–	46.27	46.07	–	47.47	48.12	–	0.06	0.01
J1217+1019	46.06	45.47	–	46.76	46.60	–	0.20	0.08	–
J1223+3707	–	45.40	45.24	–	46.79	47.64	–	0.04	0.004
J1236+1034	–	45.82	45.56	–	46.78	47.82	–	0.11	0.01
J1256+1008	–	45.44	–	–	46.46	45.70	–	0.10	–
J1319+5148	–	46.29	–	–	47.03	–	–	0.18	–
J1334+5501	–	45.83	–	–	47.10	–	–	0.05	–
J1358+5752	–	46.39	–	–	47.20	–	–	0.16	–
J1425+2404	–	46.03	45.78	–	47.21	47.30	–	0.07	0.03
J1433+3209	–	44.79	–	–	46.40	–	–	0.03	–
J1513+1011	46.59	46.20	–	47.15	47.05	–	0.27	0.14	–
J1550+3652	45.95	45.46	–	46.76	46.78	–	0.15	0.05	–
J1557+0253	45.85	45.43	–	46.06	46.20	–	0.61	0.17	–
J1557+3304	–	45.74	–	–	47.01	–	–	0.05	–
J1622+3531	–	45.63	–	–	46.77	–	–	0.07	–
J1623+3419	45.46	45.17	–	46.62	46.64	–	0.07	0.03	–
J2335−0927	46.04	44.77	–	46.43	46.18	–	0.41	0.04	–

Table A.7: Black hole masses for GRQs.

IAU name	M_{BH} CIV	M_{BH} MgII	M_{BH} Hβ
	$\times 10^8$ M$\odot$		
J0204−0944	–	1.93 ± 0.25	–
J0210+0118	–	7.80 ± 0.22	–
J0750+6541	–	3.24 ± 1.6	33.74 ± 2.13
J0754+3033	–	7.49 ± 0.25	13.56 ± 2.57
J0754+4316	–	–	29.17 ± 1.32
J0801+4736	–	–	1.48 ± 0.76
J0809+2912	–	9.98 ± 0.51	–
J0812+3031	–	1.80 ± 0.15	–
J0816+3347	–	2.14 ± 1.92	0.05 ± 0.01
J0819+0549	–	3.16 ± 2.77	–
J0842+2147	–	2.12 ± 0.48	–
J0902+5707	–	5.28 ± 1.28	–
J0918+2325	–	8.86 ± 0.46	16.95 ± 3.37
J0925+4004	–	11.28 ± 4.24	23.90 ± 2.01
J0937+2937	–	4.03 ± 0.51	4.91 ± 0.24
J0944+2331	–	5.68 ± 0.54	–
J0959+1216	–	4.59 ± 3.26	–
J1020+0447	–	4.71 ± 1.45	–
J1020+3958	–	11.52 ± 5.16	–
J1030+5310	–	3.99 ± 0.27	–
J1054+4152	–	6.34 ± 3.40	–
J1056+4100	–	3.43 ± 1.13	–
J1145−0033	18.42 ± 2.43	–	–
J1151+3355	–	6.44 ± 2.48	–
J1229+3555	–	1.67 ± 0.29	–
J1304+2454	–	7.10 ± 0.43	–
J1321+3741	–	12.23 ± 3.98	–
J1340+4232	–	5.12 ± 2.67	–
J1353+2631	–	3.87 ± 2.63	23.69 ± 2.59
J1410+2955	–	11.04 ± 6.67	–
J1427+2632	–	–	27.08 ± 4.74
J1432+1548	–	6.34 ± 1.02	–
J1445+3051	–	1.40 ± 1.05	0.045 ± 0.02
J1723+3417	–	–	3.16 ± 0.407
J2344−0032	–	4.20 ± 0.31	–

Table A.8: Black hole masses for smaller-size RQs.

IAU name	M_{BH} CIV $\times 10^8$ M⊙	M_{BH} MgII $\times 10^8$ M⊙	M_{BH} Hβ $\times 10^8$ M⊙
J0034+0118	–	5.06 ± 0.11	–
J0051−0902	–	8.73 ± 3.13	–
J0130−0135	–	10.56 ± 0.48	–
J0245+0108	–	9.23 ± 3.07	–
J0745+3142	–	17.67 ± 0.76	41.92 ± 4.52
J0811+2845	6.88 ± 0.88	8.30 ± 1.16	–
J0814+3237	–	1.99 ± 0.14	–
J0817+2237	–	6.72 ± 0.95	–
J0828+3935	–	2.85 ± 0.54	–
J0839+1921	–	4.72 ± 0.10	–
J0904+2819	–	5.88 ± 0.26	–
J0906+0832	–	4.78 ± 2.13	–
J0924+3547	–	6.09 ± 0.73	–
J0925+1444	–	4.18 ± 0.41	–
J0935+0204	–	13.22 ± 0.75	15.07 ± 1.44
J0941+3853	–	8.01 ± 1.03	28.53 ± 2.11
J0952+2352	–	4.85 ± 0.49	–
J1000+0005	–	1.65 ± 0.20	–
J1004+2225	–	4.29 ± 0.29	–
J1005+5019	3.74 ± 0.46	5.53 ± 2.99	–
J1006+3236	–	1.90 ± 0.20	–
J1009+0529	–	19.25 ± 1.07	–
J1010+4132	–	4.45 ± 0.34	4.45 ± 0.76
J1023+6357	–	10.05 ± 0.97	–
J1100+1046	–	4.79 ± 2.17	0.19 ± 0.10
J1100+2314	–	14.34 ± 4.02	77.29 ± 5.26

Table A.8 continued

IAU name	M_{BH} CIV	M_{BH} MgII	M_{BH} Hβ
	$\times10^8$ M⊙		
J1107+0547	–	3.21 ± 1.52	–
J1107+1628	–	6.57 ± 0.39	7.92 ± 0.86
J1110+0321	–	1.77 ± 0.74	–
J1118+3828	–	3.39 ± 1.22	69.97 ± 29.70
J1119+3858	–	9.47 ± 3.54	59.42 ± 20.60
J1158+6254	–	20.31 ± 2.35	89.96 ± 19.39
J1217+1019	3.96 ± 0.53	2.71 ± 1.00	–
J1223+3707	–	4.24 ± 0.95	30.00 ± 5.01
J1236+1034	–	4.13 ± 1.94	46.03 ± 9.20
J1256+1008	–	1.99 ± 0.18	–
J1319+5148	–	7.42 ± 0.80	–
J1334+5501	–	8.63 ± 0.92	–
J1358+5752	–	11.05 ± 1.92	–
J1425+2404	–	11.16 ± 1.62	13.87 ± 1.64
J1433+3209	–	1.73 ± 1.85	–
J1513+1011	–	7.72 ± 0.57	–
J1550+3652	3.97 ± 0.52	4.12 ± 1.81	–
J1557+0253	0.79 ± 0.16	1.09 ± 1.28	–
J1557+3304	–	7.05 ± 1.15	–
J1622+3531	–	4.08 ± 0.83	–
J1623+3419	2.88 ± 0.59	3.04 ± 1.78	–
J2335−0927	1.85 ± 0.26	1.04 ± 0.99	–

Table A.9: Parameters of radio structures for GRQs.

IAU name (1)	$logP_{tot}$ W/Hz (2)	$logP_{core}$ W/Hz (3)	B [^{o}] (4)	Q (5)	F (6)	i [^{o}] (7)
J0204−0944	25.76	24.92	0.0	2.06	0.59	81
J0210+0118	25.99	25.31	25.6	1.38	0.30	63
J0313−0631	25.89	24.45	5.6	1.11	0.97	87
J0439−2422	27.09	–	4.5	1.67	0.55	79
J0750+6541	26.39	25.73	5.5	1.05	0.33	65
J0754+3033	26.10	25.97	18.8	1.77	1.20	87
J0754+4316	25.63	24.68	0.2	1.07	0.36	85
J0801+4736	25.00	24.58	8.7	1.05	2.21	37
J0809+2912	27.47	26.21	1.5	1.25	0.04	28
J0812+3031	26.07	25.10	2.4	1.37	2.91	71
J0816+3347	25.54	23.88	3.8	1.16	1.08	44
J0819+0549	26.58	25.19	0.0	1.24	1.54	81
J0842+2147	26.45	25.46	0.9	2.28	0.92	85
J0902+5707	26.53	25.80	9.3	1.38	2.74	79
J0918+2325	26.17	25.59	9.4	1.48	0.99	81
J0925+4004	25.73	24.76	5.7	1.13	1.18	80
J0937+2937	25.27	24.13	4.3	1.56	0.69	81
J0944+2331	26.95	25.57	7.1	1.67	0.44	83
J0959+1216	25.96	25.21	11.0	1.17	1.80	73
J1012+4229	25.52	25.46	15.6	1.39	3.71	59
J1020+0447	26.00	27.85	6.7	1.08	3.71	61
J1020+3958	25.39	24.67	1.9	1.12	3.62	58
J1027−2312	26.21	25.38	8.2	1.15	0.82	88
J1030+5310	26.54	25.70	9.4	1.58	3.22	77
J1054+4152	25.82	24.48	18.8	1.18	4.23	75
J1056+4100	26.39	25.63	7.8	2.10	0.89	87
J1130−1320	27.20	25.40	0.7	1.13	0.29	67

Table A.9 continued

IAU name (1)	$logP_{tot}$ W/Hz (2)	$logP_{core}$ W/Hz (3)	B [^{o}] (4)	Q (5)	F (6)	i [^{o}] (7)
J1145−0033	26.47	25.72	10.2	1.29	0.59	82
J1148−0403	26.32	25.76	12.8	1.06	1.20	88
J1151+3355	26.26	25.16	11.3	1.98	0.33	32
J1229+3555	26.20	24.65	14.9	1.33	0.39	57
J1304+2454	25.76	25.41	1.6	1.46	1.82	77
J1321+3741	26.53	25.55	17.0	1.06	0.72	79
J1340+4232	26.24	25.48	3.5	1.92	0.59	89
J1353+2631	25.83	24.78	13.4	1.21	2.98	34
J1408+3054	25.93	24.82	4.9	1.41	2.72	80
J1410+2955	25.26	24.56	10.4	1.30	1.00	81
J1427+2632	26.17	25.23	9.1	1.70	0.40	45
J1432+1548	26.83	25.71	2.9	1.39	0.99	87
J1445+3051	25.72	24.46	0.9	1.41	0.34	85
J1504+6856	26.13	25.52	4.0	1.85	1.66	81
J1723+3417	26.26	25.67	1.1	1.05	2.11	51
J2042+7508	25.67	24.72	7.1	1.03	2.69	61
J2234−0224	25.89	24.71	1.9	1.49	0.18	87
J2344−0032	25.46	25.12	0.8	1.54	0.76	79

Table A.10: Parameters of radio structures for smaller-size radio quasars from the comparison sample.

IAU name (1)	$logP_{tot}$ W/Hz (2)	$logP_{core}$ W/Hz (3)	B $[^o]$ (4)	Q (5)	F (6)	i $[^o]$ (7)
J0022−0145	26.62	25.13	6.7	1.07	2.08	71
J0034+0118	27.20	24.51	7.9	1.90	0.26	60
J0051−0902	26.61	24.60	9.1	1.39	5.35	55
J0130−0135	26.18	24.68	5.9	1.90	0.15	62
J0245+0108	27.55	25.85	12.0	2.28	0.68	85
J0745+3142	26.96	26.59	5.3	1.10	0.62	88
J0811+2845	27.23	26.71	6.1	2.35	1.26	80
J0814+3237	26.84	26.49	12.8	2.40	0.37	72
J0817+2237	27.69	26.42	5.7	1.06	2.38	71
J0828+3935	26.26	24.94	0.4	1.15	0.23	79
J0839+1921	27.78	26.97	11.4	1.36	0.11	41
J0904+2819	26.83	26.22	2.3	1.07	3.15	45
J0906+0832	26.81	26.05	0.5	1.29	0.88	86
J0924+3547	26.49	25.90	1.9	1.05	0.68	84
J0925+1444	27.36	26.04	5.6	1.26	1.25	84
J0935+0204	27.06	26.47	4.3	1.62	37.20	-
J0941+3853	26.95	26.03	0.3	1.44	0.72	85
J0952+2352	26.23	26.02	17.7	2.56	0.97	89
J1000+0005	27.46	26.38	18.4	1.35	1.17	85
J1004+2225	27.40	26.05	4.7	1.25	1.03	85
J1005+5019	27.18	26.96	16.2	2.73	1.54	76
J1006+3236	27.31	26.97	0.9	2.89	1.06	80
J1009+0529	26.79	25.89	8.7	1.01	1.75	78
J1010+4132	27.35	26.57	5.5	1.69	12.73	42
J1023+6357	27.01	26.00	0.2	1.37	0.44	70
J1100+1046	26.61	26.19	1.8	1.20	0.61	78

Table A.10 continued

IAU name (1)	$logP_{tot}$ W/Hz (2)	$logP_{core}$ W/Hz (3)	B [^{o}] (4)	Q (5)	F (6)	i [^{o}] (7)
J1100+2314	26.38	25.14	–	–	3.64	68
J1107+0547	26.42	25.52	7.2	1.46	0.63	80
J1107+1628	27.09	26.53	3.4	1.05	0.67	87
J1110+0321	27.35	25.50	10.7	2.38	0.55	85
J1118+3828	26.10	24.89	3.5	1.25	3.25	55
J1119+3858	26.43	25.28	8.4	1.14	2.66	64
J1158+6254	27.03	25.32	4.3	1.53	0.46	75
J1217+1019	27.44	26.13	26.8	1.43	0.73	87
J1223+3707	26.57	25.48	3.9	1.75	0.72	83
J1236+1034	26.55	25.18	0.4	1.42	0.39	63
J1256+1008	26.98	26.51	20.3	1.14	0.30	69
J1319+5148	27.70	27.13	27.9	1.81	0.54	61
J1334+5501	27.46	25.69	0.4	1.13	0.79	89
J1358+5752	27.66	25.86	1.3	1.20	1.24	85
J1425+2404	27.37	26.62	18.9	1.41	1.60	83
J1433+3209	26.89	25.51	13.8	1.14	0.96	88
J1513+1011	27.38	26.36	20.9	1.46	1.07	83
J1550+3652	26.99	25.39	1.0	1.78	0.28	64
J1557+0253	26.78	26.40	7.4	3.62	8.05	61
J1557+3304	27.45	27.26	20.2	1.54	1.50	89
J1622+3531	27.56	26.36	17.2	2.67	0.59	82
J1623+3419	26.31	25.77	7.9	2.19	0.64	13
J2335−0927	26.72	26.11	8.0	2.74	1.66	83

Appendix B

Spectra and radio maps of giant radio quasars

This appendix presents the optical spectra and radio maps of the sample of GRQs.

In presented below graphs I plotted the observed spectra after galactic extinction and redshift correction (see Section 2.3.1); a power-law continuum (green lines); the continuum-subtracted spectra; the best fit of the iron emission (blue lines) in the UV band (1250–3090Å) or/and in the optical band (3535–7530Å).

The 1.4-GHz VLA maps of the GRQs taken from the NVSS survey and from the FIRST survey (if available) overlaid on the optical image from the DSS. The contour levels are: -1, 1, 2, 4, 8, 16, 32, 64 × 1.35 mJy/beam and -1, 1, 2, 4, 8, 16, 32, 64 × 0.6 mJy/beam for the NVSS and FIRST surveys, respectively. The ellipses in the corners represent the resolution of the NVSS and FIRST surveys. Crosses mark the position of the parent quasar.

All radio maps as well as optical spectra of GRQs were recorded on a CD which is attached to the Thesis.

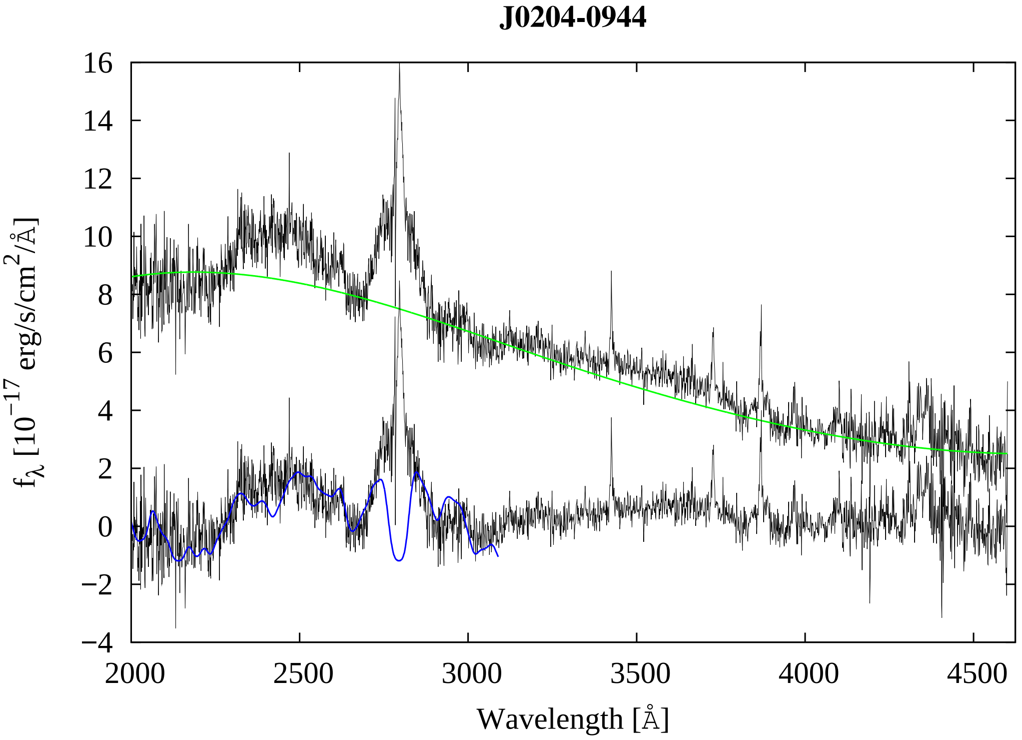
J0204-0944
f_λ [10^{-17} erg/s/cm^2/Å]
16
14
12
10
8
6
4
2
0
−2
−4
2000
2500
3000
3500
4000
4500
Wavelength [Å]

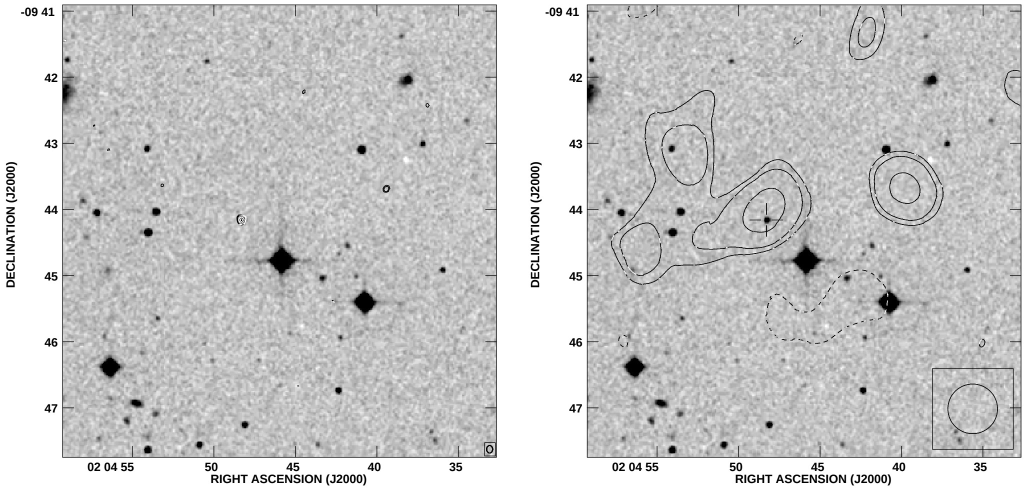
-09 41
42
43
44
45
46
47
DECLINATION (J2000)
02 04 55
50
45
40
35
RIGHT ASCENSION (J2000)
-09 41
42
43
44
45
46
47
DECLINATION (J2000)
02 04 55
50
45
40
35
RIGHT ASCENSION (J2000)

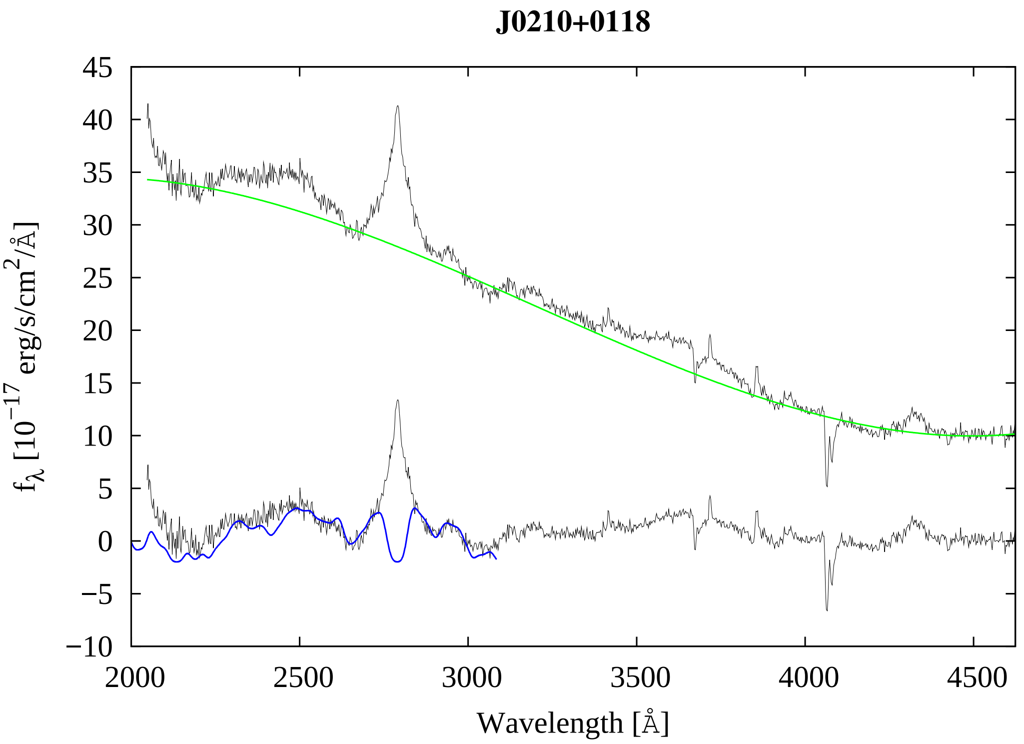
J0210+0118
f_λ [10^{-17} erg/s/cm^2/Å]
45
40
35
30
25
20
15
10
5
0
−5
−10
2000
2500
3000
3500
4000
4500
Wavelength [Å]

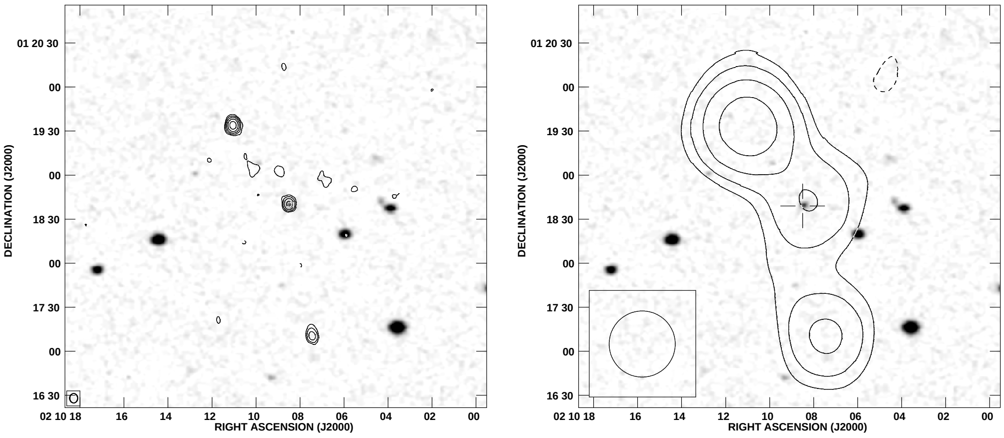
DECLINATION (J2000)
01 20 30
00
19 30
00
18 30
00
17 30
00
16 30
RIGHT ASCENSION (J2000)
02 10 18
16
14
12
10
08
06
04
02
00

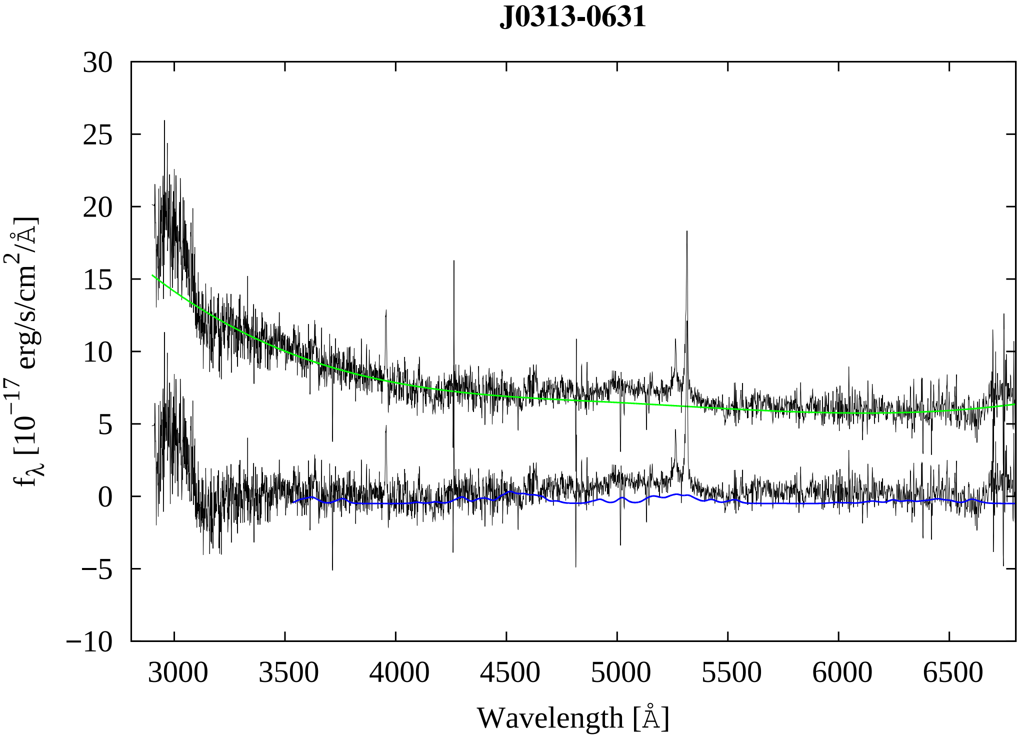
J0313-0631
30
25
20
15
10
5
0
−5
−10
f_λ [10^{-17} erg/s/cm^2/Å]
3000
3500
4000
4500
5000
5500
6000
6500
Wavelength [Å]

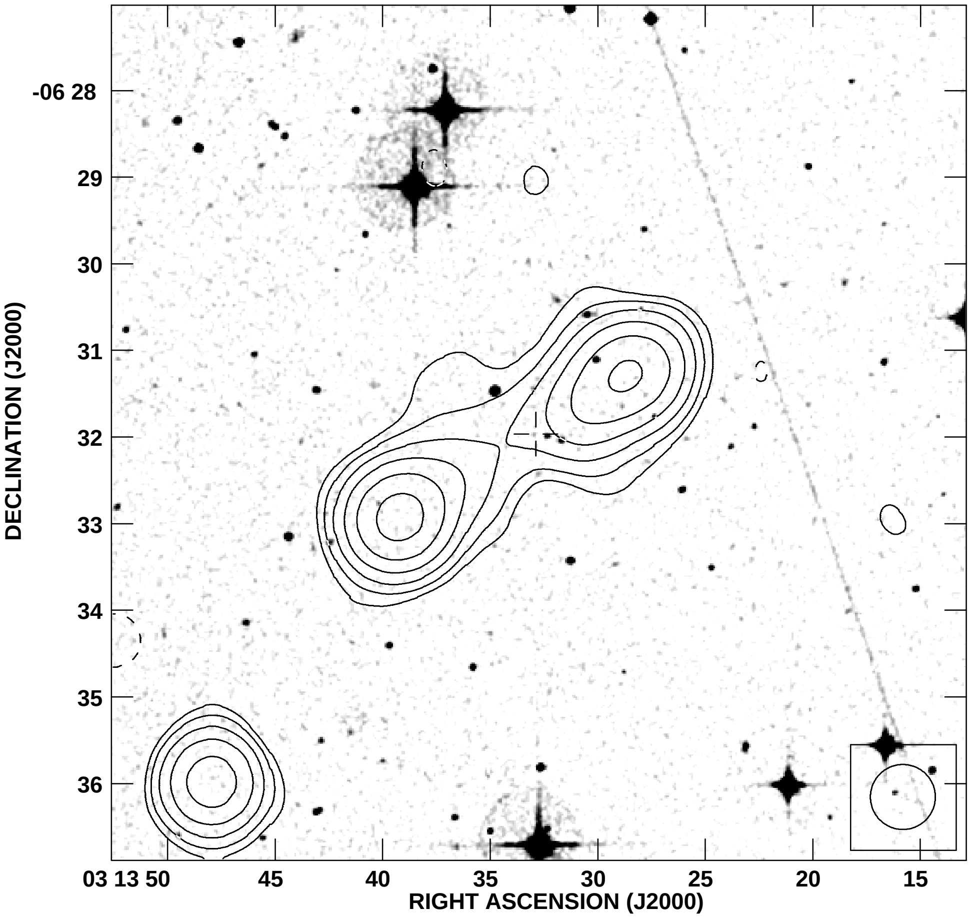
-06 28
29
30
31
32
33
34
35
36
DECLINATION (J2000)
03 13 50
45
40
35
30
25
20
15
RIGHT ASCENSION (J2000)

J0439−2422

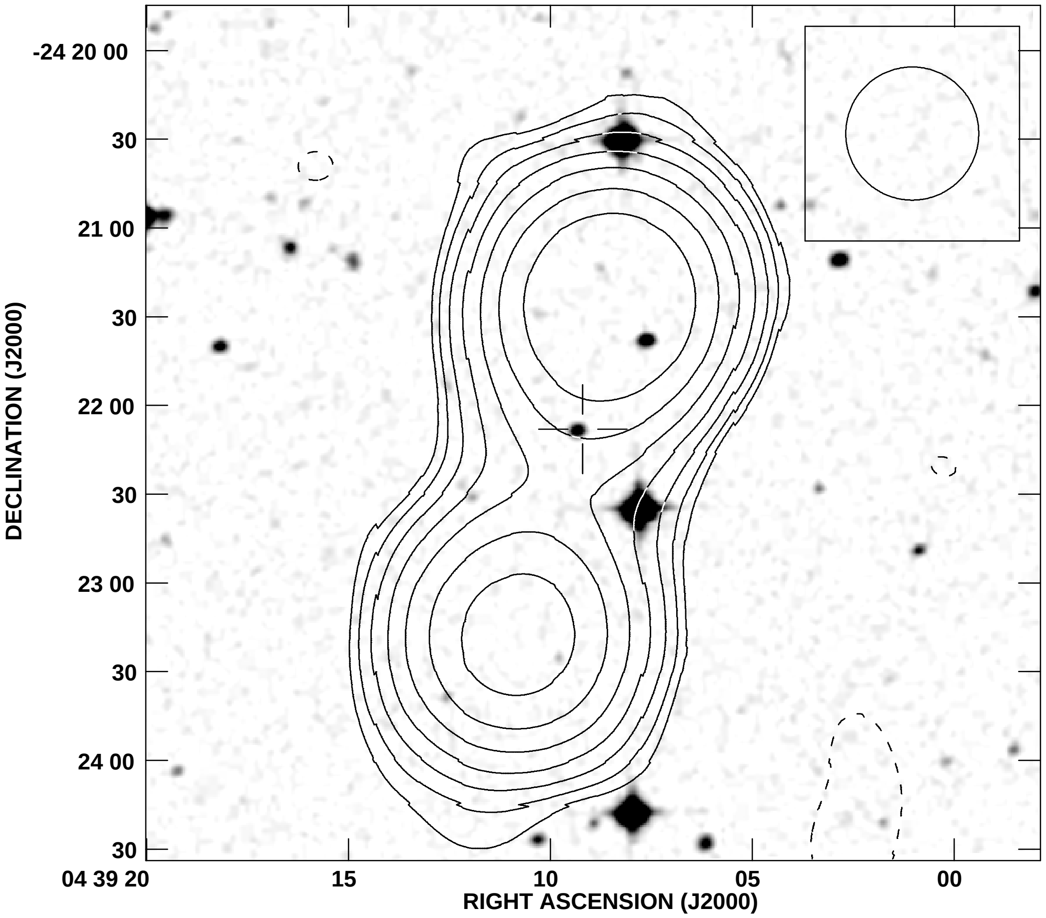
-24 20 00
30
21 00
30
22 00
30
23 00
30
24 00
30
DECLINATION (J2000)
04 39 20
15
10
05
00
RIGHT ASCENSION (J2000)

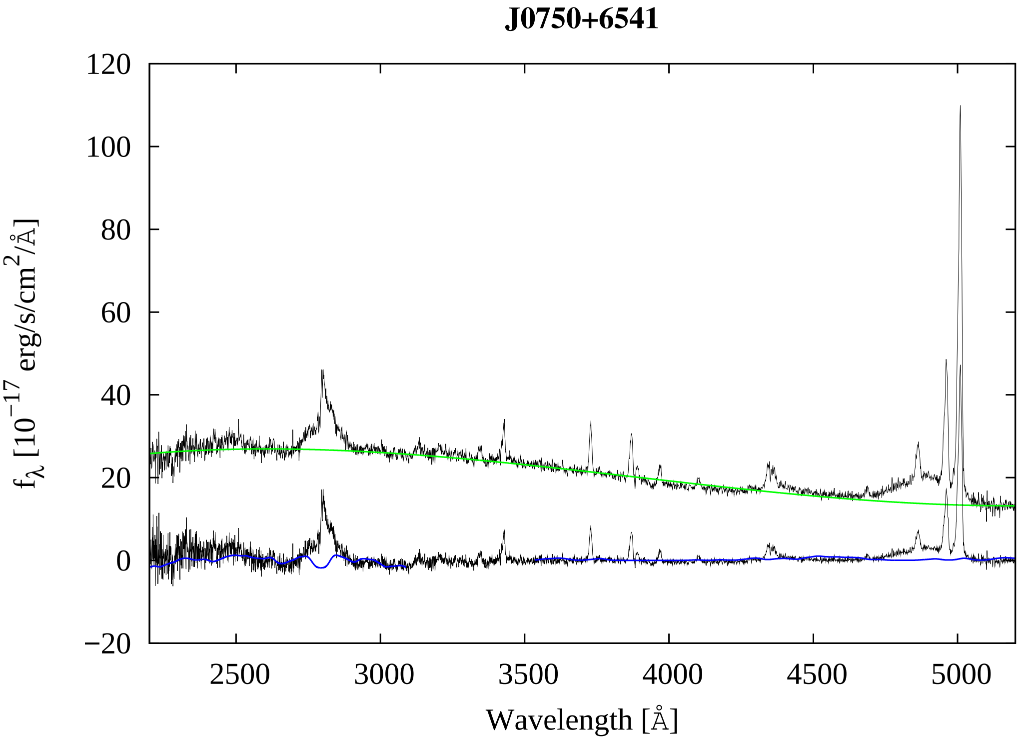
J0750+6541
120
100
80
60
40
20
0
−20
f$_\lambda$ [10^{-17} erg/s/cm^2/Å]
2500
3000
3500
4000
4500
5000
Wavelength [Å]

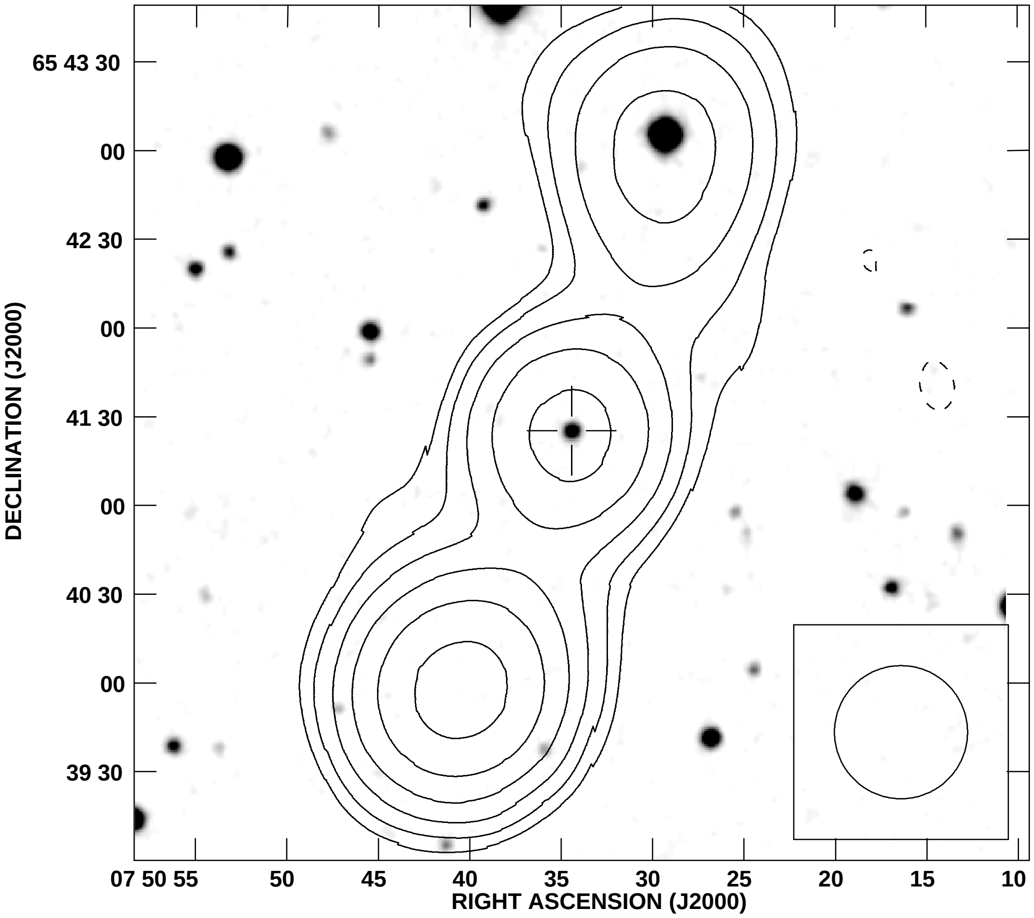
65 43 30
00
42 30
00
41 30
00
40 30
00
39 30
DECLINATION (J2000)
07 50 55
50
45
40
35
30
25
20
15
10
RIGHT ASCENSION (J2000)

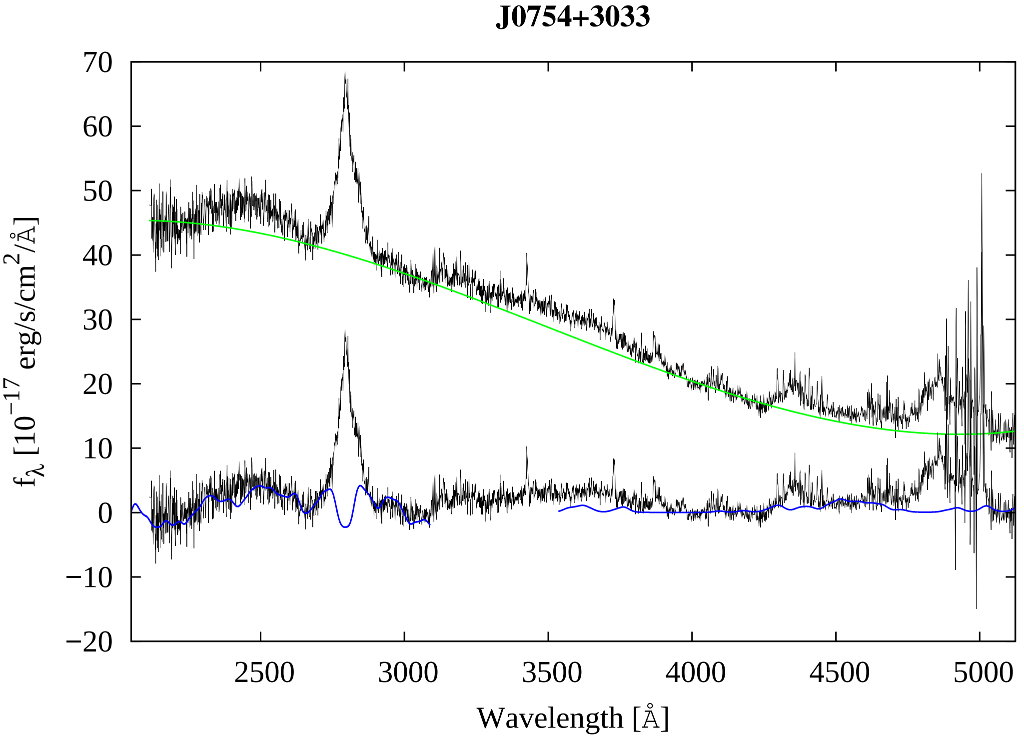
J0754+3033
70
60
50
40
30
20
10
0
−10
−20
f_λ [10^{-17} erg/s/cm^2/Å]
2500
3000
3500
4000
4500
5000
Wavelength [Å]

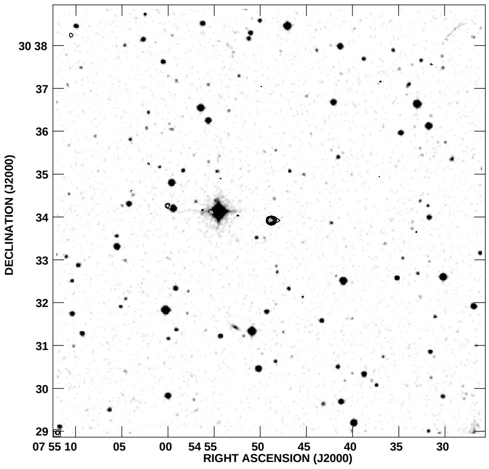
30 38
37
36
35
34
33
32
31
30
29
DECLINATION (J2000)
07 55 10
05
00
54 55
50
45
40
35
30
RIGHT ASCENSION (J2000)

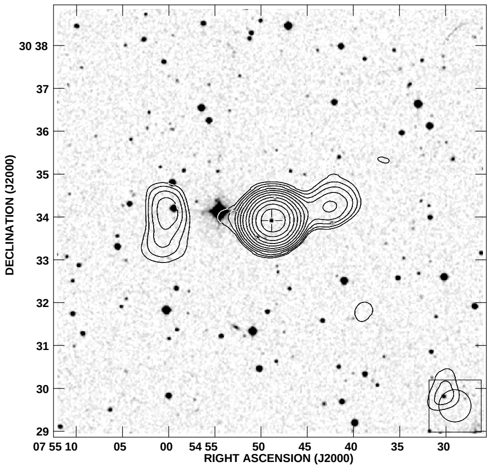
30 38
37
36
35
34
33
32
31
30
29
DECLINATION (J2000)
07 55 10
05
00
54 55
50
45
40
35
30
RIGHT ASCENSION (J2000)

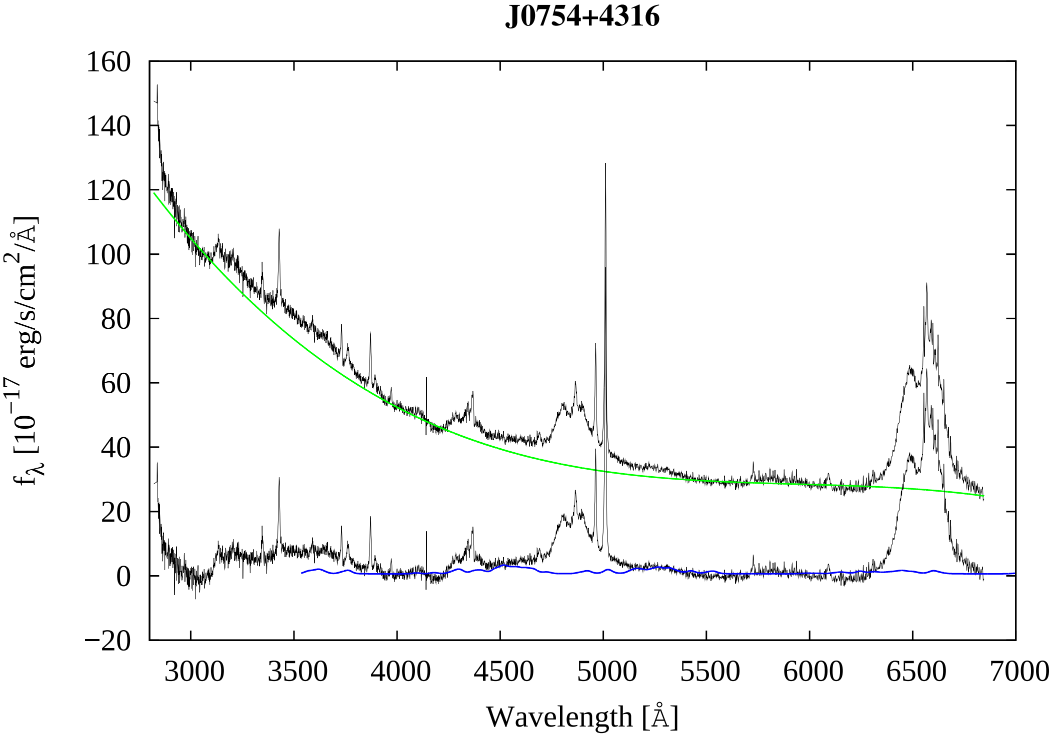
J0754+4316
f$_\lambda$ [10^{-17} erg/s/cm^2/Å]
160
140
120
100
80
60
40
20
0
−20
3000
3500
4000
4500
5000
5500
6000
6500
7000
Wavelength [Å]

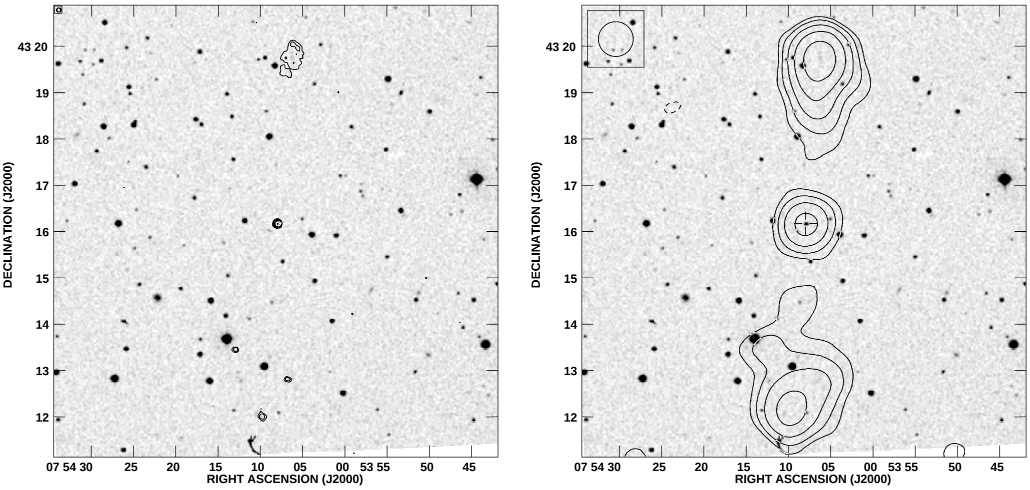
43 20
19
18
17
16
15
14
13
12
DECLINATION (J2000)
07 54 30
25
20
15
10
05
00
53 55
50
45
RIGHT ASCENSION (J2000)

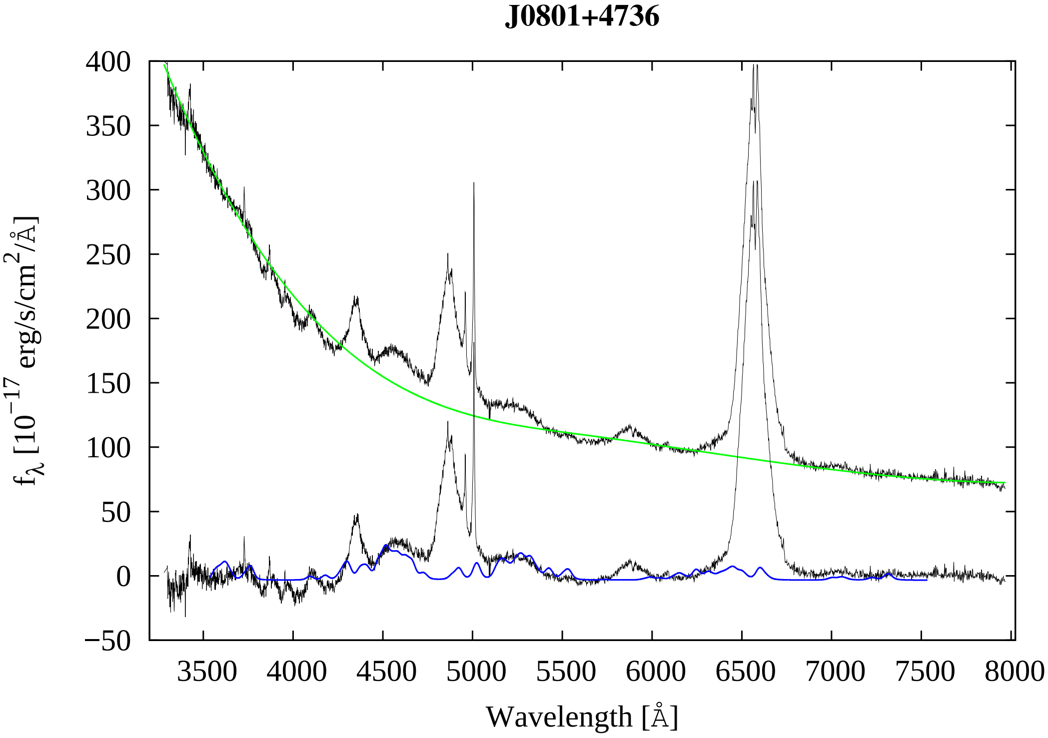
J0801+4736
f_λ [10^{-17} erg/s/cm^2/Å]
400
350
300
250
200
150
100
50
0
−50
3500
4000
4500
5000
5500
6000
6500
7000
7500
8000
Wavelength [Å]

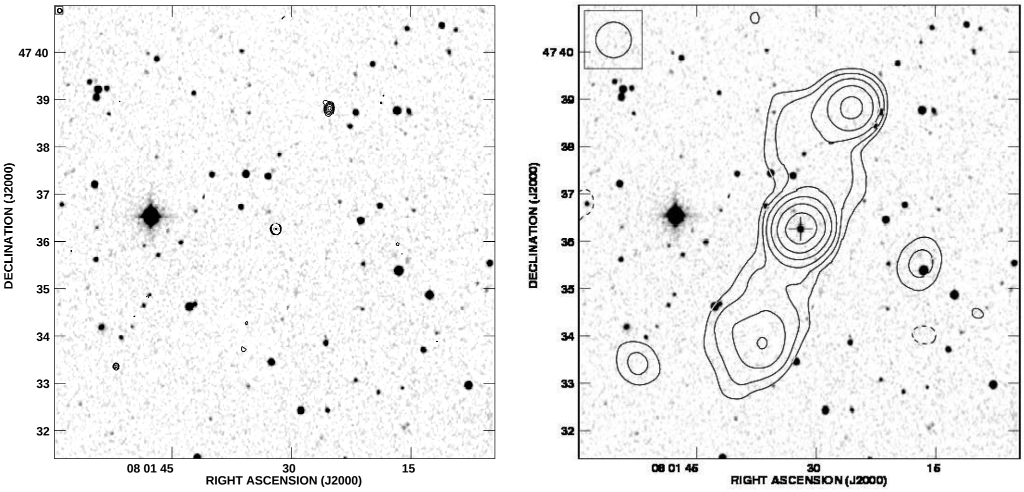
DECLINATION (J2000)
47 40
39
38
37
36
35
34
33
32
08 01 45
30
15
RIGHT ASCENSION (J2000)
DECLINATION (J2000)
47 40
39
38
37
36
35
34
33
32
08 01 45
30
15
RIGHT ASCENSION (J2000)

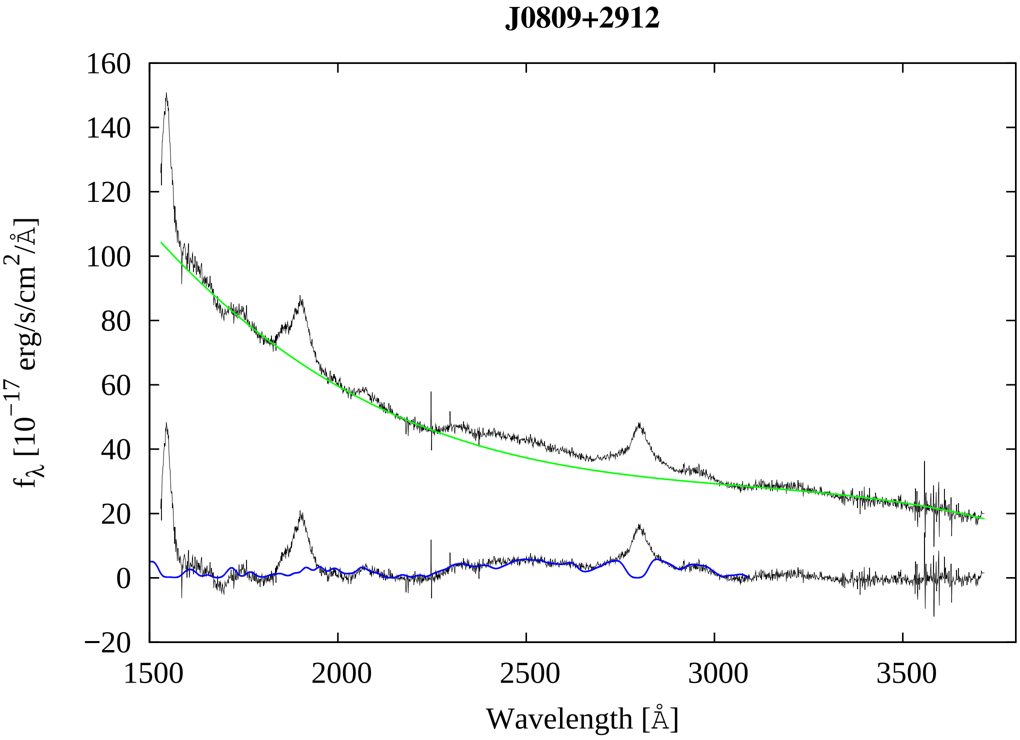
J0809+2912
160
140
120
100
80
60
40
20
0
−20
1500
2000
2500
3000
3500
Wavelength [Å]
f_λ [10^{-17} erg/s/cm^2/Å]

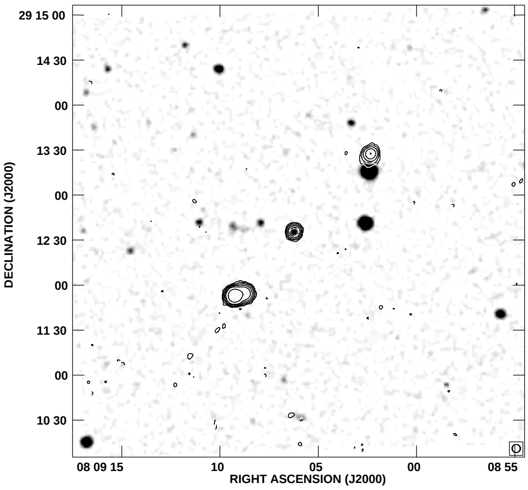
29 15 00
14 30
00
13 30
00
12 30
00
11 30
00
10 30
DECLINATION (J2000)
08 09 15
10
05
00
08 55
RIGHT ASCENSION (J2000)

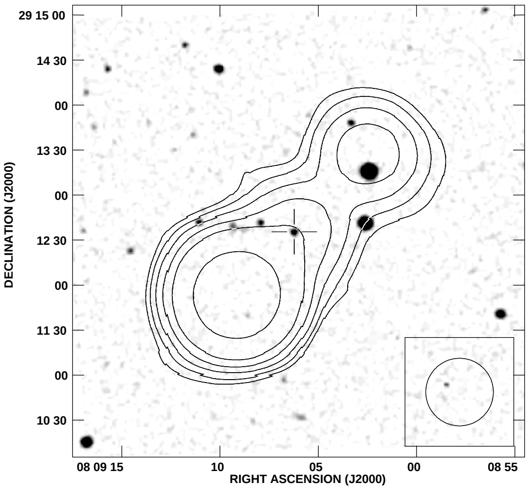
29 15 00
14 30
00
13 30
00
12 30
00
11 30
00
10 30
DECLINATION (J2000)
08 09 15
10
05
00
08 55
RIGHT ASCENSION (J2000)

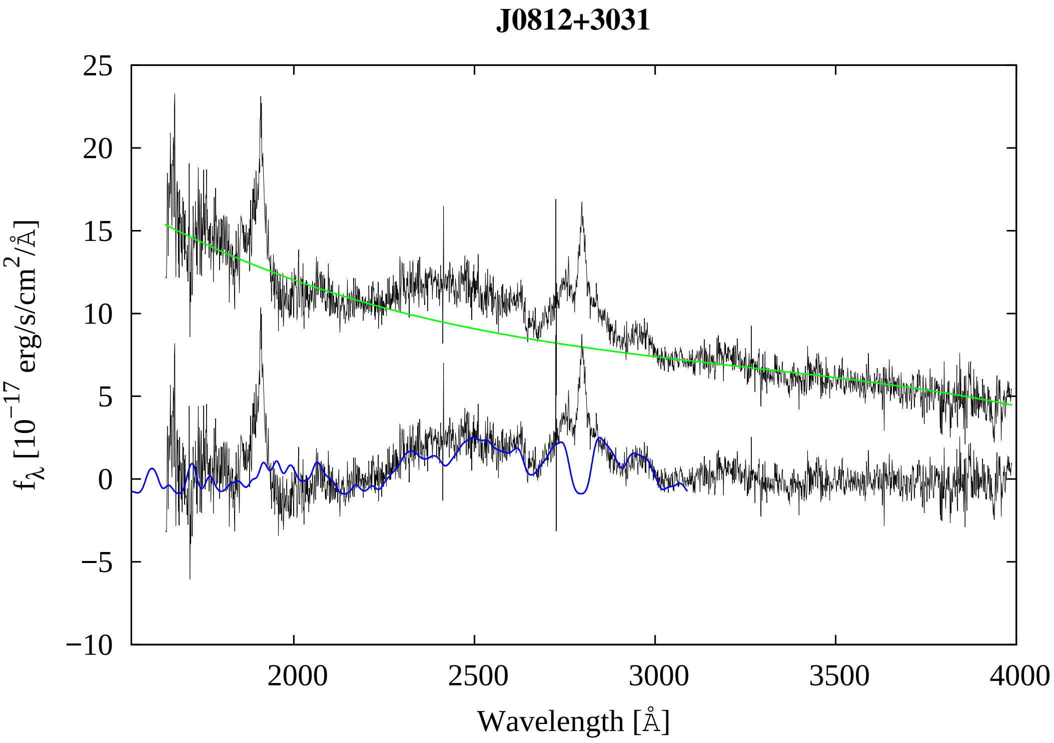
J0812+3031
25
20
15
10
5
0
−5
−10
f_λ [10^{-17} erg/s/cm^2/Å]
2000
2500
3000
3500
4000
Wavelength [Å]

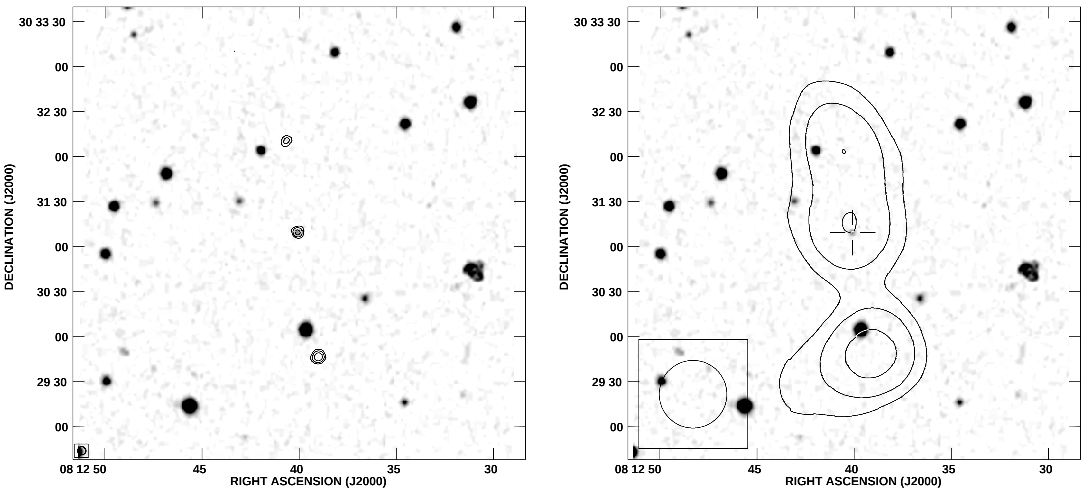
30 33 30
00
32 30
00
31 30
00
30 30
00
29 30
00
DECLINATION (J2000)
08 12 50
45
40
35
30
RIGHT ASCENSION (J2000)
30 33 30
00
32 30
00
31 30
00
30 30
00
29 30
00
DECLINATION (J2000)
08 12 50
45
40
35
30
RIGHT ASCENSION (J2000)

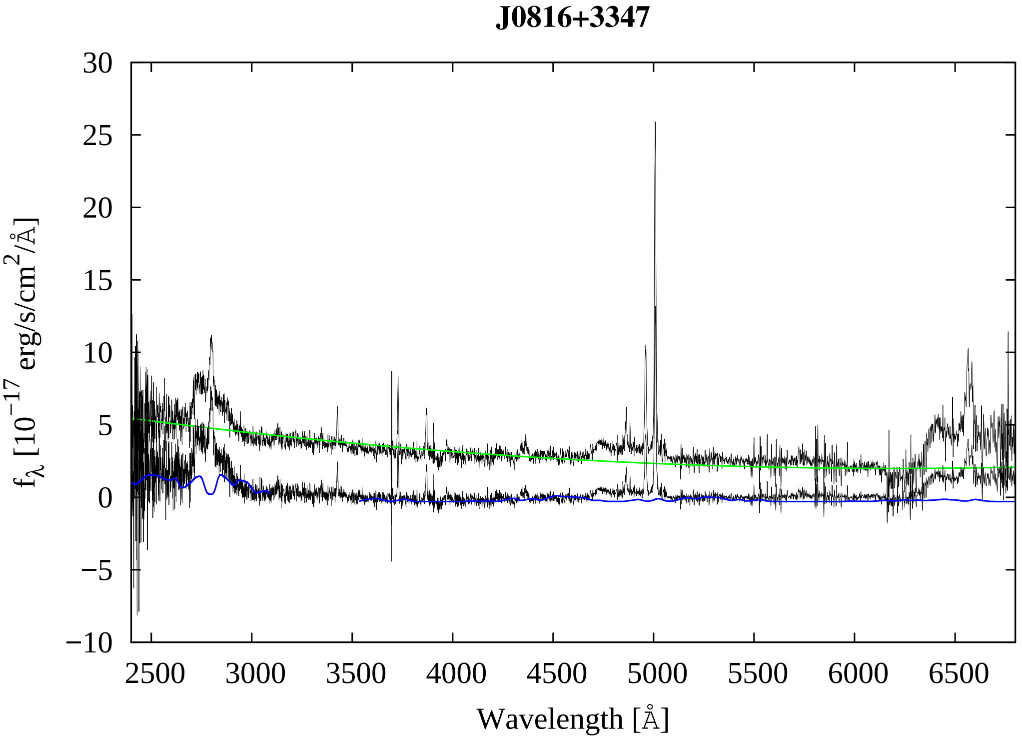
J0816+3347
30
25
20
15
10
5
0
−5
−10
f_λ [10^{-17} erg/s/cm^2/Å]
2500
3000
3500
4000
4500
5000
5500
6000
6500
Wavelength [Å]

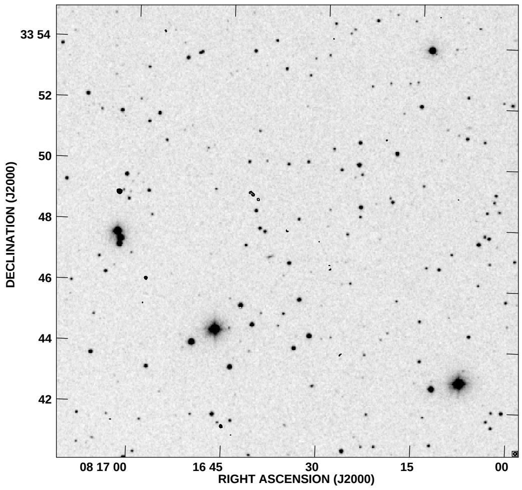
33 54
52
50
48
46
44
42
DECLINATION (J2000)
08 17 00
16 45
30
15
00
RIGHT ASCENSION (J2000)

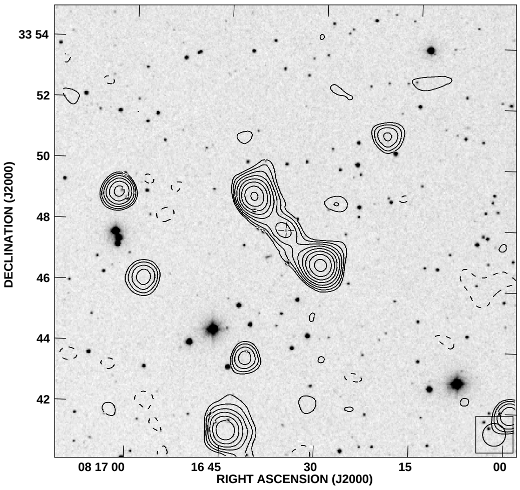
33 54
52
50
48
46
44
42
DECLINATION (J2000)
08 17 00
16 45
30
15
00
RIGHT ASCENSION (J2000)

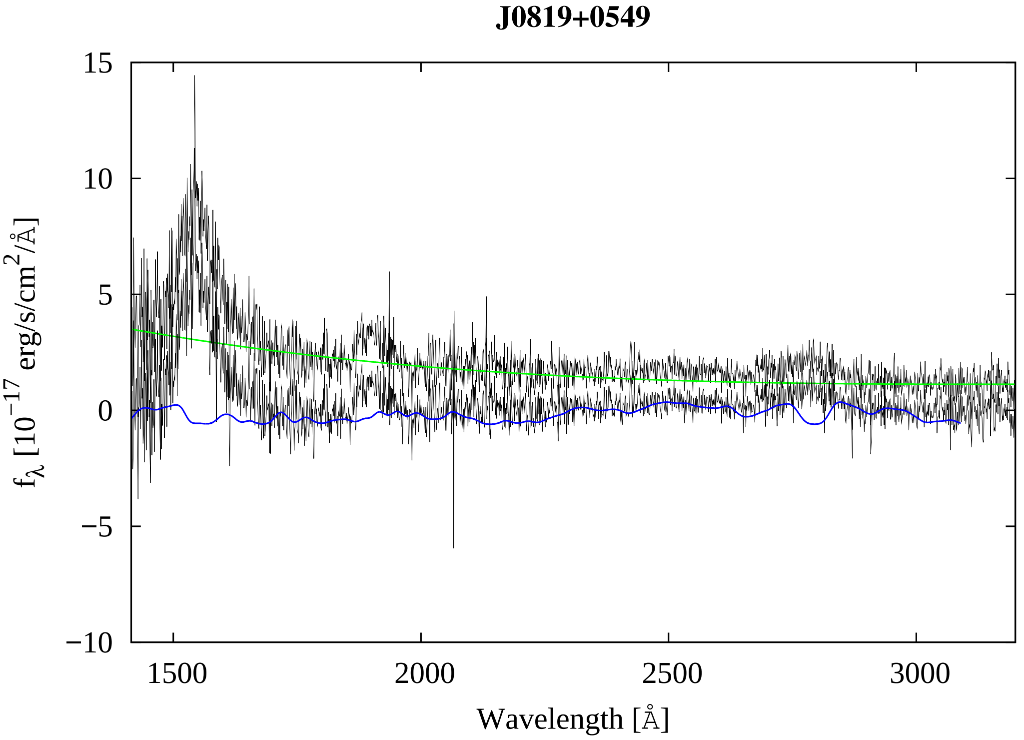
J0819+0549
15
10
5
0
−5
−10
f_λ [10^{-17} erg/s/cm^2/Å]
1500
2000
2500
3000
Wavelength [Å]

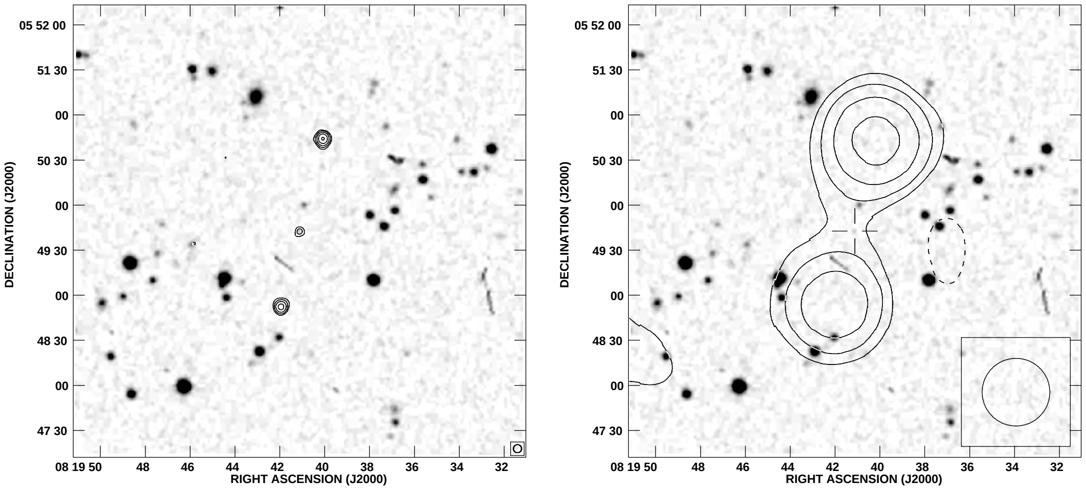
05 52 00
51 30
00
50 30
00
49 30
00
48 30
00
47 30
DECLINATION (J2000)
08 19 50
48
46
44
42
40
38
36
34
32
RIGHT ASCENSION (J2000)

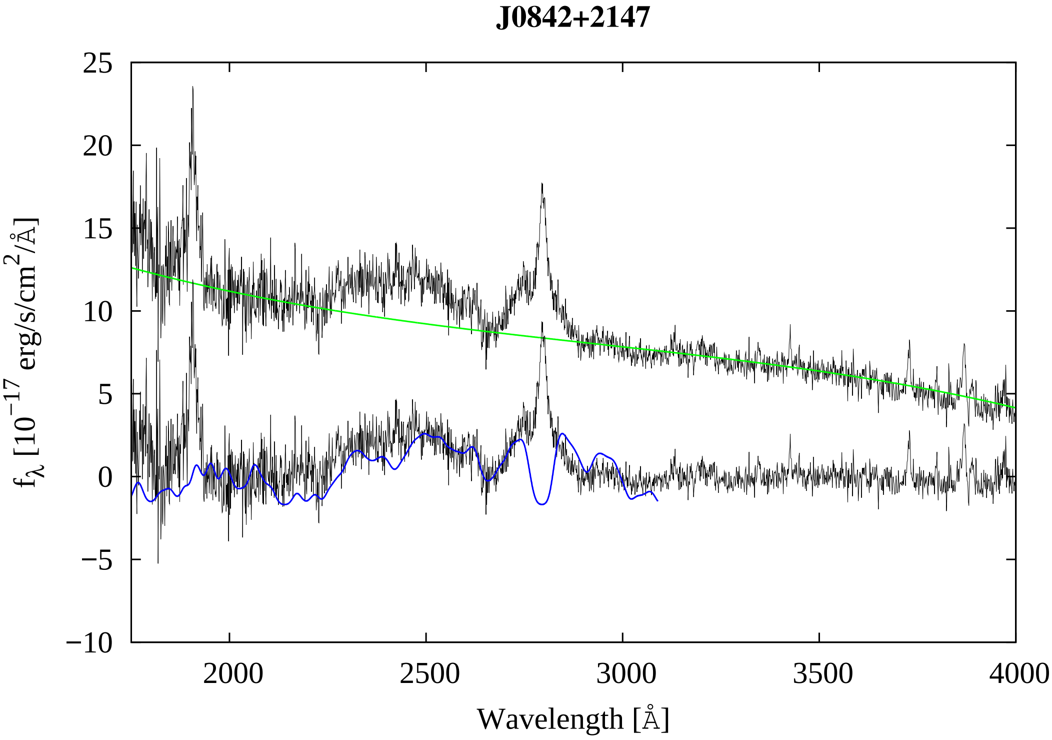
J0842+2147
f_λ [10^{-17} erg/s/cm^2/Å]
25
20
15
10
5
0
−5
−10
2000
2500
3000
3500
4000
Wavelength [Å]

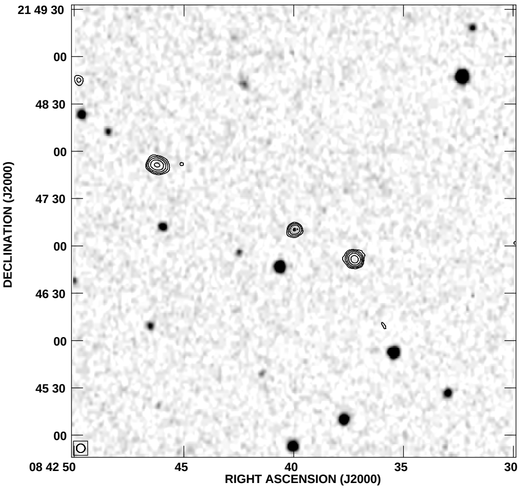
21 49 30
00
48 30
00
47 30
00
46 30
00
45 30
00
DECLINATION (J2000)
08 42 50
45
40
35
30
RIGHT ASCENSION (J2000)

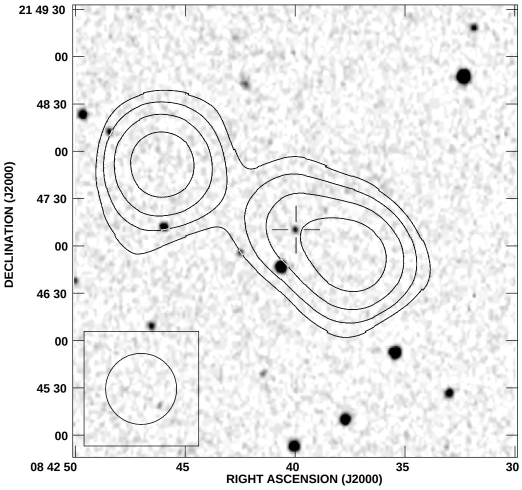
21 49 30
00
48 30
00
47 30
00
46 30
00
45 30
00
DECLINATION (J2000)
08 42 50
45
40
35
30
RIGHT ASCENSION (J2000)

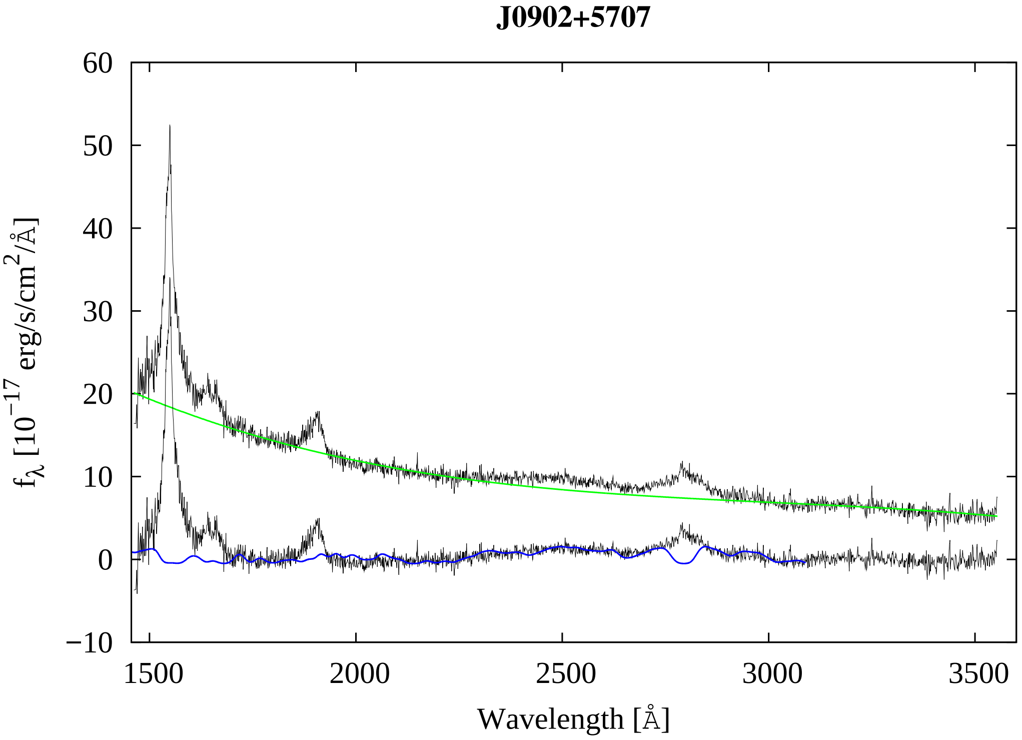
J0902+5707
60
50
40
30
20
10
0
−10
fλ [10−17 erg/s/cm2/Å]
1500
2000
2500
3000
3500
Wavelength [Å]

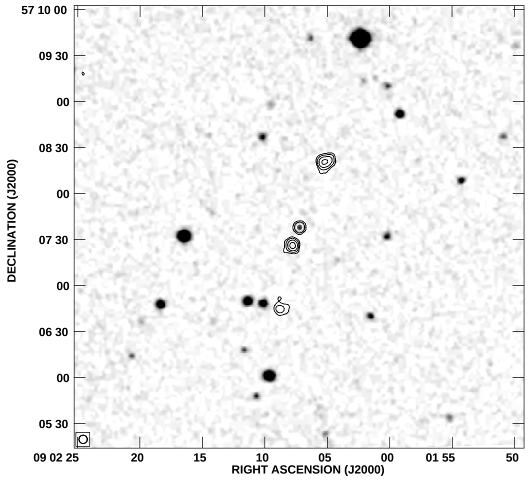
57 10 00
09 30
00
08 30
00
07 30
00
06 30
00
05 30
DECLINATION (J2000)
09 02 25
20
15
10
05
00
01 55
50
RIGHT ASCENSION (J2000)

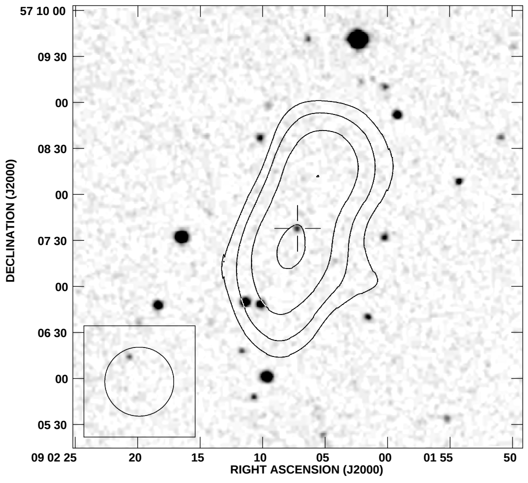
57 10 00
09 30
00
08 30
00
07 30
00
06 30
00
05 30
DECLINATION (J2000)
09 02 25
20
15
10
05
00
01 55
50
RIGHT ASCENSION (J2000)

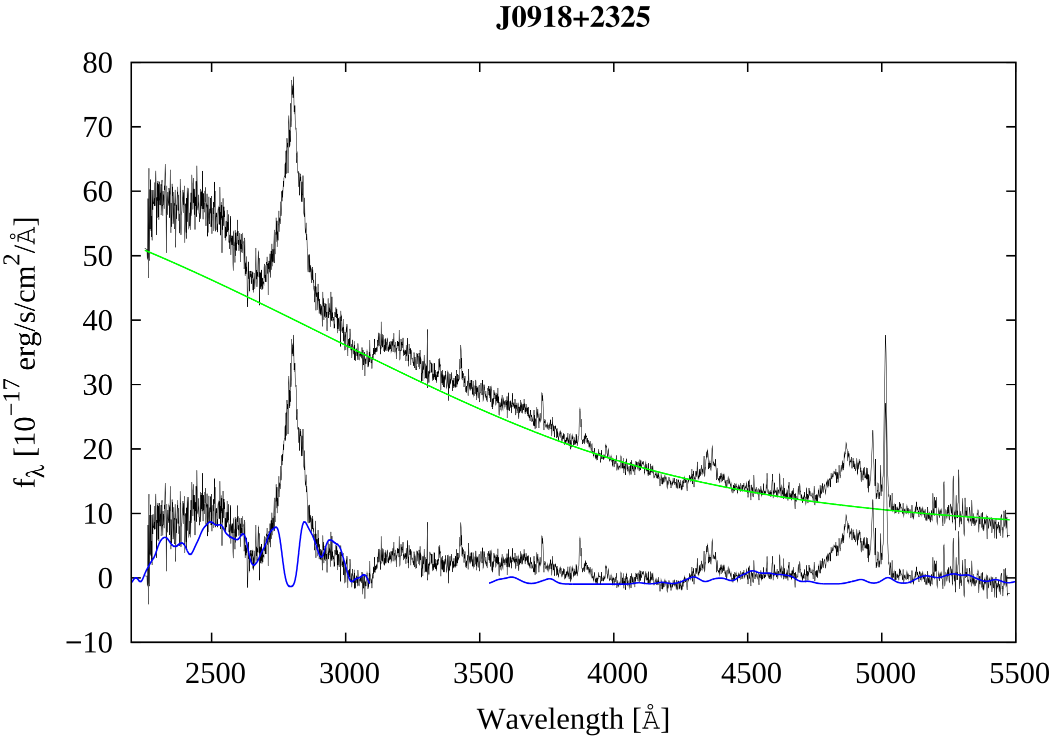
J0918+2325
80
70
60
50
40
30
20
10
0
−10
f_λ [10^{-17} erg/s/cm^2/Å]
2500
3000
3500
4000
4500
5000
5500
Wavelength [Å]

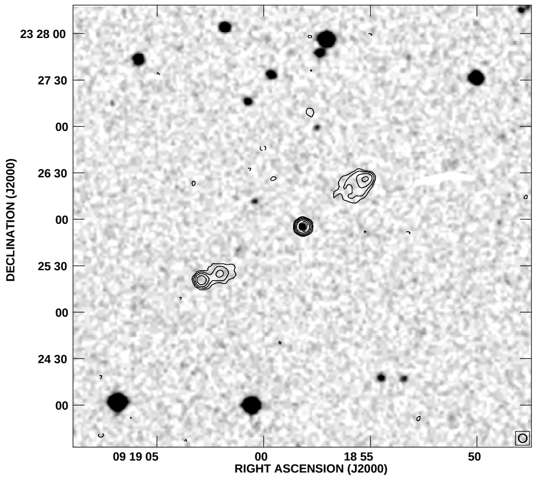
23 28 00
27 30
00
26 30
00
25 30
00
24 30
00
DECLINATION (J2000)
09 19 05
00
18 55
50
RIGHT ASCENSION (J2000)

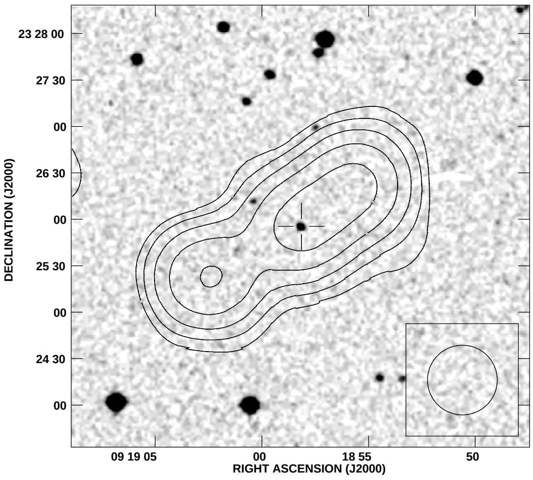
23 28 00
27 30
00
26 30
00
25 30
00
24 30
00
DECLINATION (J2000)
09 19 05
00
18 55
50
RIGHT ASCENSION (J2000)

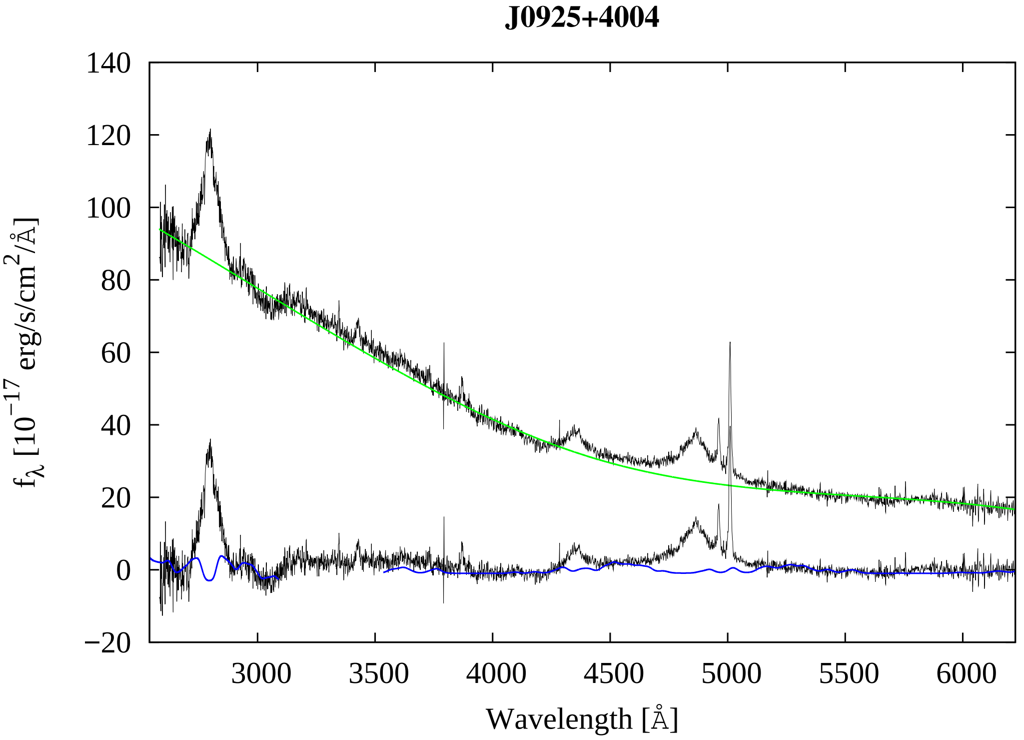
J0925+4004
140
120
100
80
60
40
20
0
−20
f_λ [10^{-17} erg/s/cm^2/Å]
3000
3500
4000
4500
5000
5500
6000
Wavelength [Å]

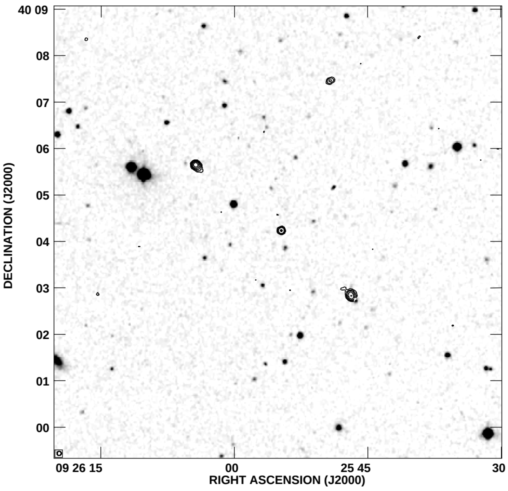
40 09
08
07
06
05
04
03
02
01
00
DECLINATION (J2000)
09 26 15
00
25 45
30
RIGHT ASCENSION (J2000)

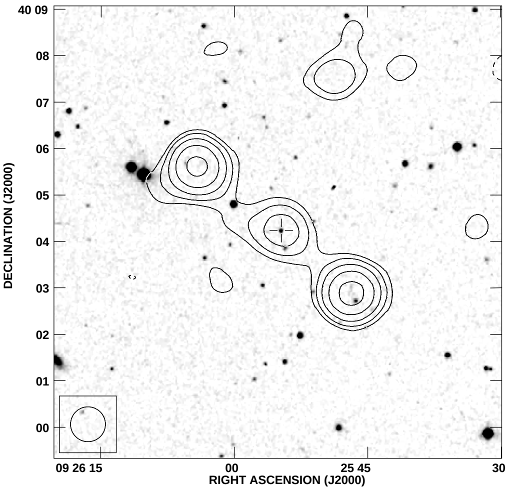
40 09
08
07
06
05
04
03
02
01
00
DECLINATION (J2000)
09 26 15
00
25 45
30
RIGHT ASCENSION (J2000)

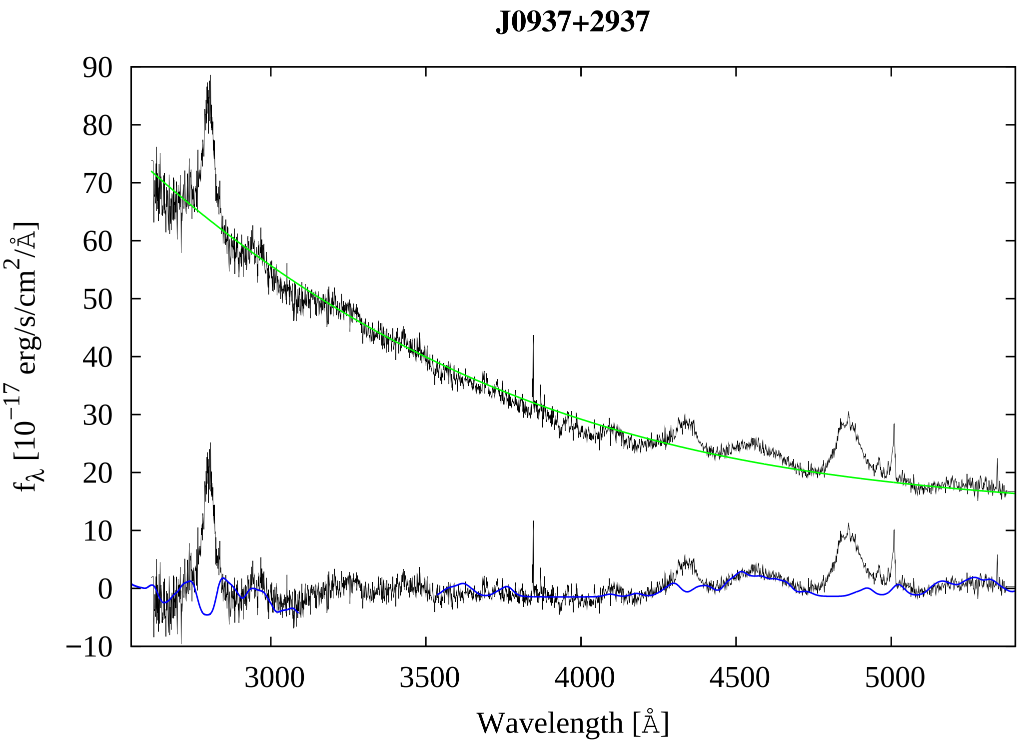
J0937+2937
90
80
70
60
50
40
30
20
10
0
−10
$f_\lambda\ [10^{-17}\ \mathrm{erg/s/cm^2/Å}]$
3000
3500
4000
4500
5000
Wavelength [Å]

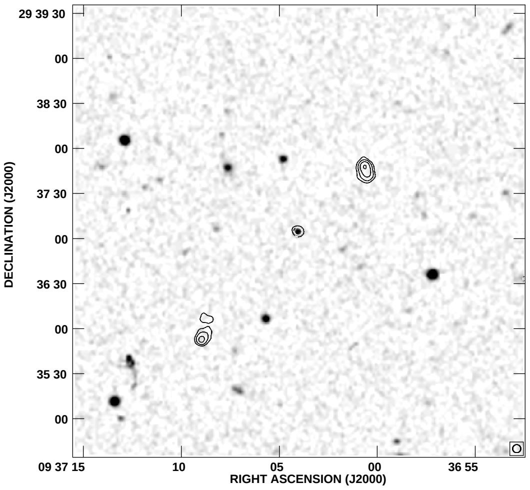
29 39 30
00
38 30
00
37 30
00
36 30
00
35 30
00
DECLINATION (J2000)
09 37 15
10
05
00
36 55
RIGHT ASCENSION (J2000)

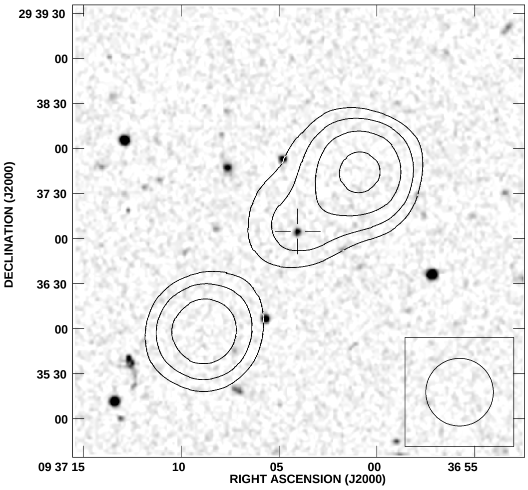
29 39 30
00
38 30
00
37 30
00
36 30
00
35 30
00
DECLINATION (J2000)
09 37 15
10
05
00
36 55
RIGHT ASCENSION (J2000)

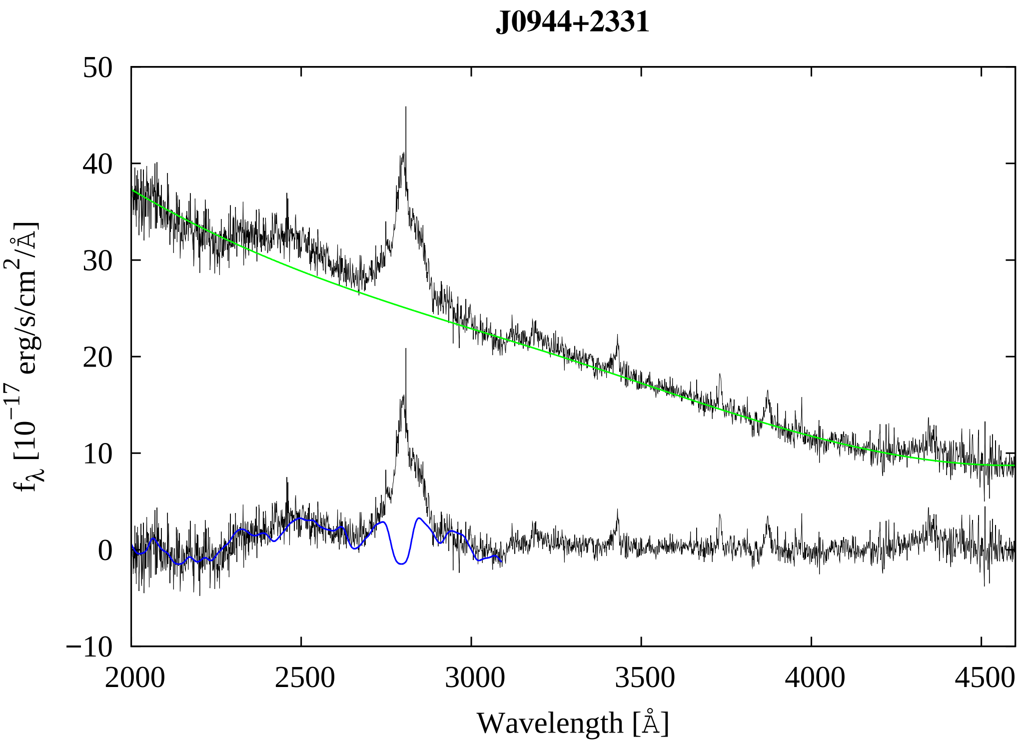
J0944+2331
50
40
30
20
10
0
−10
f_λ [10^{-17} erg/s/cm^2/Å]
2000
2500
3000
3500
4000
4500
Wavelength [Å]

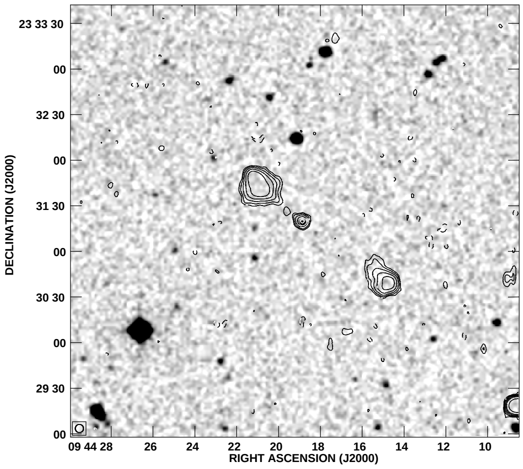
23 33 30
00
32 30
00
31 30
00
30 30
00
29 30
00
DECLINATION (J2000)
09 44 28
26
24
22
20
18
16
14
12
10
RIGHT ASCENSION (J2000)

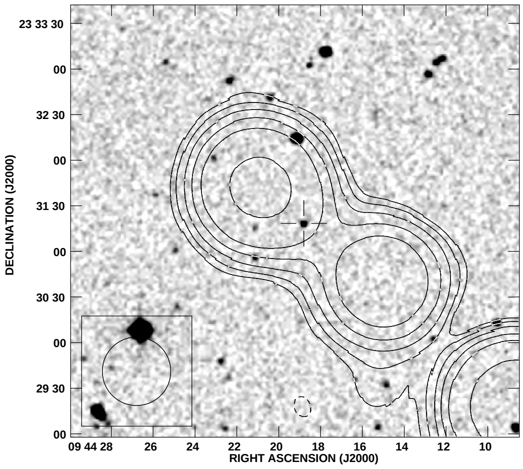
23 33 30
00
32 30
00
31 30
00
30 30
00
29 30
00
DECLINATION (J2000)
09 44 28
26
24
22
20
18
16
14
12
10
RIGHT ASCENSION (J2000)

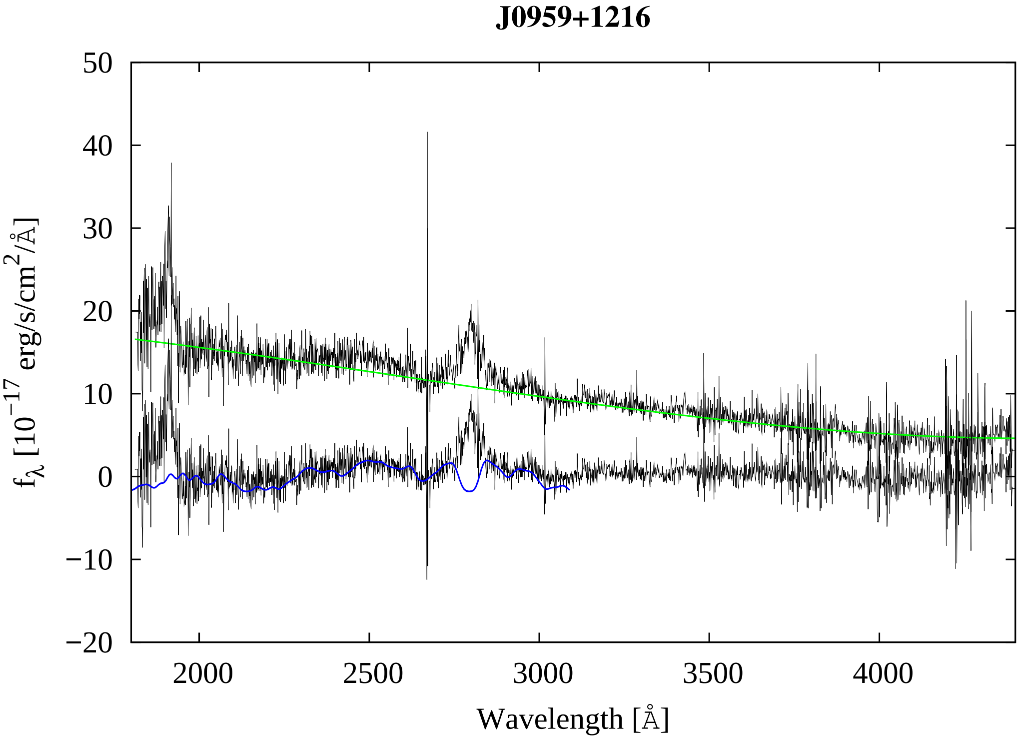
J0959+1216
f_λ [10^−17 erg/s/cm^2/Å]
50
40
30
20
10
0
−10
−20
2000
2500
3000
3500
4000
Wavelength [Å]

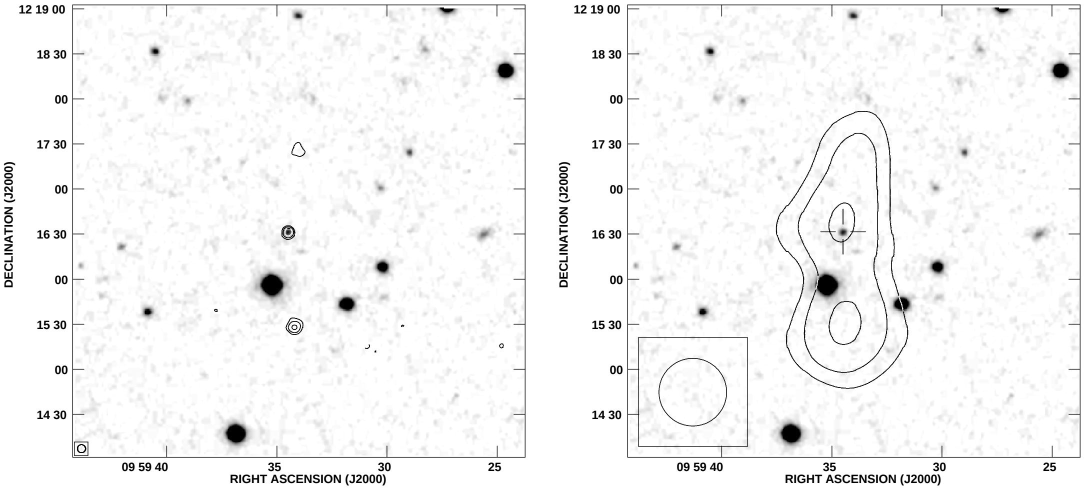
12 19 00
18 30
00
17 30
00
16 30
00
15 30
00
14 30
DECLINATION (J2000)
09 59 40
35
30
25
RIGHT ASCENSION (J2000)
12 19 00
18 30
00
17 30
00
16 30
00
15 30
00
14 30
DECLINATION (J2000)
09 59 40
35
30
25
RIGHT ASCENSION (J2000)

1012+4229

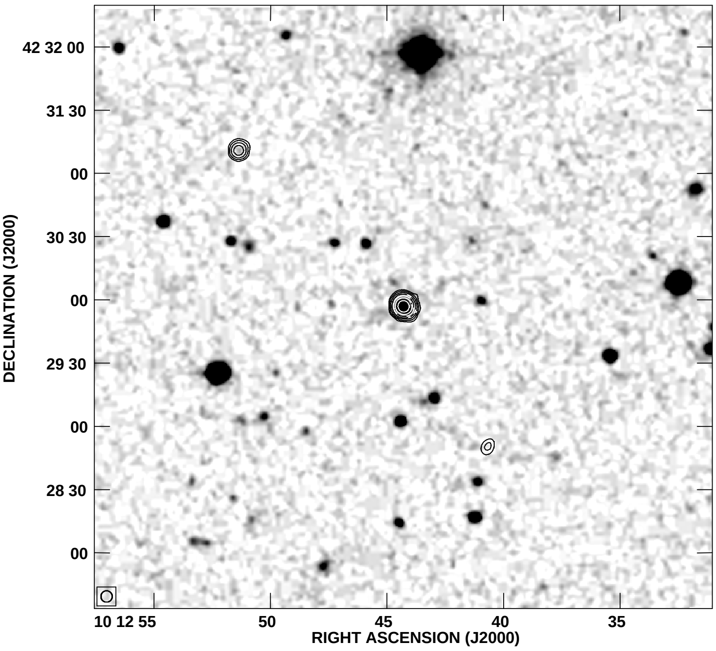
42 32 00
31 30
00
30 30
00
29 30
00
28 30
00
DECLINATION (J2000)
10 12 55
50
45
40
35
RIGHT ASCENSION (J2000)

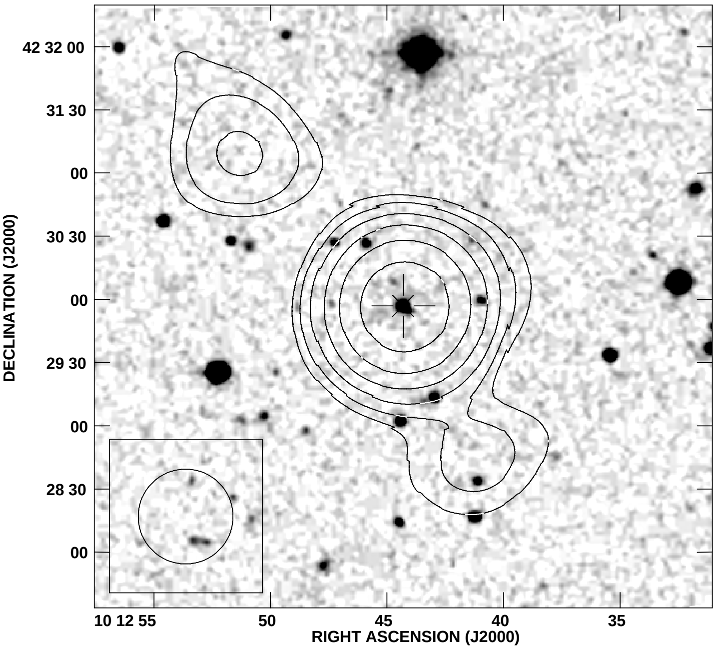
42 32 00
31 30
00
30 30
00
29 30
00
28 30
00
DECLINATION (J2000)
10 12 55
50
45
40
35
RIGHT ASCENSION (J2000)

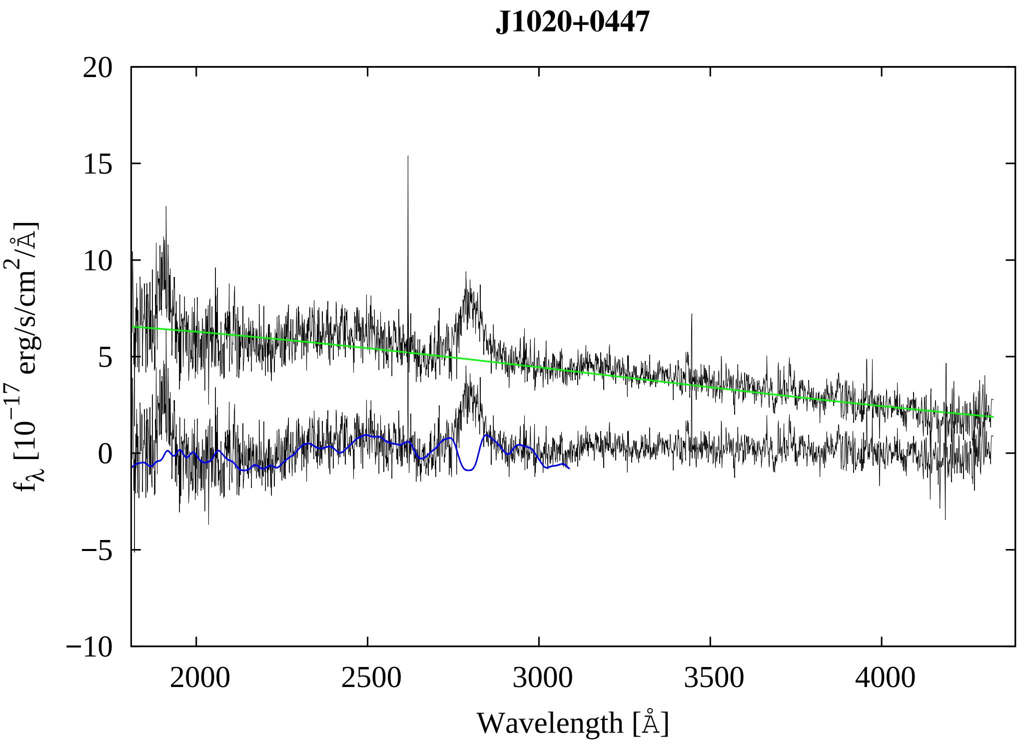
J1020+0447
f_λ [10^{-17} erg/s/cm^2/Å]
20
15
10
5
0
−5
−10
2000
2500
3000
3500
4000
Wavelength [Å]

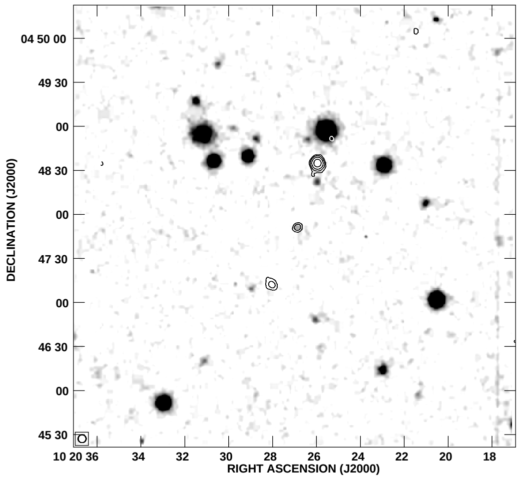
DECLINATION (J2000)
04 50 00
49 30
00
48 30
00
47 30
00
46 30
00
45 30
RIGHT ASCENSION (J2000)
10 20 36
34
32
30
28
26
24
22
20
18

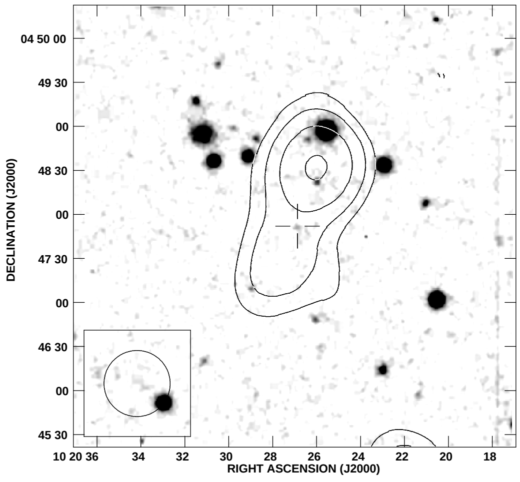
DECLINATION (J2000)
04 50 00
49 30
00
48 30
00
47 30
00
46 30
00
45 30
RIGHT ASCENSION (J2000)
10 20 36
34
32
30
28
26
24
22
20
18

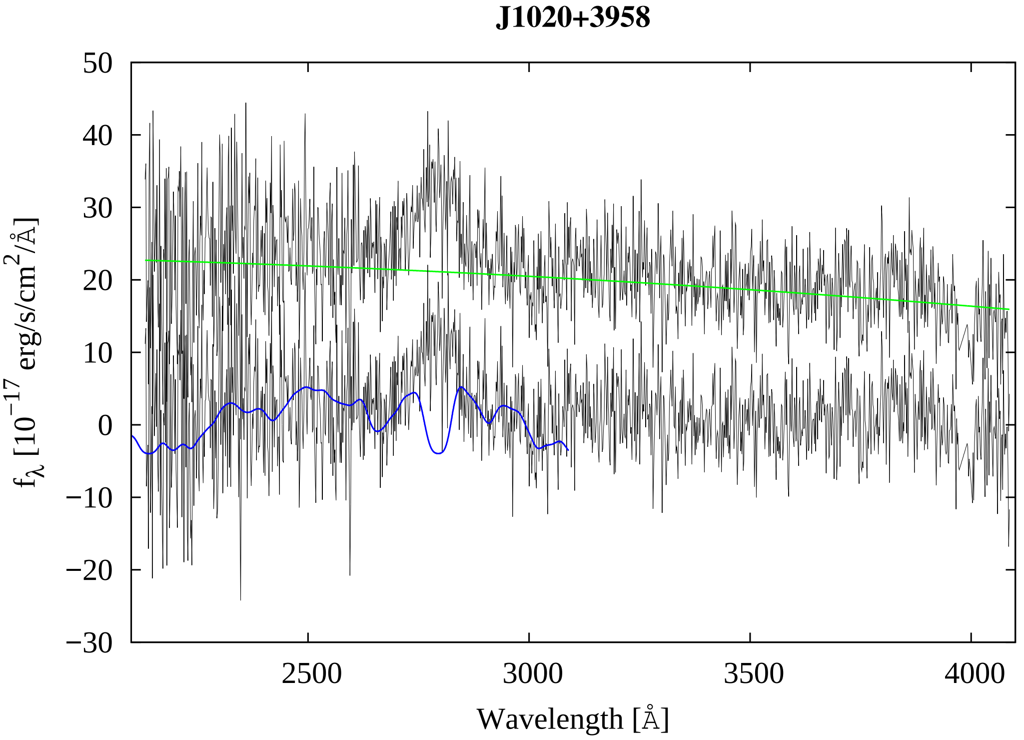
J1020+3958
50
40
30
20
10
0
−10
−20
−30
f$_\lambda$ [10^{-17} erg/s/cm^2/Å]
2500
3000
3500
4000
Wavelength [Å]

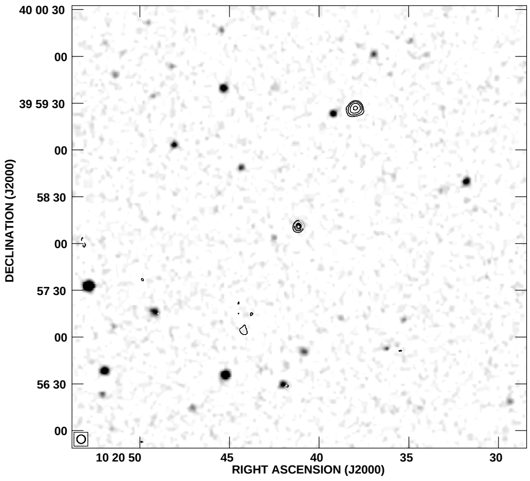
40 00 30
00
39 59 30
00
58 30
00
57 30
00
56 30
00
DECLINATION (J2000)
10 20 50
45
40
35
30
RIGHT ASCENSION (J2000)

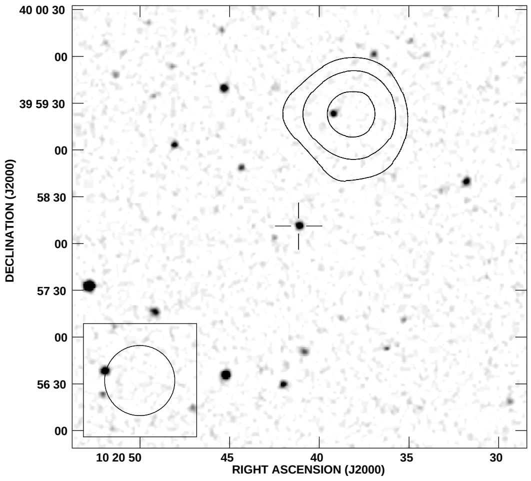
40 00 30
00
39 59 30
00
58 30
00
57 30
00
56 30
00
DECLINATION (J2000)
10 20 50
45
40
35
30
RIGHT ASCENSION (J2000)

J1027-2312

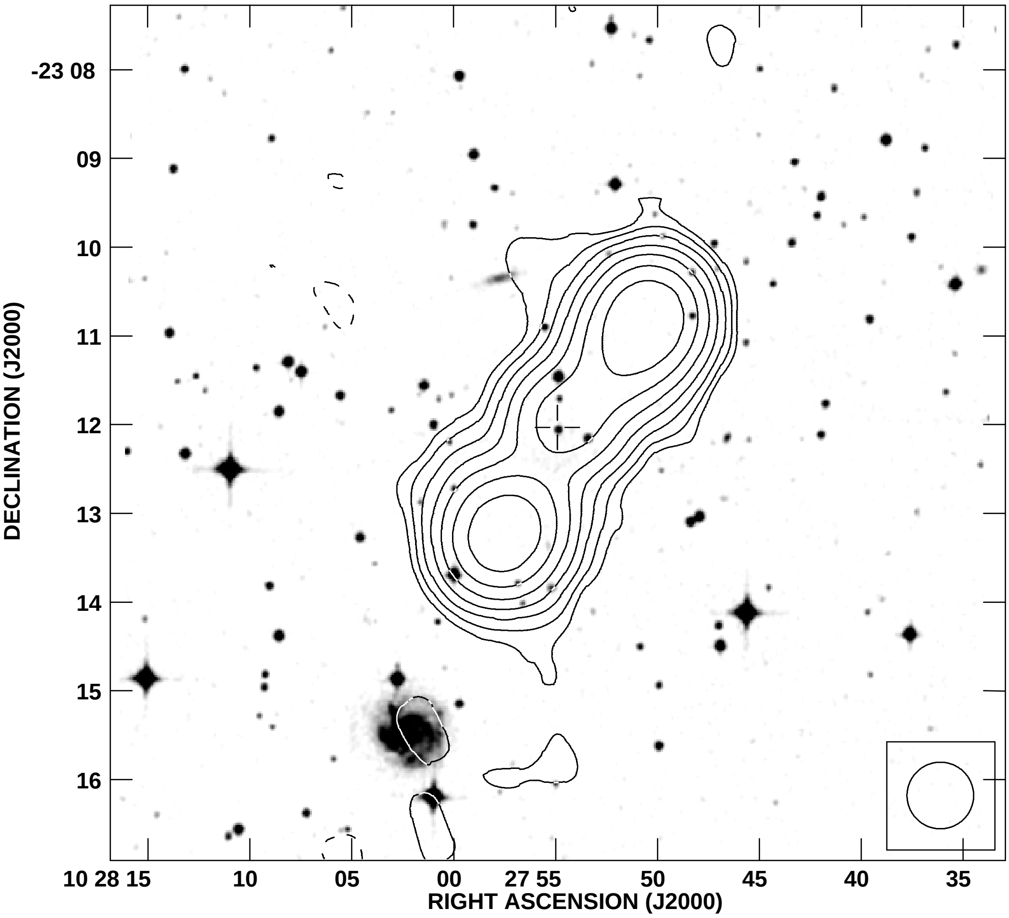
DECLINATION (J2000)
-23 08
09
10
11
12
13
14
15
16
10 28 15
10
05
00
27 55
50
45
40
35
RIGHT ASCENSION (J2000)

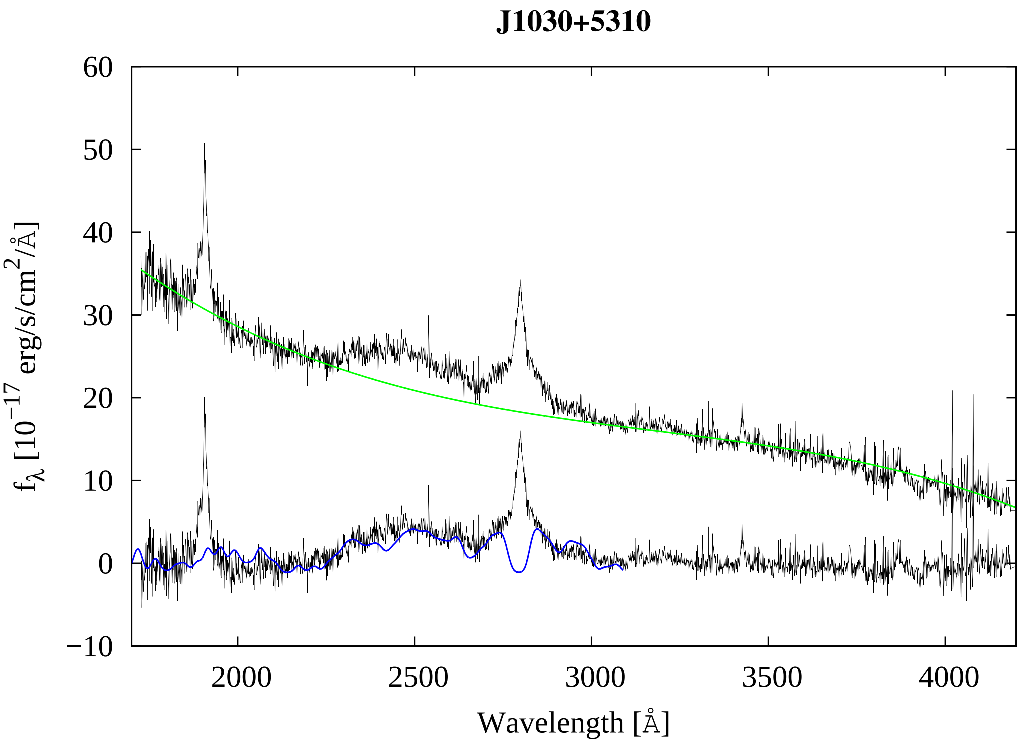
J1030+5310
f_λ [10^{-17} erg/s/cm^2/Å]
60
50
40
30
20
10
0
−10
2000
2500
3000
3500
4000
Wavelength [Å]

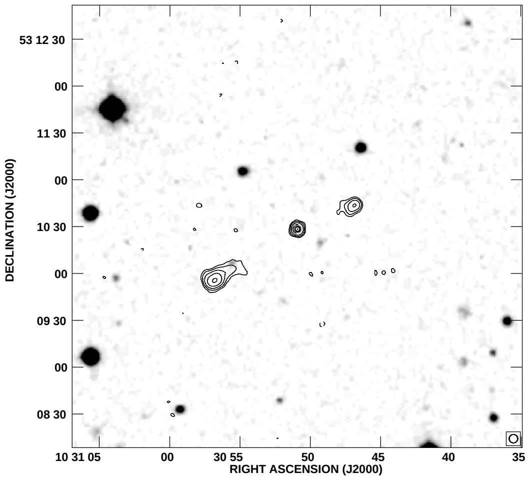
DECLINATION (J2000)
53 12 30
00
11 30
00
10 30
00
09 30
00
08 30
10 31 05
00
30 55
50
45
40
35
RIGHT ASCENSION (J2000)

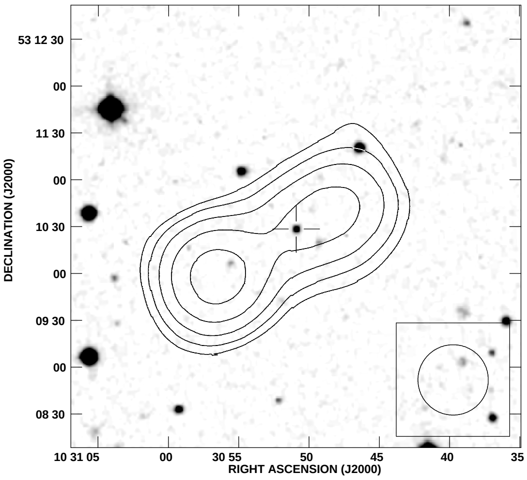
DECLINATION (J2000)
53 12 30
00
11 30
00
10 30
00
09 30
00
08 30
10 31 05
00
30 55
50
45
40
35
RIGHT ASCENSION (J2000)

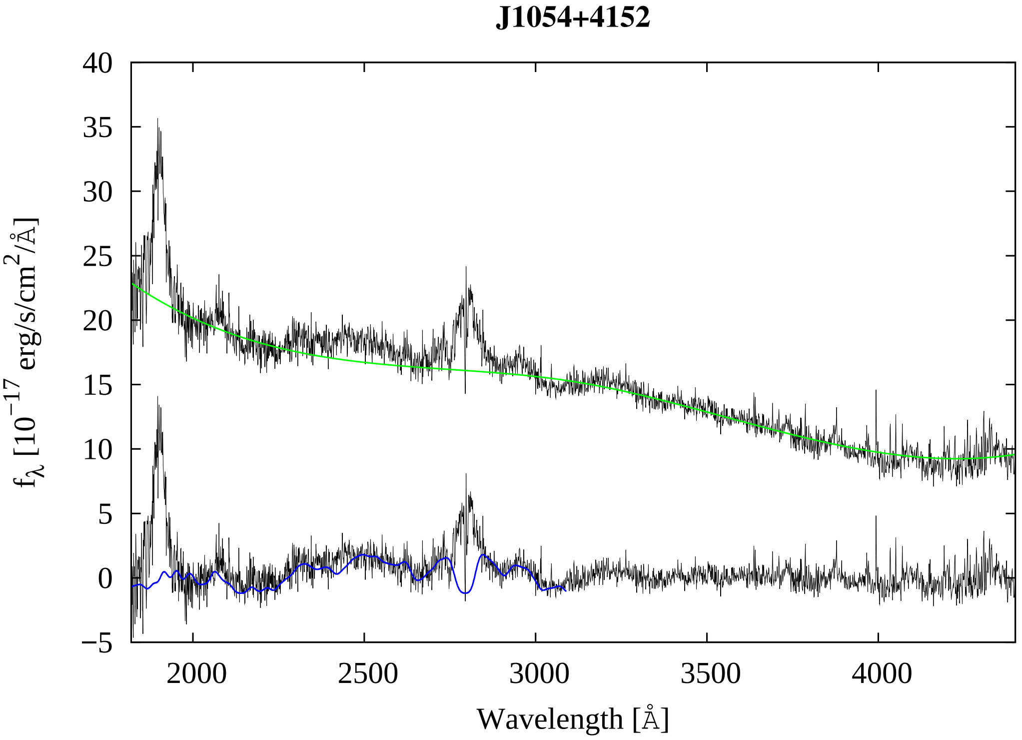
J1054+4152
f_λ [10^{-17} erg/s/cm^2/Å]
40
35
30
25
20
15
10
5
0
−5
2000
2500
3000
3500
4000
Wavelength [Å]

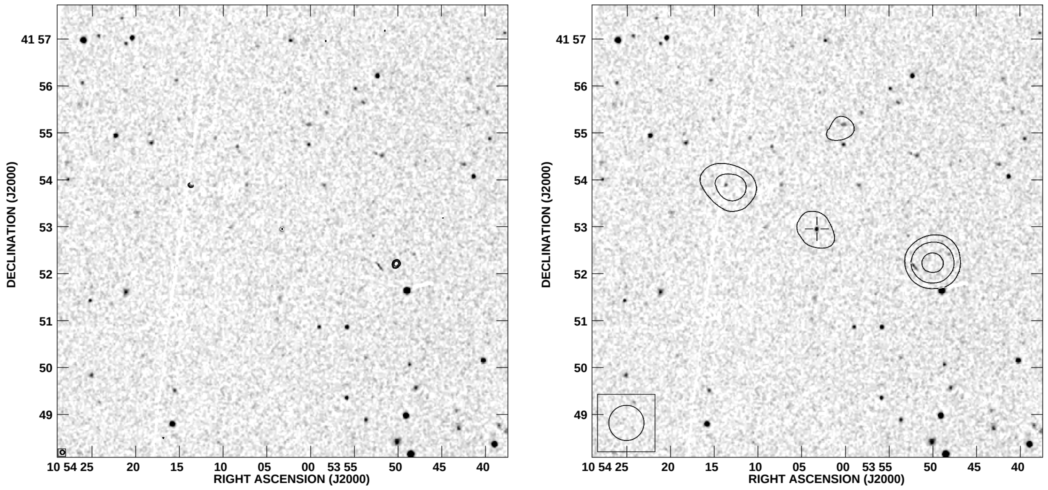
DECLINATION (J2000)
41 57
56
55
54
53
52
51
50
49
10 54 25
20
15
10
05
00
53 55
50
45
40
RIGHT ASCENSION (J2000)

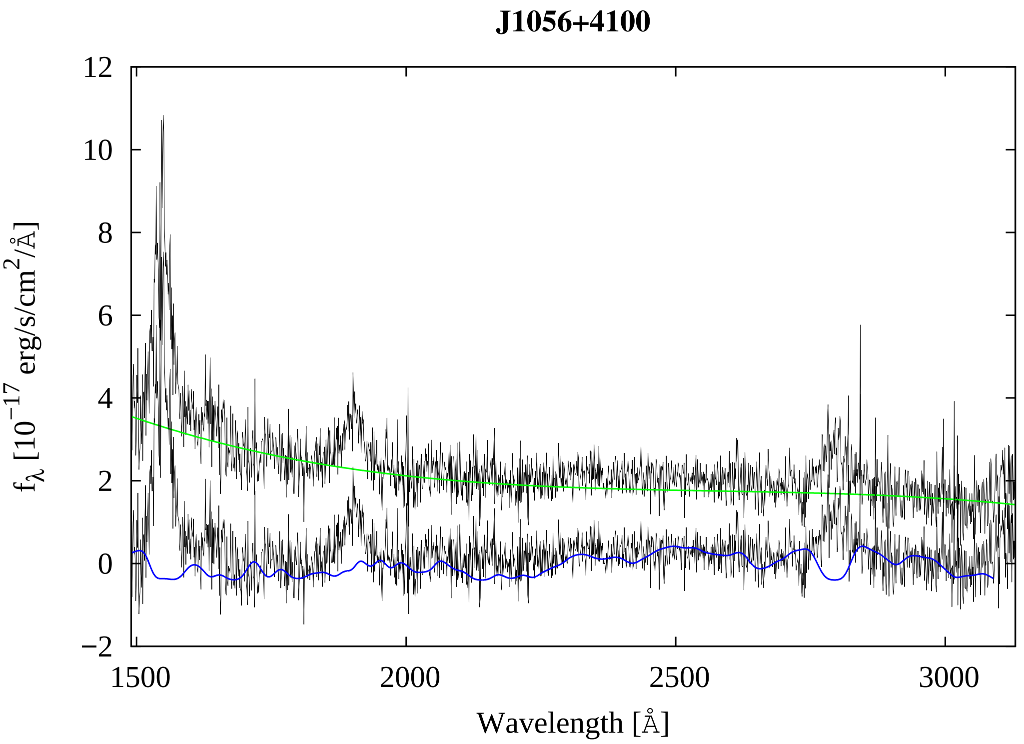
J1056+4100
12
10
8
6
4
2
0
−2
f_λ [10^{-17} erg/s/cm^2/Å]
1500
2000
2500
3000
Wavelength [Å]

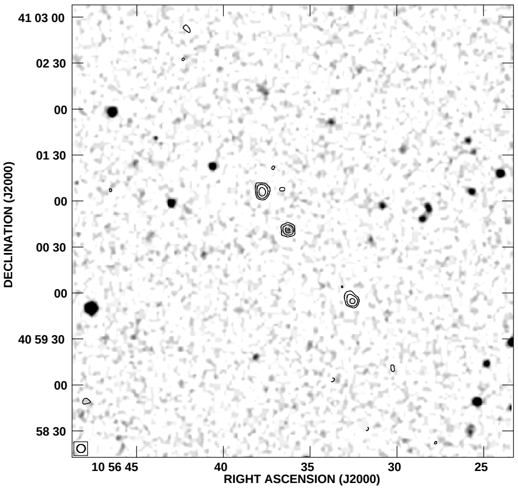
41 03 00
02 30
00
01 30
00
00 30
00
40 59 30
00
58 30
DECLINATION (J2000)
10 56 45
40
35
30
25
RIGHT ASCENSION (J2000)

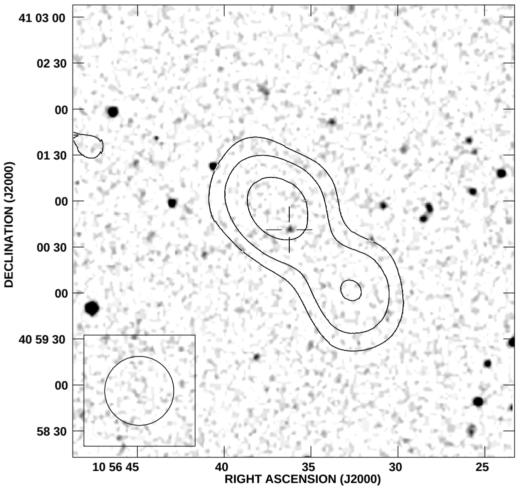
41 03 00
02 30
00
01 30
00
00 30
00
40 59 30
00
58 30
DECLINATION (J2000)
10 56 45
40
35
30
25
RIGHT ASCENSION (J2000)

J1130-1320

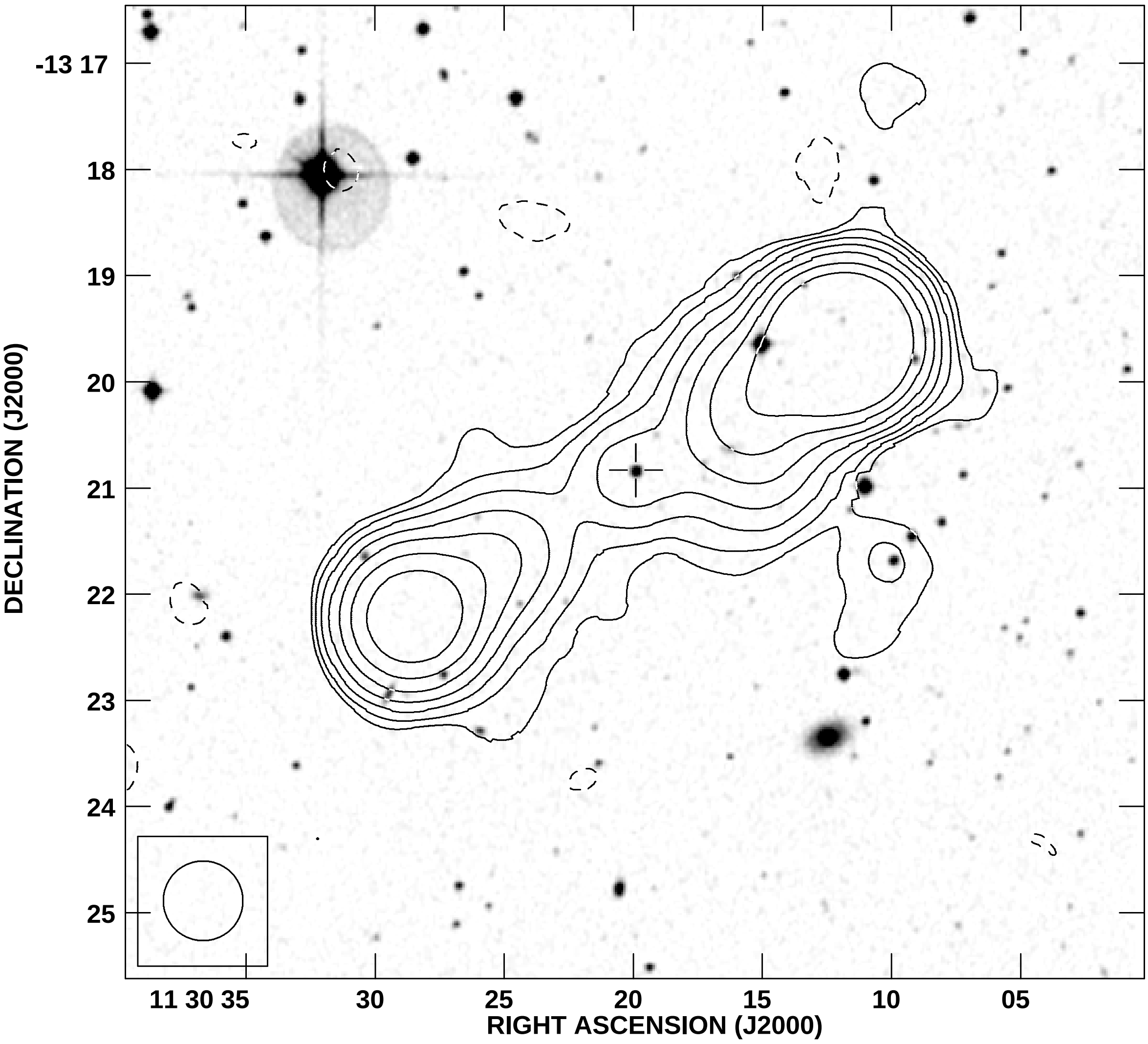
-13 17
18
19
20
21
22
23
24
25
DECLINATION (J2000)
11 30 35
30
25
20
15
10
05
RIGHT ASCENSION (J2000)

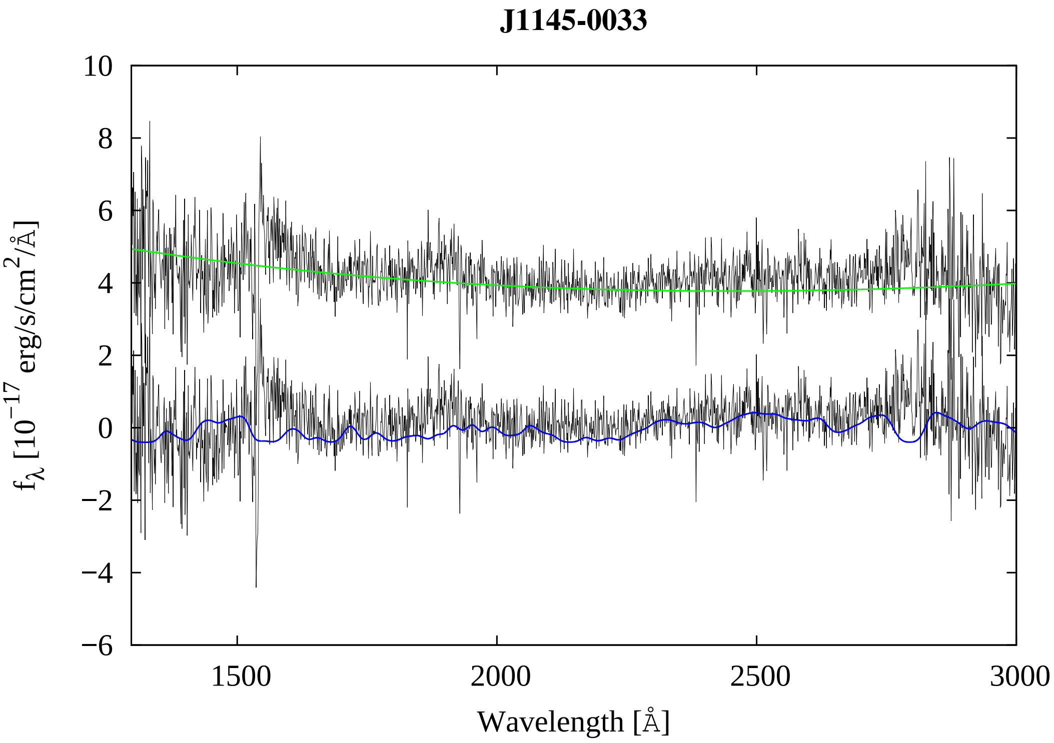
J1145-0033
f_λ [10^{-17} erg/s/cm^2/Å]
10
8
6
4
2
0
−2
−4
−6
1500
2000
2500
3000
Wavelength [Å]

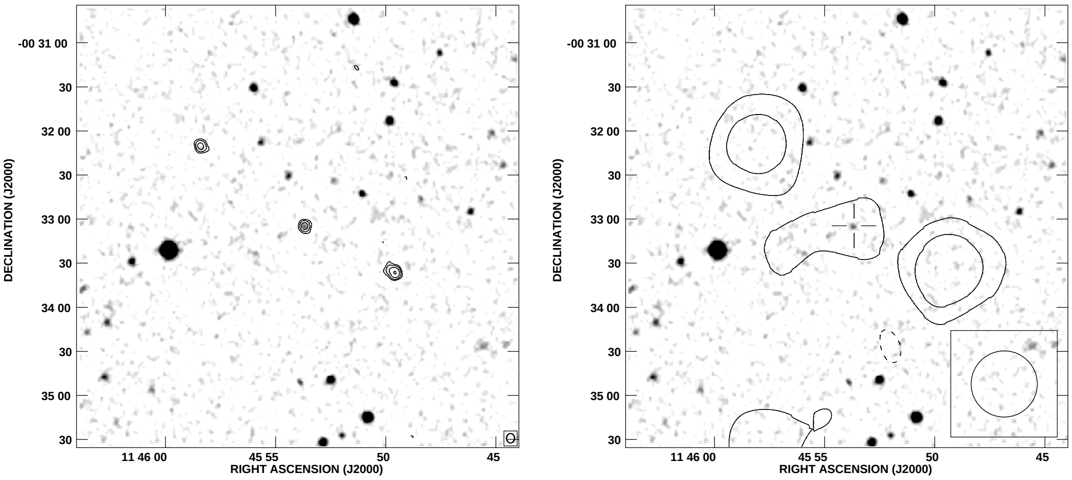
DECLINATION (J2000)
-00 31 00
30
32 00
30
33 00
30
34 00
30
35 00
30
11 46 00
45 55
50
45
RIGHT ASCENSION (J2000)
DECLINATION (J2000)
-00 31 00
30
32 00
30
33 00
30
34 00
30
35 00
30
11 46 00
45 55
50
45
RIGHT ASCENSION (J2000)

J1148-0403

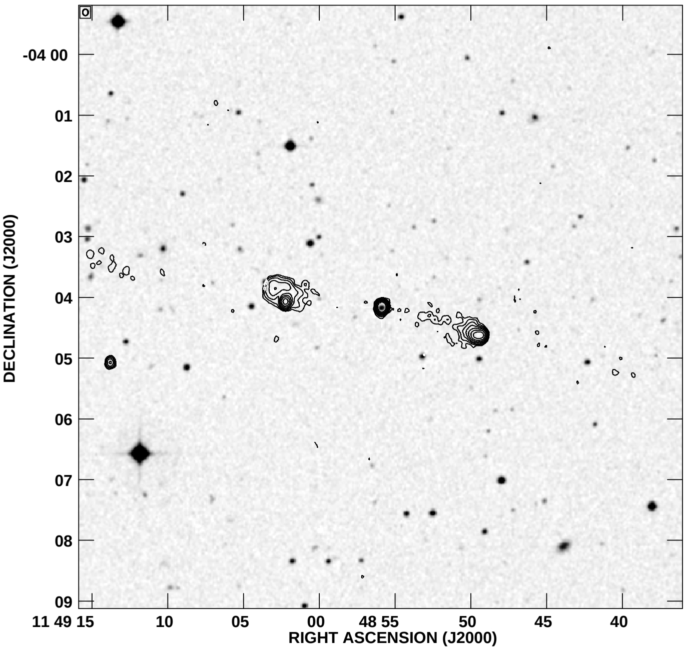
DECLINATION (J2000)
-04 00
01
02
03
04
05
06
07
08
09
11 49 15
10
05
00
48 55
50
45
40
RIGHT ASCENSION (J2000)

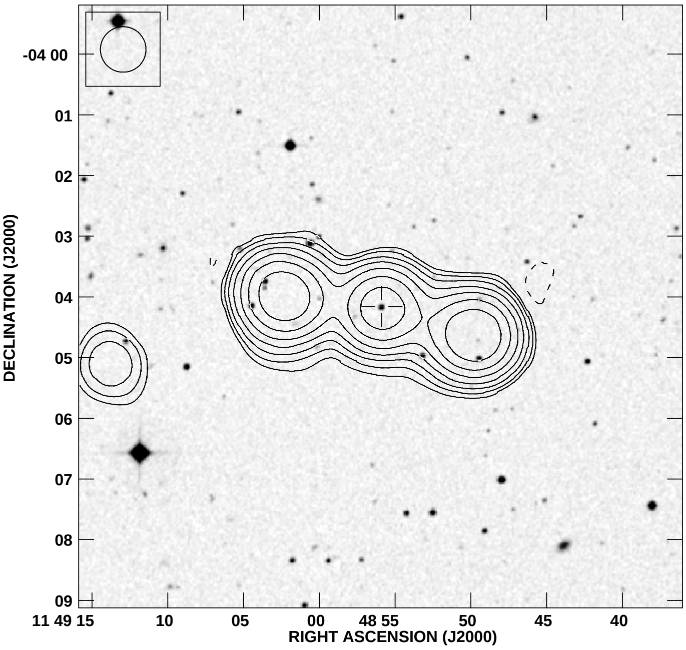
DECLINATION (J2000)
-04 00
01
02
03
04
05
06
07
08
09
11 49 15
10
05
00
48 55
50
45
40
RIGHT ASCENSION (J2000)

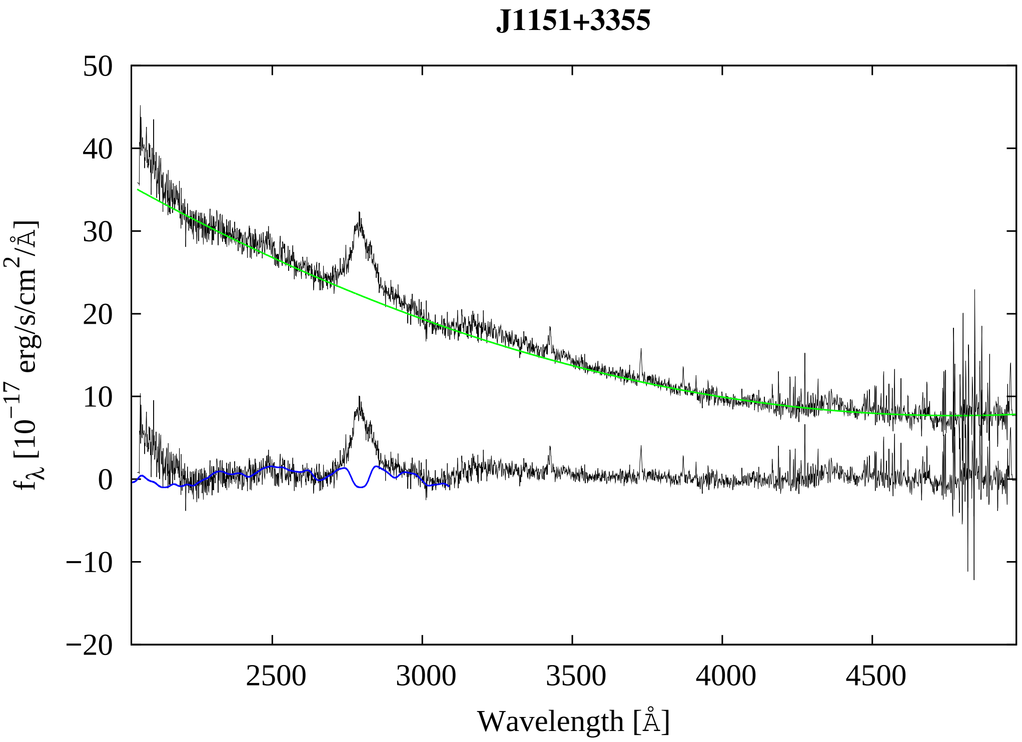
J1151+3355
50
40
30
20
10
0
−10
−20
f_λ [10^{-17} erg/s/cm^2/Å]
2500
3000
3500
4000
4500
Wavelength [Å]

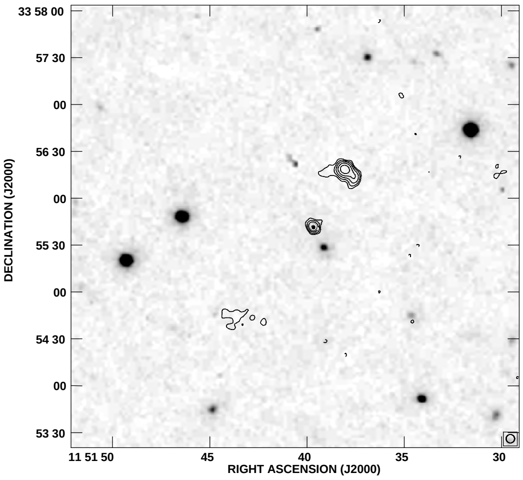
33 58 00
57 30
00
56 30
00
55 30
00
54 30
00
53 30
DECLINATION (J2000)
11 51 50
45
40
35
30
RIGHT ASCENSION (J2000)

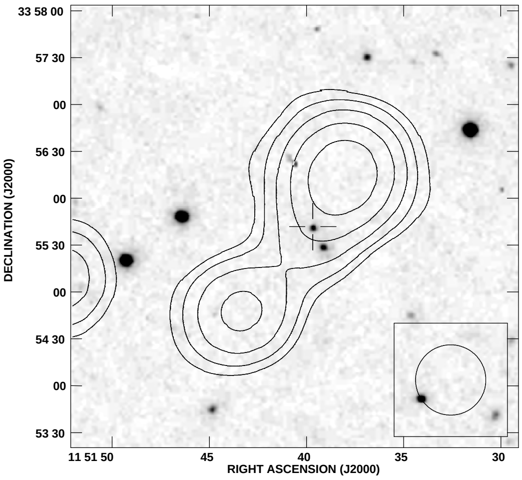
33 58 00
57 30
00
56 30
00
55 30
00
54 30
00
53 30
DECLINATION (J2000)
11 51 50
45
40
35
30
RIGHT ASCENSION (J2000)

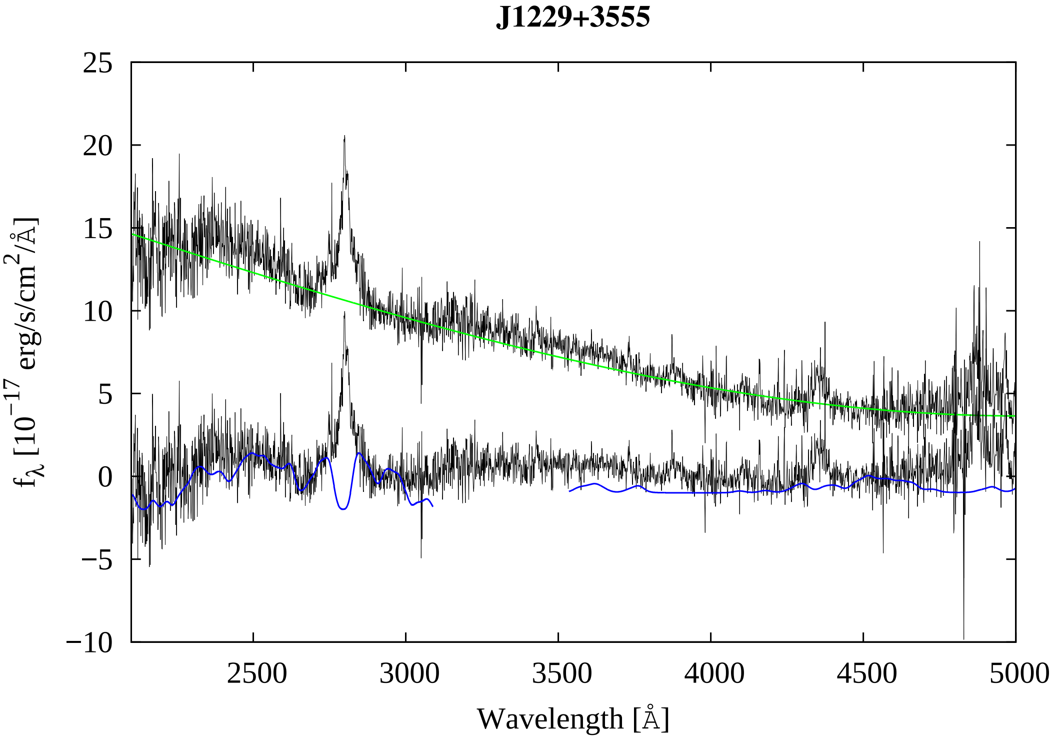
J1229+3555
25
20
15
10
5
0
−5
−10
2500
3000
3500
4000
4500
5000
Wavelength [Å]
f_λ [10^−17 erg/s/cm²/Å]

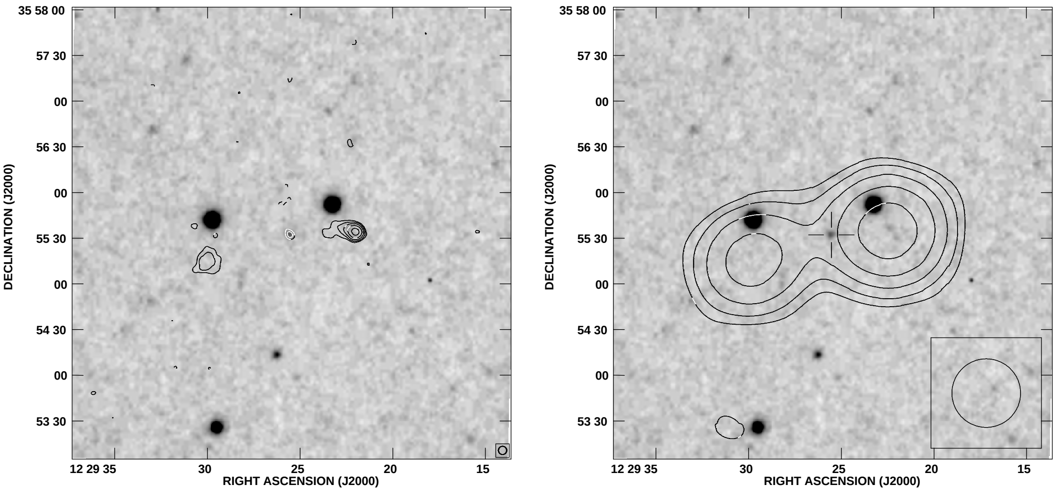
35 58 00
57 30
00
56 30
00
55 30
00
54 30
00
53 30
DECLINATION (J2000)
12 29 35
30
25
20
15
RIGHT ASCENSION (J2000)

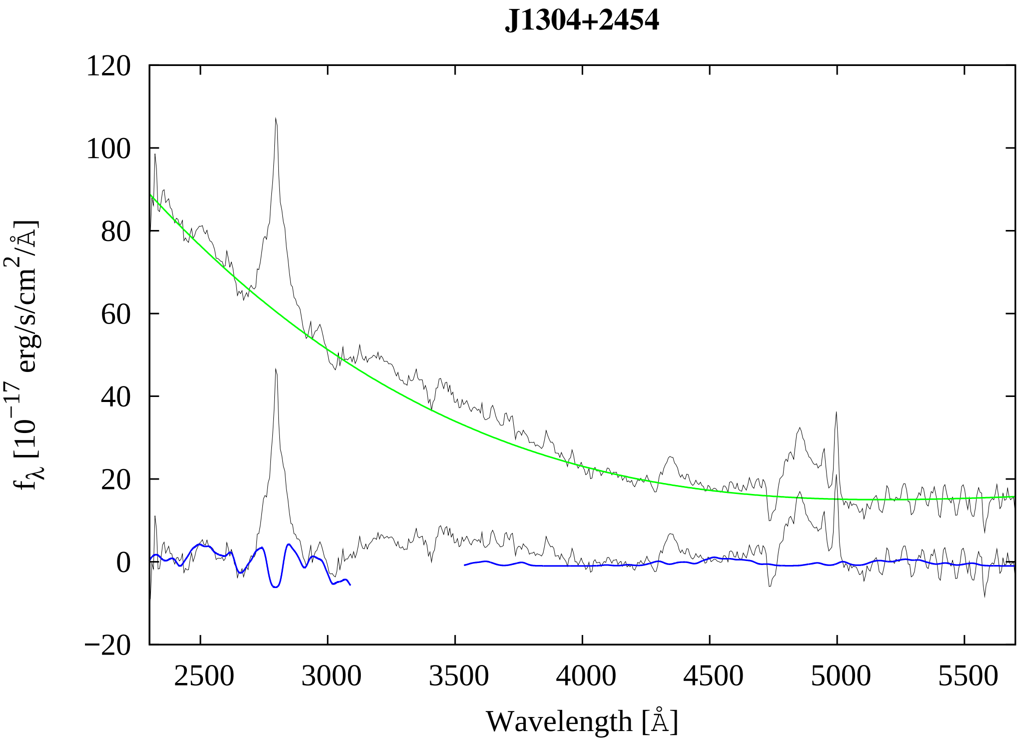
J1304+2454
120
100
80
60
40
20
0
−20
f_λ [10^{-17} erg/s/cm^2/Å]
2500
3000
3500
4000
4500
5000
5500
Wavelength [Å]

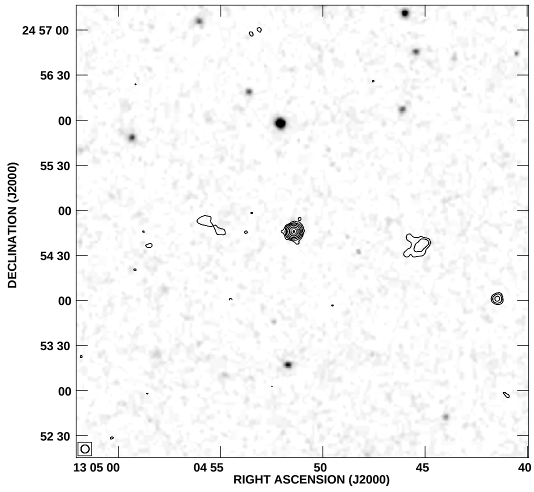
24 57 00
56 30
00
55 30
00
54 30
00
53 30
00
52 30
DECLINATION (J2000)
13 05 00
04 55
50
45
40
RIGHT ASCENSION (J2000)

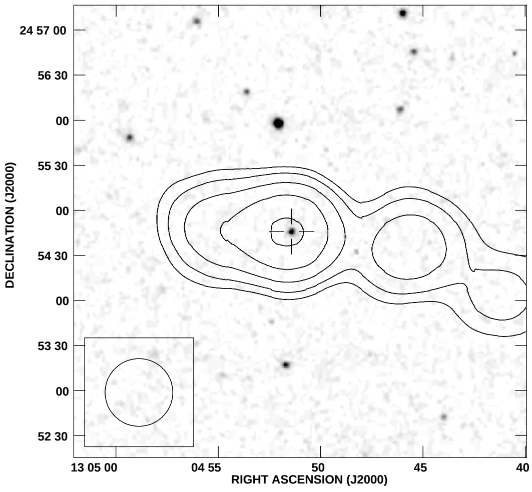
24 57 00
56 30
00
55 30
00
54 30
00
53 30
00
52 30
DECLINATION (J2000)
13 05 00
04 55
50
45
40
RIGHT ASCENSION (J2000)

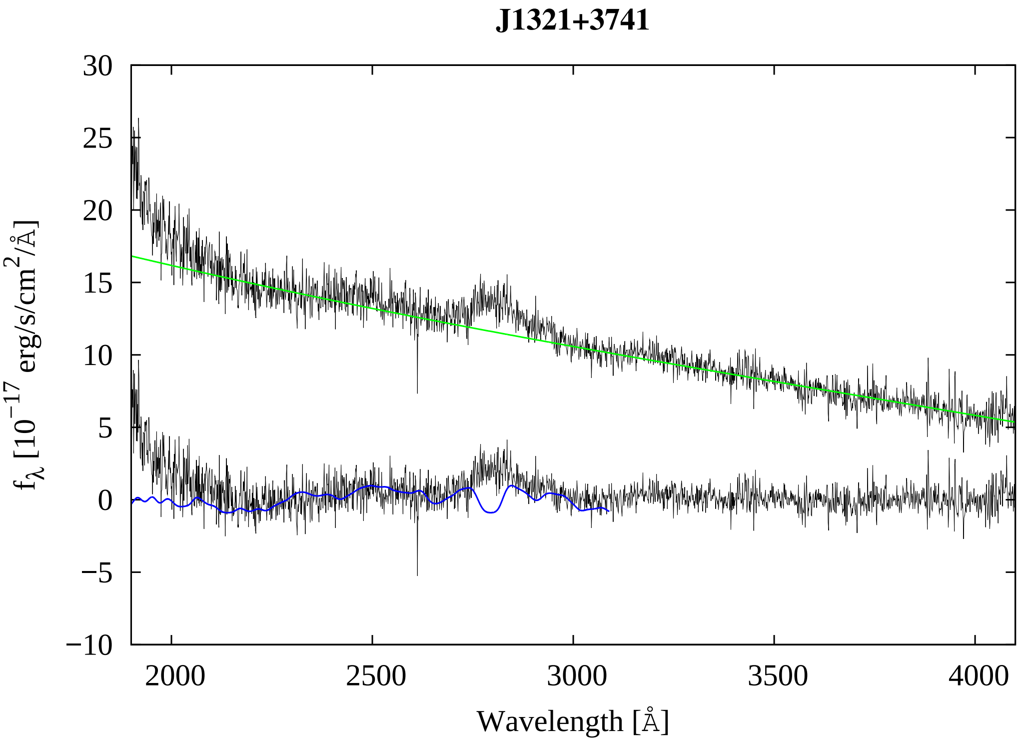
J1321+3741
f_λ [10^{-17} erg/s/cm^2/Å]
30
25
20
15
10
5
0
−5
−10
2000
2500
3000
3500
4000
Wavelength [Å]

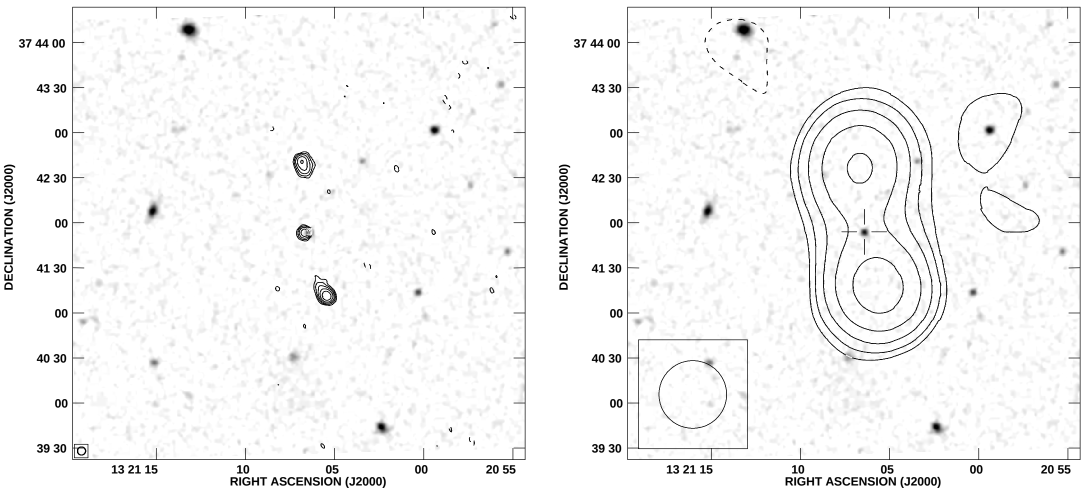
37 44 00
43 30
00
42 30
00
41 30
00
40 30
00
39 30
DECLINATION (J2000)
13 21 15
10
05
00
20 55
RIGHT ASCENSION (J2000)
37 44 00
43 30
00
42 30
00
41 30
00
40 30
00
39 30
DECLINATION (J2000)
13 21 15
10
05
00
20 55
RIGHT ASCENSION (J2000)

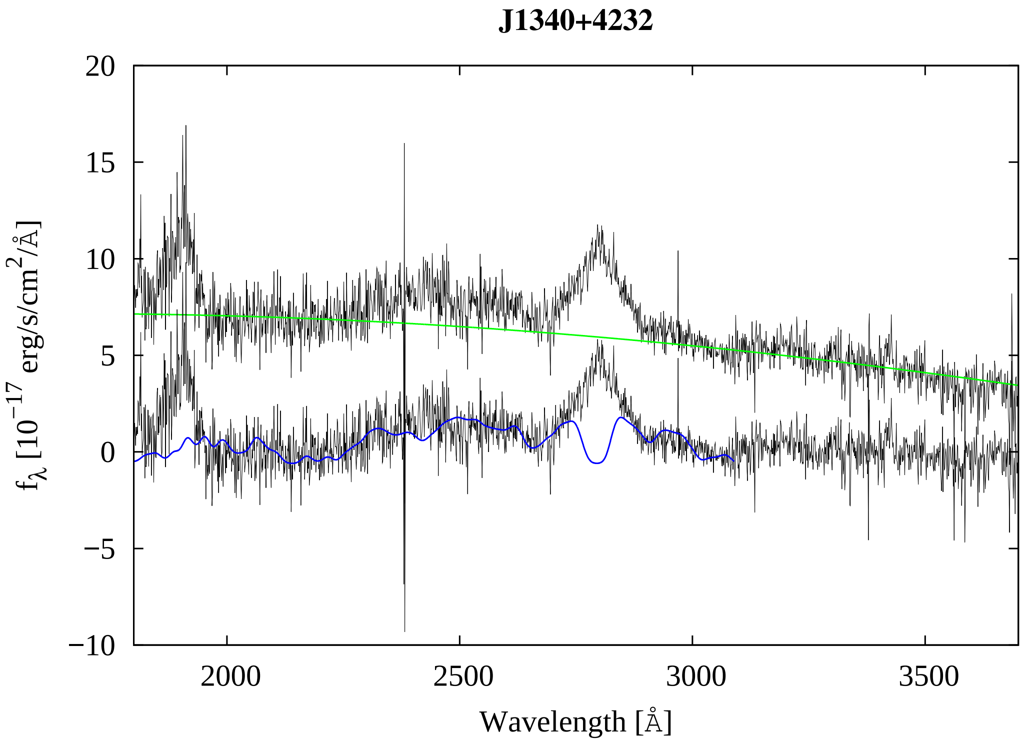
J1340+4232
20
15
10
5
0
−5
−10
f_λ [10^{-17} erg/s/cm^2/Å]
2000
2500
3000
3500
Wavelength [Å]

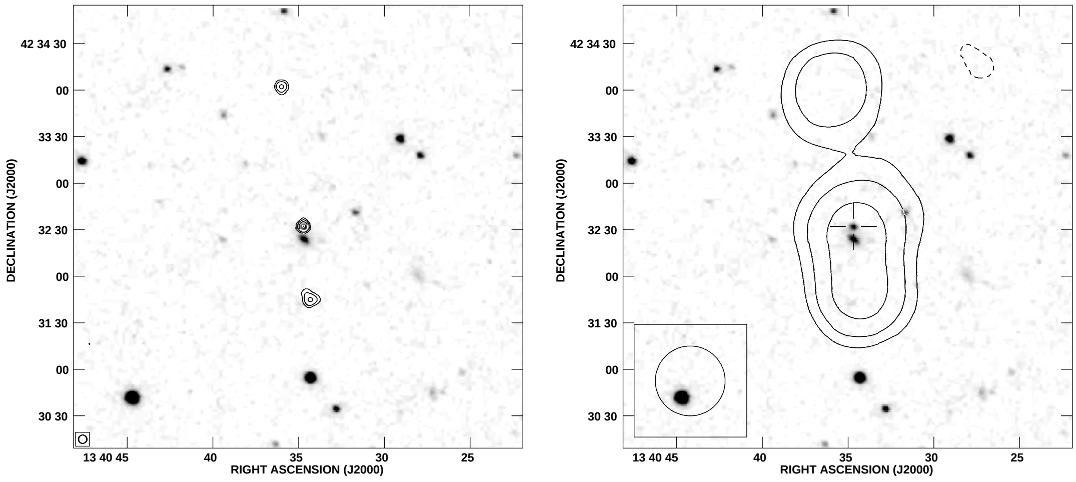
42 34 30
00
33 30
00
32 30
00
31 30
00
30 30
DECLINATION (J2000)
13 40 45
40
35
30
25
RIGHT ASCENSION (J2000)
42 34 30
00
33 30
00
32 30
00
31 30
00
30 30
DECLINATION (J2000)
13 40 45
40
35
30
25
RIGHT ASCENSION (J2000)

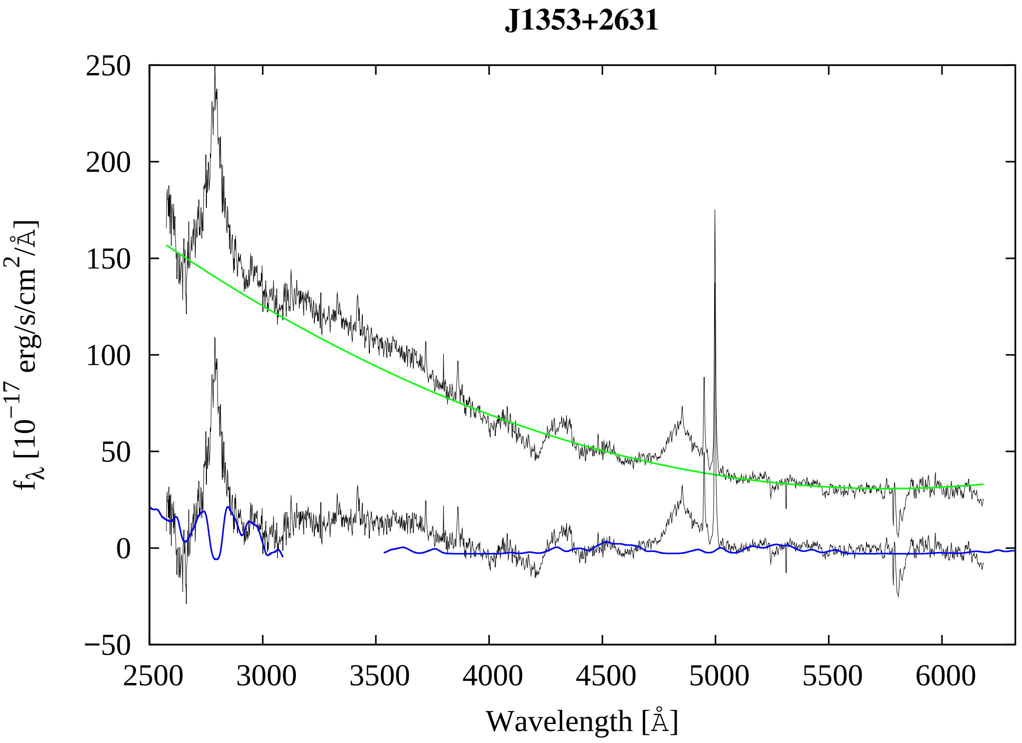
J1353+2631
250
200
150
100
50
0
−50
f_λ [10^{-17} erg/s/cm^2/Å]
2500
3000
3500
4000
4500
5000
5500
6000
Wavelength [Å]

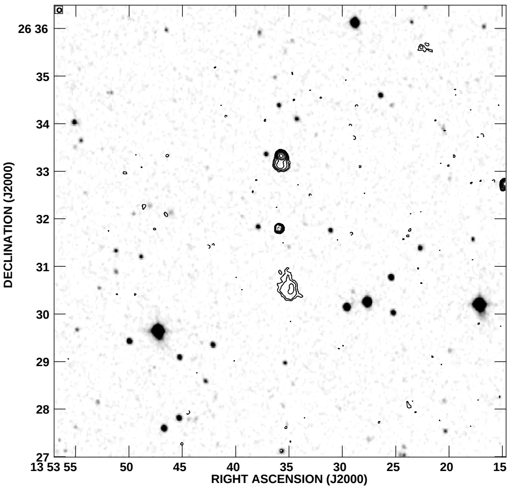
26 36
35
34
33
32
31
30
29
28
27
DECLINATION (J2000)
13 53 55
50
45
40
35
30
25
20
15
RIGHT ASCENSION (J2000)

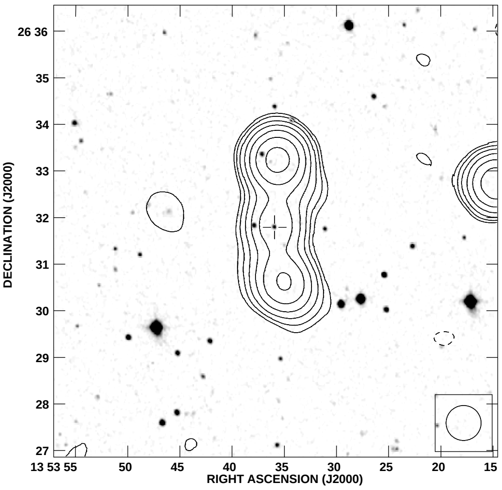
26 36
35
34
33
32
31
30
29
28
27
DECLINATION (J2000)
13 53 55
50
45
40
35
30
25
20
15
RIGHT ASCENSION (J2000)

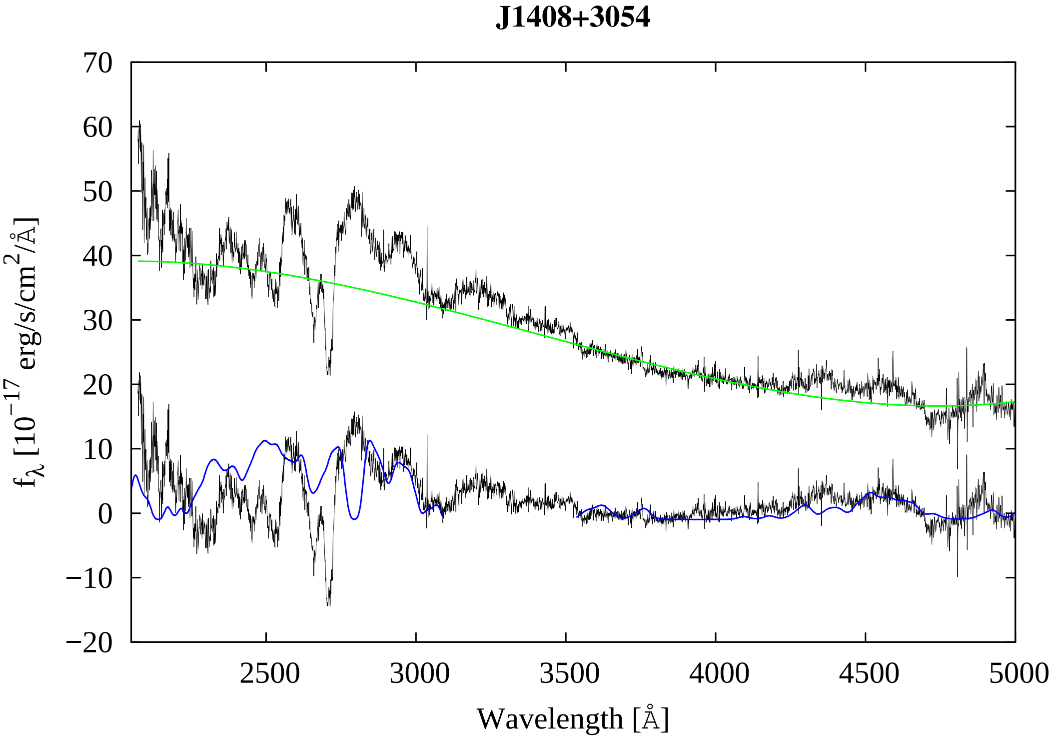
J1408+3054
f_λ [10^{-17} erg/s/cm^2/Å]
70
60
50
40
30
20
10
0
−10
−20
2500
3000
3500
4000
4500
5000
Wavelength [Å]

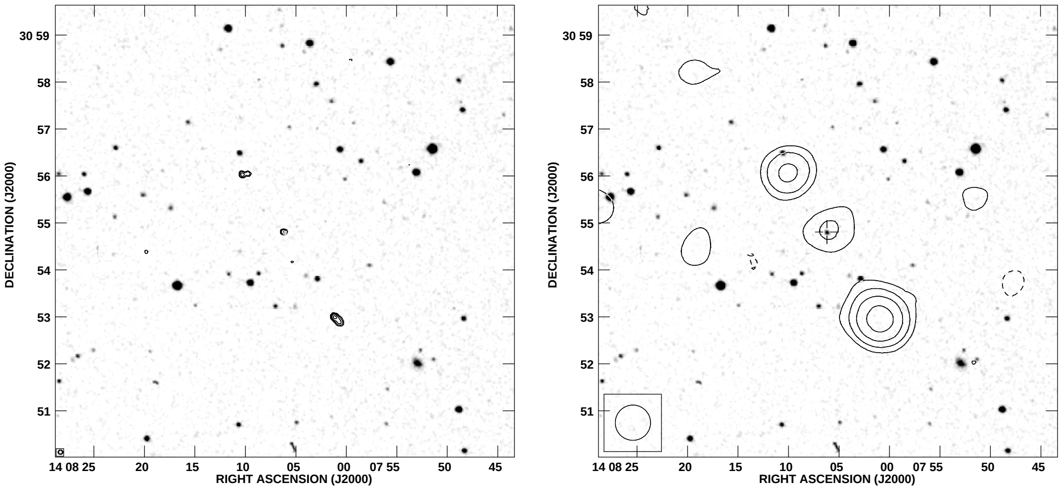
30 59
58
57
56
55
54
53
52
51
DECLINATION (J2000)
14 08 25
20
15
10
05
00
07 55
50
45
RIGHT ASCENSION (J2000)
30 59
58
57
56
55
54
53
52
51
DECLINATION (J2000)
14 08 25
20
15
10
05
00
07 55
50
45
RIGHT ASCENSION (J2000)

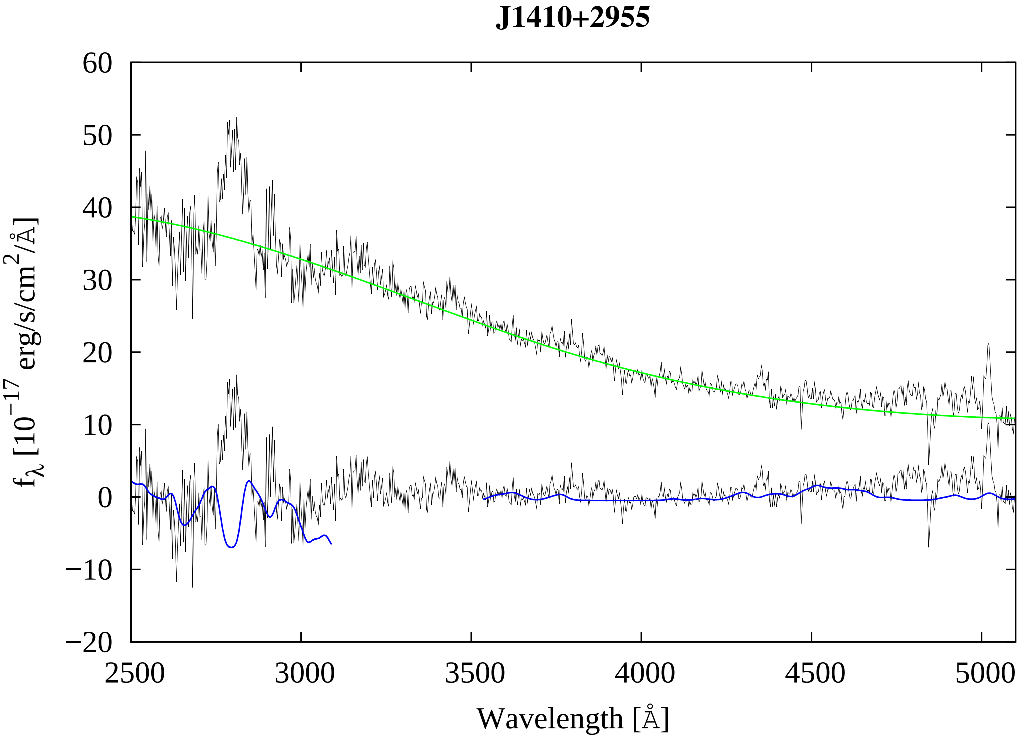
J1410+2955
60
50
40
30
20
10
0
−10
−20
f_λ [10^{-17} erg/s/cm^2/Å]
2500
3000
3500
4000
4500
5000
Wavelength [Å]

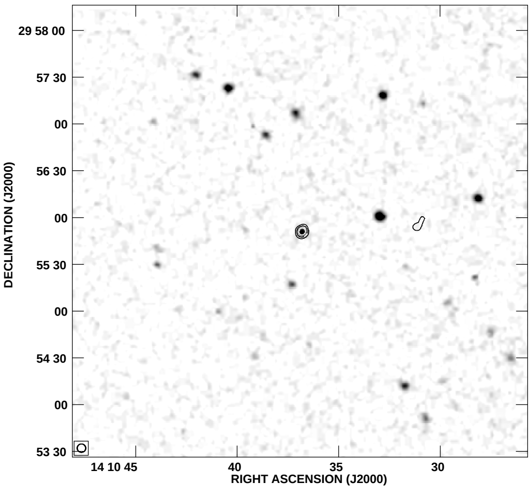
29 58 00
57 30
00
56 30
00
55 30
00
54 30
00
53 30
DECLINATION (J2000)
14 10 45
40
35
30
RIGHT ASCENSION (J2000)

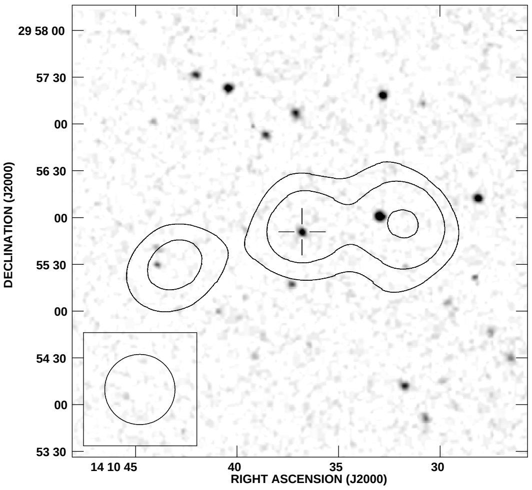
29 58 00
57 30
00
56 30
00
55 30
00
54 30
00
53 30
DECLINATION (J2000)
14 10 45
40
35
30
RIGHT ASCENSION (J2000)

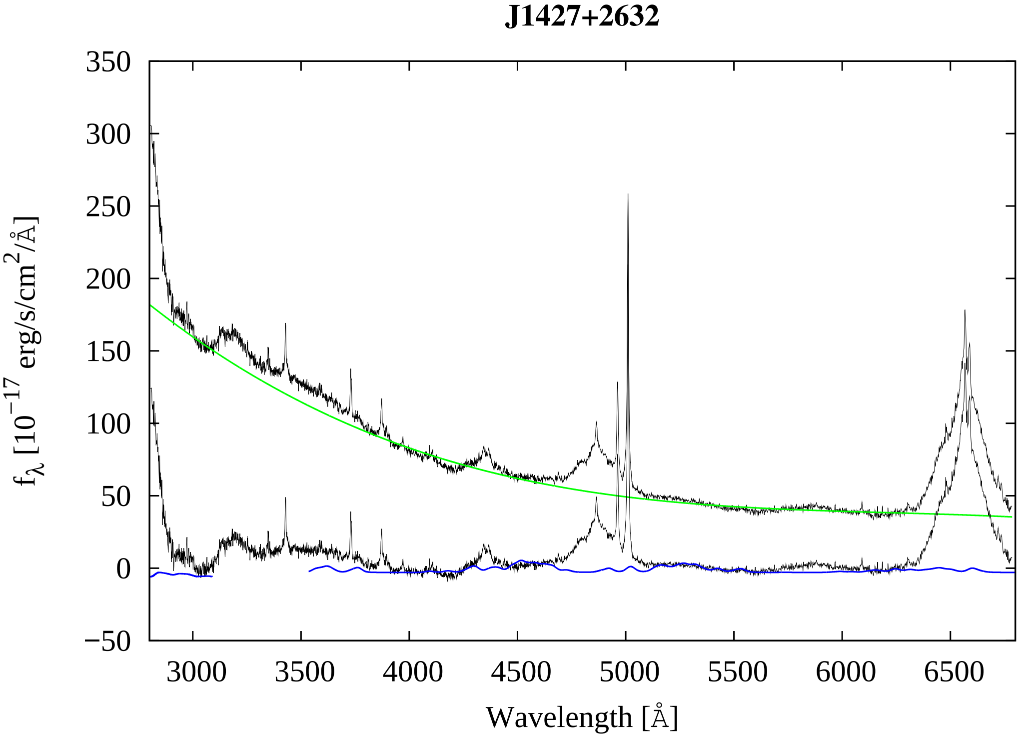
J1427+2632
f_λ [10^{-17} erg/s/cm^2/Å]
350
300
250
200
150
100
50
0
−50
3000
3500
4000
4500
5000
5500
6000
6500
Wavelength [Å]

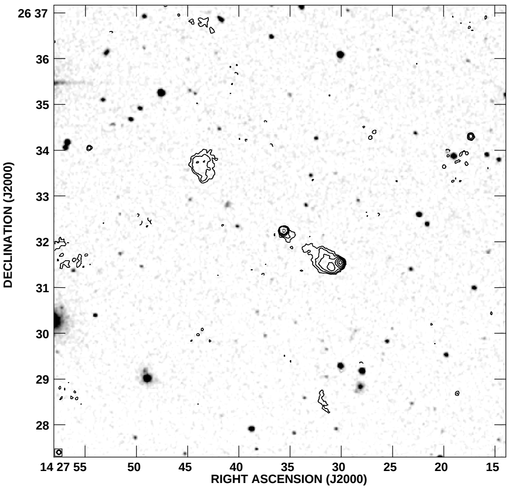
26 37
36
35
34
33
32
31
30
29
28
DECLINATION (J2000)
14 27 55
50
45
40
35
30
25
20
15
RIGHT ASCENSION (J2000)

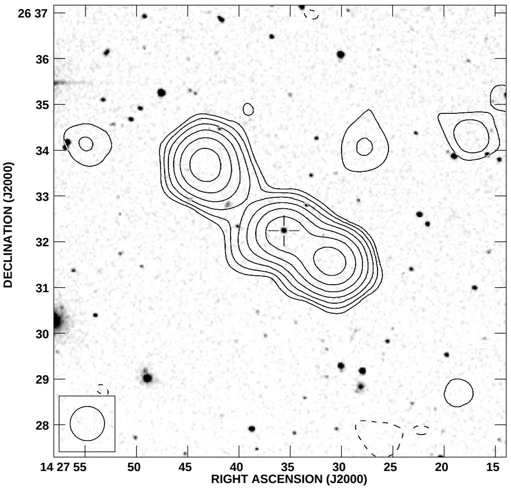
26 37
36
35
34
33
32
31
30
29
28
DECLINATION (J2000)
14 27 55
50
45
40
35
30
25
20
15
RIGHT ASCENSION (J2000)

J1432+1548

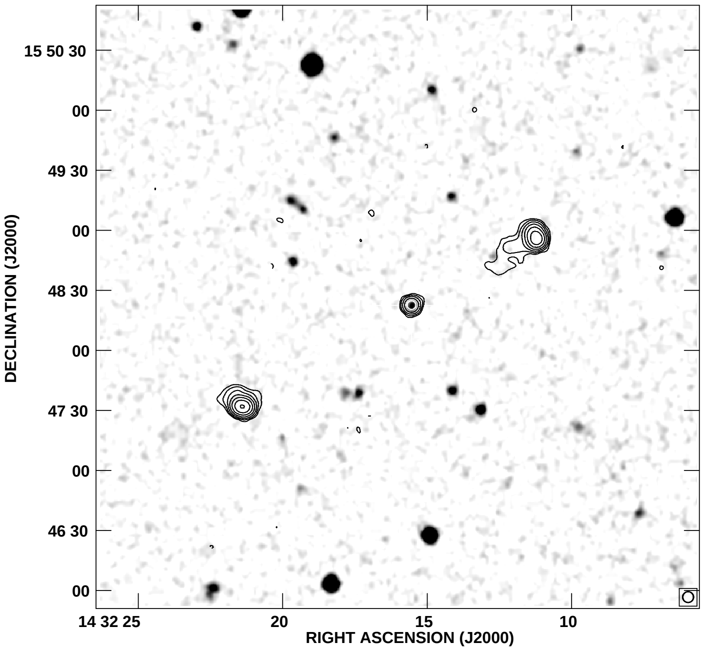
15 50 30
00
49 30
00
48 30
00
47 30
00
46 30
00
DECLINATION (J2000)
14 32 25
20
15
10
RIGHT ASCENSION (J2000)

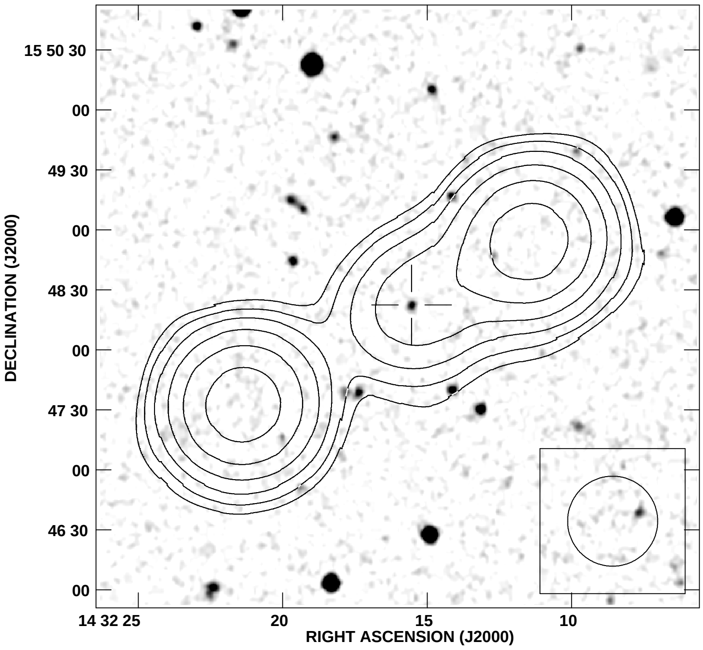
15 50 30
00
49 30
00
48 30
00
47 30
00
46 30
00
DECLINATION (J2000)
14 32 25
20
15
10
RIGHT ASCENSION (J2000)

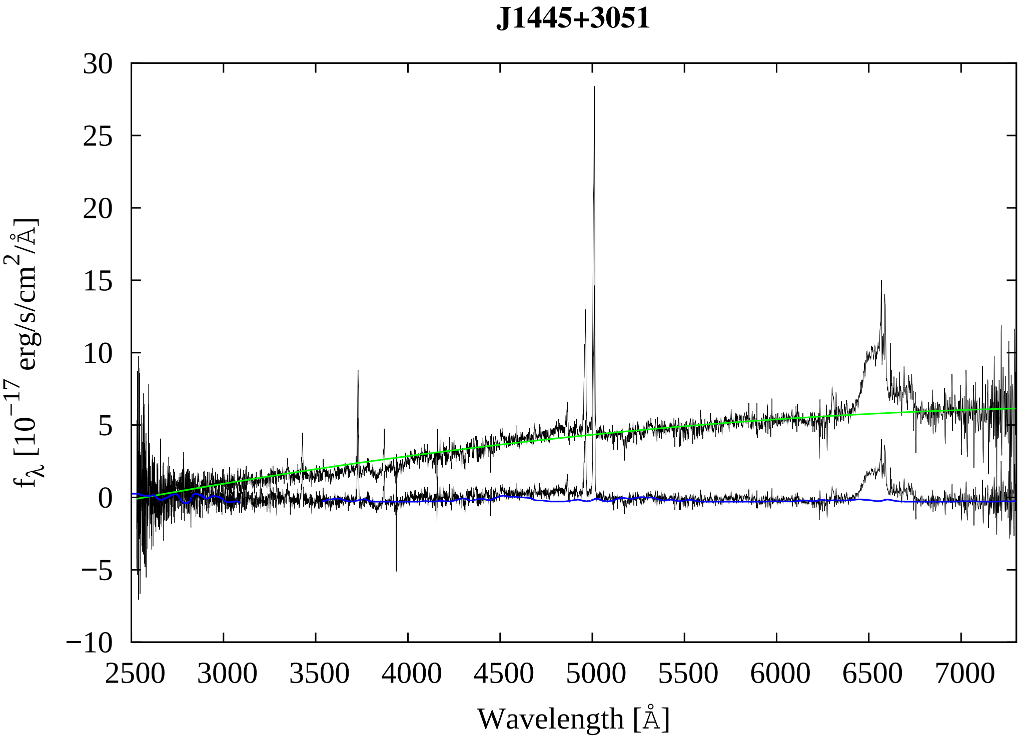
J1445+3051
30
25
20
15
10
5
0
−5
−10
f_λ [10^{-17} erg/s/cm^2/Å]
2500
3000
3500
4000
4500
5000
5500
6000
6500
7000
Wavelength [Å]

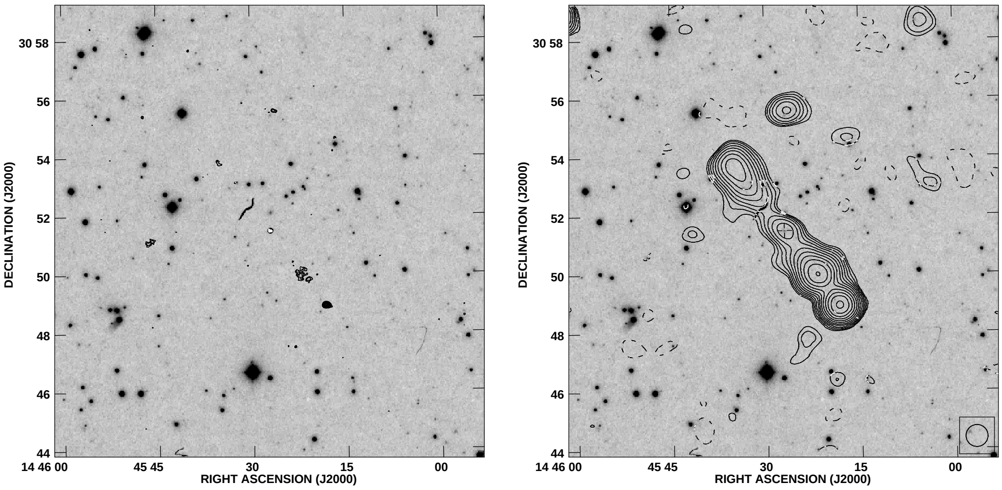
30 58
56
54
52
50
48
46
44
DECLINATION (J2000)
14 46 00
45 45
30
15
00
RIGHT ASCENSION (J2000)
30 58
56
54
52
50
48
46
44
DECLINATION (J2000)
14 46 00
45 45
30
15
00
RIGHT ASCENSION (J2000)

J1504+6856

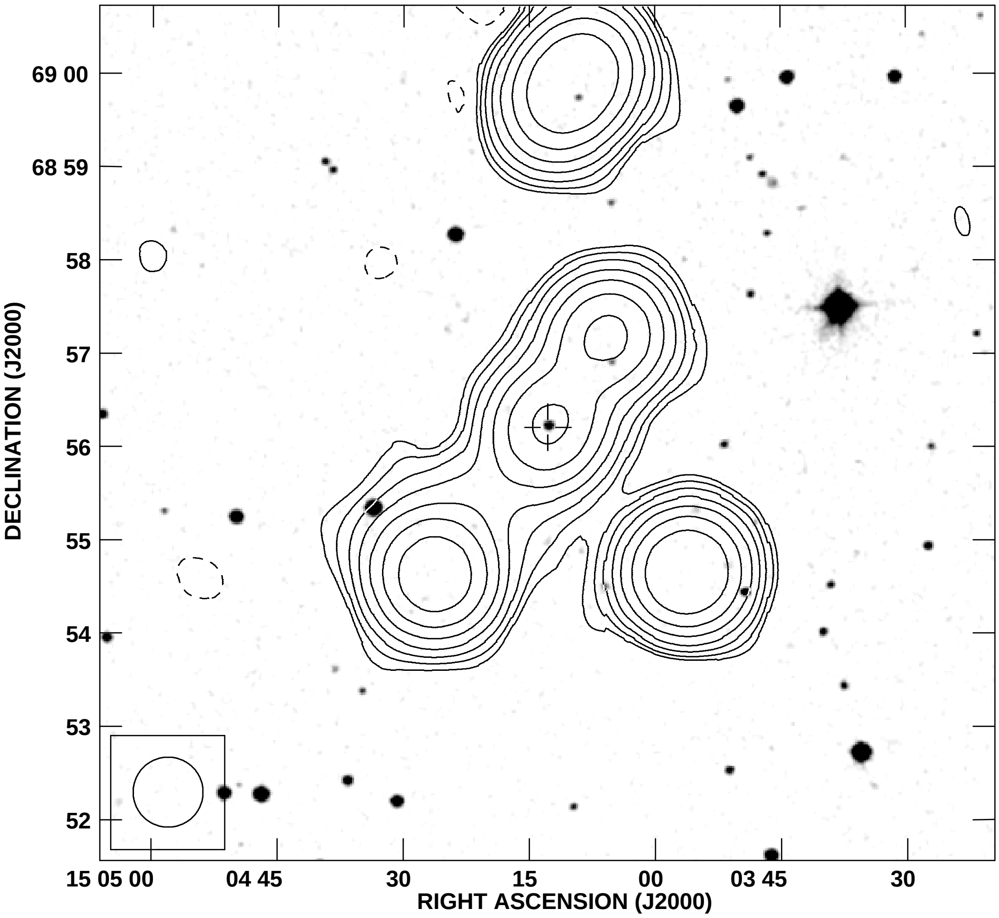
69 00
68 59
58
57
56
55
54
53
52
DECLINATION (J2000)
15 05 00
04 45
30
15
00
03 45
30
RIGHT ASCENSION (J2000)

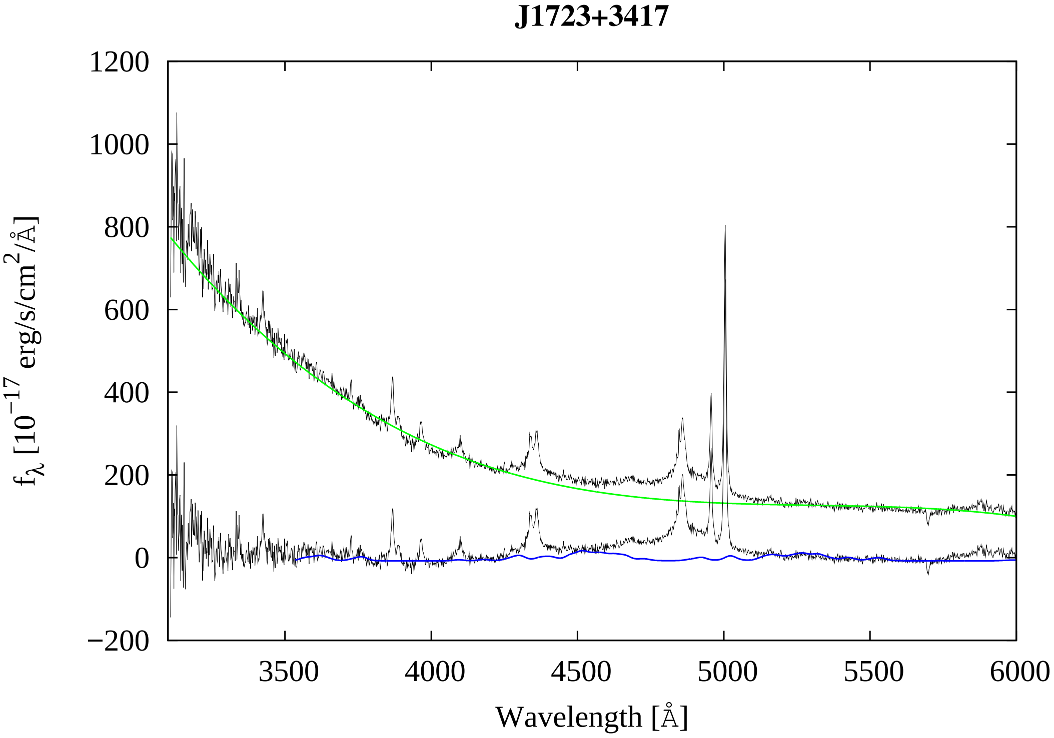
J1723+3417
1200
1000
800
600
400
200
0
−200
3500
4000
4500
5000
5500
6000
Wavelength [Å]
f_λ [10^{-17} erg/s/cm^2/Å]

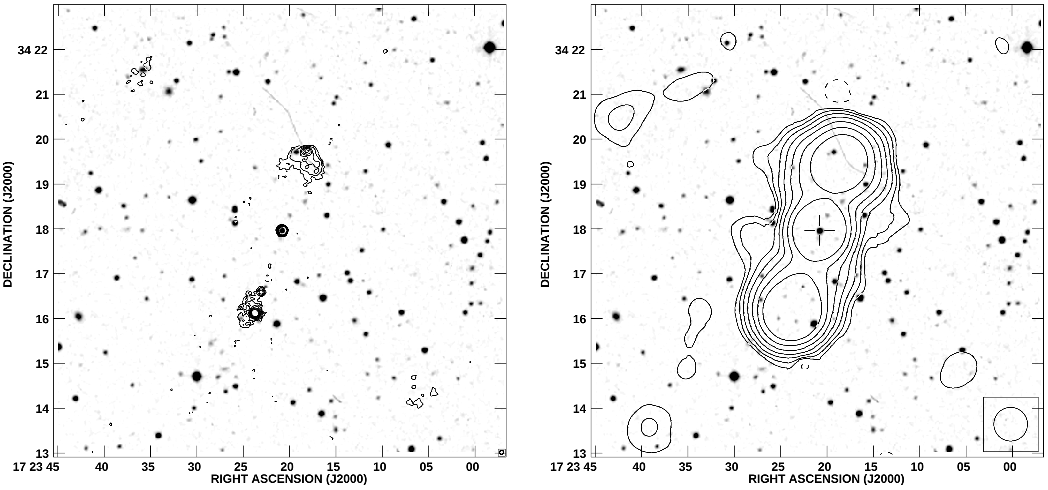
34 22
21
20
19
18
17
16
15
14
13
DECLINATION (J2000)
17 23 45
40
35
30
25
20
15
10
05
00
RIGHT ASCENSION (J2000)

J2042+7508

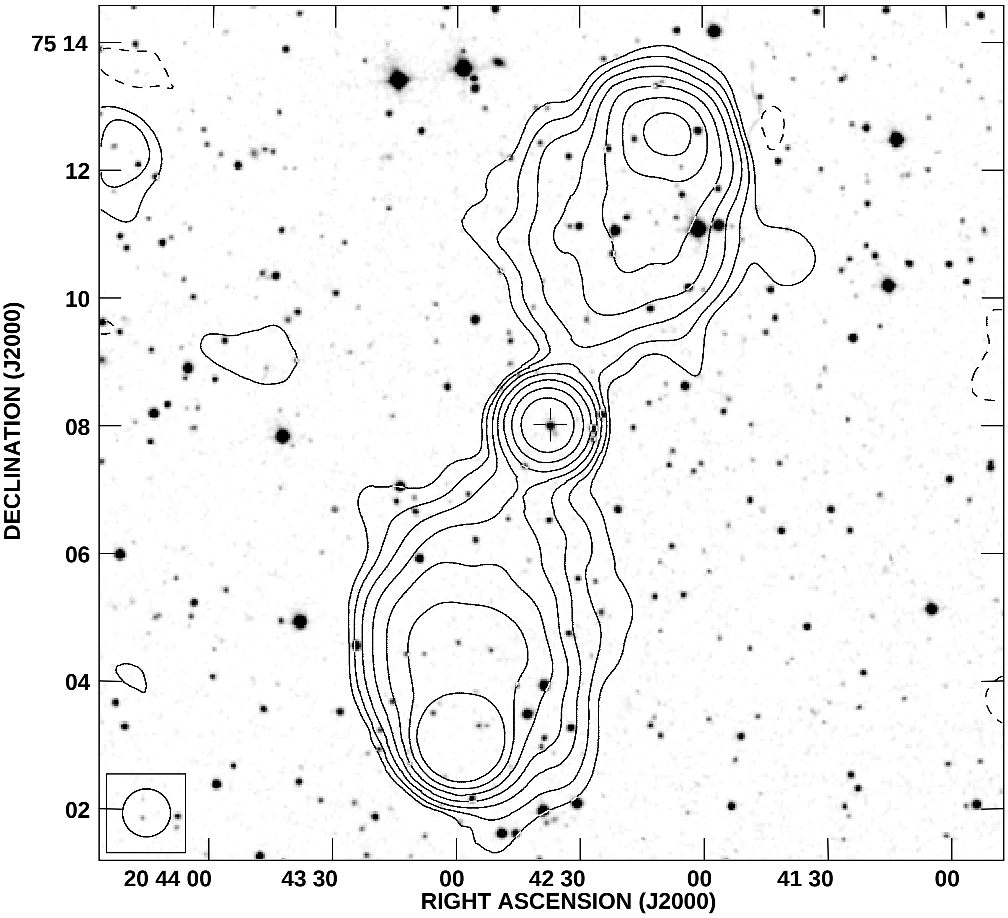
75 14
12
10
08
06
04
02
DECLINATION (J2000)
20 44 00
43 30
00
42 30
00
41 30
00
RIGHT ASCENSION (J2000)

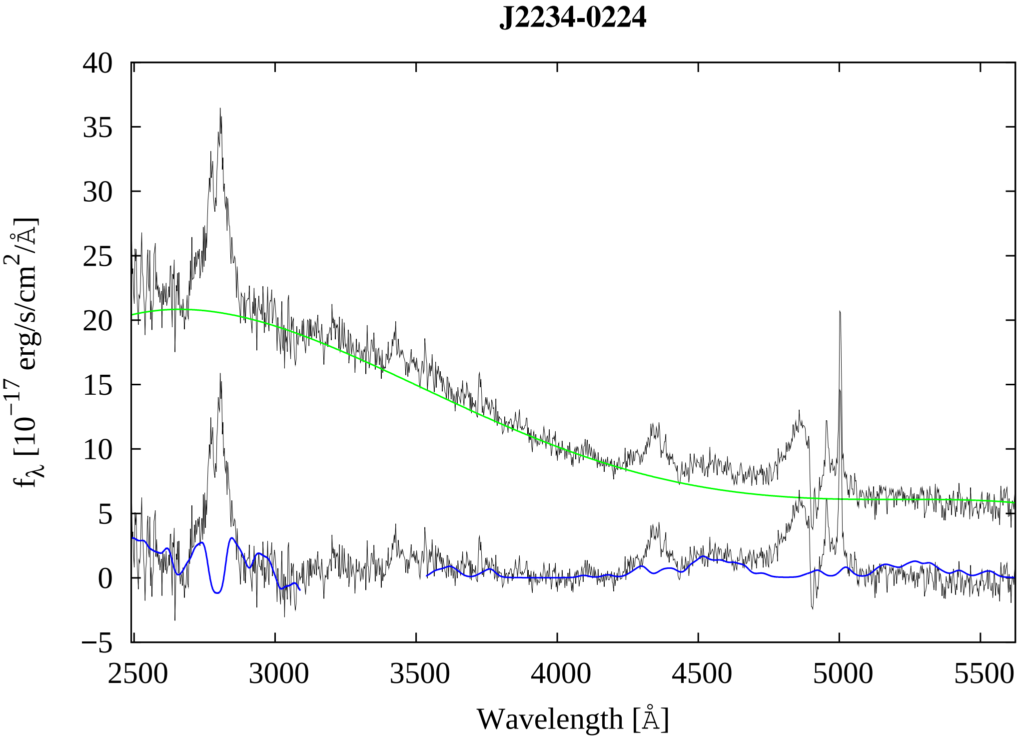
J2234-0224
f_λ [10^{-17} erg/s/cm^2/Å]
40
35
30
25
20
15
10
5
0
−5
2500
3000
3500
4000
4500
5000
5500
Wavelength [Å]

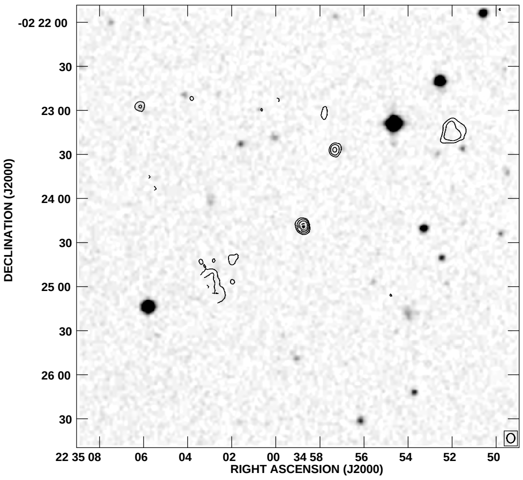
-02 22 00
30
23 00
30
24 00
30
25 00
30
26 00
30
DECLINATION (J2000)
22 35 08
06
04
02
00
34 58
56
54
52
50
RIGHT ASCENSION (J2000)

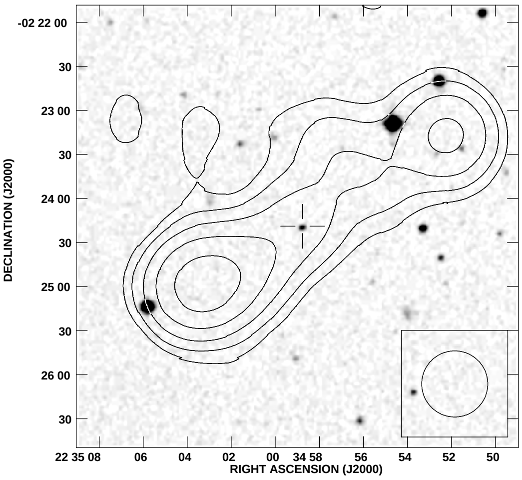
-02 22 00
30
23 00
30
24 00
30
25 00
30
26 00
30
DECLINATION (J2000)
22 35 08
06
04
02
00
34 58
56
54
52
50
RIGHT ASCENSION (J2000)

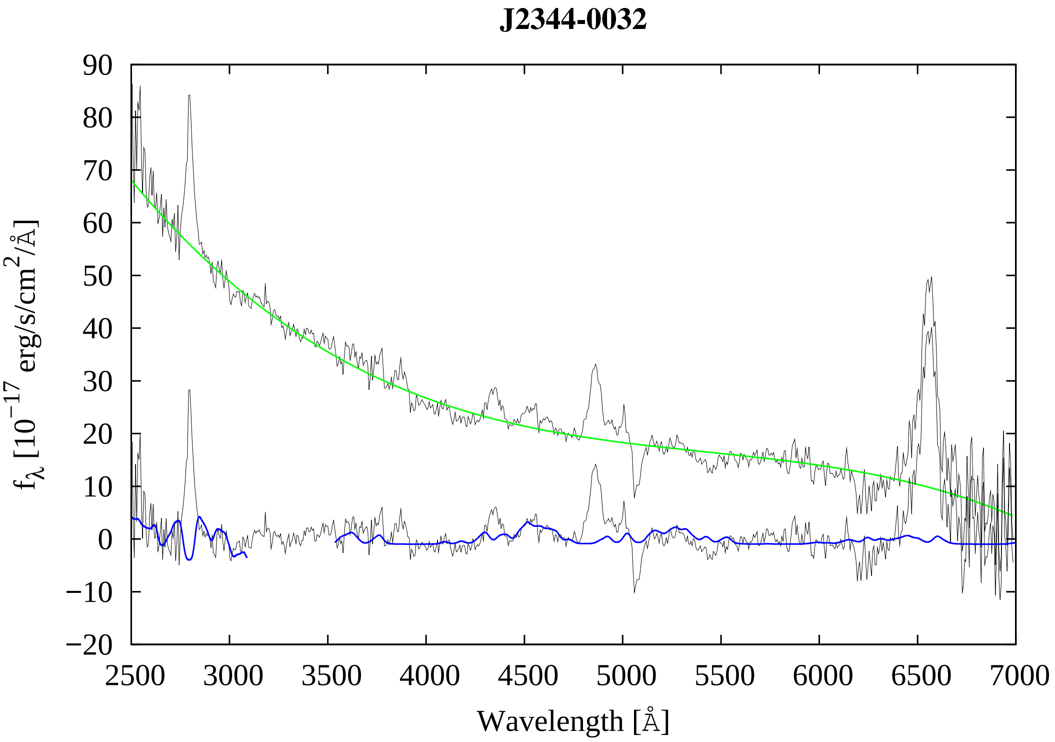
J2344-0032
f_λ [10^{-17} erg/s/cm^2/Å]
90
80
70
60
50
40
30
20
10
0
−10
−20
2500
3000
3500
4000
4500
5000
5500
6000
6500
7000
Wavelength [Å]

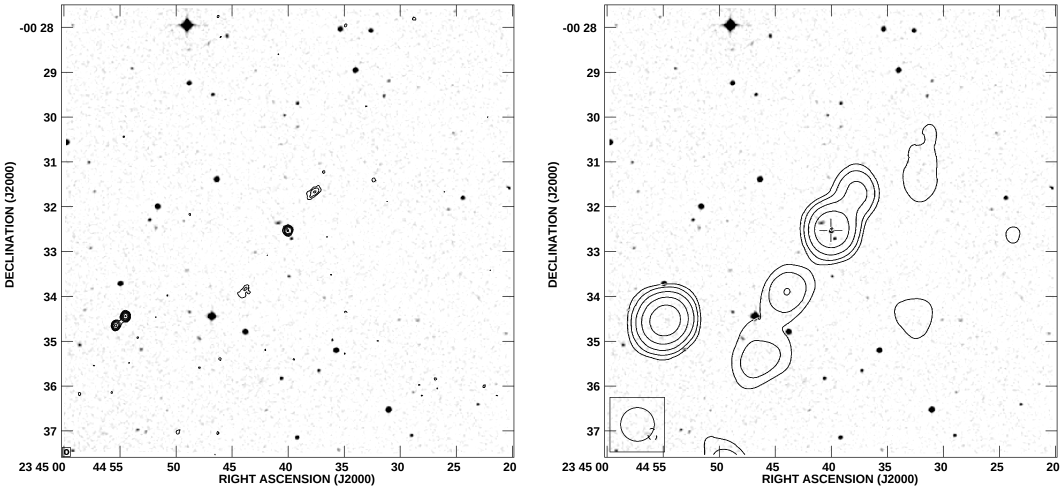
-00 28
29
30
31
32
33
34
35
36
37
DECLINATION (J2000)
23 45 00
44 55
50
45
40
35
30
25
20
RIGHT ASCENSION (J2000)
-00 28
29
30
31
32
33
34
35
36
37
DECLINATION (J2000)
23 45 00
44 55
50
45
40
35
30
25
20
RIGHT ASCENSION (J2000)

Appendix C

Parameters of GRGs

This appendix presents the samples of GRGs (Tables C.1). The description of the columns is as follows:

Column 1: J2000.0 IAU name.

Column 2 and *Column 3:* J2000.0 right ascension and declination of the central position of the optical galaxy.

Column 4: Redshift of the host galaxy.

Column 5: Angular size in arcmin.

Column 6: Projected linear size in Mpc.

Column 7: Availability of the spectrum from the SDSS survey (S), or INT data archive (I); availability of radio maps from NVSS or FIRST (N or F, respectively).

Column 8: References to the identified object.

The GRGs marked by single asterisk are also DDRGs, by double and triple asterisk giant and double-double RGs which were excluded from sample of FRII radio galaxies (Kozieł-Wierzbowska & Stasińska 2011) respectively.

In next tables I listed the measured and calculated parameters of GRGs (Tables C.3, C.2).

In Table C.2 - velocity dispersions and BH masses (Section 3.2):

Column 1: J2000.0 IAU name.

Column 2: Velocity dispersion.

Column 3: Black hole mass derived using Equation 3.1 with constants given by Graham (2011) (Section 3.2)

In Table C.3 I placed radio data described in Section 3.2:

Column 1: J2000.0 IAU name.

Column 2: Logarithm of total radio power.

Column 3: Logarithm of core radio power.

Column 4: Bending angle.

Column 5: Arm-length ratio.

Column 6: Flux-density ratio.

Column 7: Inclination.

In Table C.4 - basic parameters of GRGs, DDRGs, smaller FRII RSs and CSS RSs with estimations of t_{RS}. (Section 3.5):

Column 1: J2000.0 IAU name.

Column 2 and *Column 3:* J2000.0 right ascension and declination of the central position of the optical galaxy.

Column 4: Redshift of the host galaxy.

Column 5: Projected linear size of outer radio structure in kpc.

Column 6: Projected linear size of iner radio structure in kpc.

Column 7: Logarithm of total radio power.

Column 8: Logarithm of core radio power.

Column 9: Age of radio structure - t_{RS}.

Column 10: Velocity dispersion.

Column 11: Black hole mass derived using Equation 3.1.

Column 12: References to the identified object.

Column 13: References to the t_{RS} estimation.

Table C.1: List of giant-size (> 0.72 Mpc) radio galaxies.

IAU name (1)	α(J2000.0) (h m s) (2)	δ(J2000.0) (^{o} ’ ”) (3)	z (4)	d arcmin (5)	D Mpc (6)	Avail. Data (7)	Ref. (8)
J0010−1108**	00 10 49.69	-11 08 12.9	0.077	8.68	752.75	S,N,F	1
J0037+0027	00 37 54.59	+00 27 17.4	0.589	4.96	1967.72	S,N,F	2
J0053+4031	00 53 31.71	+40 31 26.5	0.149	7.36	1135.08	I,N,F	3
J0112+4928	01 12 02.23	+49 28 35.2	0.067	10.39	790.13	I,N	4
J0134−0107	01 34 12.80	-01 07 28.2	0.079	10.14	896.47	S,N,F	1
J0200+4049	02 00 30.83	+40 48 54.1	0.083	9.22	852.87	I,N	3
J0214+3251	02 14 15.23	+32 51 06.1	0.261	4.91	1177.67	I,N	5
J0300−0728	03 00 59.02	-07 28 31.0	0.491	4.58	1652.93	S,N	1
J0313+4120	03 13 01.96	+41 20 01.2	0.136	5.32	760.22	I,N	5
J0318+6829	03 18 18.98	+68 29 31.4	0.090	14.55	1448.74	I,N	6
J0748+5548	07 48 36.76	+55 48 57.3	0.036	21.55	913.07	I,N,F	7
J0751+4231**	07 51 08.79	+42 31 23.6	0.203	4.89	970.46	S,N,F	8
J0918+3151	09 18 59.42	+31 51 40.6	0.062	11.00	778.80	S,N,F	9
J0949+7314	09 49 46.05	+73 14 22.9	0.058	14.21	945.51	I,N	10
J1006+3454*	10 06 01.77	+34 54 10.2	0.100	38.44	4181.22	S,N,F	11
J1021+0519**	10 21 31.47	+05 19 01.0	0.156	12.62	2025.64	S,N,F	1
J1021+1217***	10 21 24.22	+12 17 05.3	0.129	13.65	1868.84	S,N,F	1
J1032+2756	10 32 14.09	+27 56 00.2	0.085	10.51	994.11	S,N,F	8
J1032+5644	10 32 59.02	+56 44 53.8	0.045	14.83	777.04	S,N	12
J1048+1108**	10 48 43.42	+11 08 02.1	0.157	4.92	792.20	S,N,F	1
J1108+0202	11 08 45.51	+02 02 40.5	0.157	8.36	1350.48	S,N,F	1
J1111+2657	11 11 24.97	+26 57 46.6	0.033	25.36	990.55	S,N,F	13
J1147+3501	11 47 22.12	+35 01 08.0	0.063	11.46	823.42	S,N,F	8
J1216+4159	12 16 09.63	+41 59 28.1	0.243	5.06	1152.75	S,N,F	5
J1216+6724**	12 16 37.28	+67 24 41.0	0.362	4.81	1447.11	S,N	10
J1220+6341**	12 20 36.38	+63 41 44.3	0.188	4.93	920.88	S,N,F	14
J1242+3838*	12 42 36.89	+38 38 06.3	0.408	2.61	847.62	S,N	3

Table C.1 continued

IAU name (1)	α(J2000.0) (h m s) (2)	δ(J2000.0) (^{o} ’ ”) (3)	z (4)	d arcmin (5)	D Mpc (6)	Avail. Data (7)	Ref. (8)
J1247+6723***	12 47 33.32	+67 23 15.9	0.107	10.47	1218.55	S,N	5
J1253+4041**	12 53 12.28	+40 41 23.7	0.229	4.34	946.48	S,N	8
J1308+6154**	13 08 44.78	+61 54 15.3	0.163	8.58	1422.81	S,N,F	5
J1311+4059**	13 11 43.06	+40 59 00.0	0.111	6.19	739.41	S,N,F	15
J1313+6937	13 13 58.86	+69 37 18.7	0.106	6.27	721.58	I,N	14
J1328−0129	13 28 34.16	-01 29 17.8	0.151	5.40	844.30	S,N,F	1
J1328−0307**	13 28 34.33	-03 07 45.0	0.085	13.61	1288.99	S,N,F	8
J1345+5403**	13 45 57.56	+54 03 16.6	0.163	4.87	807.83	S,N,F	11
J1400+3019	14 00 43.44	+30 19 18.2	0.206	10.36	2079.00	S,N,F	16
J1409−0302*	14 09 48.86	-03 02 32.5	0.138	7.06	1019.00	S,N	17
J1418+3746**	14 18 37.67	+37 46 24.9	0.135	6.38	905.56	S,N	8
J1428+2918	14 28 19.24	+29 18 44.2	0.087	15.05	1453.30	S,N,F	5
J1453+3308***	14 53 02.92	+33 08 42.7	0.248	5.64	1304.31	S,N,F	5
J1605+0711*	16 05 13.74	+07 11 52.6	0.311	2.69	730.96	S,N	18
J1628+5146	16 28 04.04	+51 46 31.7	0.056	18.56	1194.92	I,N,F	5
J1635+3608	16 35 22.54	+36 08 04.7	0.165	4.82	810.55	S,N,F	8
J1738+3733	17 38 20.98	+37 33 33.7	0.124	5.85	772.57	I,N	8
J2145+8154	21 45 31.76	+81 54 55.2	0.146	17.72	2687.41	I,N,F	5

References: (1): Best et al. (2005), (2): Sadler et al. (2007), (3): Saikia, Konar & Kulkarni (2006), (4): Laing, Riley & Longair (1983), (5): Schoenmakers et al. (2000), (6): Schoenmakers et al. (1998), (7): Mack et al. (1997), (8): Schoenmakers et al. (2001), (9): Jägers (1987); (10): Lara et al. (2001), (11): Nilsson (1998), (12): Hine (1979), (13): Liu & Zhang (2002), (14): Lara et al. (2001), (15): Djorgovski et al. (1990), (16): Parma et al. (1996), (17): Lin et al. (2010), (18): White, Becker& Robert (1992)

* - DDGRG; ** - GRG from Kozieł-Wierzbowska & Stasińska (2011); *** - DDGRG from Kozieł-Wierzbowska & Stasińska (2011).

Table C.2: Velocity dispersions and black hole masses for GRGs.

IAU name (1)	σ^* km/s (2)	$log\mathrm{M}_{\sigma *}$ $\mathrm{M}_{\odot}$ (3)
J0010−1108	239.91	8.54
J0037+0027	223.62	8.38
J0053+4031	189.40	8.01
J0112+4928	268.27	8.78
J0134−0107	262.75	8.74
J0200+4049	–	–
J0214+3251	214.66	8.29
J0300−0728	260.29	8.72
J0313+4120	448.75	9.93
J0318+6829	–	–
J0748+5548	243.55	8.57
J0751+4231	264.77	8.76
J0918+3151	220.43	8.35
J0949+7314	173.30	7.81
J1006+3454	251.97	8.64
J1021+1217	238.40	8.52
J1021+1217	234.66	8.49
J1032+2756	182.95	7.93
J1032+5644	285.01	8.92
J1048+1108	258.68	8.70
J1108+0202	179.40	7.89
J1111+2657	285.45	8.92
J1147+3501	226.82	8.41
J1216+4159	204.83	8.18
J1216+6724	154.15	7.55
J1220+6341	252.29	8.65
J1242+3838	242.37	8.56
J1247+6723	241.75	8.55
J1253+4041	209.96	8.24

Table C.2 continued

IAU name (1)	σ^* km/s (2)	$log\mathrm{M}_{\sigma*}$ $\mathrm{M}_\odot$ (3)
J1308+6154	209.81	8.24
J1311+4059	98.28	6.55
J1313+6937	256.21	8.68
J1328−0129	193.67	8.06
J1328−0307	90.05	6.35
J1345+5403	194.70	8.07
J1400+3019	260.71	8.72
J1409−0302	135.68	7.27
J1418+3746	223.84	8.38
J1428+2918	245.16	8.58
J1453+3308	276.88	8.85
J1605+0711	188.18	7.99
J1628+5146	284.19	8.91
J1635+3608	272.75	8.82
J1738+3733	–	–
J2145+8154	411.48	9.74

Table C.3: Parameters of radio structures for GRGs.

IAU name (1)	$logP_{tot}$ W/Hz (2)	$logP_{core}$ W/Hz (3)	B [^{o}] (4)	Q (5)	F (6)	i [^{o}] (7)
J0010−1108	23.97	23.04	6.16	1.34	0.84	79
J0037+0027	26.25	24.17	0.26	1.26	0.94	87
J0053+4031	25.43	23.76	3.44	1.29	1.95	78
J0112+4928	25.31	23.63	5.34	1.05	1.24	77
J0134−0107	24.65	24.05	21.64	1.82	4.84	70
J0200+4049	24.70	-	15.07	2.03	0.74	87
J0214+3251	25.95	-	1.23	1.36	1.26	86
J0300−0728	25.68	24.41	4.17	1.53	0.94	86
J0313+4120	25.38	25.24	24.78	2.49	0.16	41
J0318+6829	25.20	23.88	5.08	1.44	0.26	52
J0748+5548	24.45	23.76	2.45	1.11	2.18	19
J0751+4231	25.26	22.56	17.65	1.19	1.20	80
J0918+3151	24.43	22.97	10.98	1.64	0.08	60
J0949+7314	25.29	22.60	16.42	1.26	2.16	69
J1006+3454	26.04	25.88	0.63	1.66	0.75	69
J1021+0519	25.05	23.53	3.00	1.74	1.76	86
J1021+1217	24.77	23.83	15.46	1.14	1.09	84
J1032+2756	24.70	23.78	0.44	1.60	1.34	83
J1032+5644	24.36	23.79	2.11	1.18	0.42	82
J1048+1108	25.17	23.28	0.97	1.31	0.81	79
J1108+0202	25.81	25.63	3.89	1.06	4.23	45
J1111+2657	23.55	23.32	6.85	1.08	0.63	78
J1147+3501	24.87	24.74	10.67	1.26	0.81	80
J1216+4159	25.84	24.45	0.35	1.25	0.82	67
J1216+6724	25.88	24.01	5.64	2.18	0.51	74
J1220+6341	25.38	23.38	2.53	1.25	0.74	88
J1242+3838	25.25	23.67	5.56	1.03	1.72	86

Table C.3 continued

IAU name (1)	$logP_{tot}$ W/Hz (2)	$logP_{core}$ W/Hz (3)	B $[^o]$ (4)	Q (5)	F (6)	i $[^o]$ (7)
J1247+6723	25.03	24.86	3.77	1.18	1.13	87
J1253+4041	24.86	-	0.05	1.16	1.64	81
J1308+6154	24.85	23.83	11.56	1.18	1.14	80
J1311+4059	25.24	-	1.86	1.07	1.38	86
J1328−0129	25.30	23.92	2.97	1.02	0.73	81
J1313+6937	25.59	-	8.28	1.40	0.58	78
J1328−0307	24.58	23.17	2.51	1.18	0.50	76
J1345+5403	25.36	23.77	3.09	1.18	0.85	85
J1400+3019	25.69	23.28	7.65	2.48	0.54	79
J1409−0302	24.93	-	12.60	2.15	0.50	63
J1418+3746	24.42	23.50	2.64	1.95	1.81	87
J1428+2918	24.89	23.39	4.54	1.31	1.01	85
J1453+3308	25.90	23.51	10.48	1.31	0.55	77
J1605+0711	25.89	-	11.90	1.01	1.23	78
J1628+5146	24.67	23.50	7.24	1.53	0.43	77
J1635+3608	24.83	23.55	16.04	1.31	0.72	60
J1738+3733	24.95	24.60	3.20	1.38	1.16	85
J2145+8154	25.36	23.82	11.48	1.14	0.78	89

TABLE C.4: Basic parameters of GRGs, DDRGs, smaller-size FRII RSs and CSS RSs with estimations of t_{RS}.

IAU name (1)	α(J2000.0) (h m s) (2)	δ(J2000.0) (^{o} ’ ”) (3)	z (4)	D_{out} kpc (5)	D_{in} kpc 6)	$logP_{tot}$ [W/Hz] (7)	$logP_{core}$ [W/Hz] (8)	$t_{\rm RS}$ [Myr] (9)	v_σ km/s (10)	$log M_\sigma$ M⊙ (11)	Ref. obj. (12)	Ref. t_{RS} (13)
GRGs RG												
J0112+4928		All data in Tables C.1, C.3, C.2						48.1				8
J0748+5548								10.0				9
J1313+6937								35.4				10
DDRGs												
J0924+0602	09 24 49.05	+06 02 42.9	0.2306	369.68	77.36	25.16	23.41	-	269.20	8.79	1	
J1006+3454	10 06 01.77	+34 54 10.2	0.1560	4181.22	-	26.04	25.88	20.3	251.97	8.64	2	9
J1158+2621	11 58 20.12	+26 21 12.1	0.1120	490.92	138.65	25.50	22.42	-	177.06	7.86	3	
J1326+1924	13 26 13.67	+19 24 23.8	0.1763	155.12	22.34	24.85	-	-	279.69	8.88	3	
J1328+2752	13 28 48.45	+27 52 27.8	0.0911	363.84	121.43	24.65	22.68	-	165.08	7.70	3	
J1344−0030	13 44 46.92	-00 30 09.3	0.5801	653.30	134.86	25.92	-	-	276.49	8.85	3	
J1352+3126	13 52 17.88	+31 26 46.5	0.0452	197.25	76.79	25.36	25.21	-	194.73	8.07	4	
J1453+3308	14 53 02.92	+33 08 42.7	0.2480	1304.31	141.12	25.90	23.51	52.5	276.88	8.85	5	11
J1528+0544	15 28 04.95	+05 44 28.3	0.0411	619.70	15.56	24.22	22.85	-	143.92	7.40	1	
J1545+5047	15 45 17.21	+50 47 54.2	0.4309	338.62	50.76	25.83	-	-	212.00	8.26	3	
FRII RG												
J0911+3724	09 11 53.2	+37 24 10	0.1040	454.20	-	25.24	-	14.0	301.9	9.44	6	12
CSS RSs												
J0141+1353	01 41 09.1	+13 53 28	0.6210	-	5.53	27.54	-	0.0013	338.1	9.3	7	13
J1008+0730	10 08 00.0	+07 30 16	0.8770	-	9.03	28.24	-	0.0181	71.18	5.83	7	13
J1028+3844	10 28 44.3	+38 44 37	0.3610	-	5.1	26.40	-	0.0060	389.49	9.61	7	13
J1247+6723	12 47 33.3	+67 23 16	0.1073	1218.55	0.1	24.86	-	0.0002	242.74	8.56	7	13
J1609+2641	16 09 13.3	+26 41 29	0.4730	-	0.26	27.52	-	0.0005	191.42	8.03	7	13

References: (1): this work; (2): Willis, Strom, & Wilson (1974); (3): Nandi & Saikia (2012); (4): Joshi et al. (2011); (5): Konar et al. (2006); (6): Kozieł-Wierzbowska & Stasińska (2011), (7): Czerny et al. (2009). References to t_{RS} estimations: (8): Schoenmakers et al. (2000); (9): Jamrozy et al. (2009); (10): Jamrozy et al. (2008); (11): Jamrozy et al. (2009); (12): Machalski et al. (2007); (13): Czerny et al. (2009).

Appendix D

Spectra and radio maps of giant radio galaxies

This appendix presents the optical spectra and radio maps of the sample of GRGs.

In presented below graphs I plotted the observed spectra after galactic extinction and redshift correction (see Section 2.3.1); a spectral continuum modelled using Starlight Spectral Synthesis Code (green lines); the continuum-subtracted spectra. For four GRGs it was not possible to obtain a good stellar continuum fit, therefore, I plot the spectra of those galaxies withought continuum fit.

The 1.4-GHz VLA maps of the GRQs taken from the NVSS survey and from the FIRST survey (if available) overlaid on the optical image from the DSS. The contour levels are: -1, $\sqrt{2^n}$; n=0, 1, 2 ... $\times$ 1.35 mJy/beam and -1, $\sqrt{n}$; n=0, 1, 2 ... $\times$ 0.6 mJy/beam for the NVSS and FIRST surveys, respectively. The ellipses in the corners represent the resolution of the NVSS and FIRST surveys. Crosses mark the position of the parent galaxy.

All radio maps as well as optical spectra of GRGs were recorded on a CD which is attached to the Thesis.

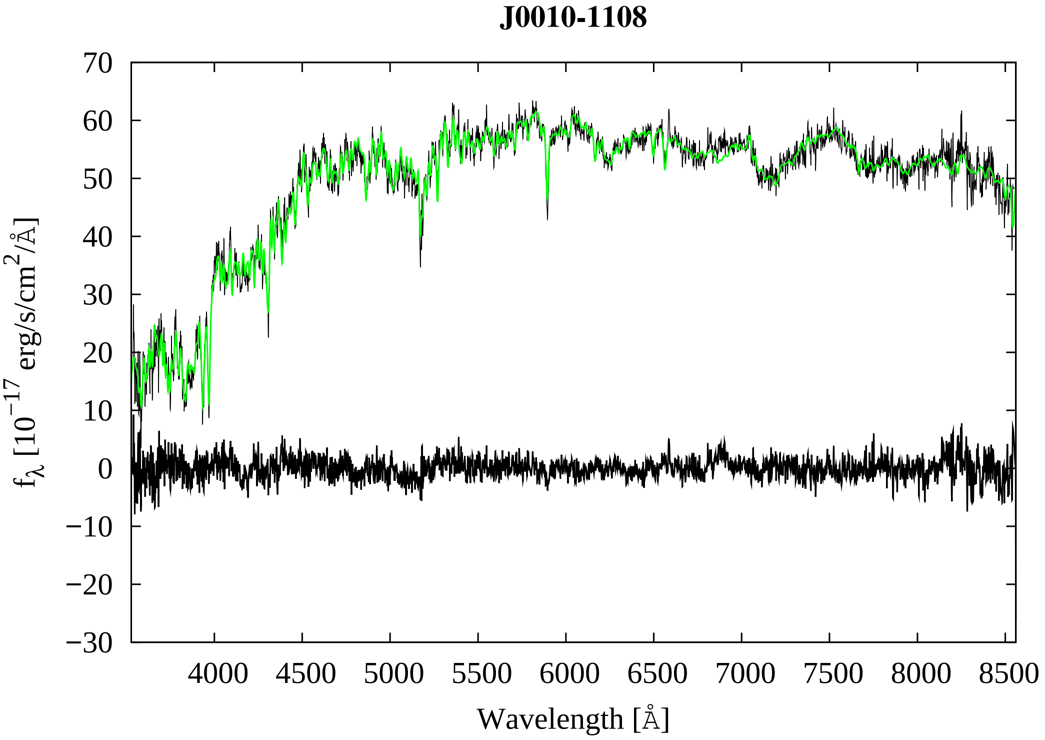
J0010-1108
70
60
50
40
30
20
10
0
−10
−20
−30
f_λ [10^{-17} erg/s/cm^2/Å]
4000
4500
5000
5500
6000
6500
7000
7500
8000
8500
Wavelength [Å]

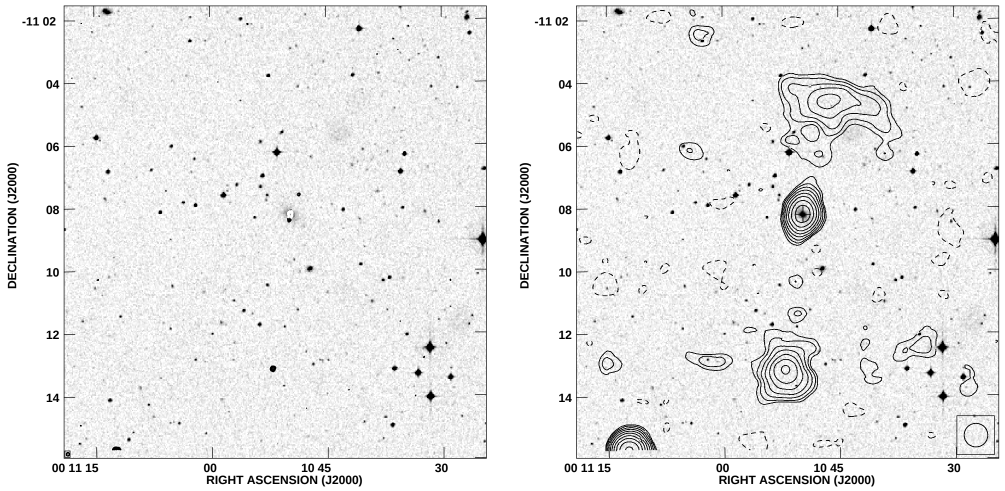
-11 02
04
06
08
10
12
14
DECLINATION (J2000)
00 11 15
00
10 45
30
RIGHT ASCENSION (J2000)
-11 02
04
06
08
10
12
14
DECLINATION (J2000)
00 11 15
00
10 45
30
RIGHT ASCENSION (J2000)

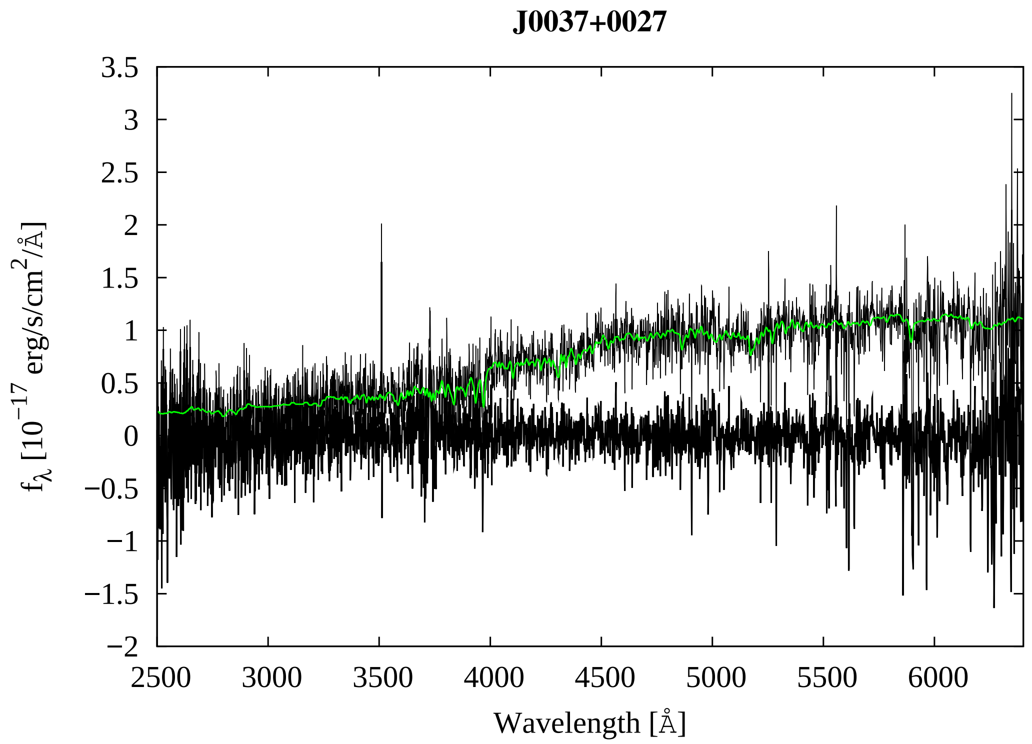
J0037+0027
f_λ [10^{-17} erg/s/cm^2/Å]
3.5
3
2.5
2
1.5
1
0.5
0
−0.5
−1
−1.5
−2
2500
3000
3500
4000
4500
5000
5500
6000
Wavelength [Å]

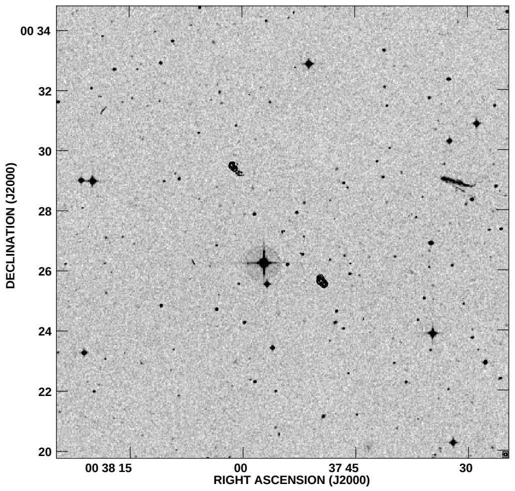
DECLINATION (J2000)
00 34
32
30
28
26
24
22
20
00 38 15
00
37 45
30
RIGHT ASCENSION (J2000)

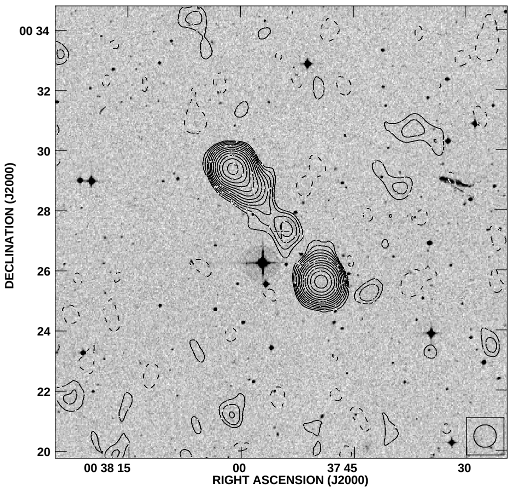
DECLINATION (J2000)
00 34
32
30
28
26
24
22
20
00 38 15
00
37 45
30
RIGHT ASCENSION (J2000)

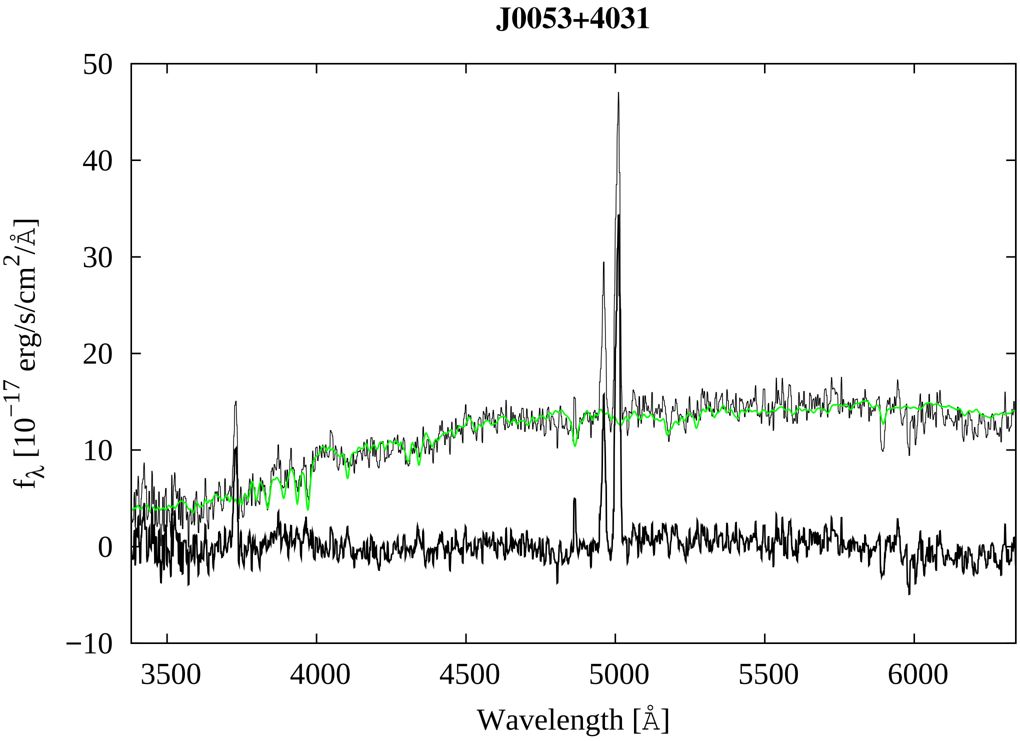
J0053+4031
f_λ [10^{-17} erg/s/cm^2/Å]
50
40
30
20
10
0
−10
3500
4000
4500
5000
5500
6000
Wavelength [Å]

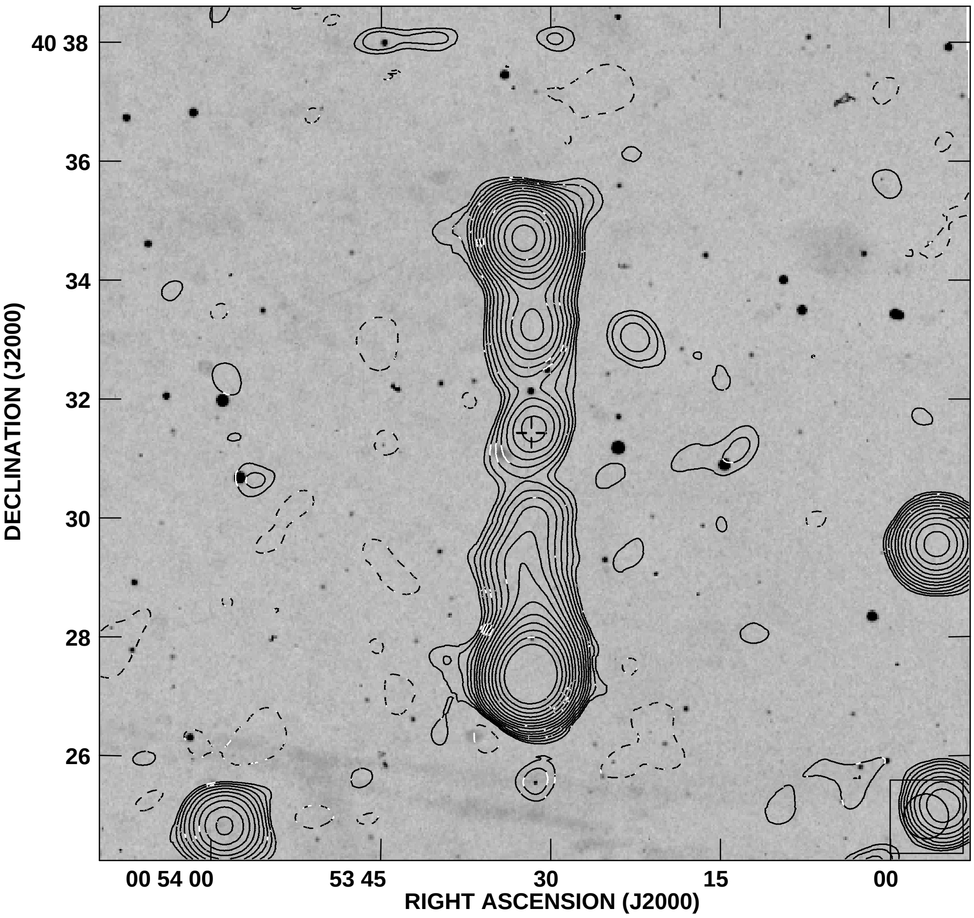
DECLINATION (J2000)
40 38
36
34
32
30
28
26
00 54 00
53 45
30
15
00
RIGHT ASCENSION (J2000)

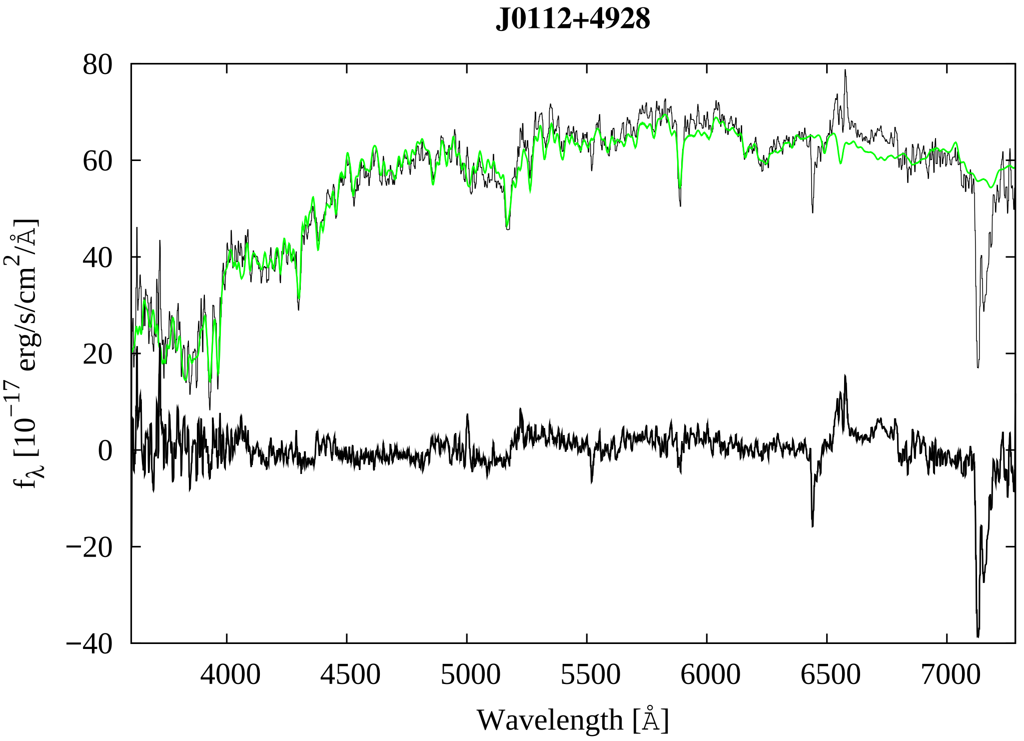
J0112+4928
80
60
40
20
0
−20
−40
f_λ [10^{-17} erg/s/cm^2/Å]
4000
4500
5000
5500
6000
6500
7000
Wavelength [Å]

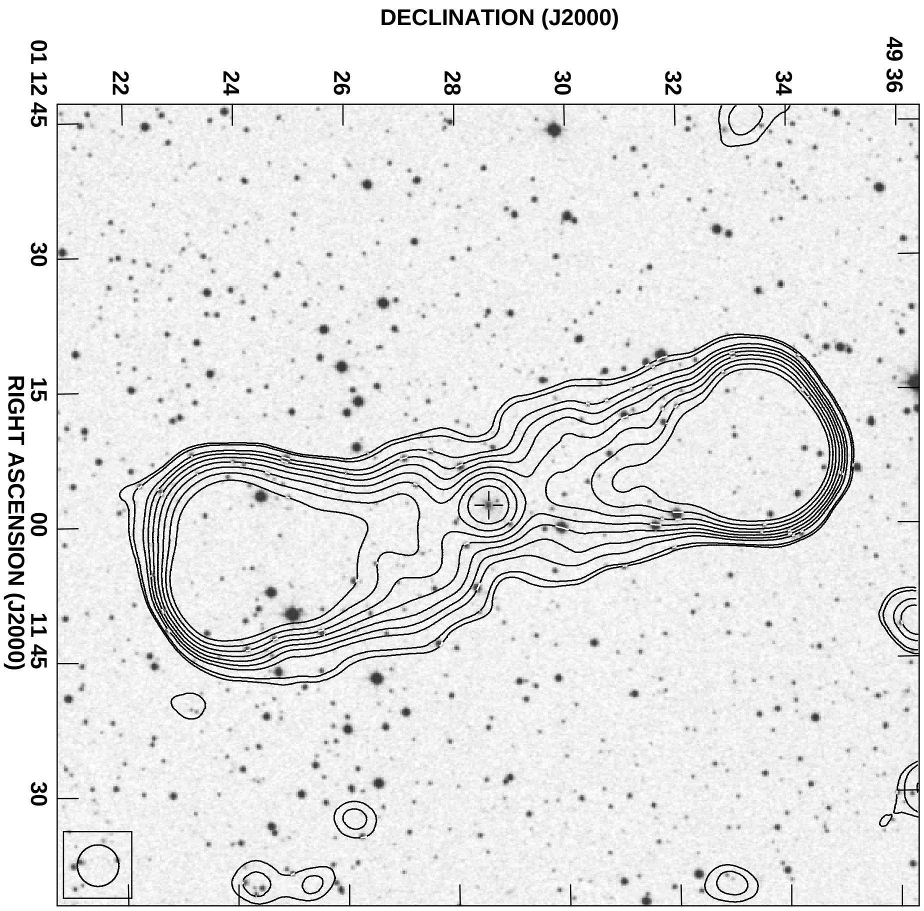
DECLINATION (J2000)
01 12 45
22
24
26
28
30
32
34
49 36
RIGHT ASCENSION (J2000)
30
15
00
11 45
30

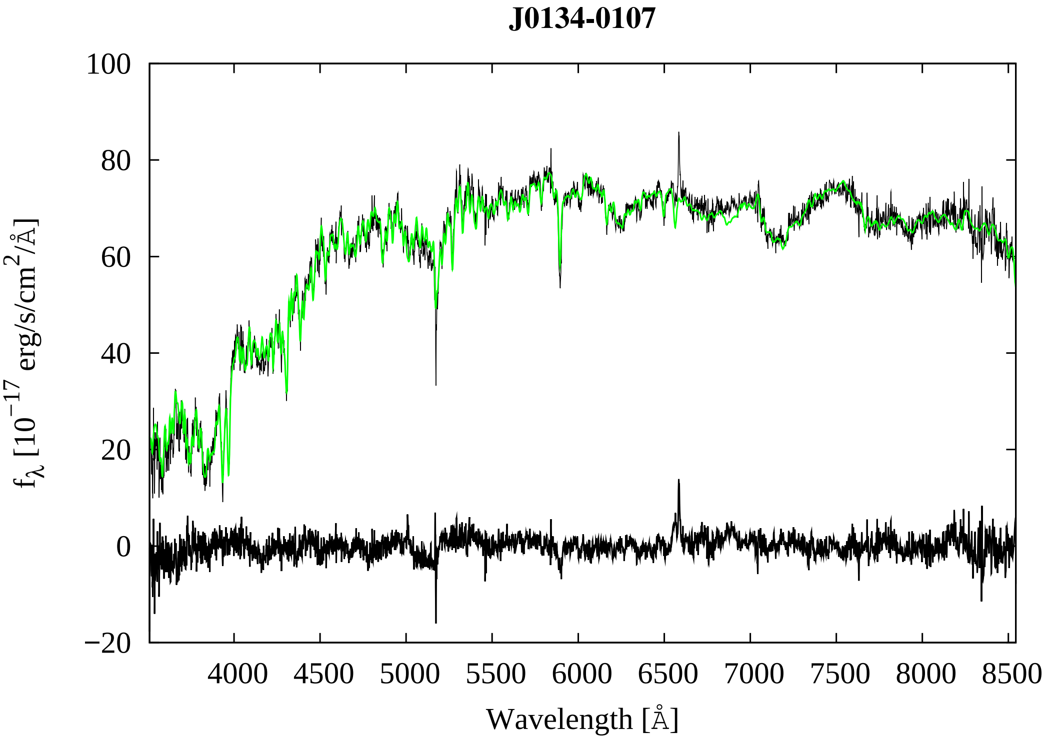
J0134-0107
100
80
60
40
20
0
−20
f$_\lambda$ [10^{-17} erg/s/cm^2/Å]
4000 4500 5000 5500 6000 6500 7000 7500 8000 8500
Wavelength [Å]

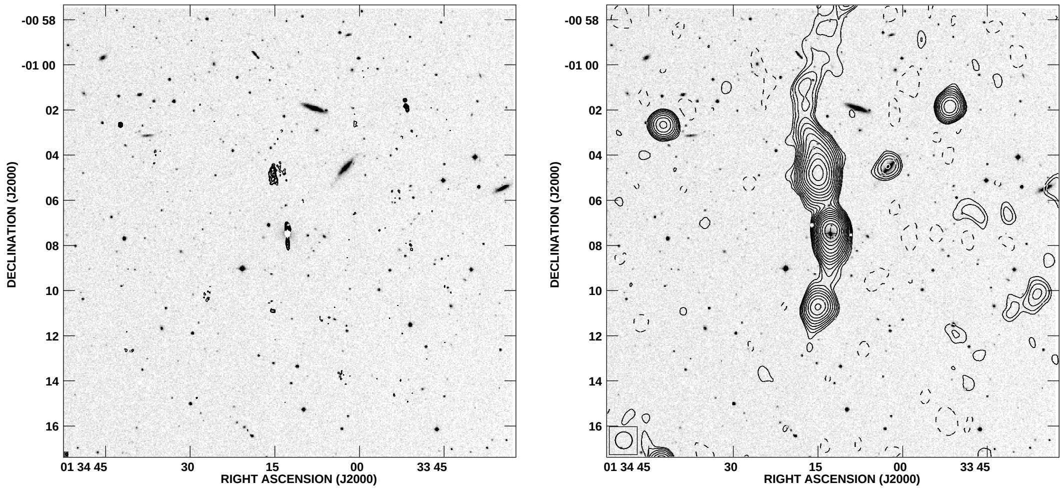
-00 58
-01 00
02
04
06
08
10
12
14
16
DECLINATION (J2000)
01 34 45
30
15
00
33 45
RIGHT ASCENSION (J2000)

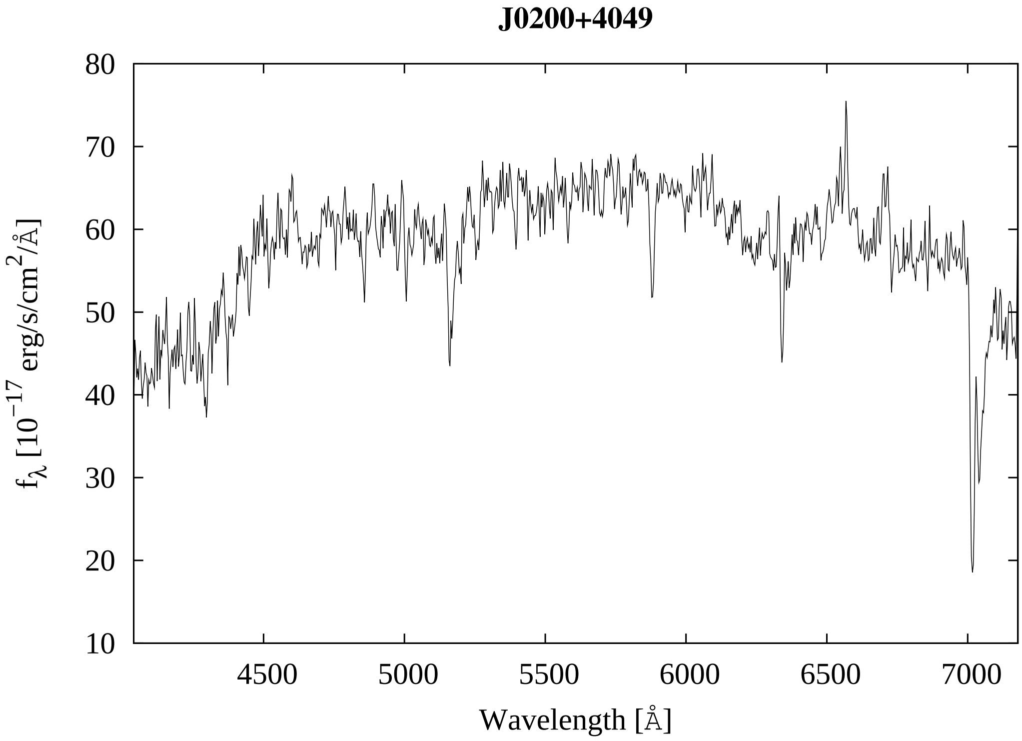
J0200+4049
80
70
60
50
40
30
20
10
f$_\lambda$ [10^{-17} erg/s/cm^2/Å]
4500
5000
5500
6000
6500
7000
Wavelength [Å]

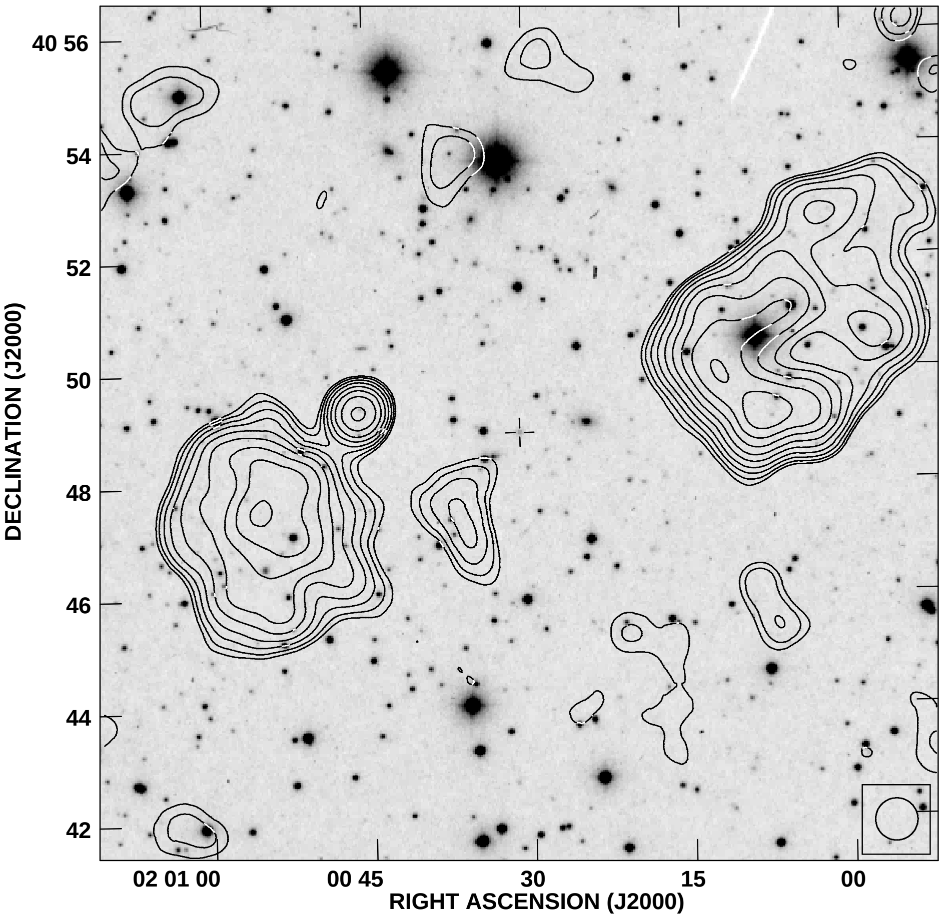
40 56
54
52
50
48
46
44
42
DECLINATION (J2000)
02 01 00
00 45
30
15
00
RIGHT ASCENSION (J2000)

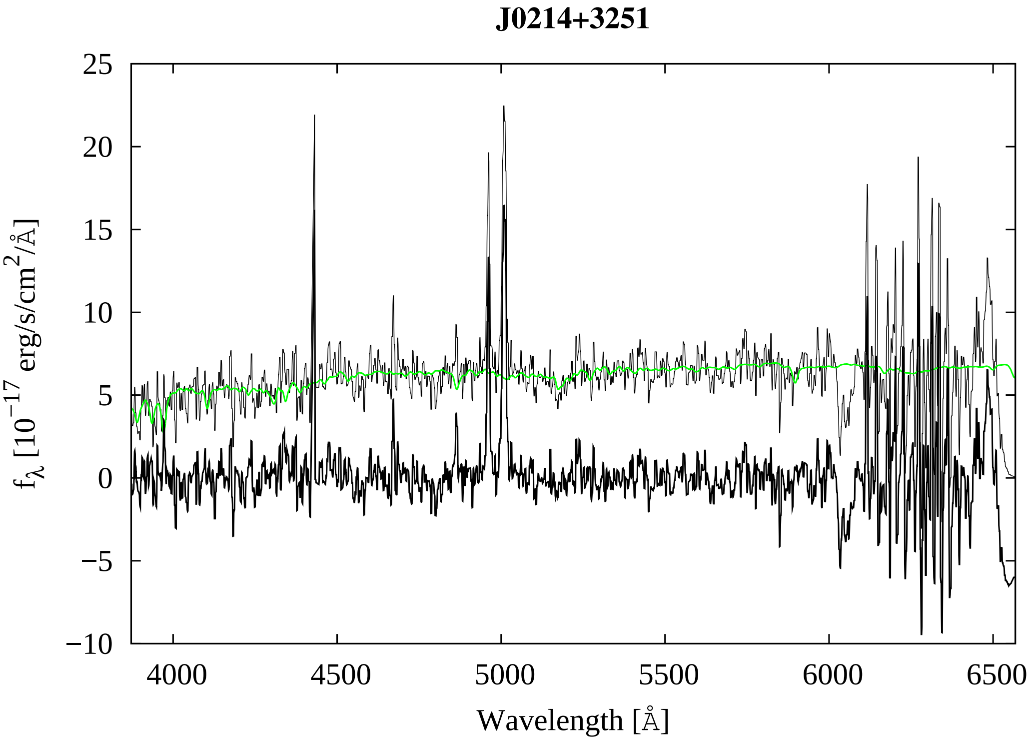
J0214+3251
25
20
15
10
5
0
−5
−10
f_λ [10^{-17} erg/s/cm^2/Å]
4000
4500
5000
5500
6000
6500
Wavelength [Å]

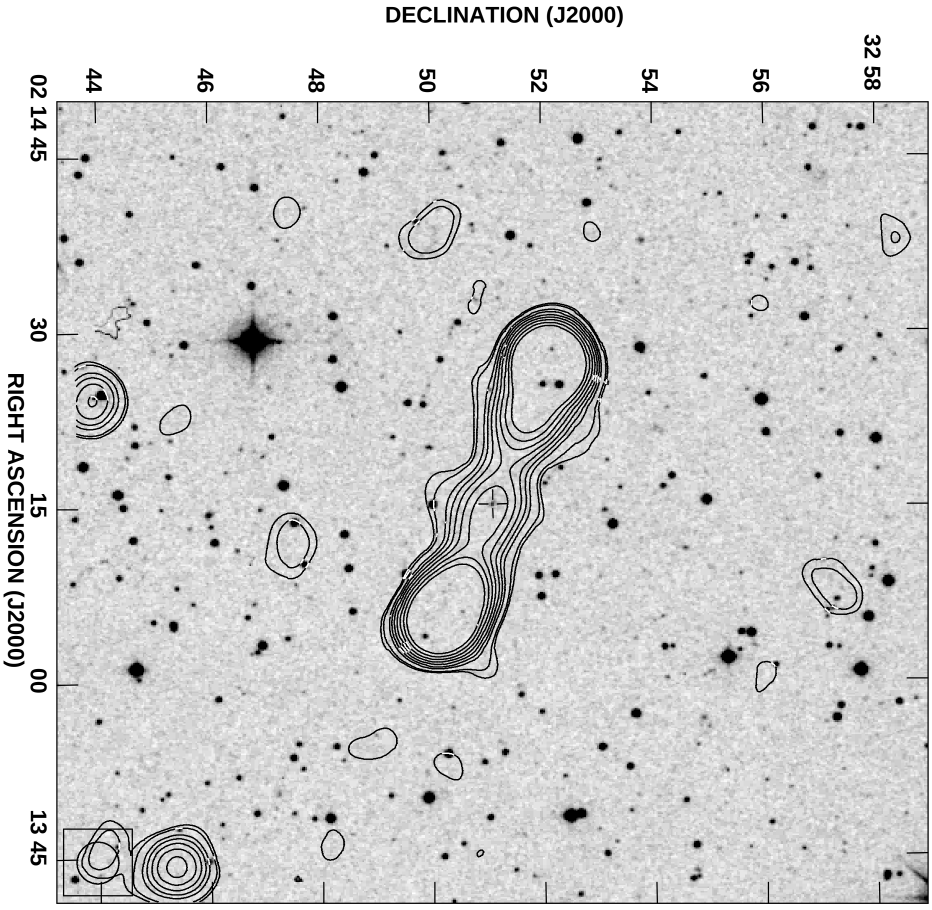
DECLINATION (J2000)
44
46
48
50
52
54
56
32 58
RIGHT ASCENSION (J2000)
02 14 45
30
15
00
13 45

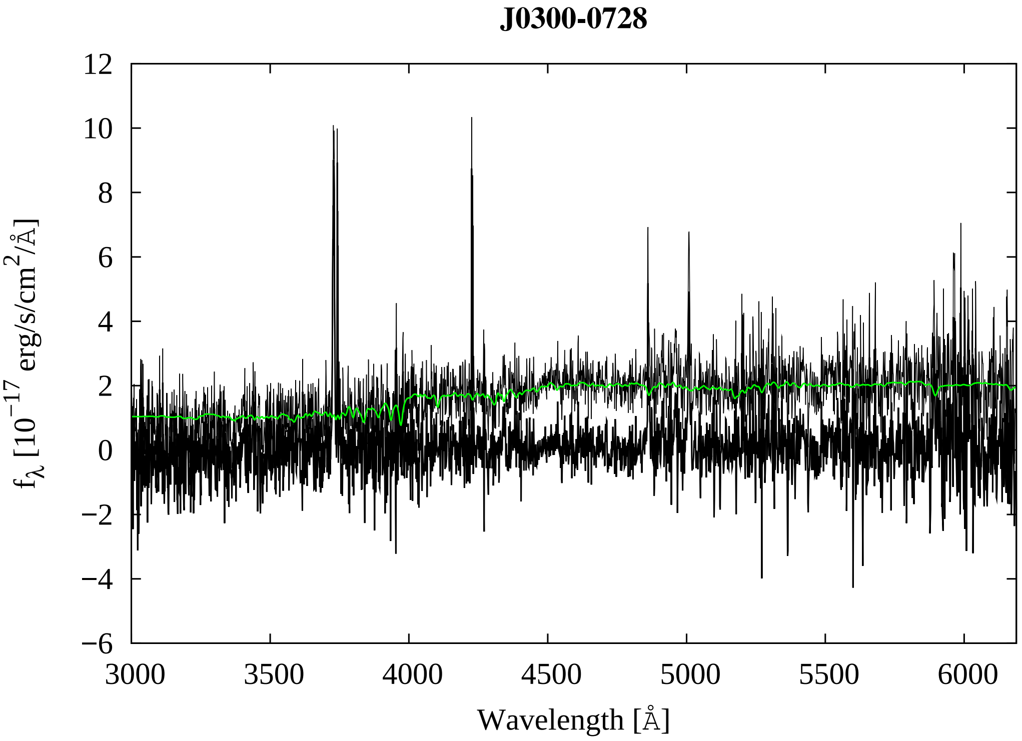
J0300-0728
12
10
8
6
4
2
0
−2
−4
−6
f_λ [10^{-17} erg/s/cm^2/Å]
3000
3500
4000
4500
5000
5500
6000
Wavelength [Å]

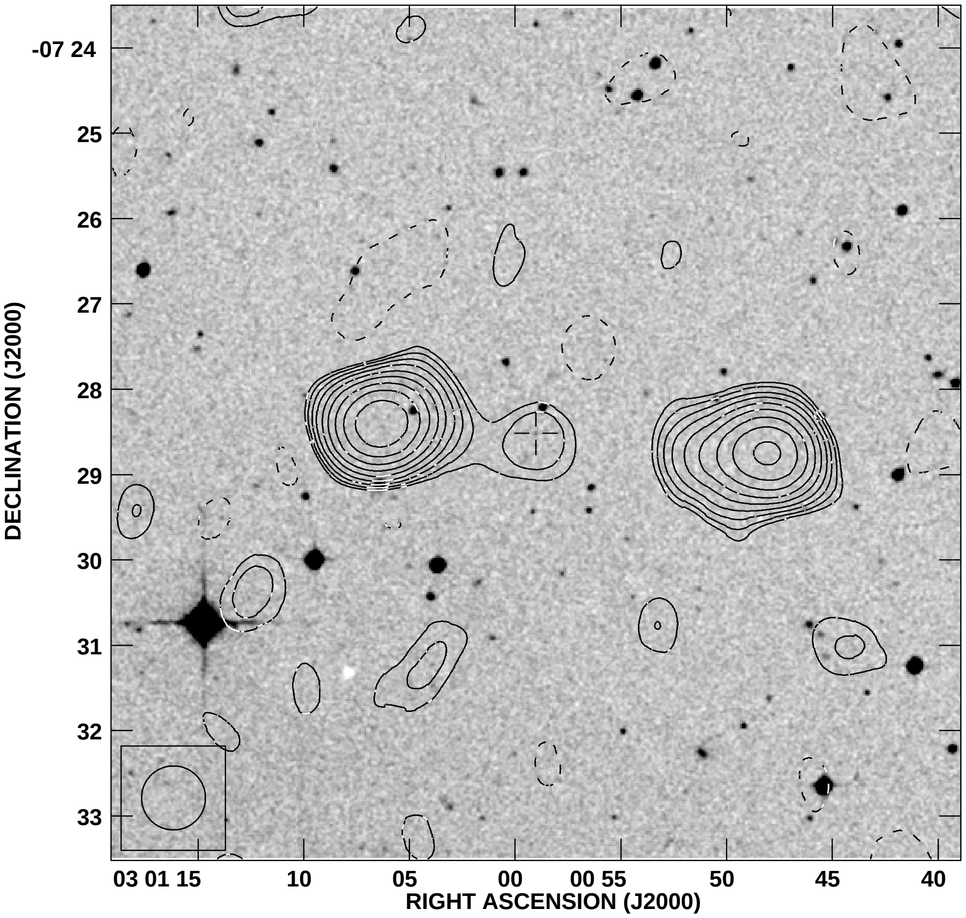
-07 24
25
26
27
28
29
30
31
32
33
DECLINATION (J2000)
03 01 15
10
05
00
00 55
50
45
40
RIGHT ASCENSION (J2000)

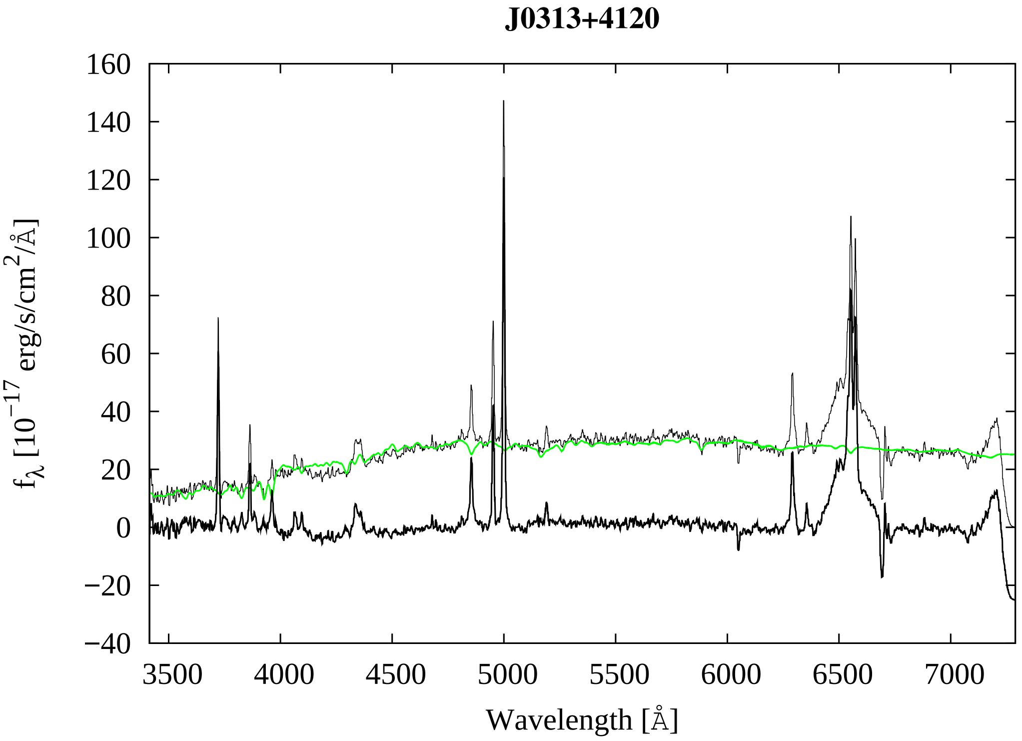
J0313+4120
160
140
120
100
80
60
40
20
0
−20
−40
f_λ [10^{-17} erg/s/cm^2/Å]
3500
4000
4500
5000
5500
6000
6500
7000
Wavelength [Å]

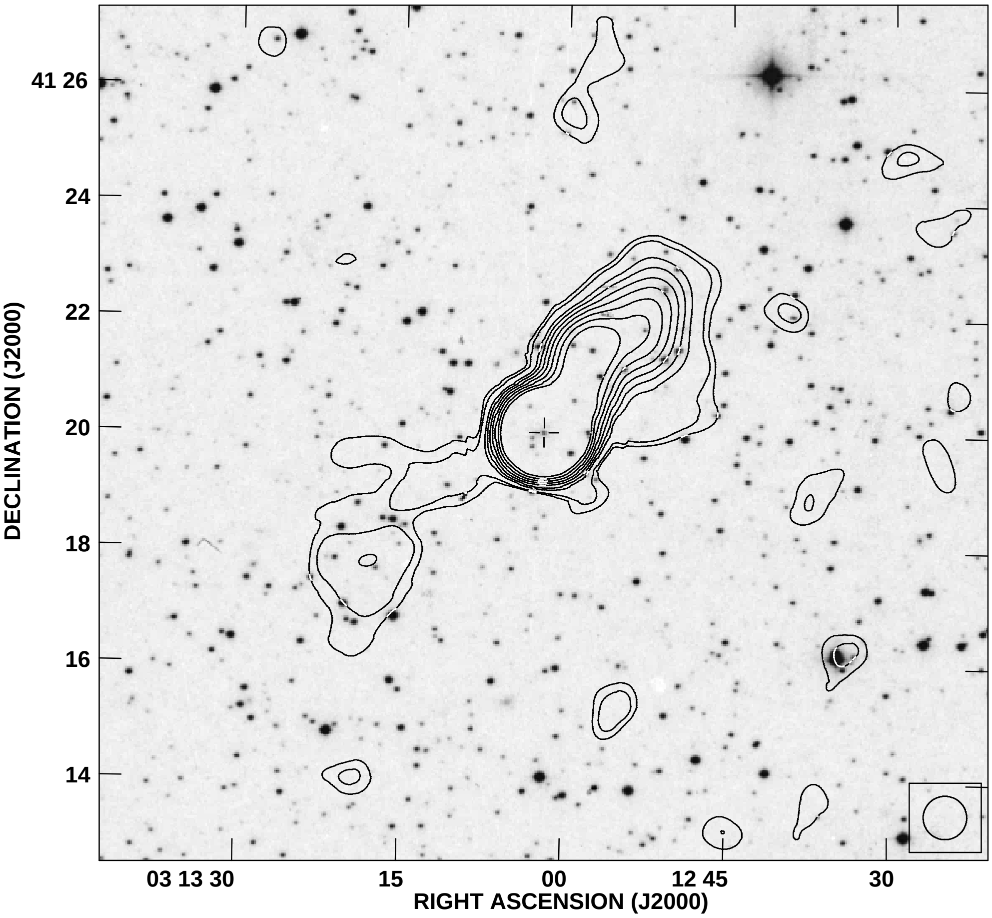
41 26
24
22
20
18
16
14
DECLINATION (J2000)
03 13 30
15
00
12 45
30
RIGHT ASCENSION (J2000)

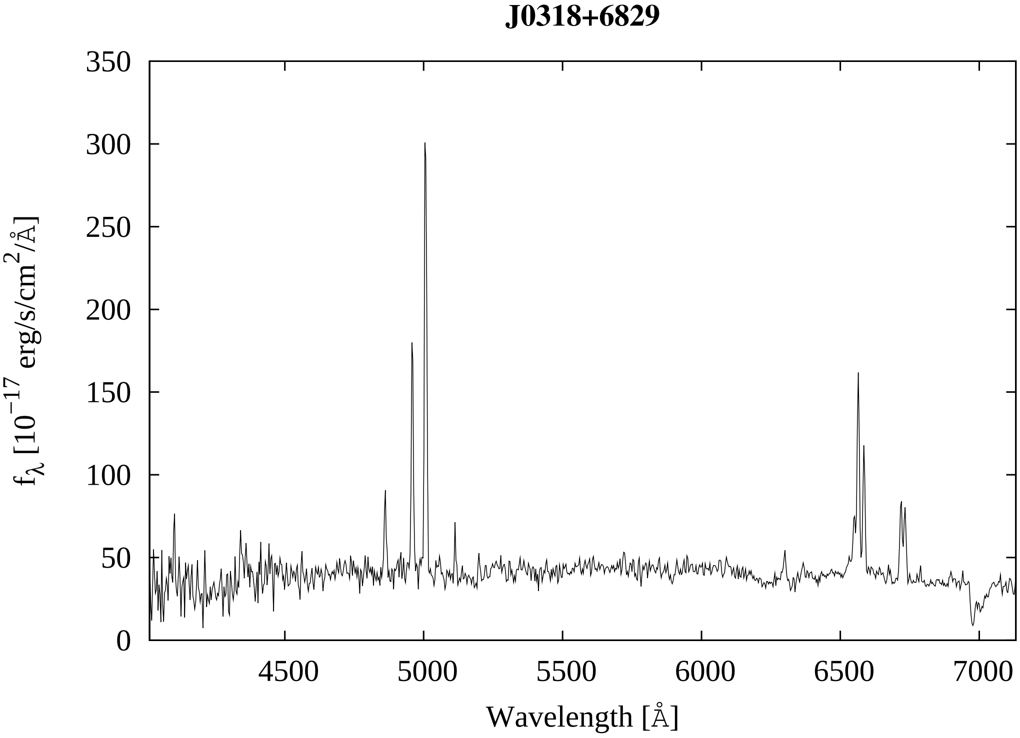
J0318+6829
0
50
100
150
200
250
300
350
f_λ [10^{-17} erg/s/cm^2/Å]
4500
5000
5500
6000
6500
7000
Wavelength [Å]

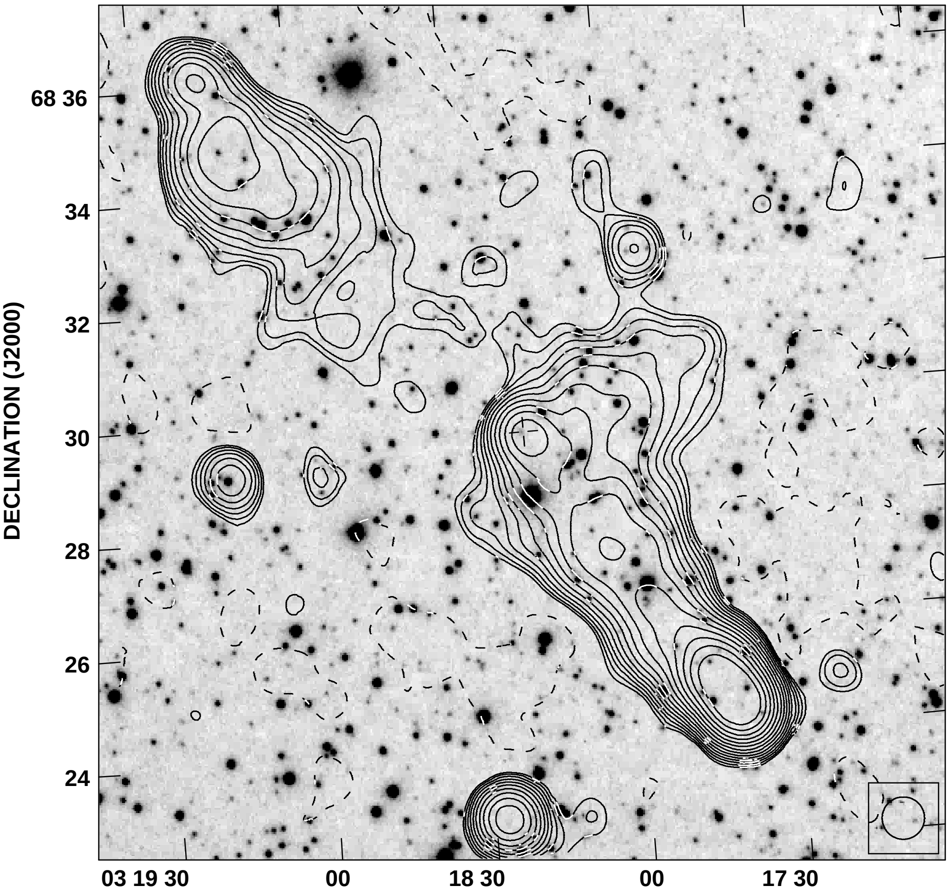
68 36
34
32
30
28
26
24
DECLINATION (J2000)
03 19 30
00
18 30
00
17 30
RIGHT ASCENSION (J2000)

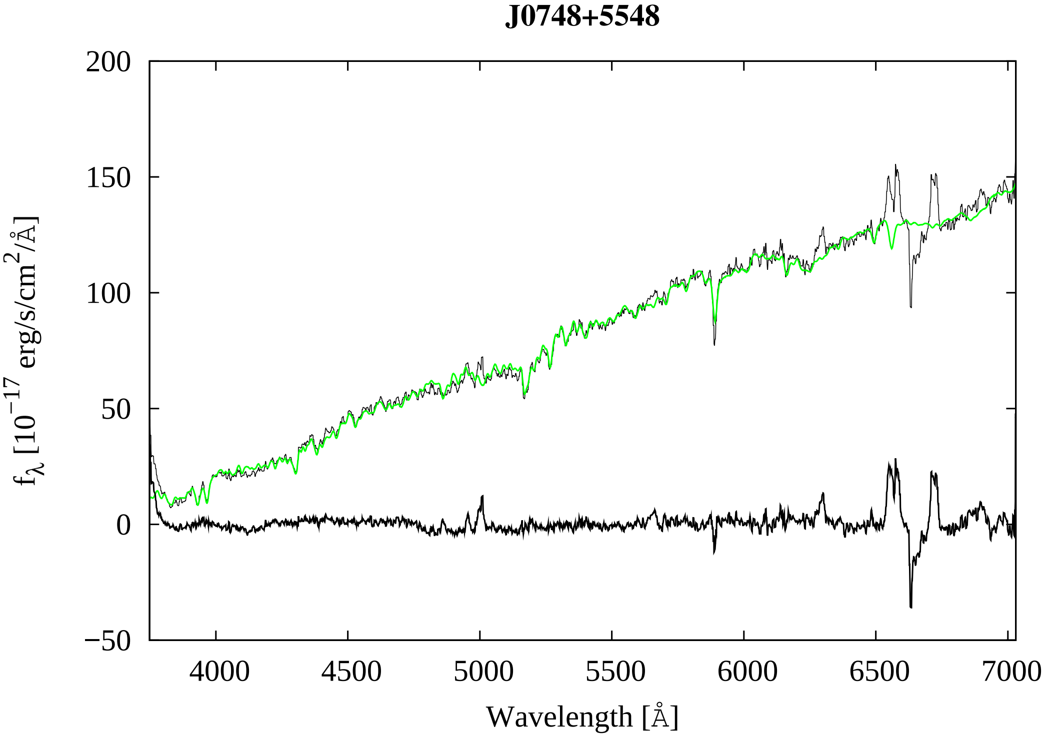
J0748+5548
200
150
100
50
0
−50
f_λ [10^{-17} erg/s/cm^2/Å]
4000
4500
5000
5500
6000
6500
7000
Wavelength [Å]

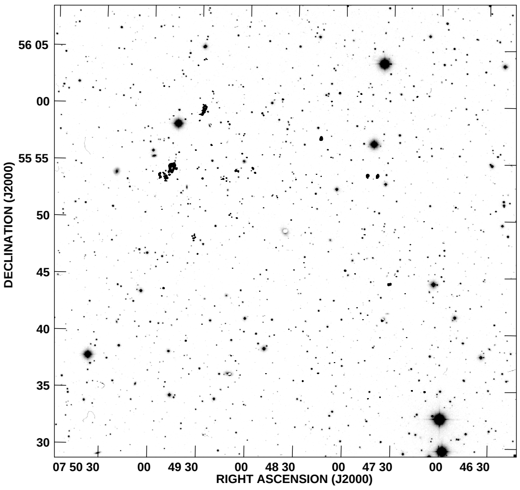
56 05
00
55 55
50
45
40
35
30
DECLINATION (J2000)
07 50 30
00
49 30
00
48 30
00
47 30
00
46 30
RIGHT ASCENSION (J2000)

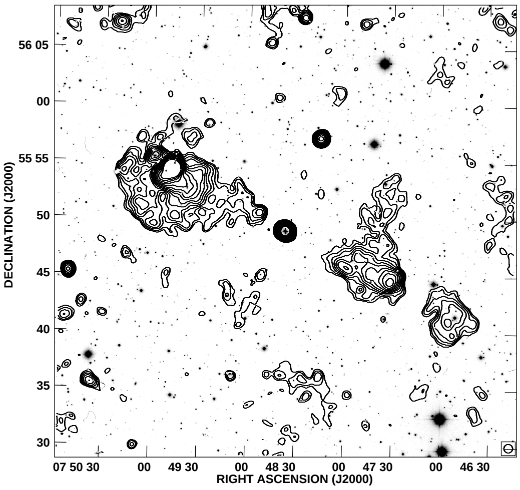
56 05
00
55 55
50
45
40
35
30
DECLINATION (J2000)
07 50 30
00
49 30
00
48 30
00
47 30
00
46 30
RIGHT ASCENSION (J2000)

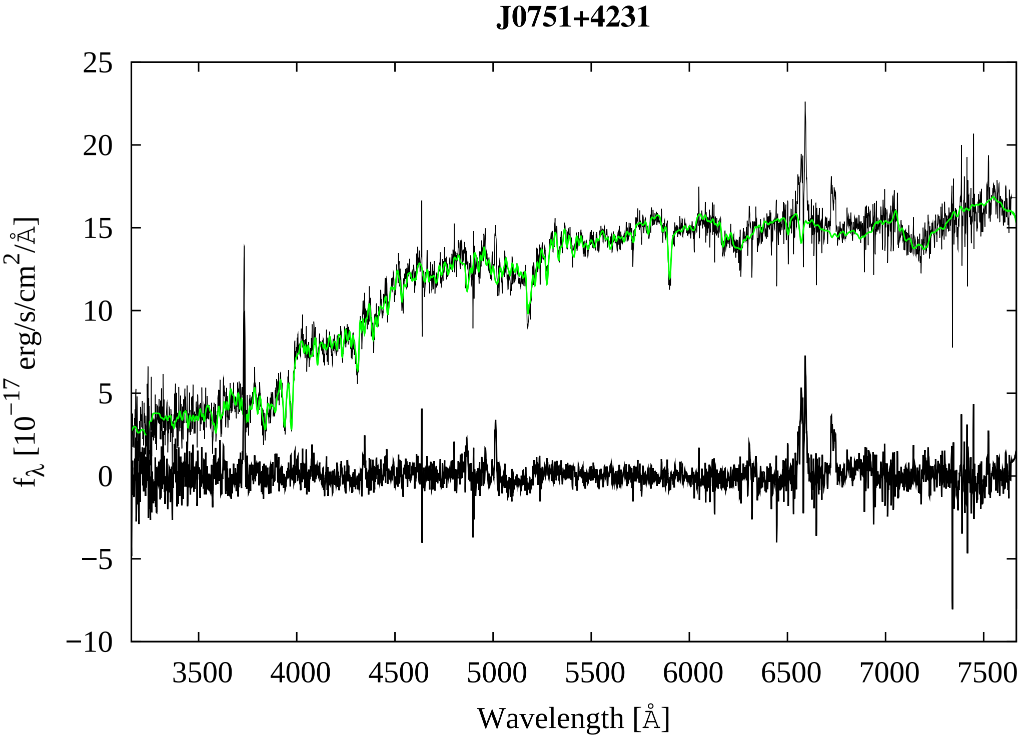
J0751+4231
f$_\lambda$ [10^{-17} erg/s/cm^2/Å]
25
20
15
10
5
0
−5
−10
3500
4000
4500
5000
5500
6000
6500
7000
7500
Wavelength [Å]

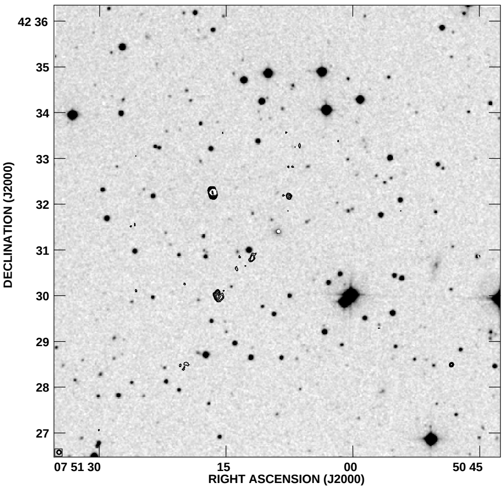
42 36
35
34
33
32
31
30
29
28
27
DECLINATION (J2000)
07 51 30
15
00
50 45
RIGHT ASCENSION (J2000)

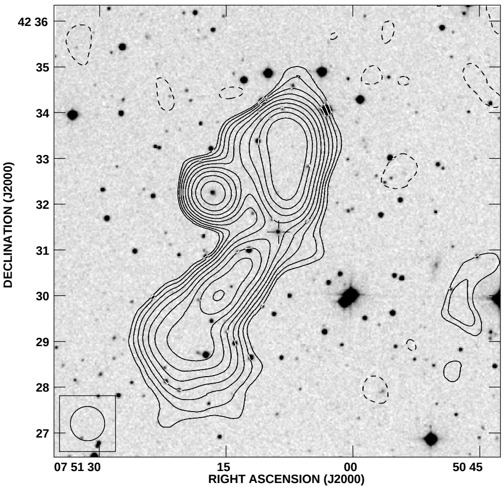
42 36
35
34
33
32
31
30
29
28
27
DECLINATION (J2000)
07 51 30
15
00
50 45
RIGHT ASCENSION (J2000)

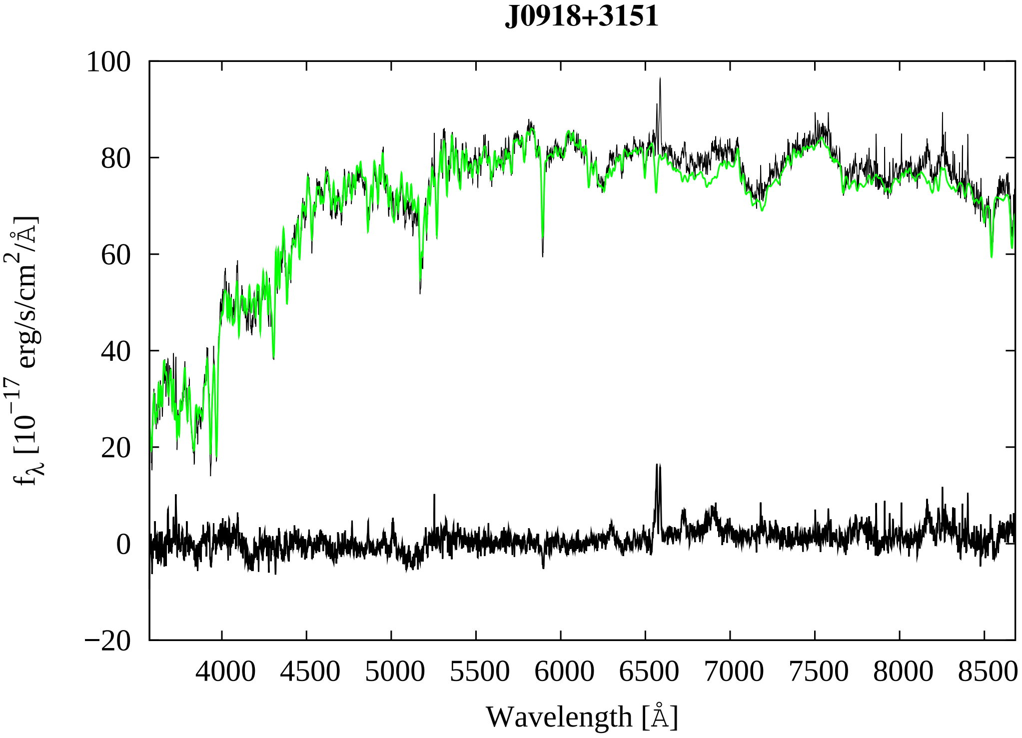
J0918+3151
f$_\lambda$ [10^{-17} erg/s/cm^2/Å]
100
80
60
40
20
0
−20
4000
4500
5000
5500
6000
6500
7000
7500
8000
8500
Wavelength [Å]

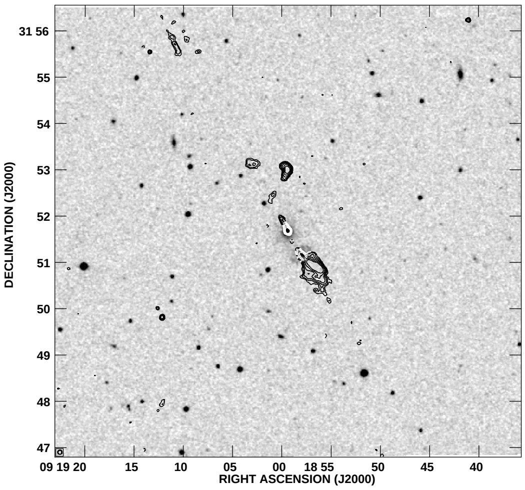
DECLINATION (J2000)
31 56
55
54
53
52
51
50
49
48
47
09 19 20
15
10
05
00
18 55
50
45
40
RIGHT ASCENSION (J2000)

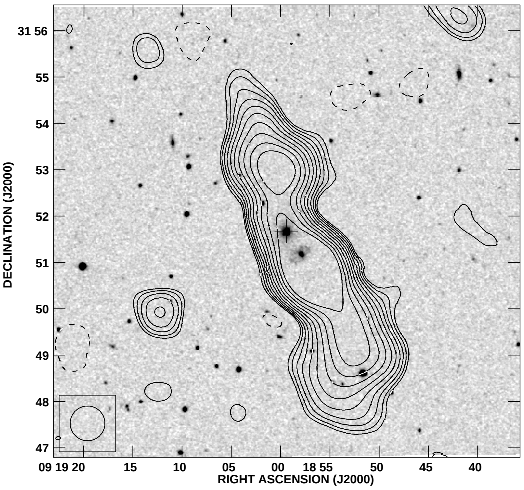
DECLINATION (J2000)
31 56
55
54
53
52
51
50
49
48
47
09 19 20
15
10
05
00
18 55
50
45
40
RIGHT ASCENSION (J2000)

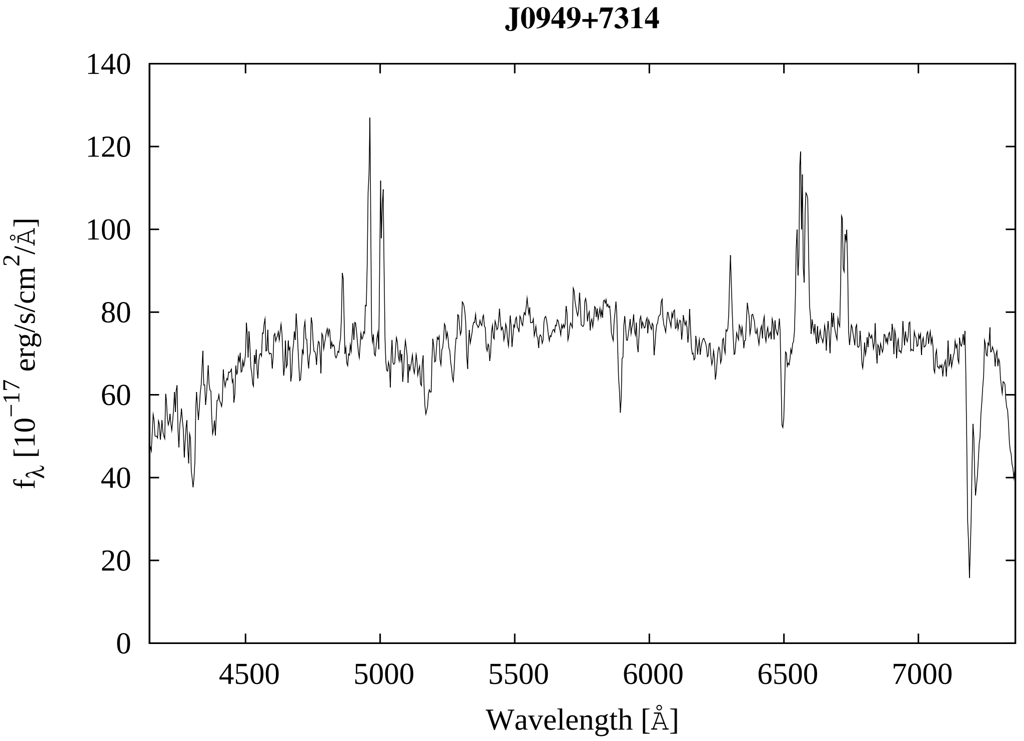
J0949+7314
140
120
100
80
60
40
20
0
f_λ [10^{-17} erg/s/cm^2/Å]
4500
5000
5500
6000
6500
7000
Wavelength [Å]

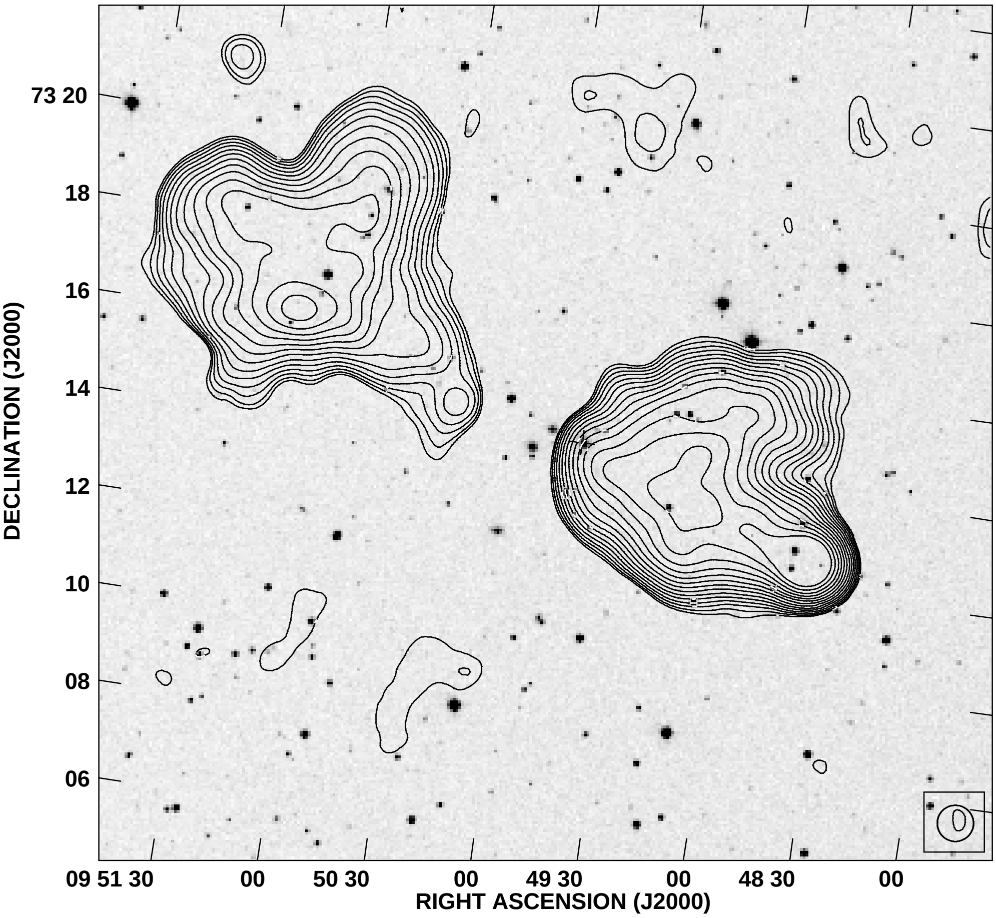
73 20
18
16
14
12
10
08
06
DECLINATION (J2000)
09 51 30
00
50 30
00
49 30
00
48 30
00
RIGHT ASCENSION (J2000)

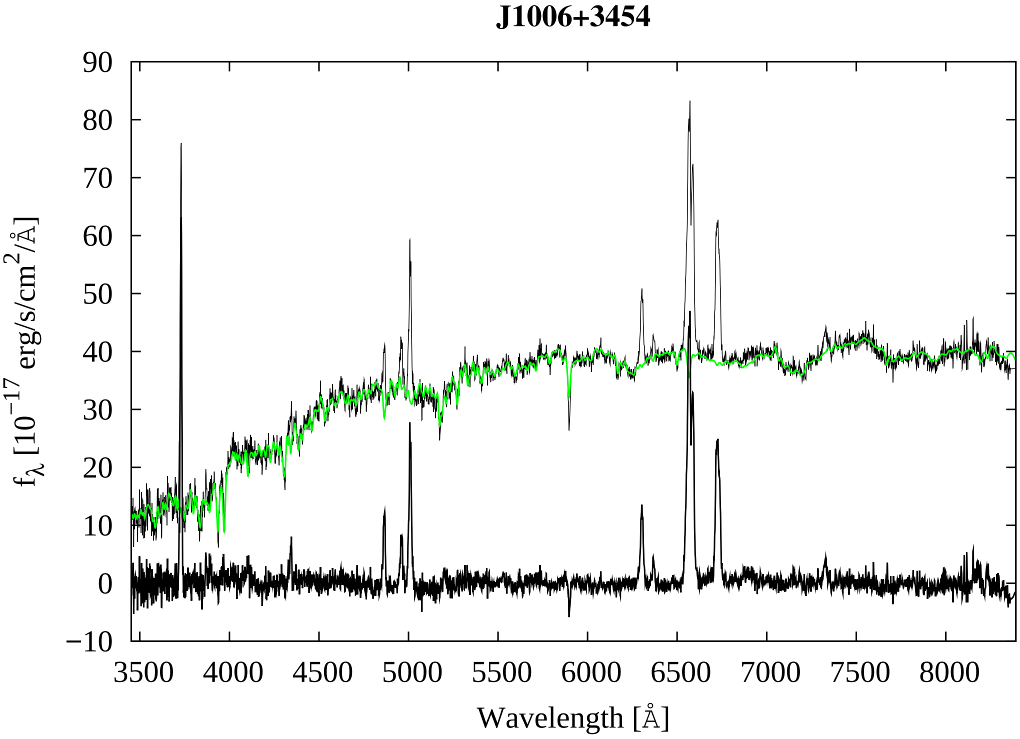
J1006+3454
90
80
70
60
50
40
30
20
10
0
−10
f_λ [10^{-17} erg/s/cm^2/Å]
3500
4000
4500
5000
5500
6000
6500
7000
7500
8000
Wavelength [Å]

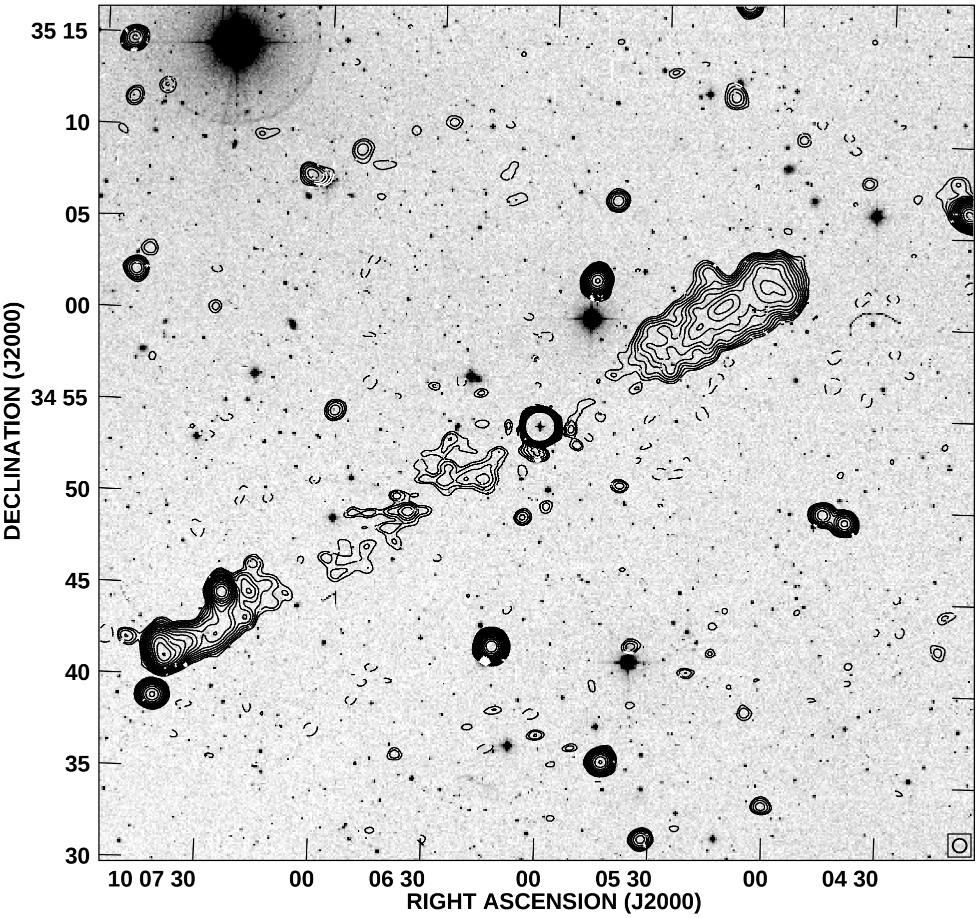
35 15
10
05
00
34 55
50
45
40
35
30
DECLINATION (J2000)
10 07 30
00
06 30
00
05 30
00
04 30
RIGHT ASCENSION (J2000)

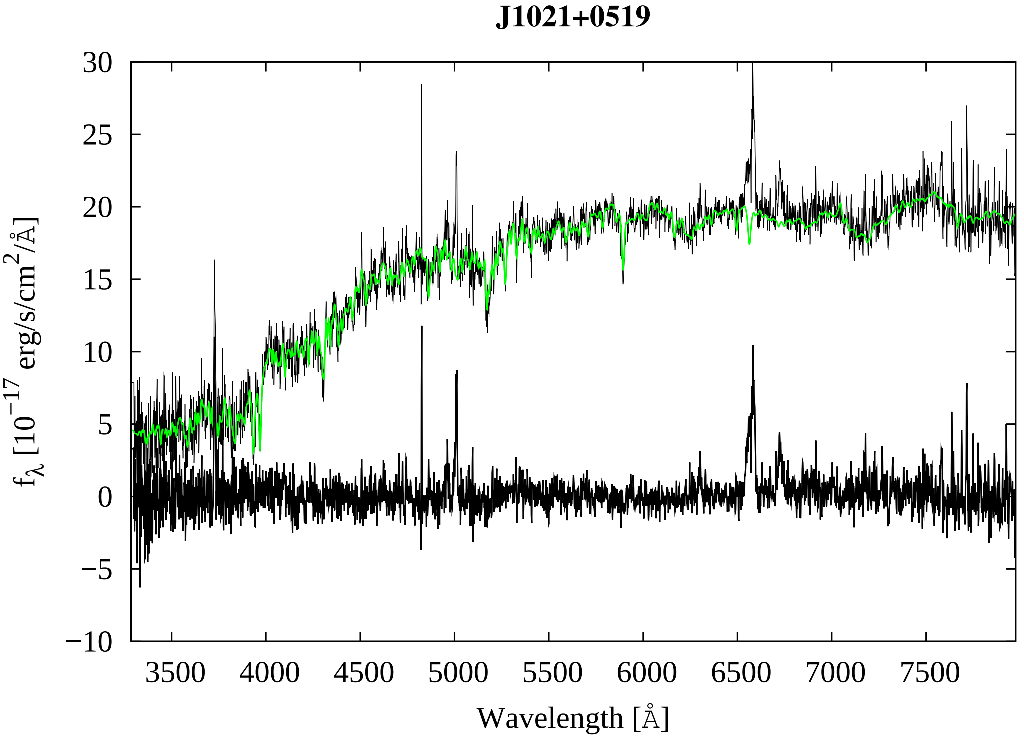
J1021+0519
30
25
20
15
10
5
0
−5
−10
3500
4000
4500
5000
5500
6000
6500
7000
7500
Wavelength [Å]
f_λ [10^{-17} erg/s/cm^2/Å]

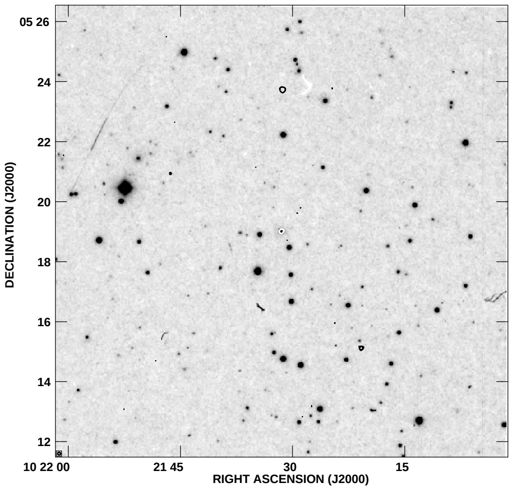
05 26
24
22
20
18
16
14
12
DECLINATION (J2000)
10 22 00
21 45
30
15
RIGHT ASCENSION (J2000)

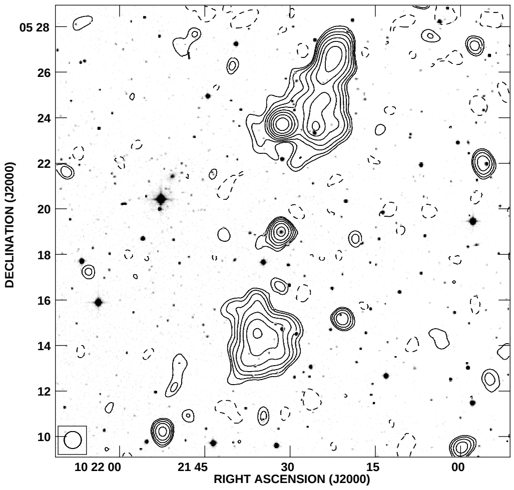
05 28
26
24
22
20
18
16
14
12
10
DECLINATION (J2000)
10 22 00
21 45
30
15
00
RIGHT ASCENSION (J2000)

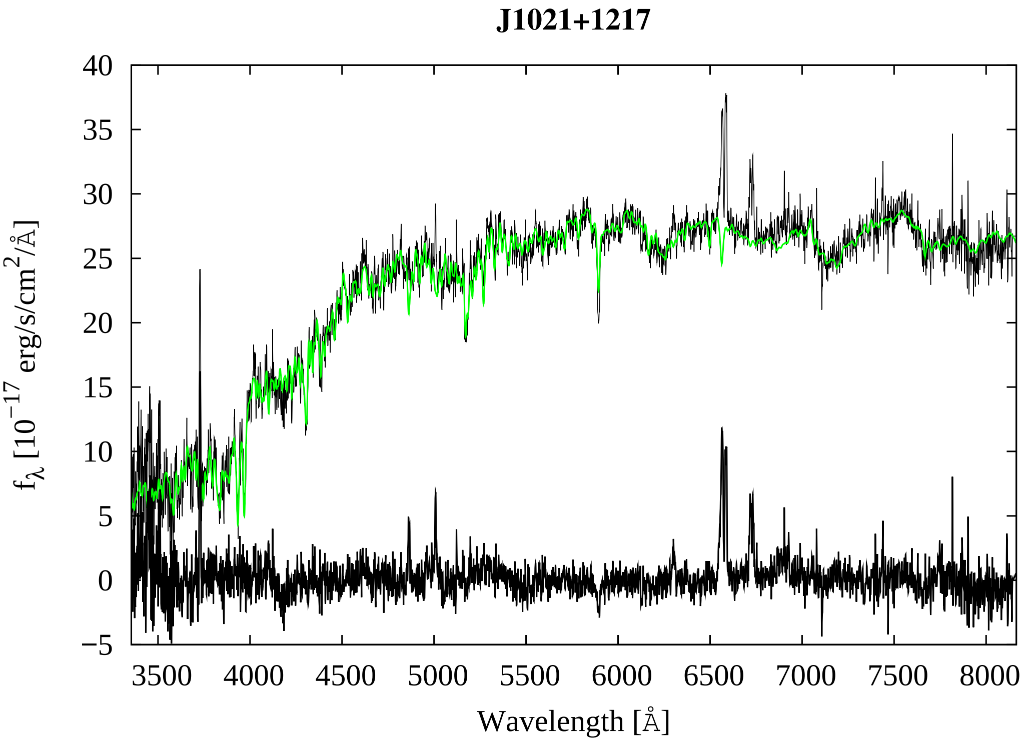
J1021+1217
f$_\lambda$ [10^{-17} erg/s/cm^2/Å]
40
35
30
25
20
15
10
5
0
−5
3500
4000
4500
5000
5500
6000
6500
7000
7500
8000
Wavelength [Å]

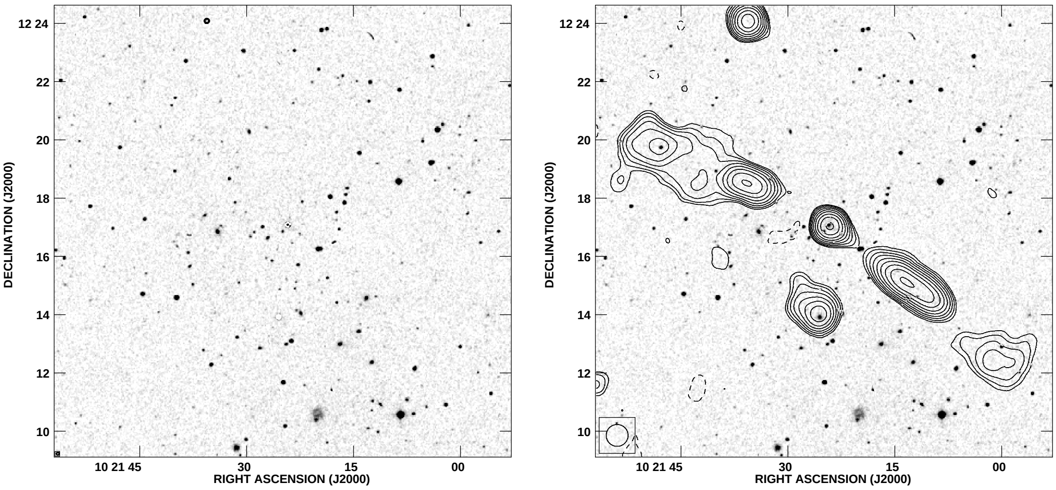
DECLINATION (J2000)
12 24
22
20
18
16
14
12
10
10 21 45
30
15
00
RIGHT ASCENSION (J2000)
DECLINATION (J2000)
12 24
22
20
18
16
14
12
10
10 21 45
30
15
00
RIGHT ASCENSION (J2000)

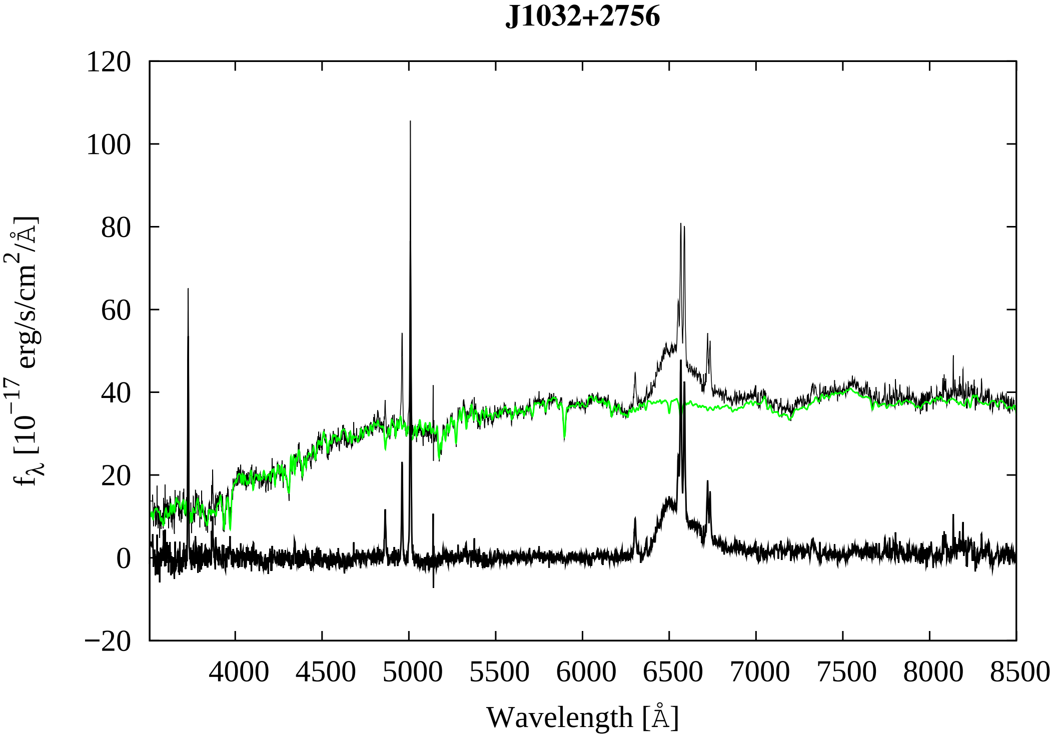
J1032+2756
f_λ [10^{-17} erg/s/cm^2/Å]
120
100
80
60
40
20
0
−20
4000
4500
5000
5500
6000
6500
7000
7500
8000
8500
Wavelength [Å]

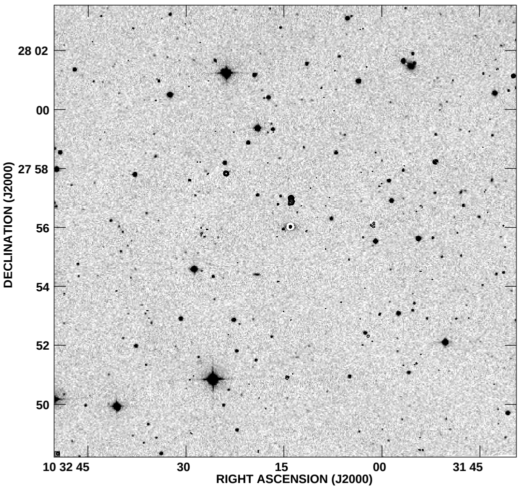
DECLINATION (J2000)
28 02
00
27 58
56
54
52
50
10 32 45
30
15
00
31 45
RIGHT ASCENSION (J2000)

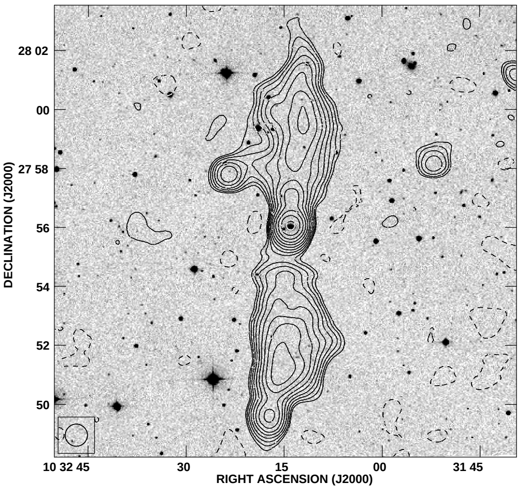
DECLINATION (J2000)
28 02
00
27 58
56
54
52
50
10 32 45
30
15
00
31 45
RIGHT ASCENSION (J2000)

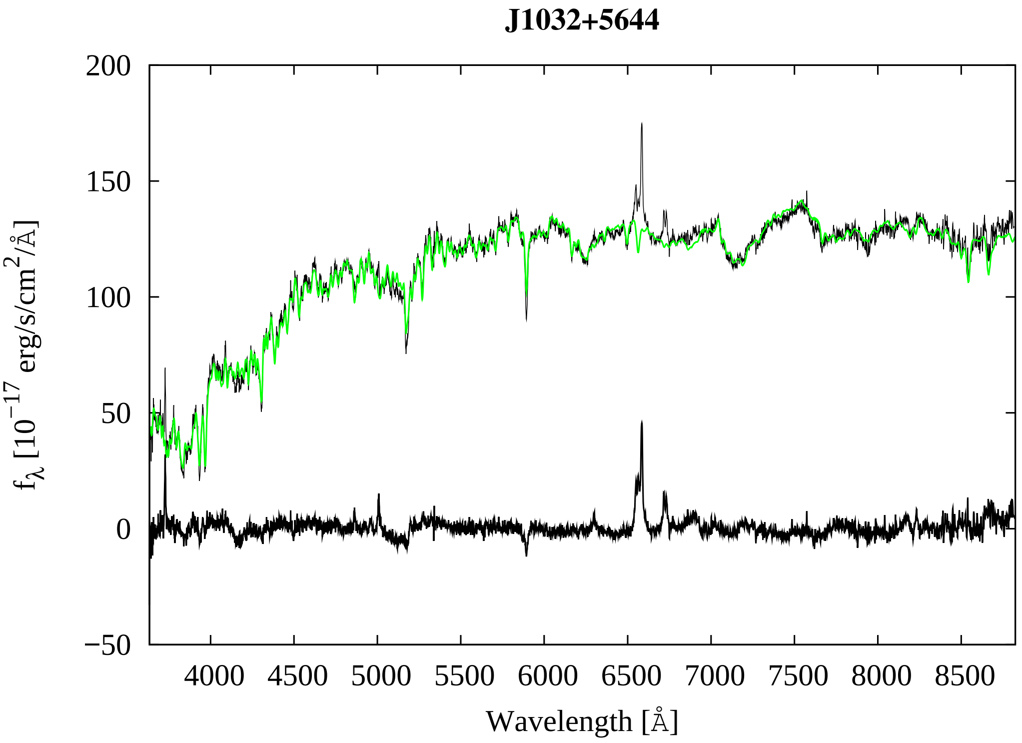
J1032+5644
200
150
100
50
0
−50
f_λ [10^{-17} erg/s/cm^2/Å]
4000
4500
5000
5500
6000
6500
7000
7500
8000
8500
Wavelength [Å]

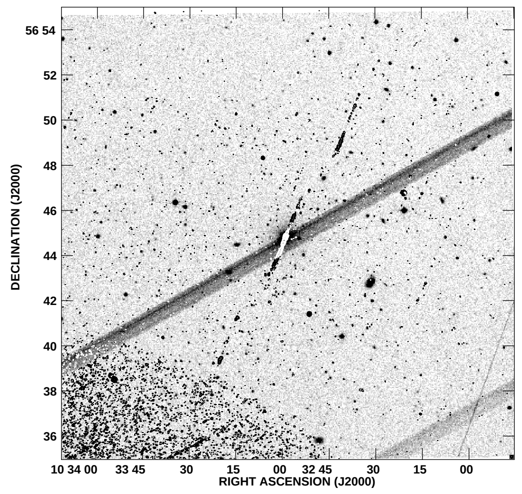
DECLINATION (J2000)
56 54
52
50
48
46
44
42
40
38
36
10 34 00
33 45
30
15
00
32 45
30
15
00
RIGHT ASCENSION (J2000)

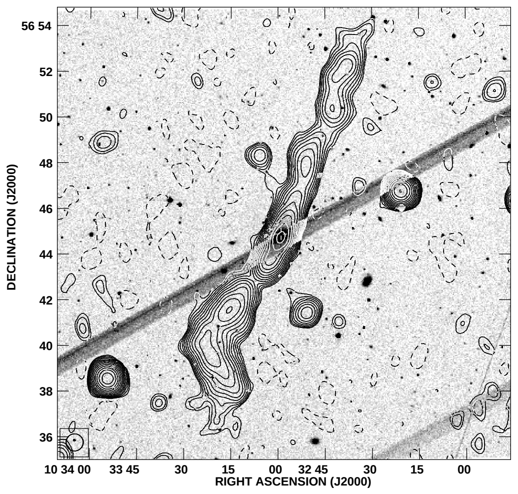
DECLINATION (J2000)
56 54
52
50
48
46
44
42
40
38
36
10 34 00
33 45
30
15
00
32 45
30
15
00
RIGHT ASCENSION (J2000)

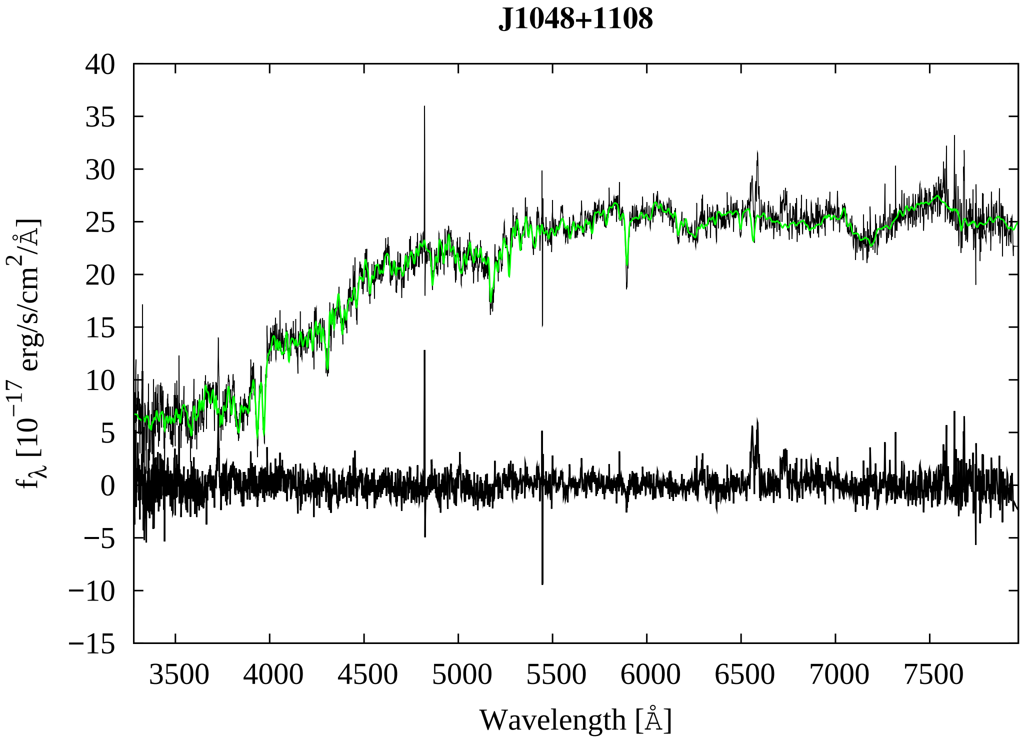
J1048+1108
f_λ [10^{-17} erg/s/cm^2/Å]
40
35
30
25
20
15
10
5
0
−5
−10
−15
3500
4000
4500
5000
5500
6000
6500
7000
7500
Wavelength [Å]

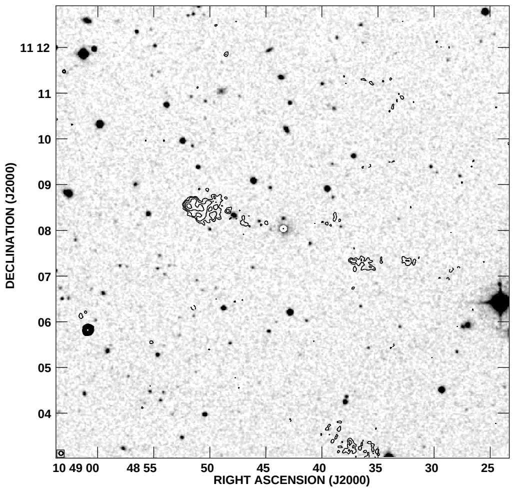
DECLINATION (J2000)
11 12
11
10
09
08
07
06
05
04
10 49 00
48 55
50
45
40
35
30
25
RIGHT ASCENSION (J2000)

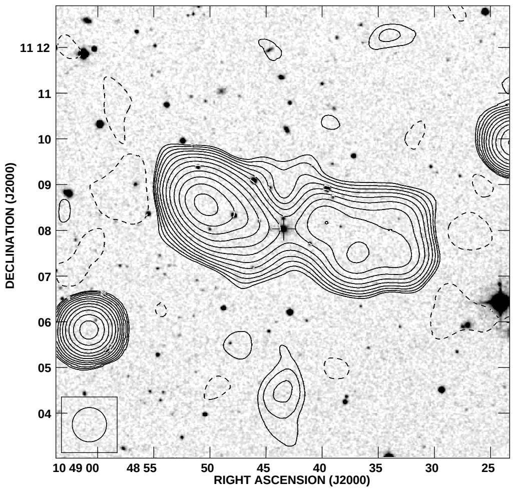
DECLINATION (J2000)
11 12
11
10
09
08
07
06
05
04
10 49 00
48 55
50
45
40
35
30
25
RIGHT ASCENSION (J2000)

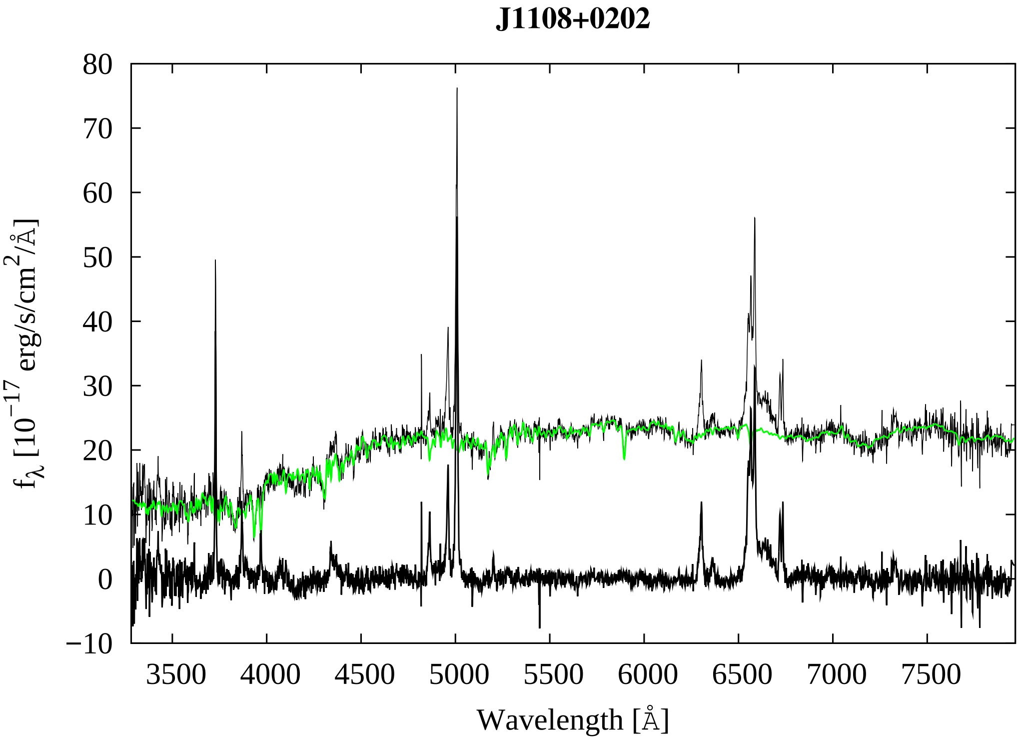
J1108+0202
80
70
60
50
40
30
20
10
0
−10
f_λ [10^{-17} erg/s/cm^2/Å]
3500
4000
4500
5000
5500
6000
6500
7000
7500
Wavelength [Å]

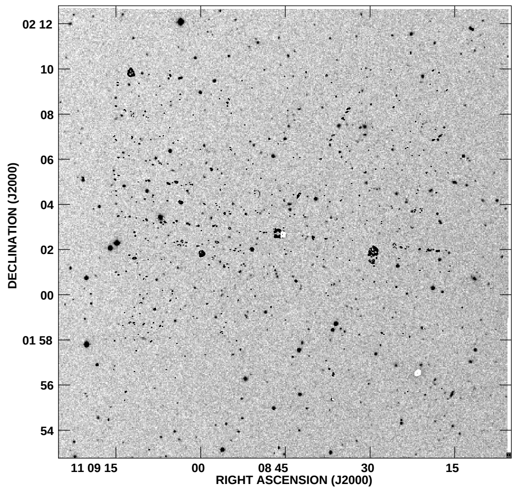
02 12
10
08
06
04
02
00
01 58
56
54
DECLINATION (J2000)
11 09 15
00
08 45
30
15
RIGHT ASCENSION (J2000)

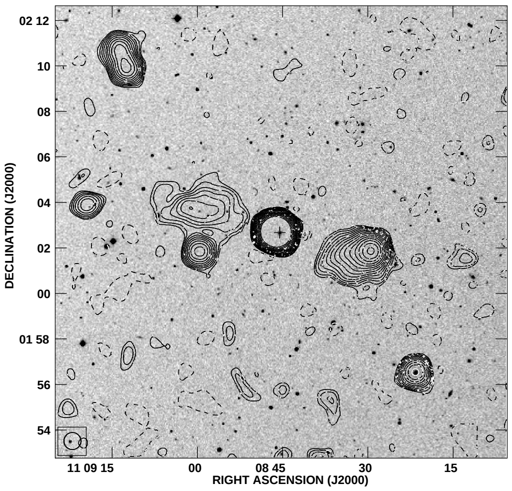
02 12
10
08
06
04
02
00
01 58
56
54
DECLINATION (J2000)
11 09 15
00
08 45
30
15
RIGHT ASCENSION (J2000)

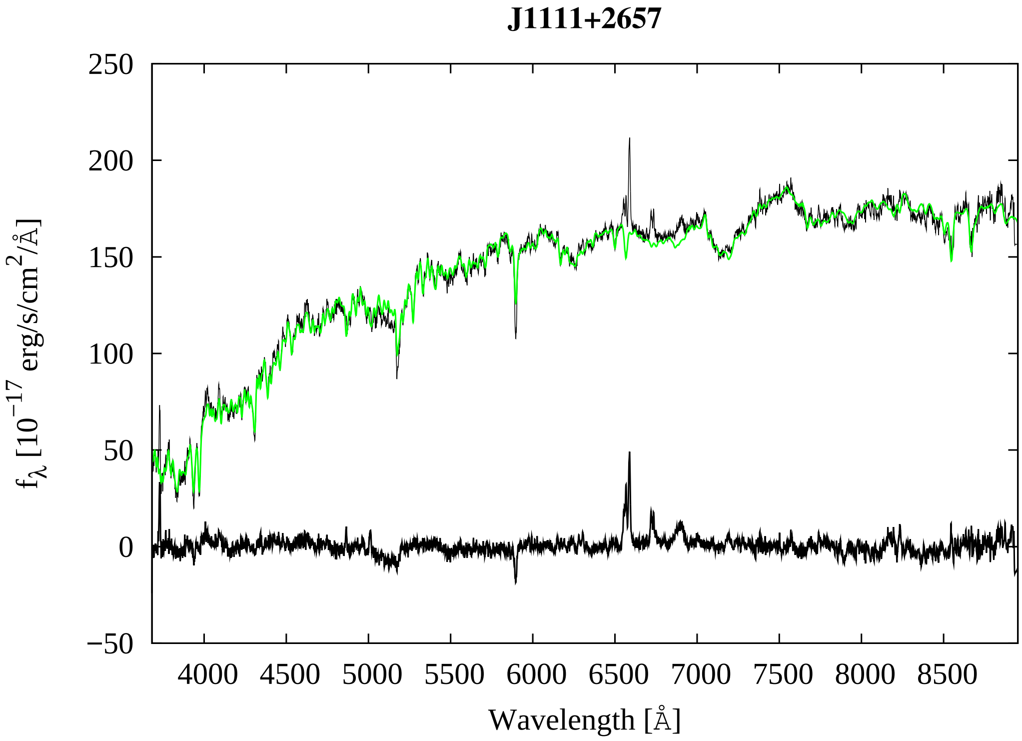
J1111+2657
250
200
150
100
50
0
−50
f_λ [10^{-17} erg/s/cm^2/Å]
4000
4500
5000
5500
6000
6500
7000
7500
8000
8500
Wavelength [Å]

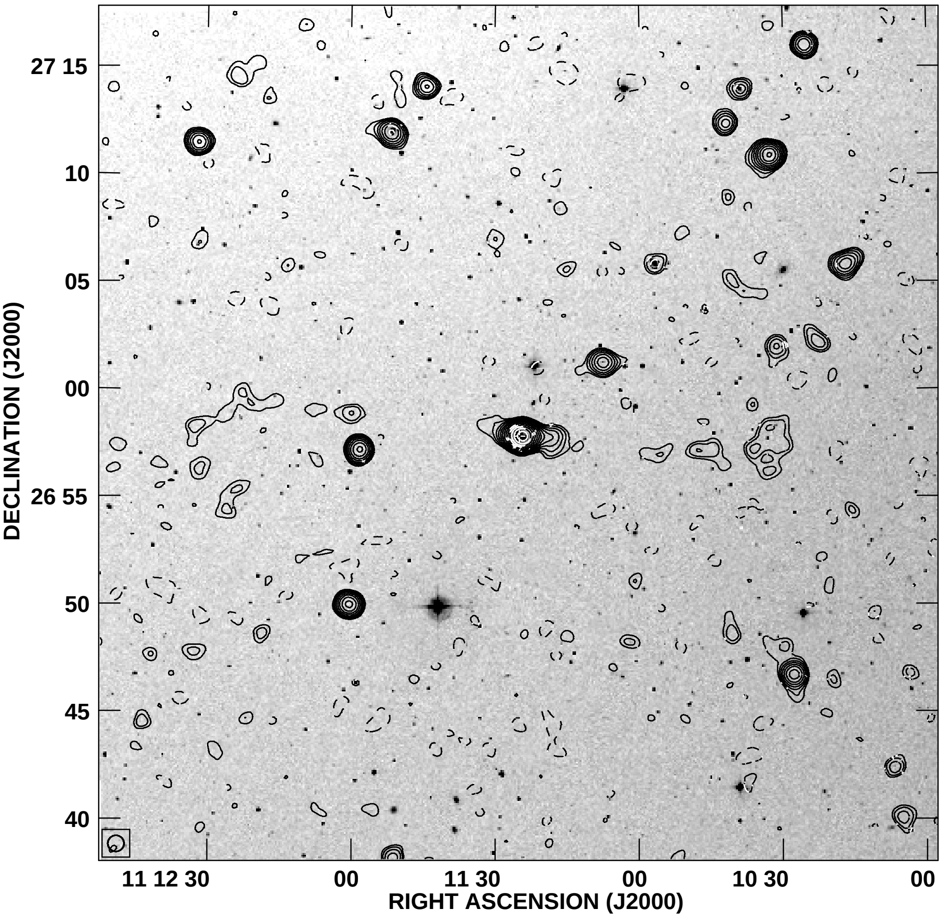
27 15
10
05
00
26 55
50
45
40
DECLINATION (J2000)
11 12 30
00
11 30
00
10 30
00
RIGHT ASCENSION (J2000)

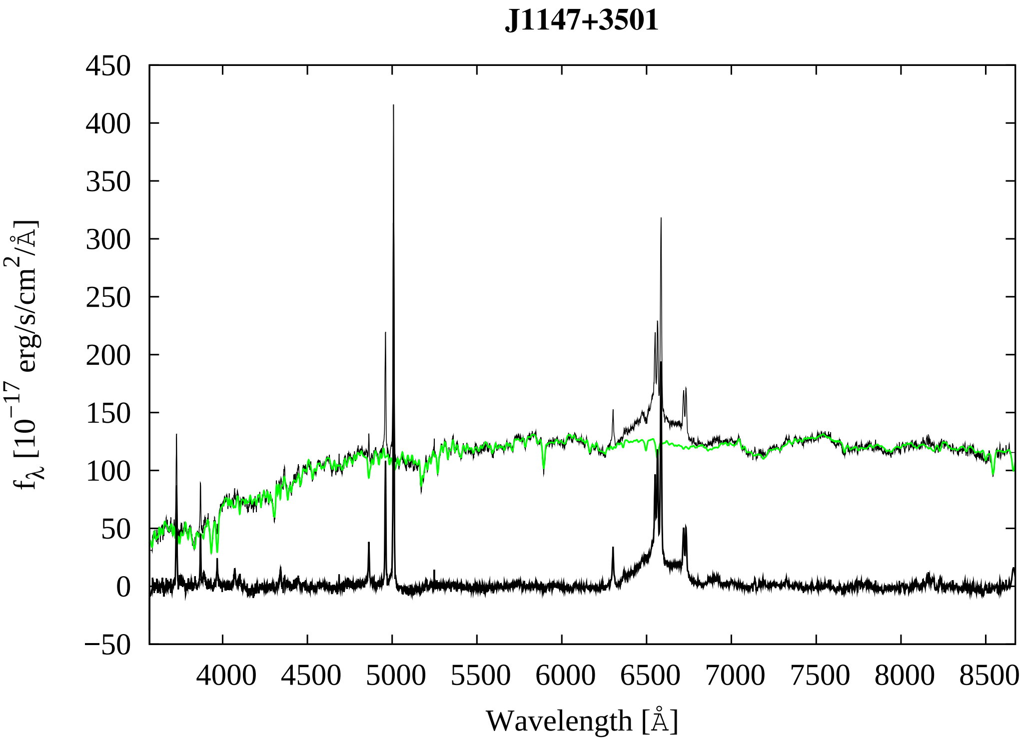
J1147+3501
450
400
350
300
250
200
150
100
50
0
−50
f_λ [10^{-17} erg/s/cm^2/Å]
4000
4500
5000
5500
6000
6500
7000
7500
8000
8500
Wavelength [Å]

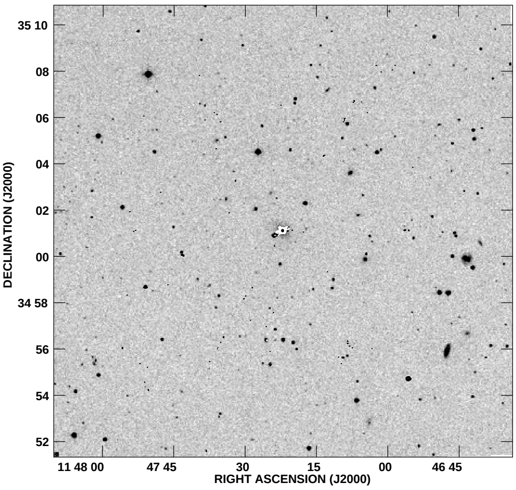
35 10
08
06
04
02
00
34 58
56
54
52
DECLINATION (J2000)
11 48 00
47 45
30
15
00
46 45
RIGHT ASCENSION (J2000)

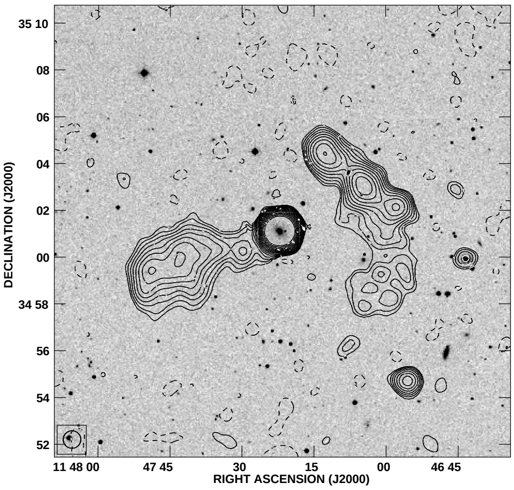
35 10
08
06
04
02
00
34 58
56
54
52
DECLINATION (J2000)
11 48 00
47 45
30
15
00
46 45
RIGHT ASCENSION (J2000)

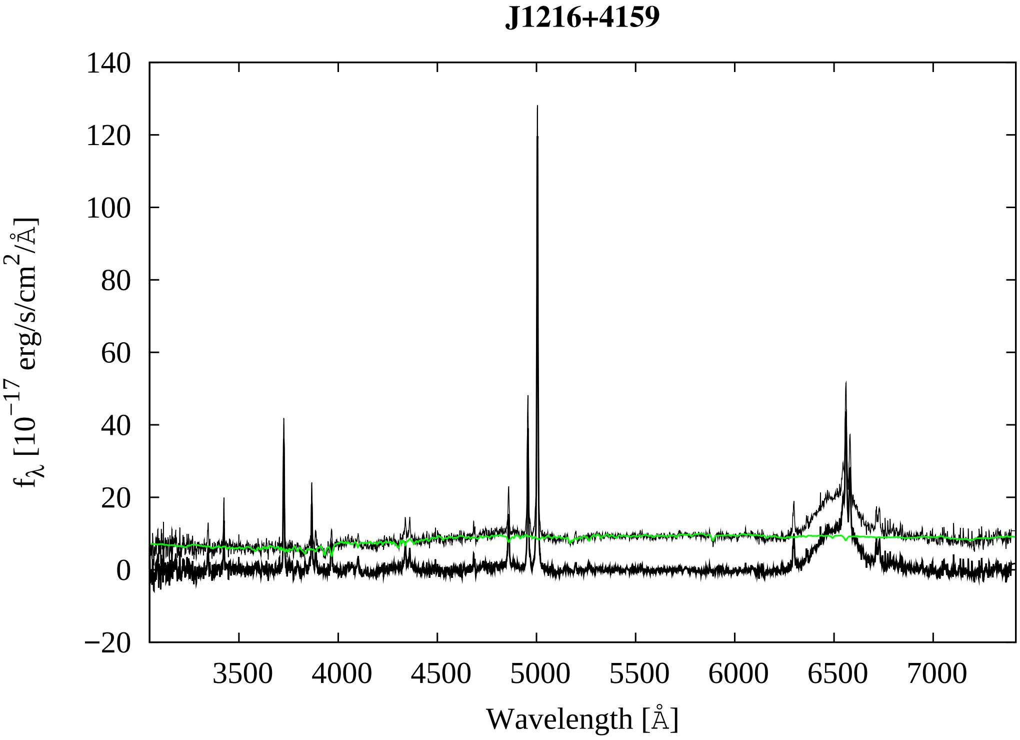
J1216+4159
140
120
100
80
60
40
20
0
−20
f_λ [10^{-17} erg/s/cm^2/Å]
3500
4000
4500
5000
5500
6000
6500
7000
Wavelength [Å]

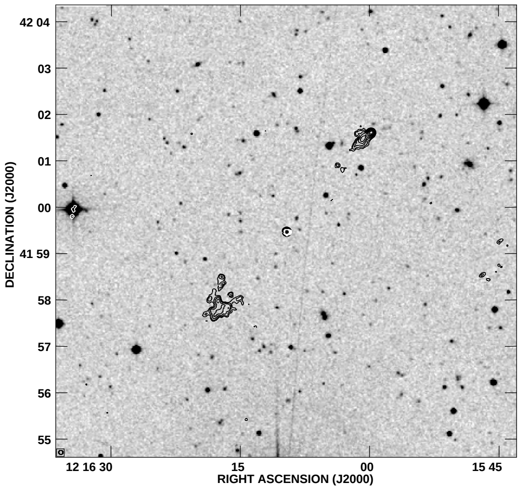
42 04
03
02
01
00
41 59
58
57
56
55
DECLINATION (J2000)
12 16 30
15
00
15 45
RIGHT ASCENSION (J2000)

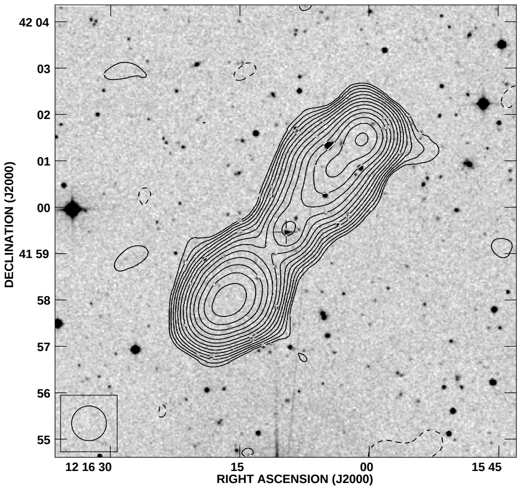
42 04
03
02
01
00
41 59
58
57
56
55
DECLINATION (J2000)
12 16 30
15
00
15 45
RIGHT ASCENSION (J2000)

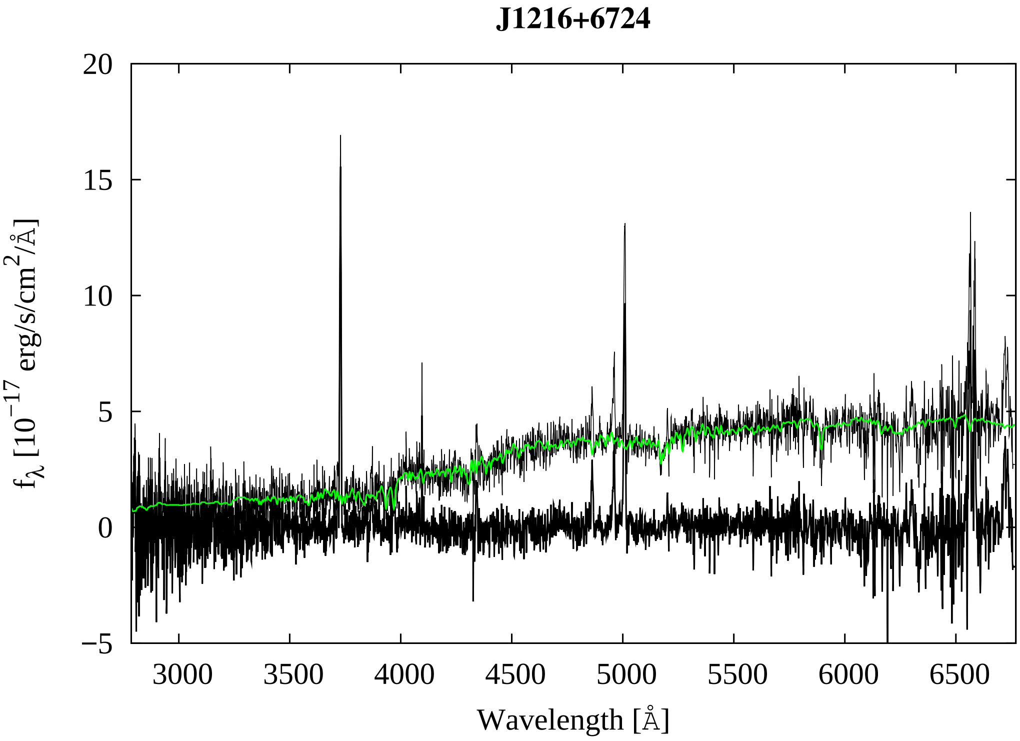
J1216+6724
20
15
10
5
0
−5
3000
3500
4000
4500
5000
5500
6000
6500
Wavelength [Å]
f_λ [10^{-17} erg/s/cm^2/Å]

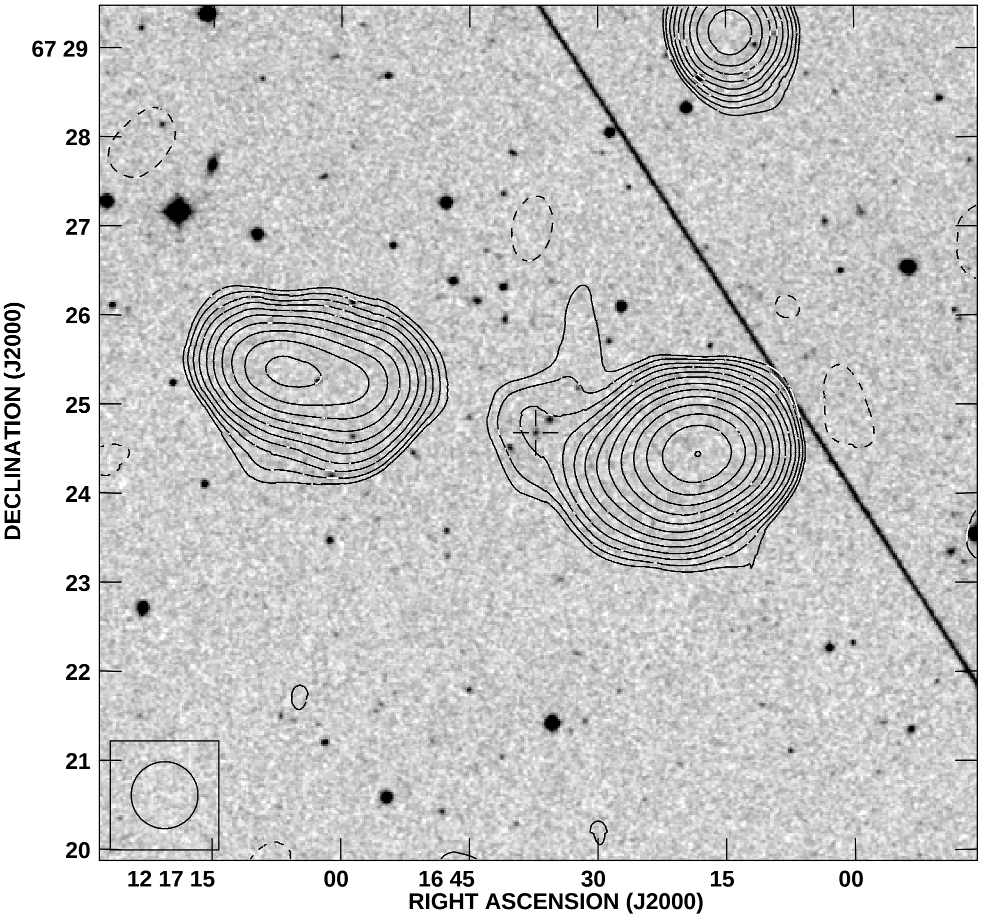
67 29
28
27
26
25
24
23
22
21
20
DECLINATION (J2000)
12 17 15
00
16 45
30
15
00
RIGHT ASCENSION (J2000)

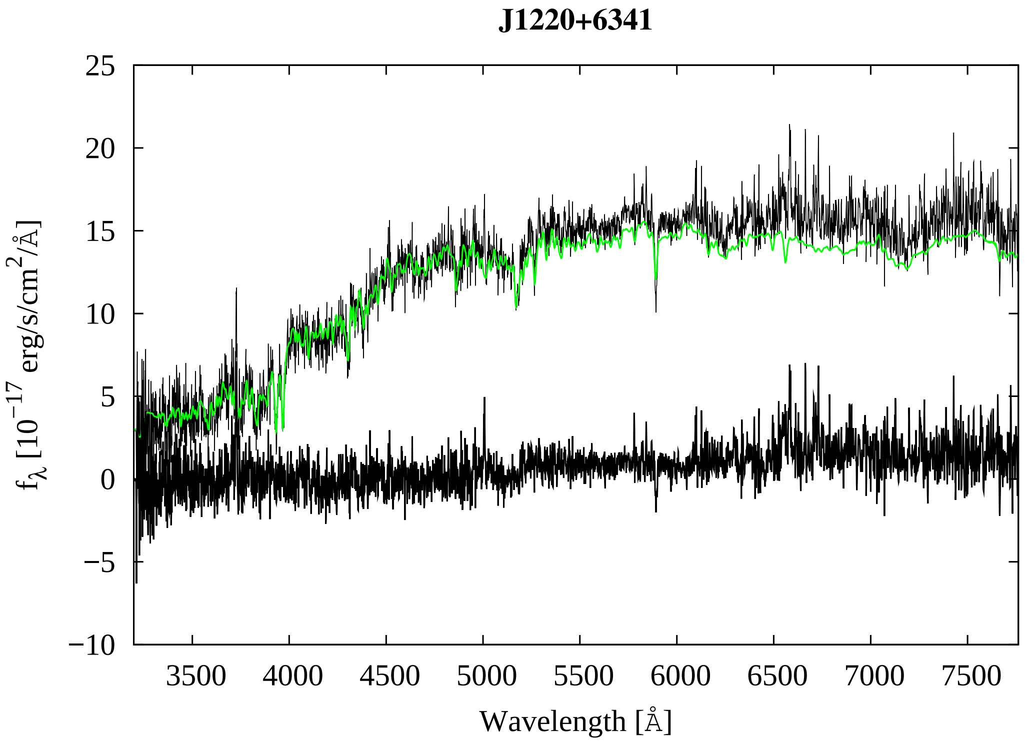
J1220+6341
f_λ [10^{-17} erg/s/cm^2/Å]
25
20
15
10
5
0
−5
−10
3500
4000
4500
5000
5500
6000
6500
7000
7500
Wavelength [Å]

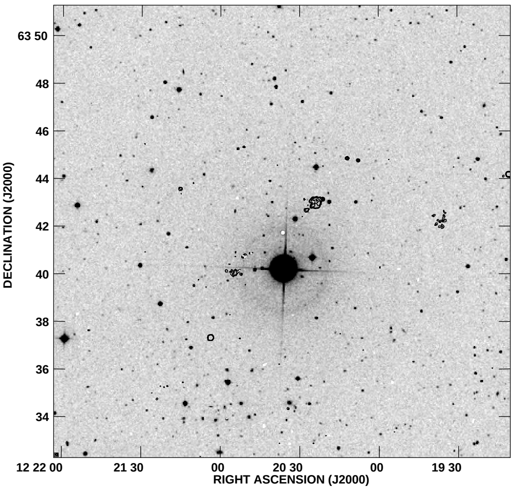
63 50
48
46
44
42
40
38
36
34
DECLINATION (J2000)
12 22 00
21 30
00
20 30
00
19 30
RIGHT ASCENSION (J2000)

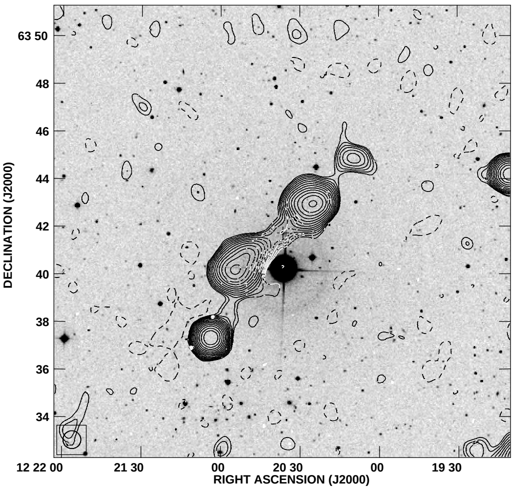
63 50
48
46
44
42
40
38
36
34
DECLINATION (J2000)
12 22 00
21 30
00
20 30
00
19 30
RIGHT ASCENSION (J2000)

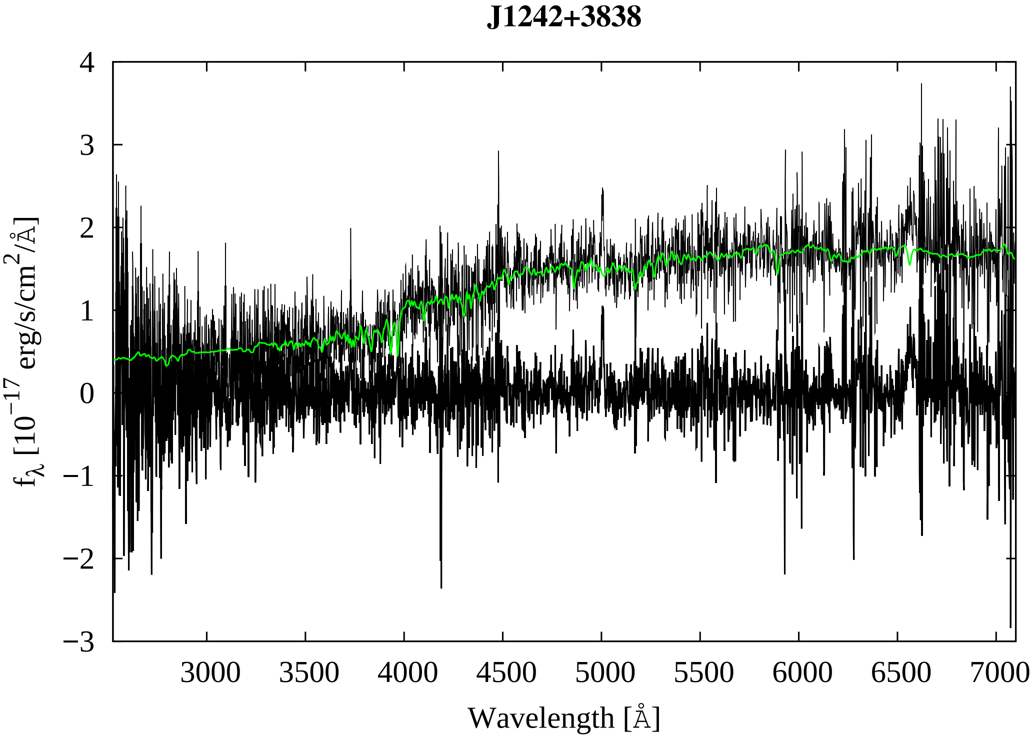
J1242+3838
4
3
2
1
0
−1
−2
−3
f$_\lambda$ [10^{-17} erg/s/cm^2/Å]
3000
3500
4000
4500
5000
5500
6000
6500
7000
Wavelength [Å]

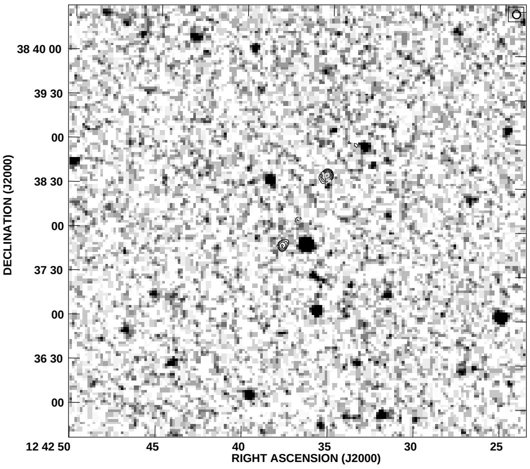
38 40 00
39 30
00
38 30
00
37 30
00
36 30
00
DECLINATION (J2000)
12 42 50
45
40
35
30
25
RIGHT ASCENSION (J2000)

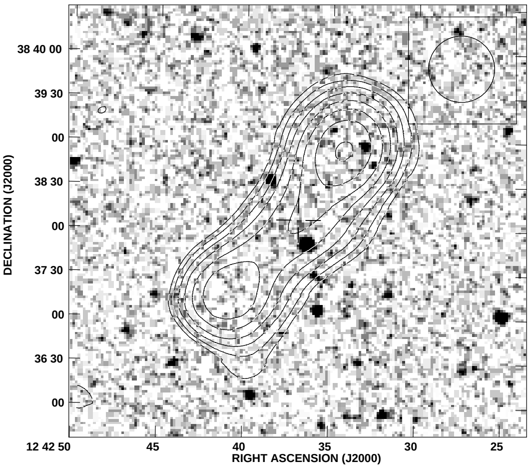
38 40 00
39 30
00
38 30
00
37 30
00
36 30
00
DECLINATION (J2000)
12 42 50
45
40
35
30
25
RIGHT ASCENSION (J2000)

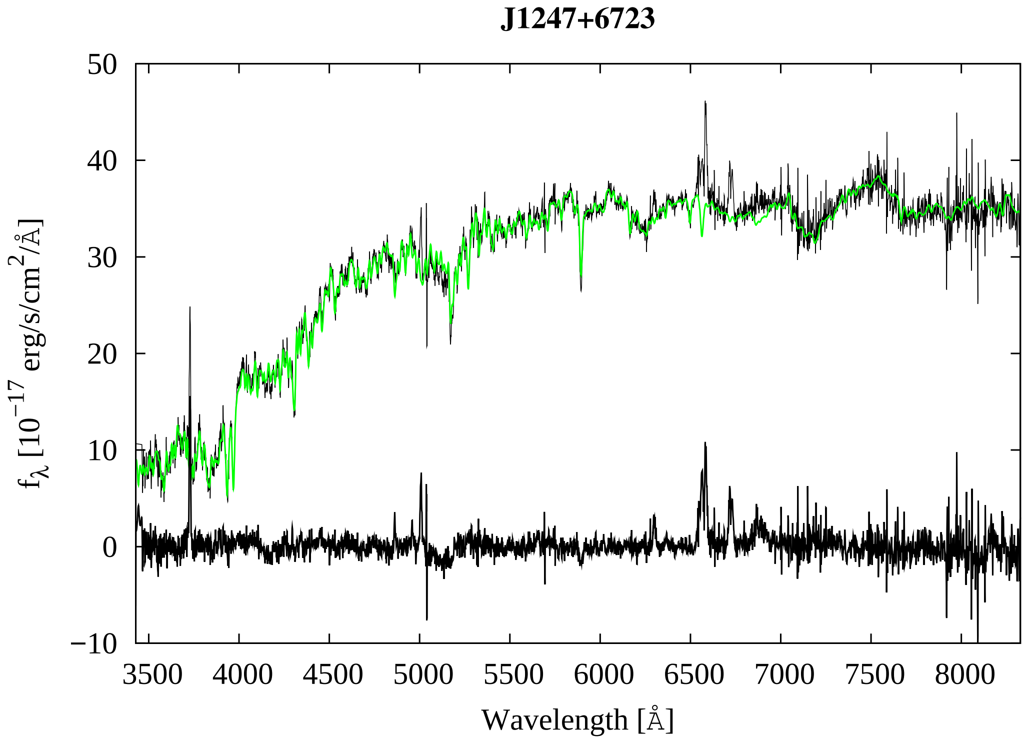
J1247+6723
50
40
30
20
10
0
−10
3500
4000
4500
5000
5500
6000
6500
7000
7500
8000
f_λ [10^{-17} erg/s/cm^2/Å]
Wavelength [Å]

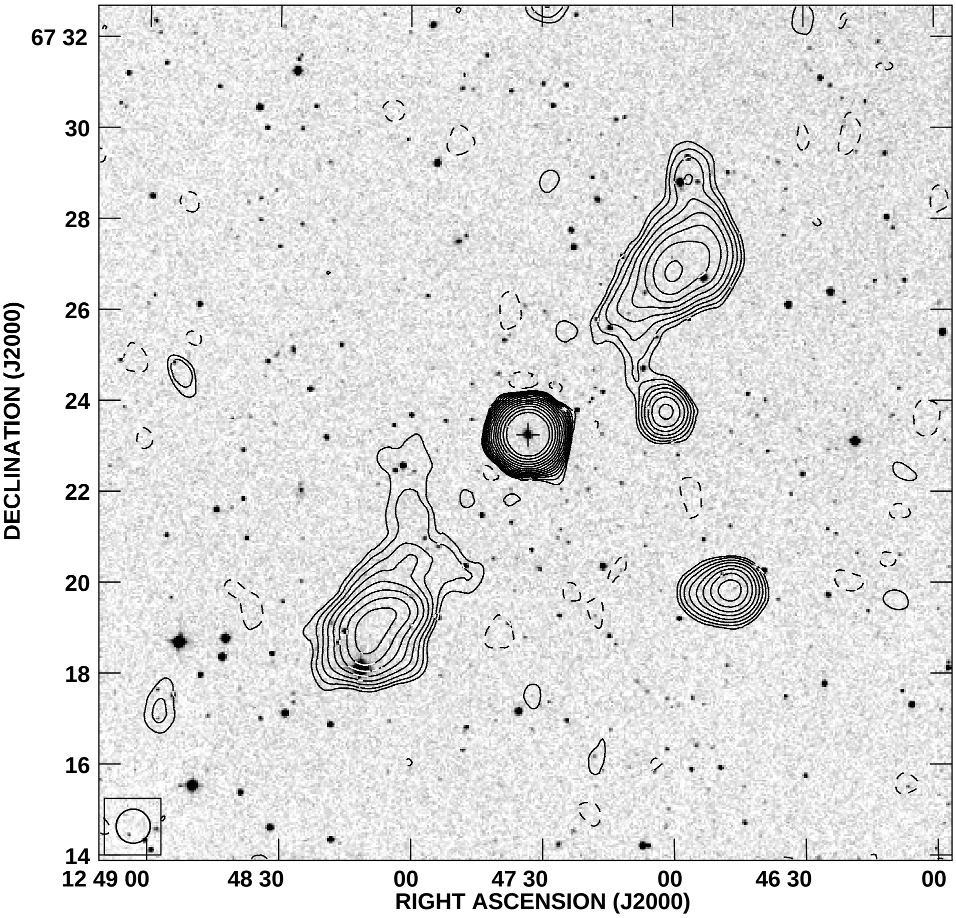
67 32
30
28
26
24
22
20
18
16
14
DECLINATION (J2000)
12 49 00
48 30
00
47 30
00
46 30
00
RIGHT ASCENSION (J2000)

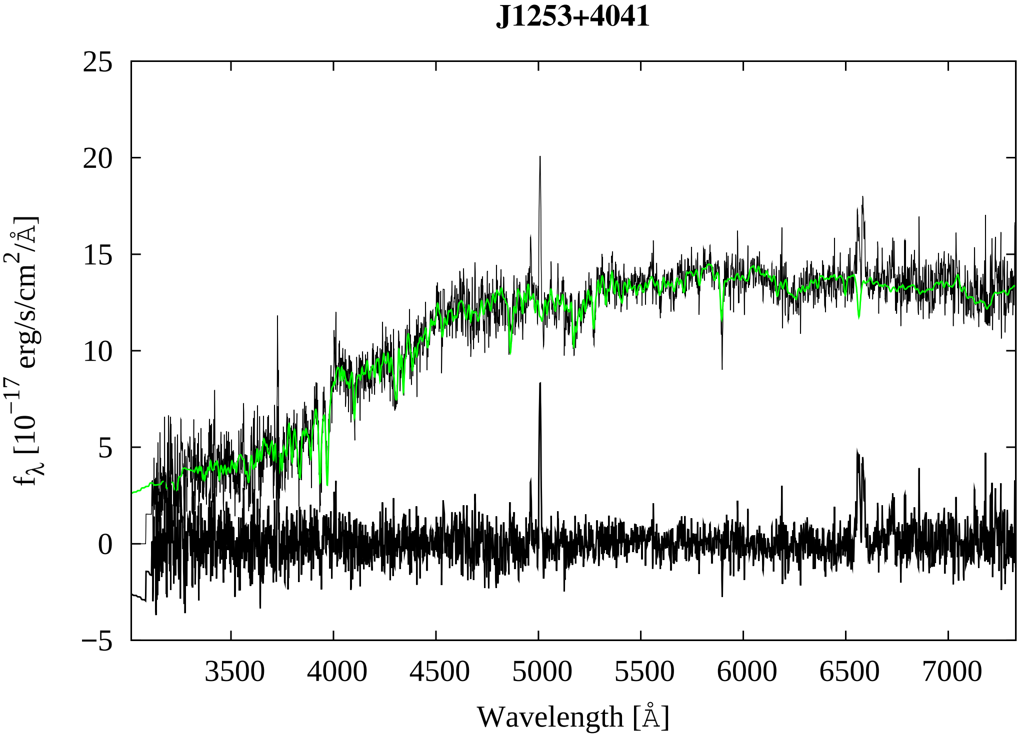
J1253+4041
25
20
15
10
5
0
−5
f_λ [10^{-17} erg/s/cm^2/Å]
3500
4000
4500
5000
5500
6000
6500
7000
Wavelength [Å]

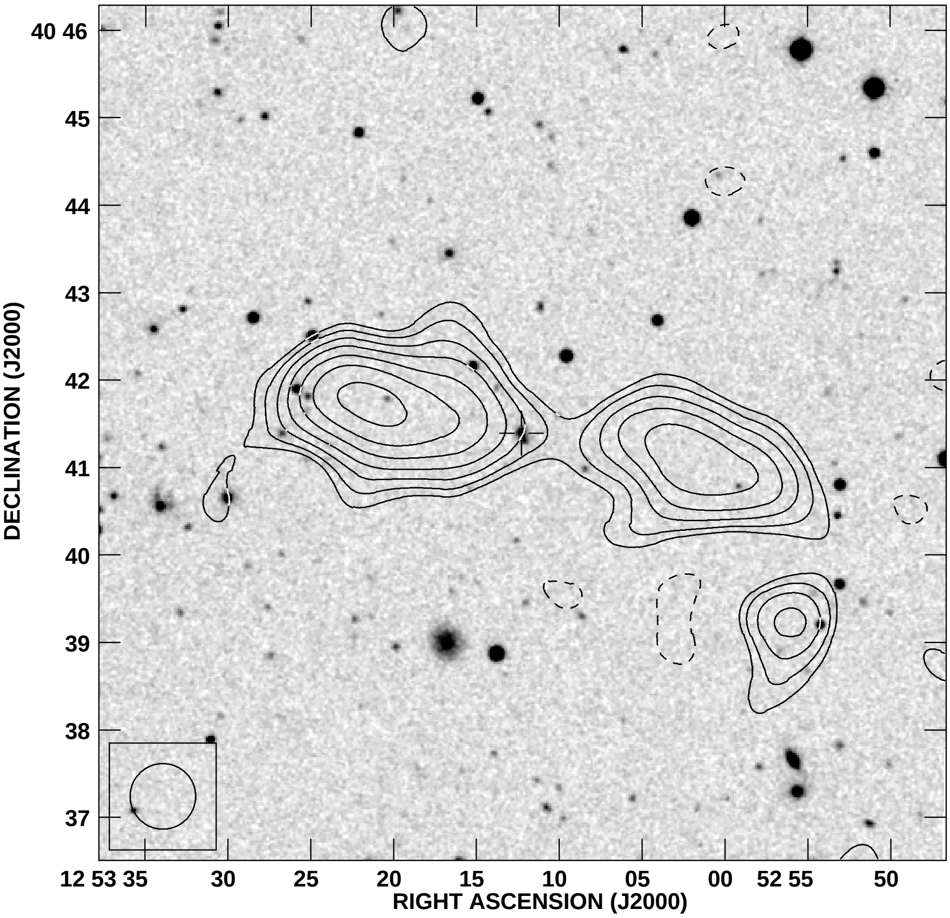
40 46
45
44
43
42
41
40
39
38
37
DECLINATION (J2000)
12 53 35
30
25
20
15
10
05
00
52 55
50
RIGHT ASCENSION (J2000)

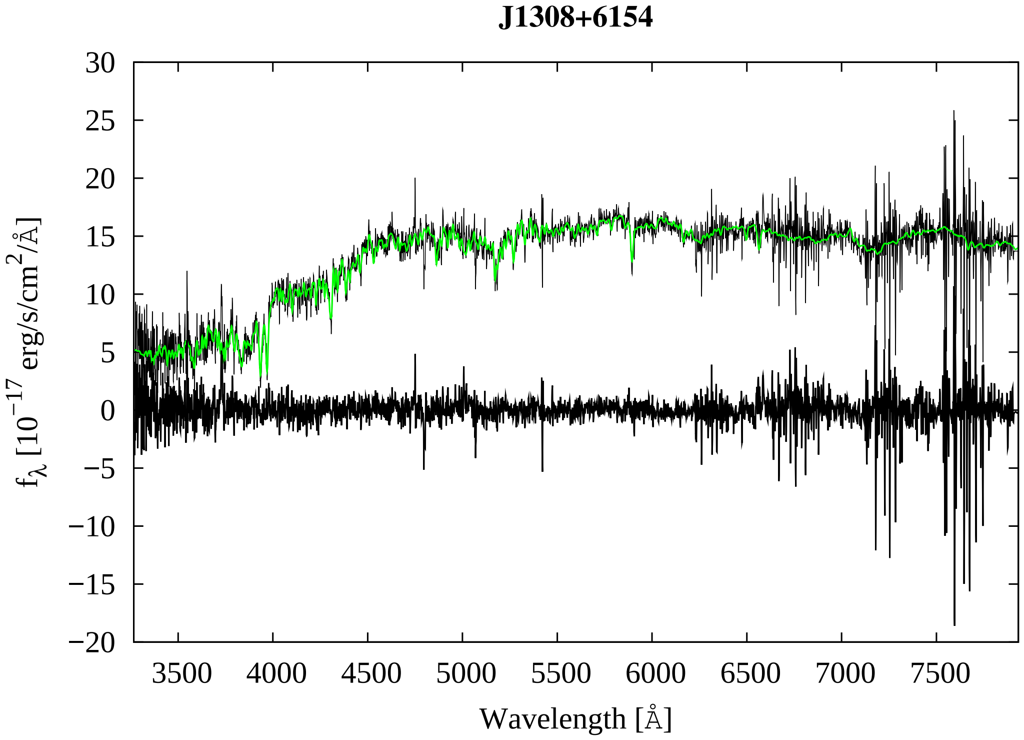
J1308+6154
30
25
20
15
10
5
0
−5
−10
−15
−20
f_λ [10^{-17} erg/s/cm^2/Å]
3500
4000
4500
5000
5500
6000
6500
7000
7500
Wavelength [Å]

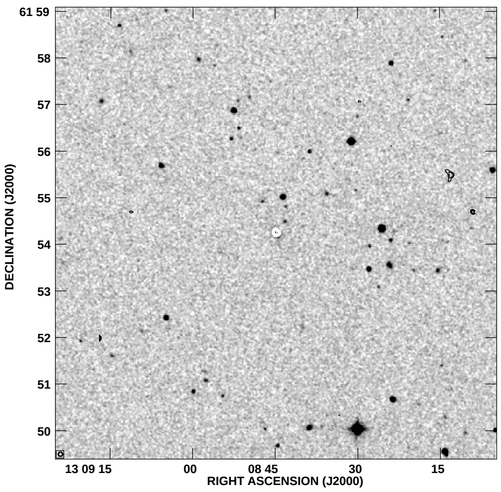
61 59
58
57
56
55
54
53
52
51
50
DECLINATION (J2000)
13 09 15
00
08 45
30
15
RIGHT ASCENSION (J2000)

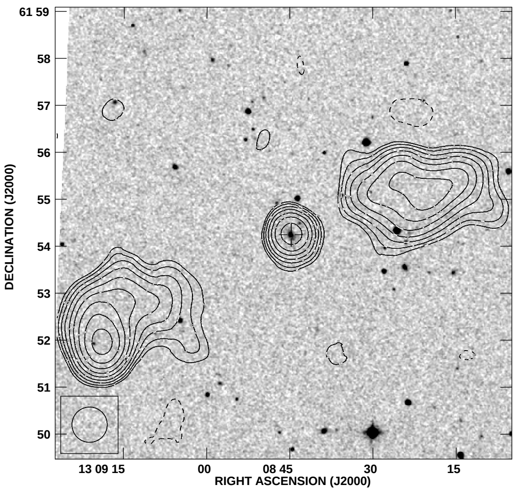
61 59
58
57
56
55
54
53
52
51
50
DECLINATION (J2000)
13 09 15
00
08 45
30
15
RIGHT ASCENSION (J2000)

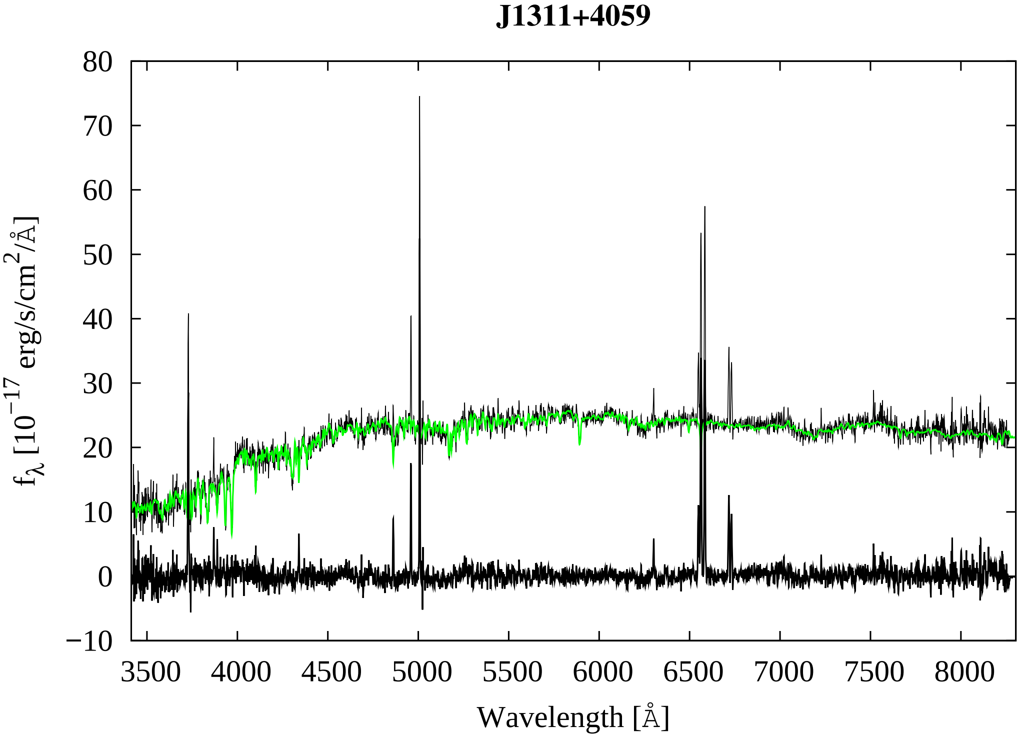
J1311+4059
80
70
60
50
40
30
20
10
0
−10
f_λ [10^{-17} erg/s/cm^2/Å]
3500
4000
4500
5000
5500
6000
6500
7000
7500
8000
Wavelength [Å]

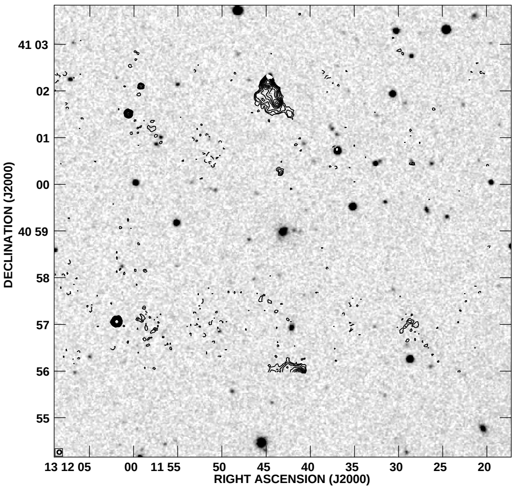
41 03
02
01
00
40 59
58
57
56
55
DECLINATION (J2000)
13 12 05
00
11 55
50
45
40
35
30
25
20
RIGHT ASCENSION (J2000)

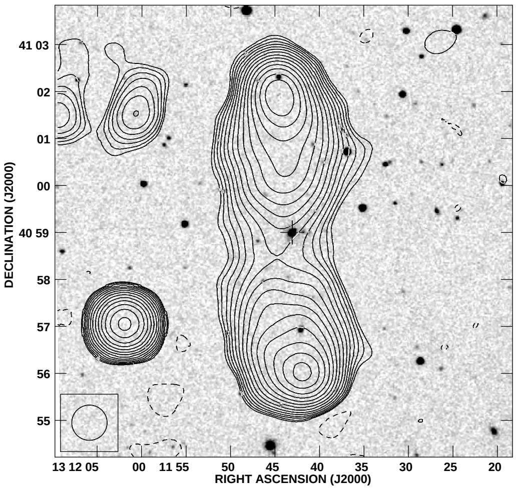
41 03
02
01
00
40 59
58
57
56
55
DECLINATION (J2000)
13 12 05
00
11 55
50
45
40
35
30
25
20
RIGHT ASCENSION (J2000)

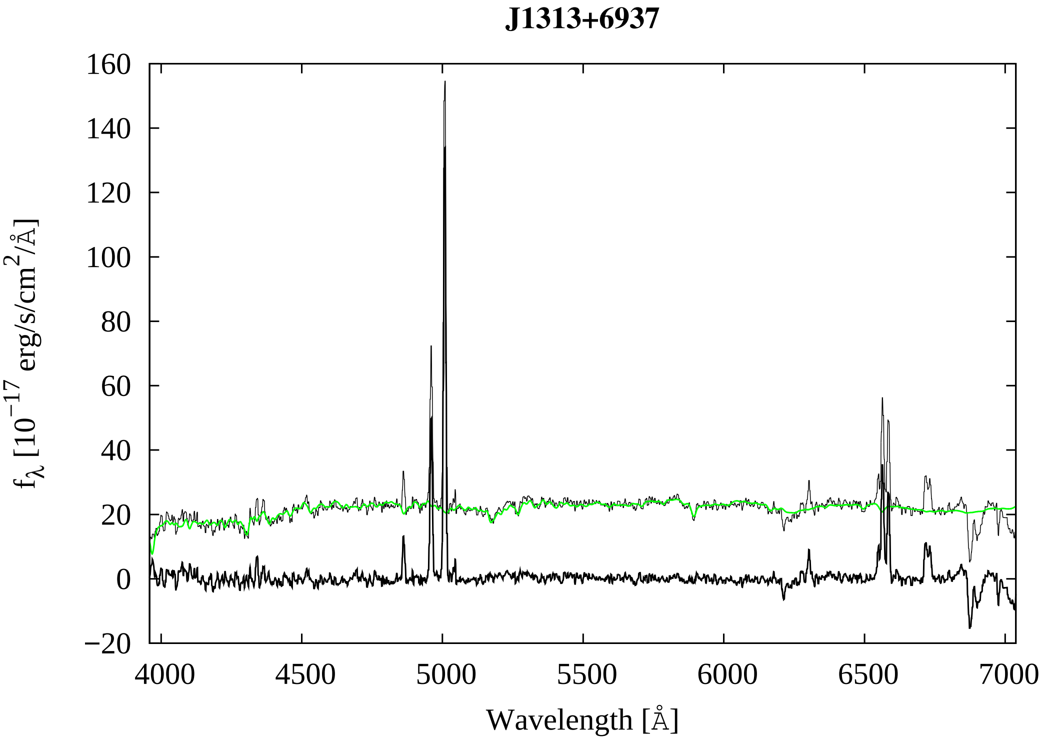
J1313+6937
160
140
120
100
80
60
40
20
0
−20
f$_\lambda$ [10^{-17} erg/s/cm^2/Å]
4000
4500
5000
5500
6000
6500
7000
Wavelength [Å]

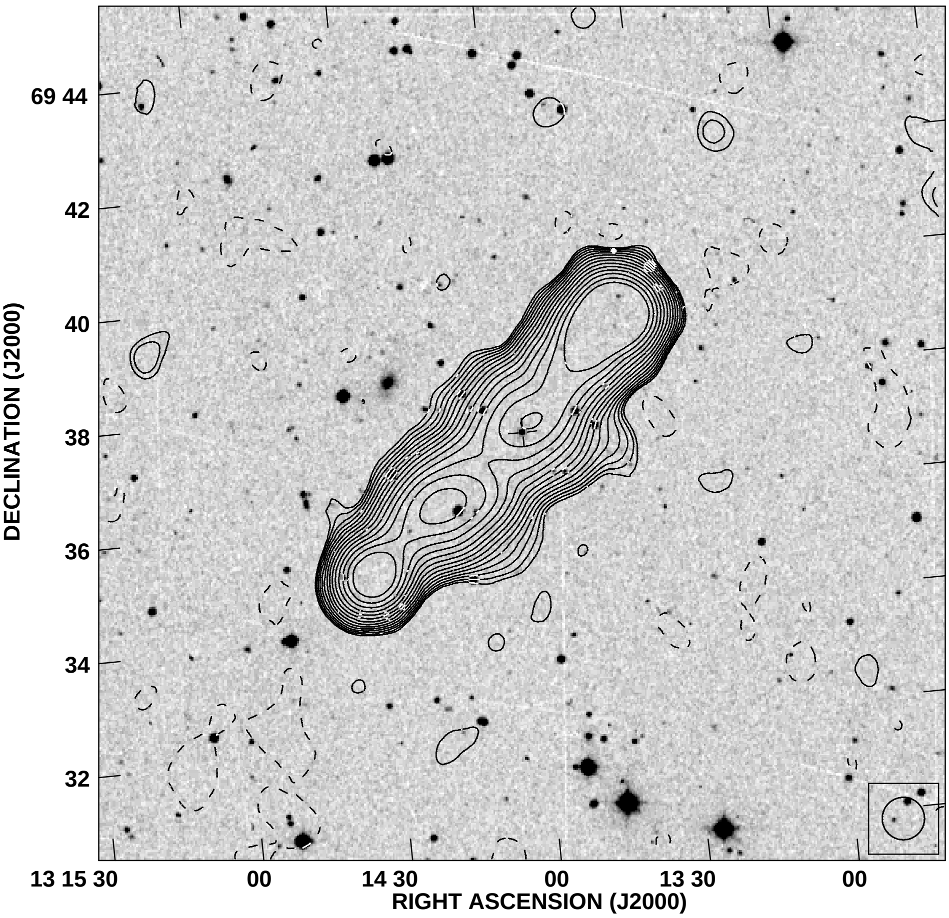
69 44
42
40
38
36
34
32
DECLINATION (J2000)
13 15 30
00
14 30
00
13 30
00
RIGHT ASCENSION (J2000)

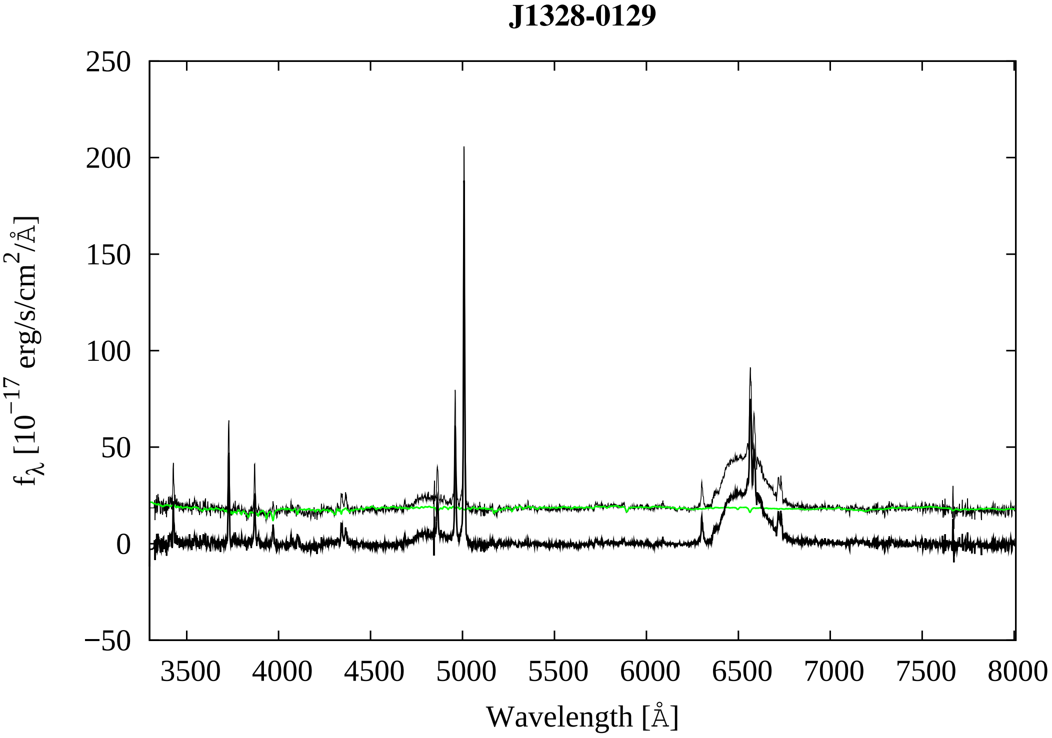
J1328-0129
f_λ [10^{-17} erg/s/cm^2/Å]
250
200
150
100
50
0
−50
3500
4000
4500
5000
5500
6000
6500
7000
7500
8000
Wavelength [Å]

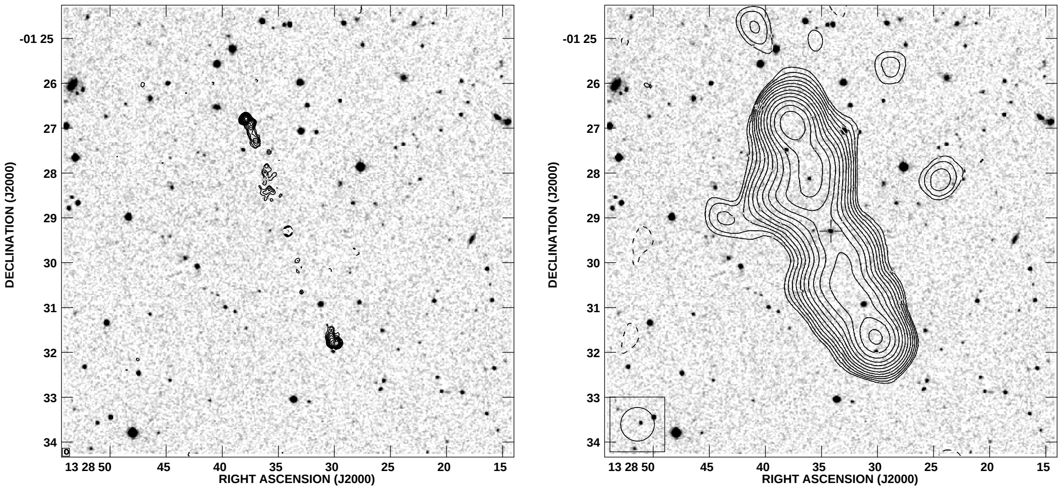
DECLINATION (J2000)
-01 25
26
27
28
29
30
31
32
33
34
13 28 50
45
40
35
30
25
20
15
RIGHT ASCENSION (J2000)

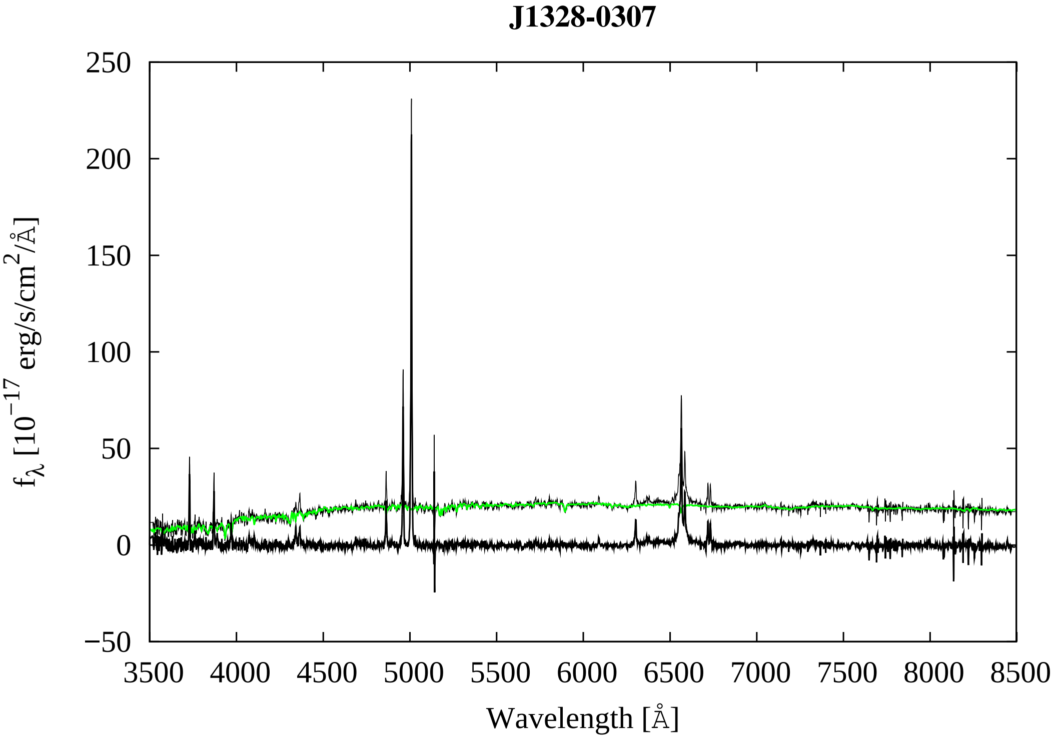
J1328-0307
f$_\lambda$ [10^{-17} erg/s/cm^2/Å]
250
200
150
100
50
0
−50
3500
4000
4500
5000
5500
6000
6500
7000
7500
8000
8500
Wavelength [Å]

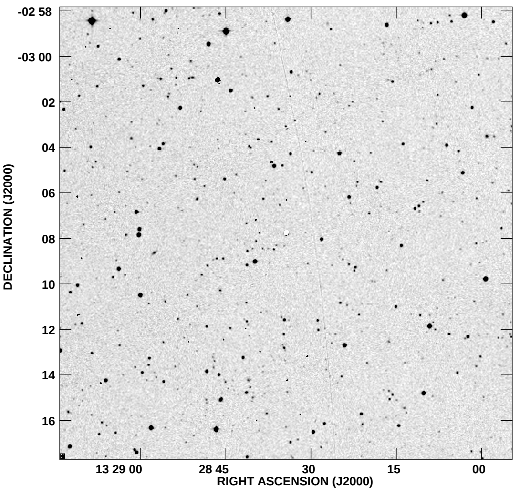
-02 58
-03 00
02
04
06
08
10
12
14
16
DECLINATION (J2000)
13 29 00
28 45
30
15
00
RIGHT ASCENSION (J2000)

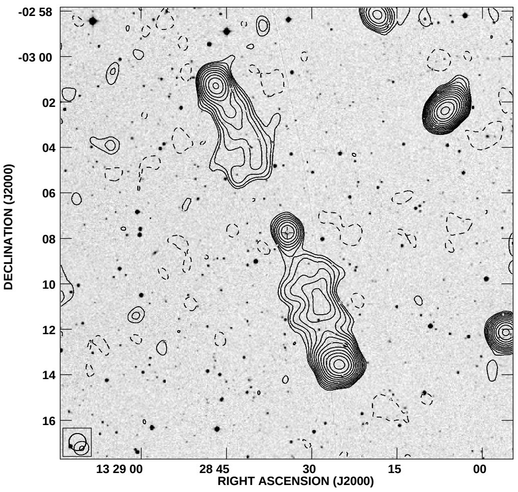
-02 58
-03 00
02
04
06
08
10
12
14
16
DECLINATION (J2000)
13 29 00
28 45
30
15
00
RIGHT ASCENSION (J2000)

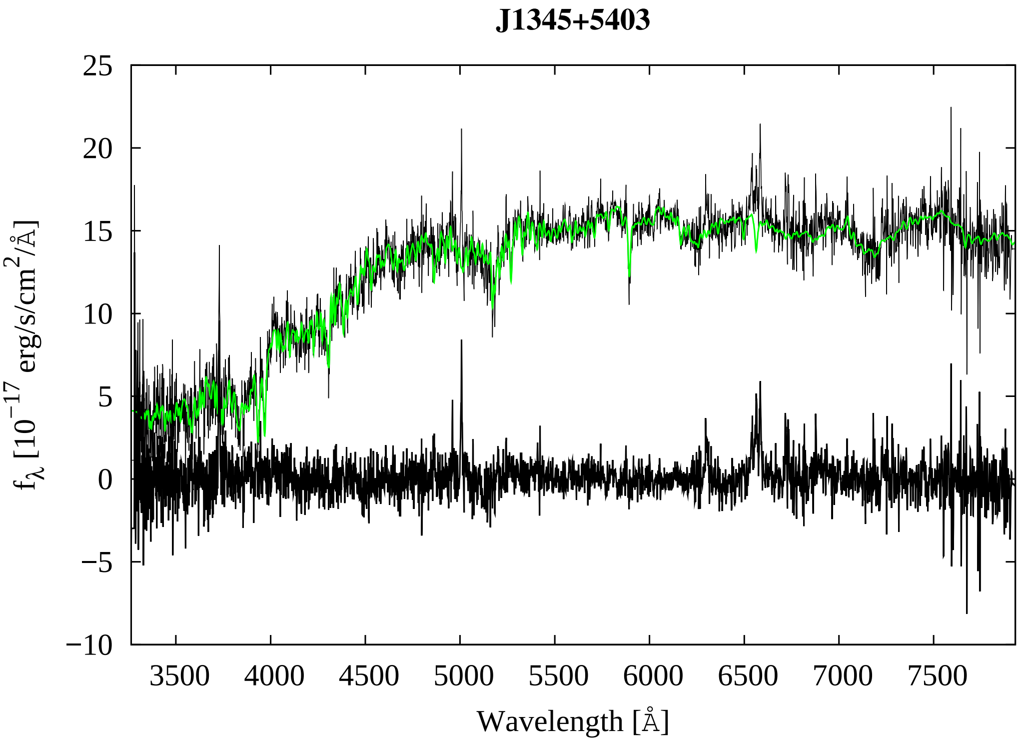
J1345+5403
25
20
15
10
5
0
−5
−10
f_λ [10^{-17} erg/s/cm^2/Å]
3500
4000
4500
5000
5500
6000
6500
7000
7500
Wavelength [Å]

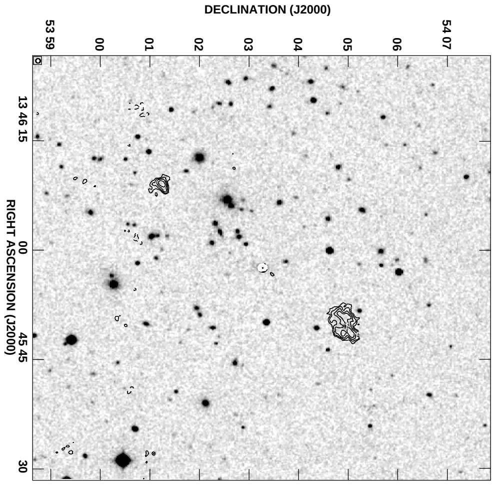
DECLINATION (J2000)
53 59
00
01
02
03
04
05
06
54 07
RIGHT ASCENSION (J2000)
13 46 15
00
45 45
30

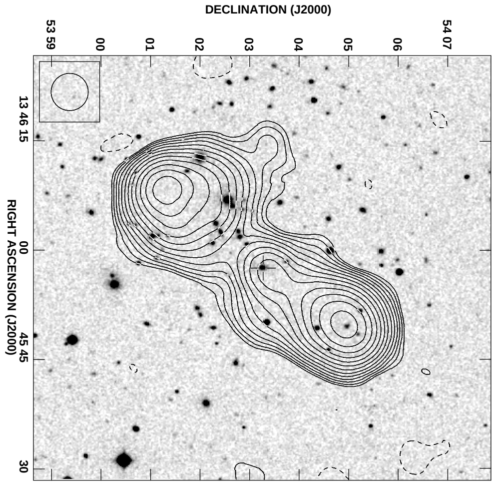
DECLINATION (J2000)
53 59
00
01
02
03
04
05
06
54 07
RIGHT ASCENSION (J2000)
13 46 15
00
45 45
30

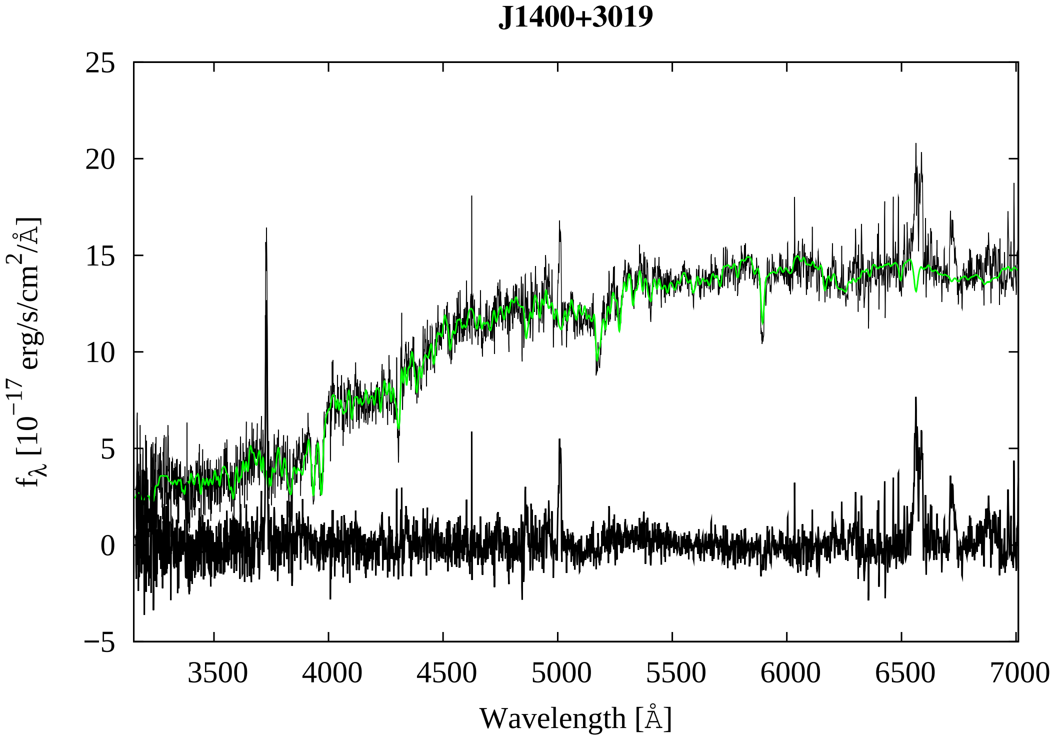
J1400+3019
25
20
15
10
5
0
−5
f_λ [10^{-17} erg/s/cm^2/Å]
3500
4000
4500
5000
5500
6000
6500
7000
Wavelength [Å]

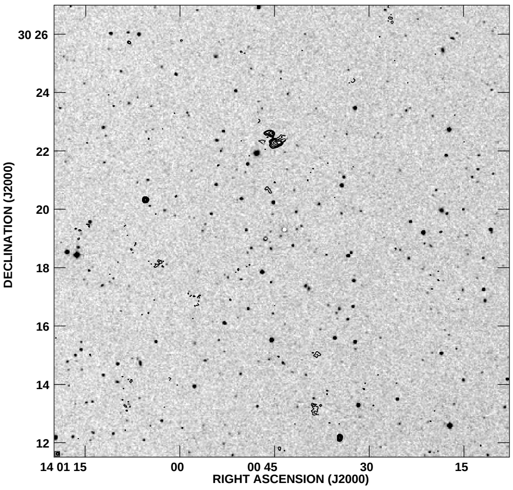
30 26
24
22
20
18
16
14
12
DECLINATION (J2000)
14 01 15
00
00 45
30
15
RIGHT ASCENSION (J2000)

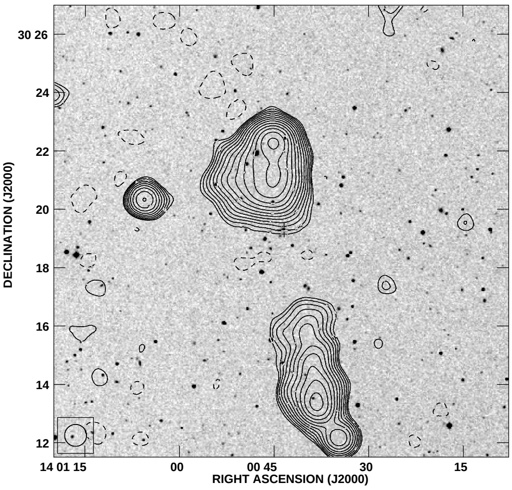
30 26
24
22
20
18
16
14
12
DECLINATION (J2000)
14 01 15
00
00 45
30
15
RIGHT ASCENSION (J2000)

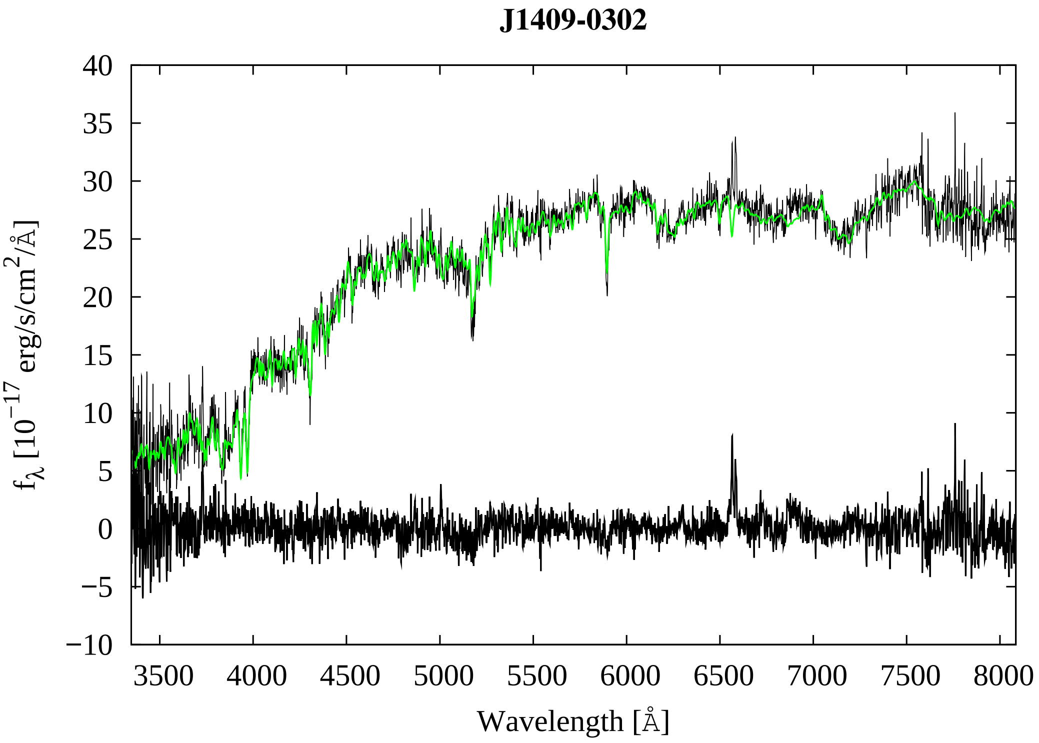
J1409-0302
40
35
30
25
20
15
10
5
0
−5
−10
3500
4000
4500
5000
5500
6000
6500
7000
7500
8000
Wavelength [Å]
f$_\lambda$ [10^{-17} erg/s/cm^2/Å]

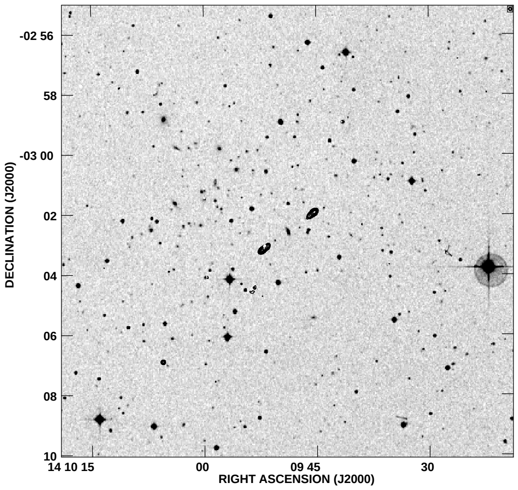
-02 56
58
-03 00
02
04
06
08
10
DECLINATION (J2000)
14 10 15
00
09 45
30
RIGHT ASCENSION (J2000)

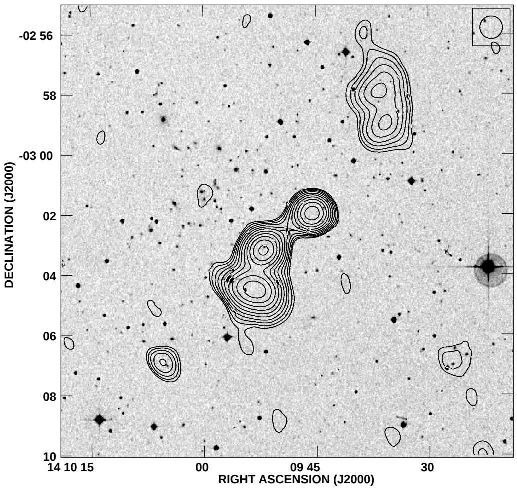
-02 56
58
-03 00
02
04
06
08
10
DECLINATION (J2000)
14 10 15
00
09 45
30
RIGHT ASCENSION (J2000)

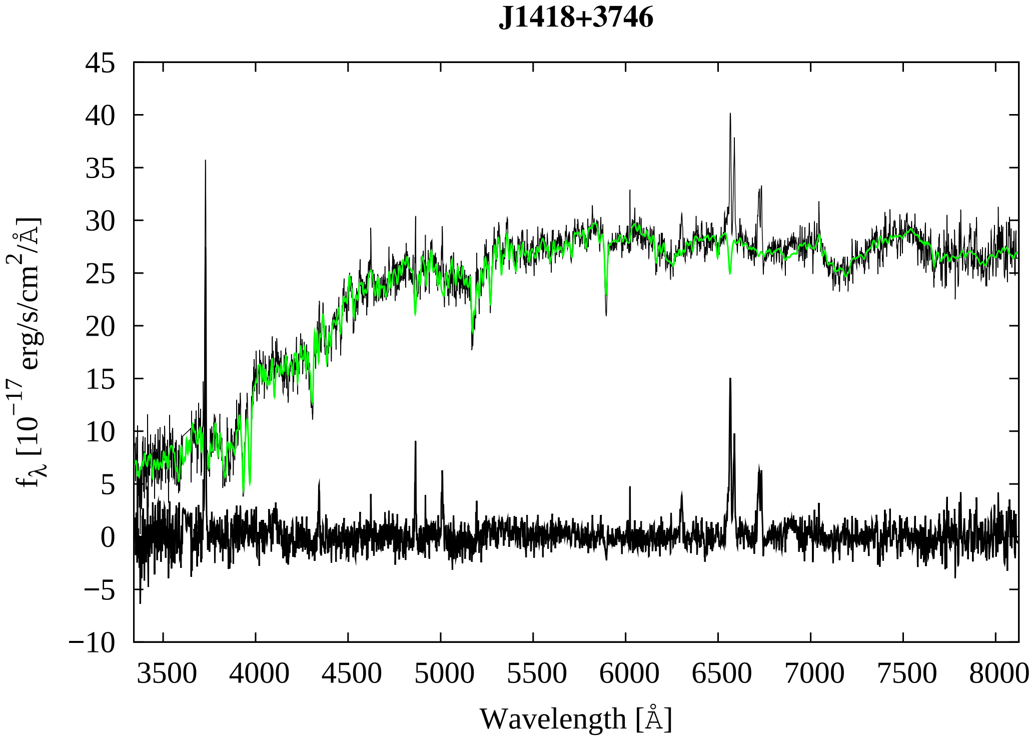
J1418+3746
45
40
35
30
25
20
15
10
5
0
−5
−10
3500
4000
4500
5000
5500
6000
6500
7000
7500
8000
f_λ [10^{-17} erg/s/cm^2/Å]
Wavelength [Å]

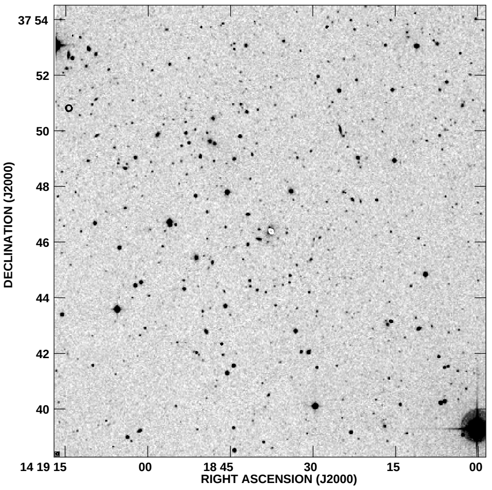
37 54
52
50
48
46
44
42
40
DECLINATION (J2000)
14 19 15
00
18 45
30
15
00
RIGHT ASCENSION (J2000)

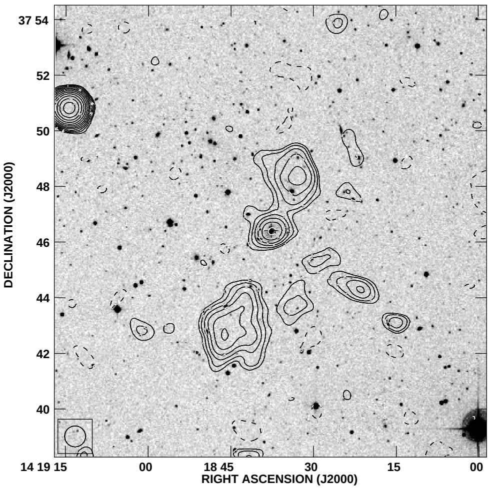
37 54
52
50
48
46
44
42
40
DECLINATION (J2000)
14 19 15
00
18 45
30
15
00
RIGHT ASCENSION (J2000)

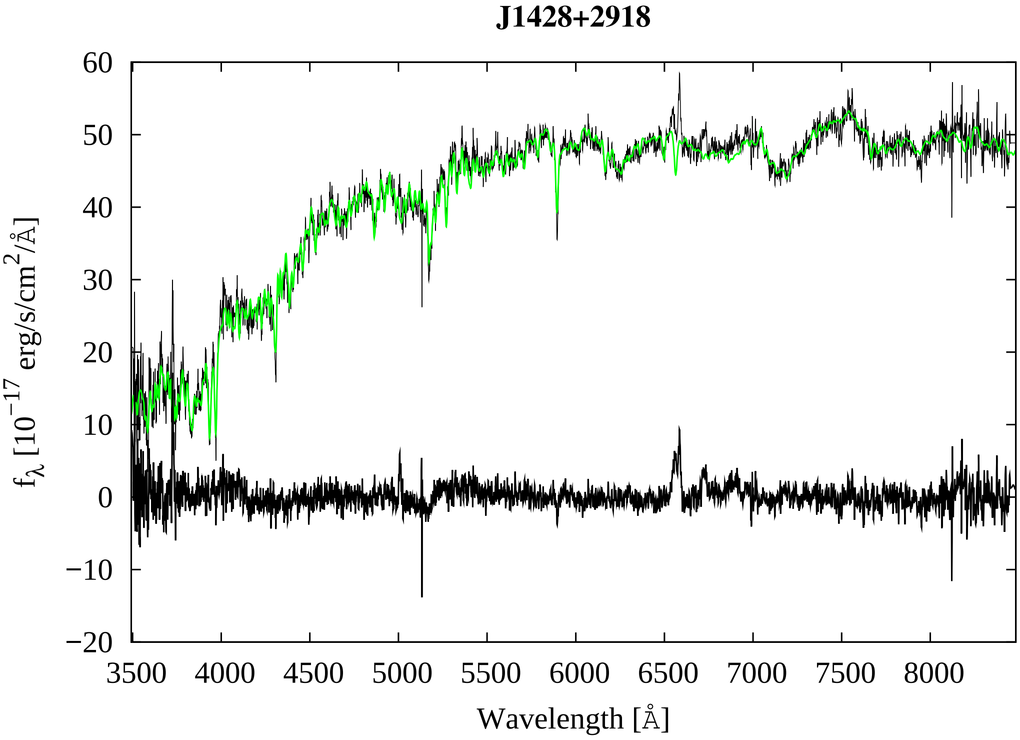
J1428+2918
f_λ [10^{-17} erg/s/cm^2/Å]
60
50
40
30
20
10
0
−10
−20
3500
4000
4500
5000
5500
6000
6500
7000
7500
8000
Wavelength [Å]

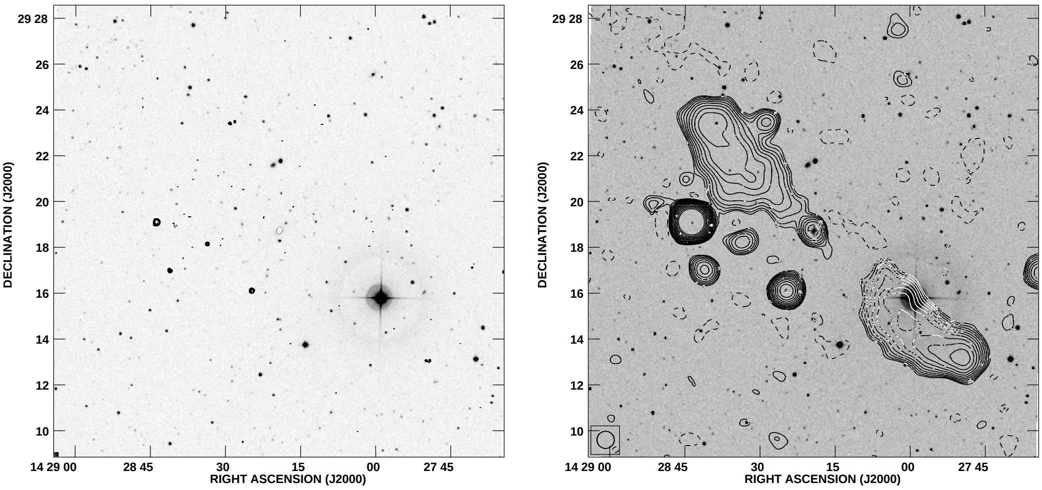
DECLINATION (J2000)
29 28
26
24
22
20
18
16
14
12
10
14 29 00
28 45
30
15
00
27 45
RIGHT ASCENSION (J2000)

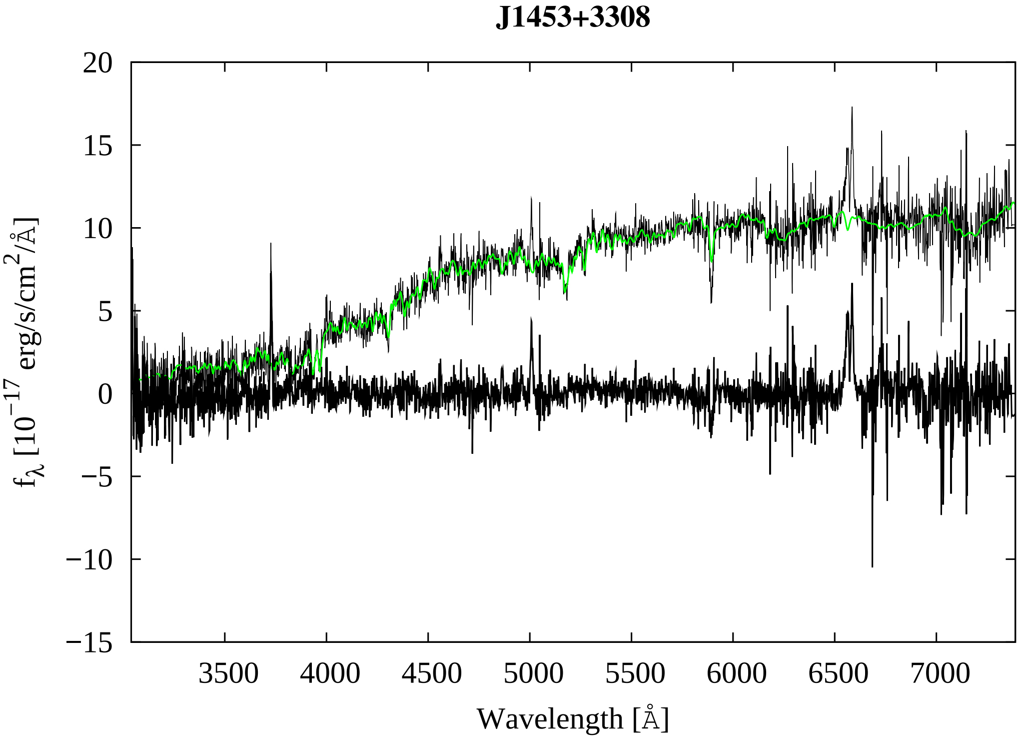
J1453+3308
20
15
10
5
0
−5
−10
−15
3500
4000
4500
5000
5500
6000
6500
7000
Wavelength [Å]
f_λ [10^{-17} erg/s/cm^2/Å]

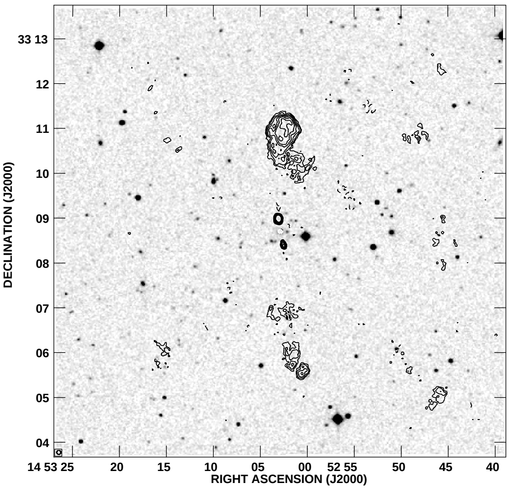
33 13
12
11
10
09
08
07
06
05
04
DECLINATION (J2000)
14 53 25
20
15
10
05
00
52 55
50
45
40
RIGHT ASCENSION (J2000)

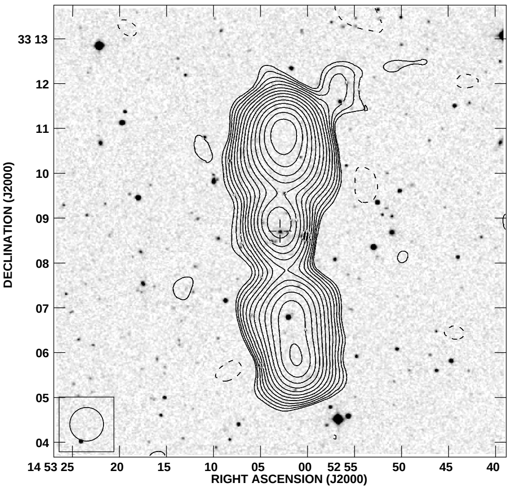
33 13
12
11
10
09
08
07
06
05
04
DECLINATION (J2000)
14 53 25
20
15
10
05
00
52 55
50
45
40
RIGHT ASCENSION (J2000)

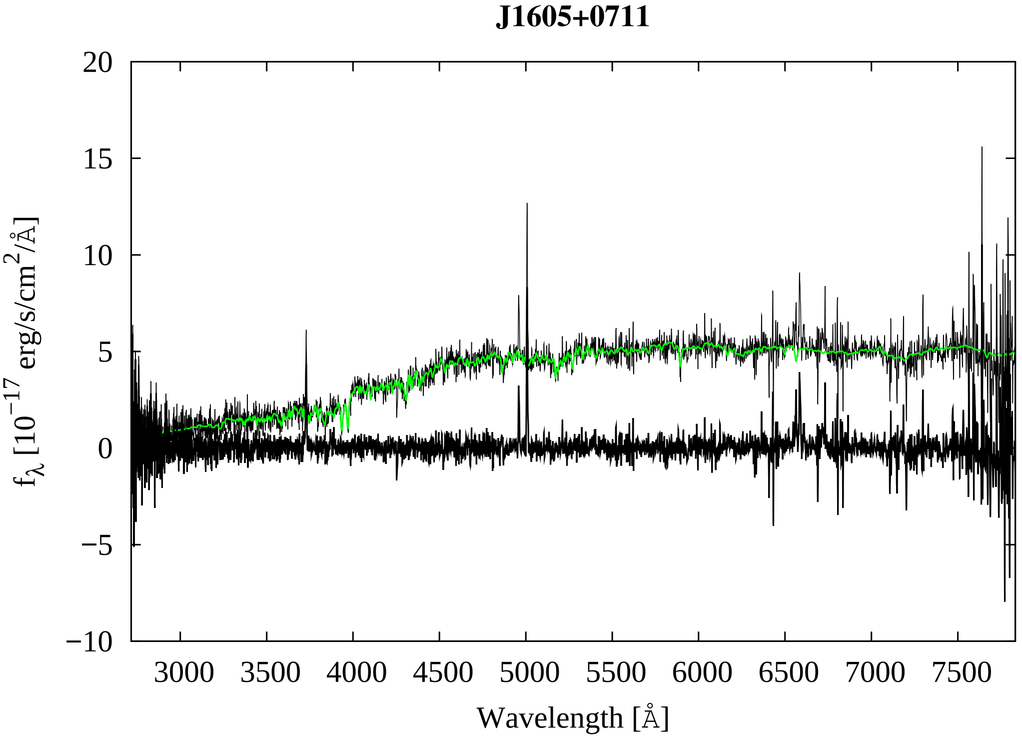
J1605+0711
20
15
10
5
0
−5
−10
3000
3500
4000
4500
5000
5500
6000
6500
7000
7500
f_λ [10^{-17} erg/s/cm^2/Å]
Wavelength [Å]

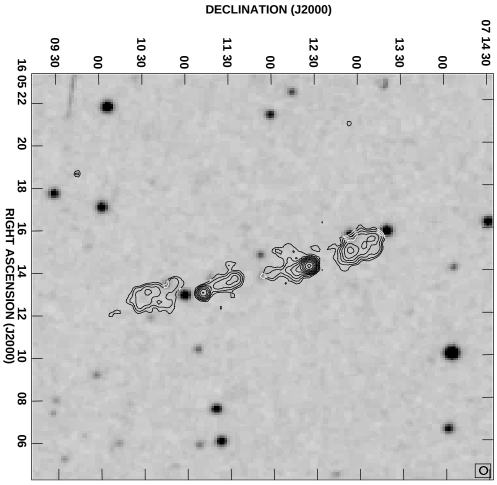
DECLINATION (J2000)
09 30
00
10 30
00
11 30
00
12 30
00
13 30
00
07 14 30
16 05 22
20
18
16
14
12
10
08
06
RIGHT ASCENSION (J2000)

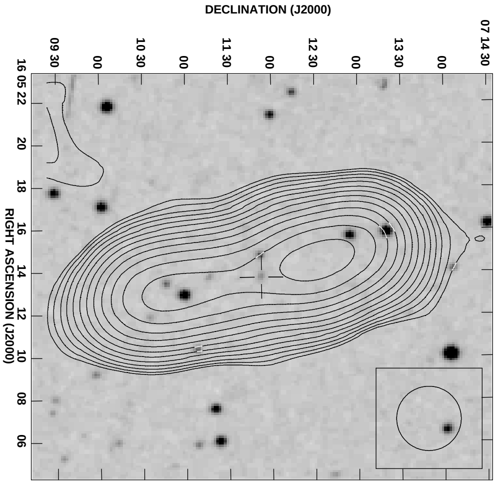
DECLINATION (J2000)
09 30
00
10 30
00
11 30
00
12 30
00
13 30
00
07 14 30
16 05 22
20
18
16
14
12
10
08
06
RIGHT ASCENSION (J2000)

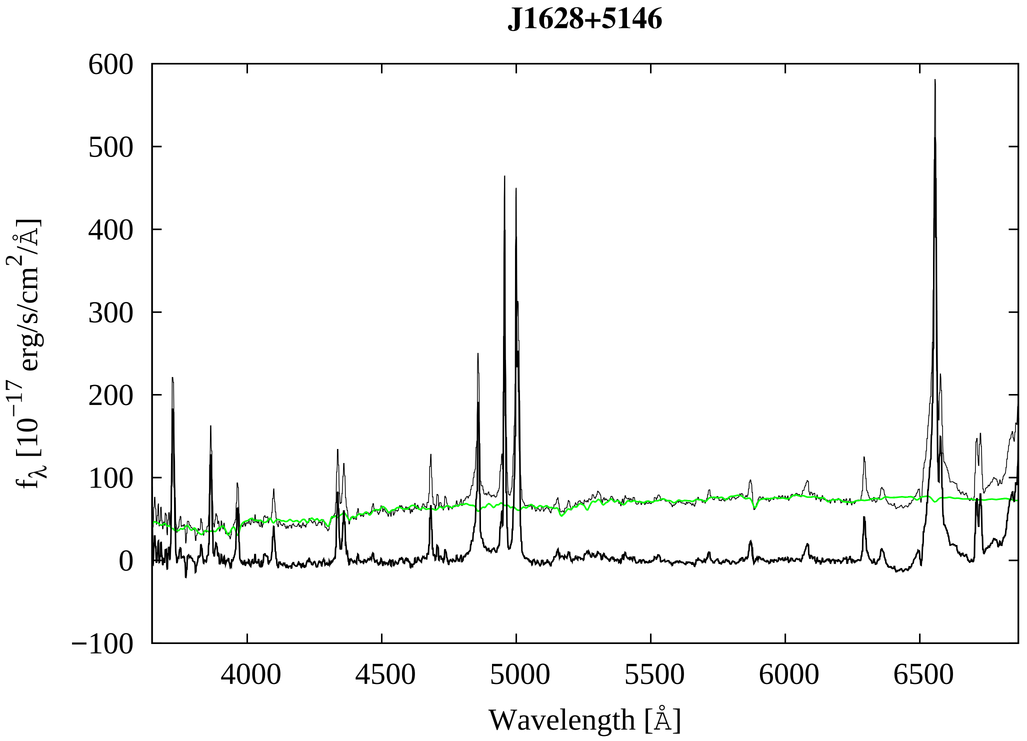
J1628+5146
f$_\lambda$ [10^{-17} erg/s/cm^2/Å]
600
500
400
300
200
100
0
−100
4000
4500
5000
5500
6000
6500
Wavelength [Å]

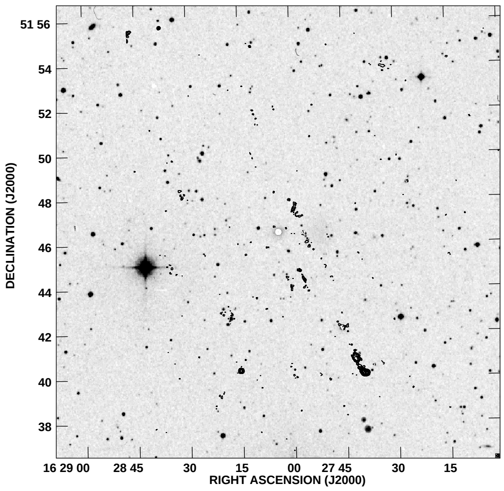
DECLINATION (J2000)
51 56
54
52
50
48
46
44
42
40
38
16 29 00
28 45
30
15
00
27 45
30
15
RIGHT ASCENSION (J2000)

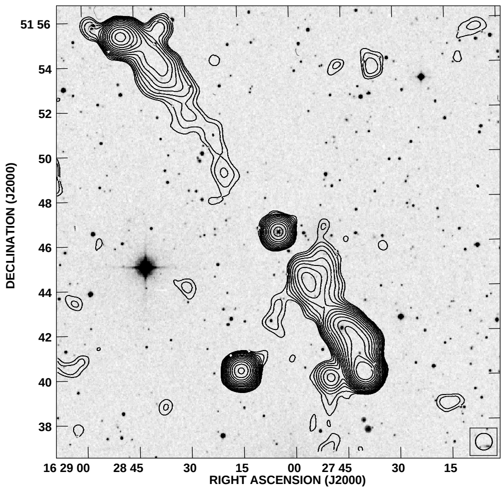
DECLINATION (J2000)
51 56
54
52
50
48
46
44
42
40
38
16 29 00
28 45
30
15
00
27 45
30
15
RIGHT ASCENSION (J2000)

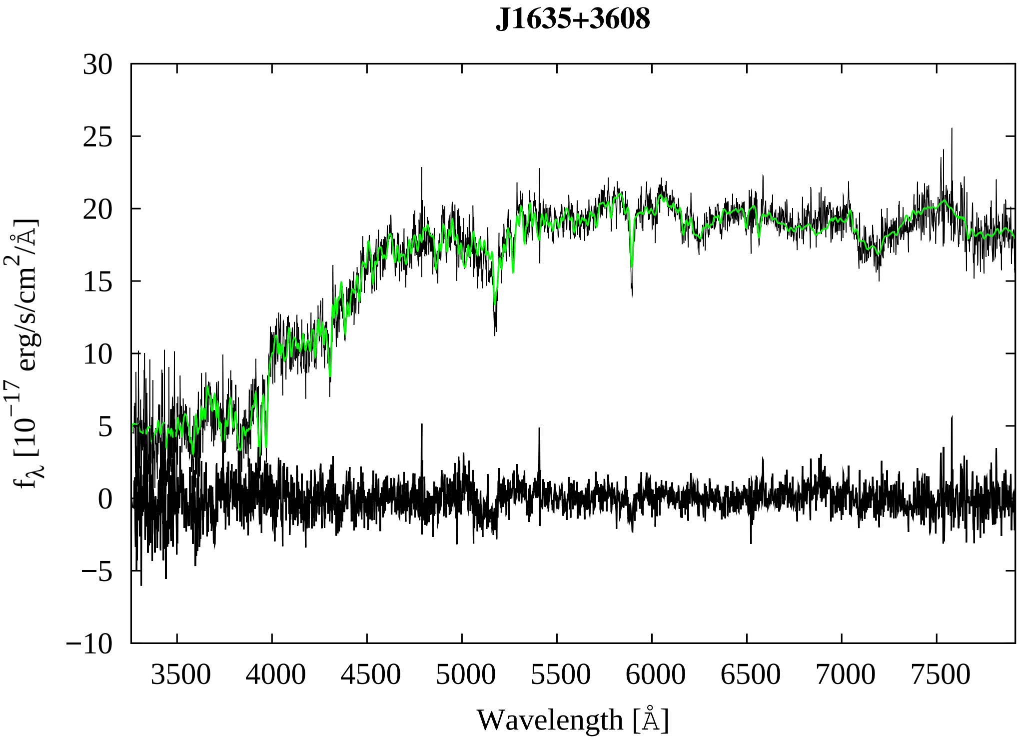
J1635+3608
f_λ [10^{-17} erg/s/cm^2/Å]
30
25
20
15
10
5
0
−5
−10
3500
4000
4500
5000
5500
6000
6500
7000
7500
Wavelength [Å]

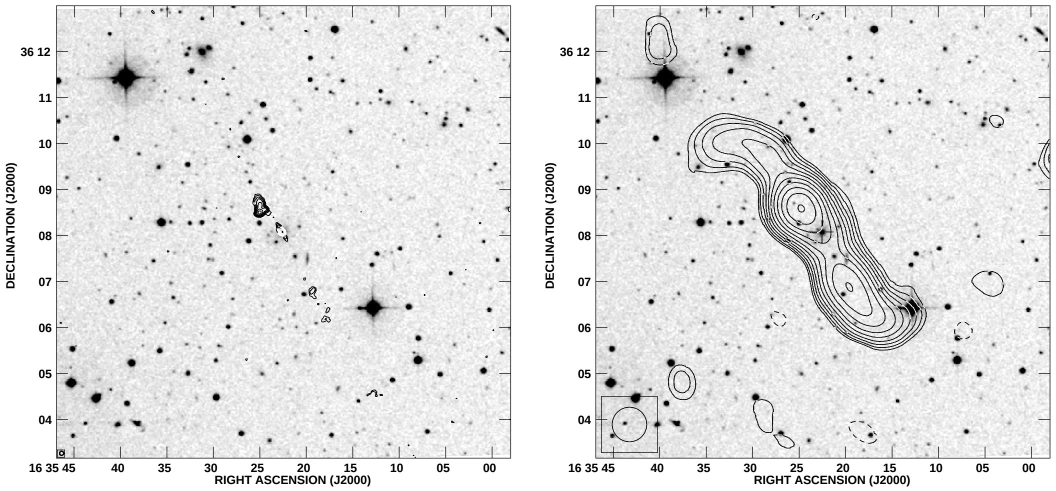
36 12
11
10
09
08
07
06
05
04
DECLINATION (J2000)
16 35 45
40
35
30
25
20
15
10
05
00
RIGHT ASCENSION (J2000)
36 12
11
10
09
08
07
06
05
04
DECLINATION (J2000)
16 35 45
40
35
30
25
20
15
10
05
00
RIGHT ASCENSION (J2000)

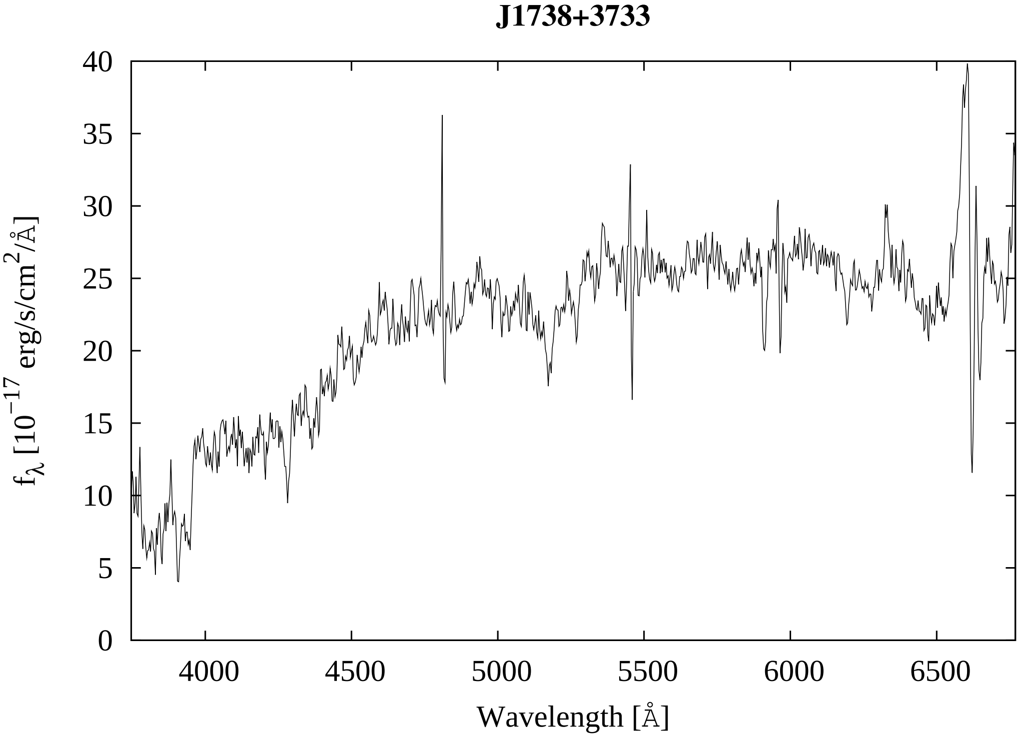
J1738+3733
f_λ [10^{-17} erg/s/cm^2/Å]
0
5
10
15
20
25
30
35
40
4000
4500
5000
5500
6000
6500
Wavelength [Å]

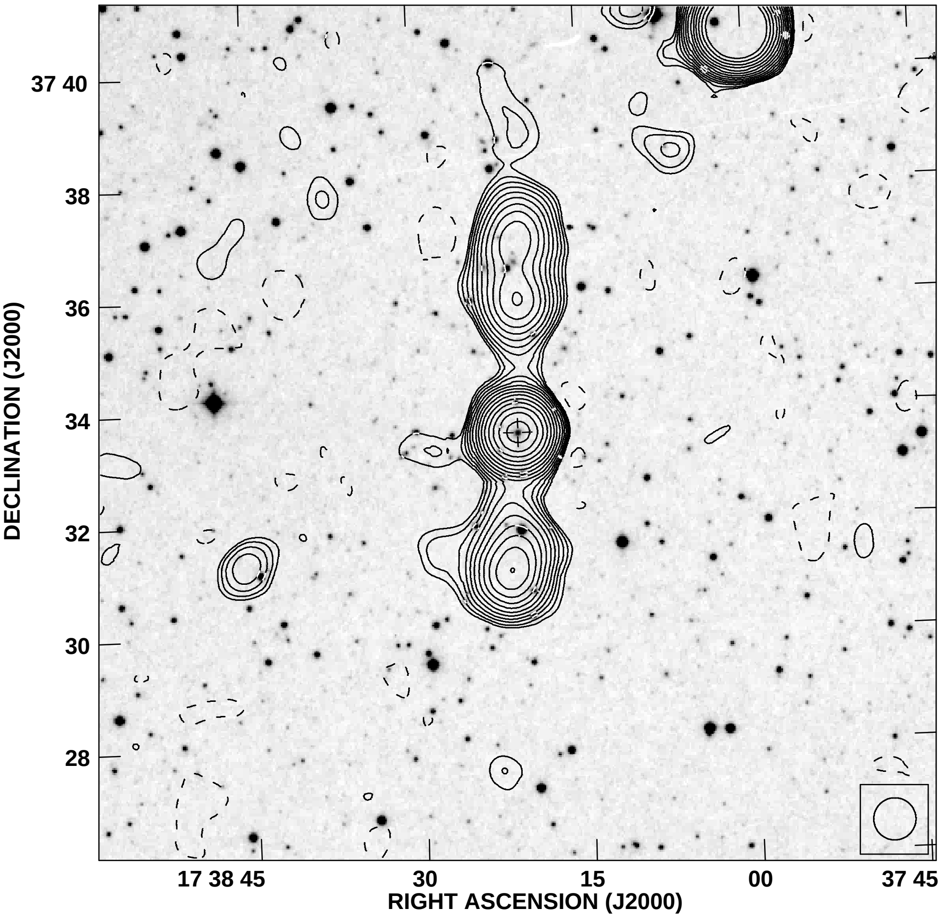
DECLINATION (J2000)
37 40
38
36
34
32
30
28
17 38 45
30
15
00
37 45
RIGHT ASCENSION (J2000)

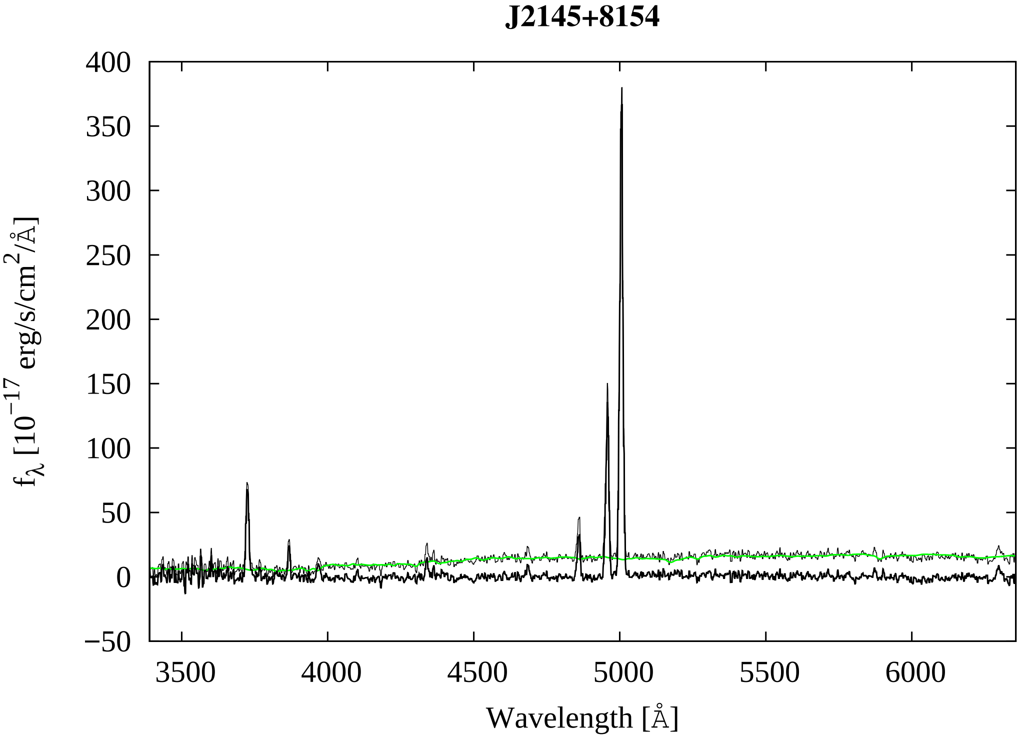
J2145+8154
f$_\lambda$ [10^{-17} erg/s/cm^2/Å]
400
350
300
250
200
150
100
50
0
−50
3500
4000
4500
5000
5500
6000
Wavelength [Å]

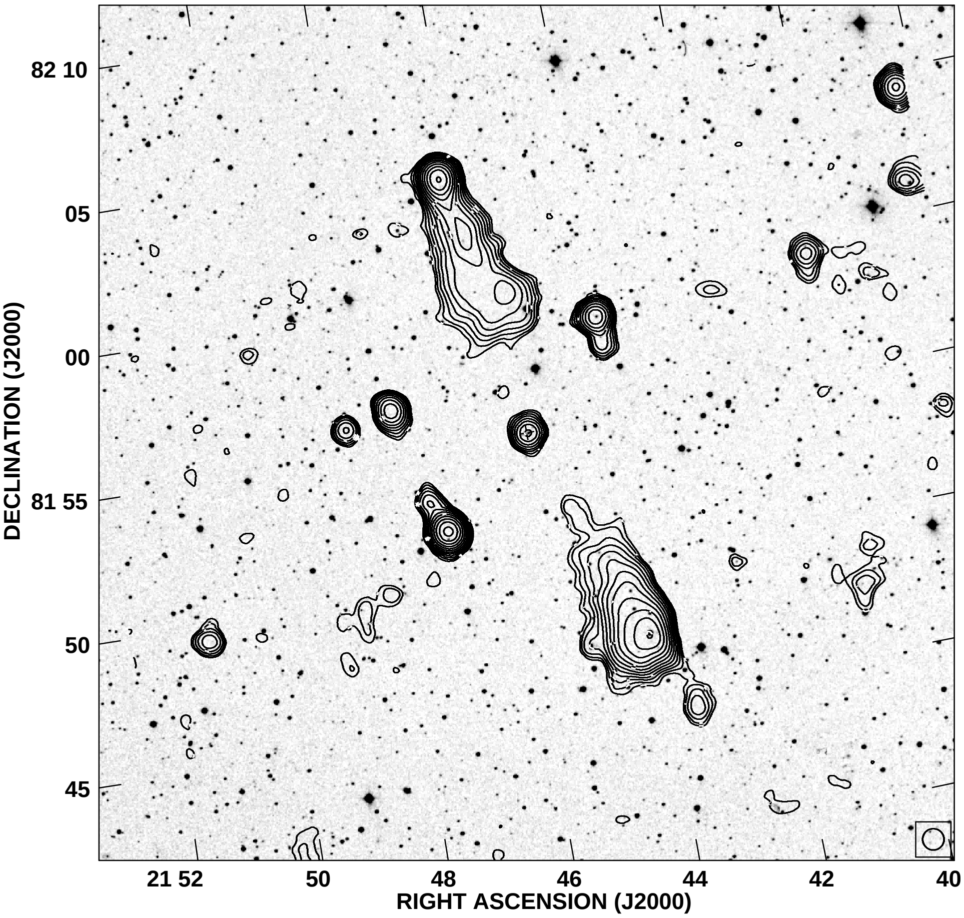
DECLINATION (J2000)
82 10
05
00
81 55
50
45
21 52
50
48
46
44
42
40
RIGHT ASCENSION (J2000)